SELF-CONSISTENT FIELD ERROR EFFECTS

IN

REVERSED FIELD PINCH PLASMAS

Kenneth Lee Sidikman

Under the supervision of Professor James D. Callen

This work concerns magnetic field perturbations induced inside a reversed field pinch (RFP) plasma by field errors at the plasma edge. Such perturbations can have an important effect on the plasma behavior. Some of the key features of the RFP depend upon an edge region of reversed toroidal field. Perturbations with poloidal mode number (m) equal to zero resonate with the plasma at the field reversal point and threaten to disrupt this region. Perturbations with m=1 can influence the instabilities that play a role in maintaining the RFP state. In assessing these effects, it must be remembered that interaction with the plasma can also alter the perturbations. Thus, the plasma-perturbation interaction should be calculated self-consistently.

Such a calculation was undertaken, combining a field error model with a model of the RFP equilibrium and allowing their interaction to be computed via the three-dimensional magnetohydrodynamic (3-D MHD) equations. Realistic plasma features, such as a partially-relaxed equilibrium (finite gradient in $\lambda \equiv J/B$), were incorporated. In addition,

the use of a set of dynamical equations allowed perturbed flow and finite resistivity (η) and viscosity (ν_0) to come into play. It is shown that all of these have measurable effects.

Numerical simulations of the 3-D MHD equations were performed using a static equilibrium. Of the three types of field errors considered, only perturbations from a gap in the conducting shell seriously affected the RFP equilibrium. Interaction with the equilibrium increased the amplitude of the radial magnetic field for $m=1$ modes and decreased it for $m=0$ modes, at their resonant surfaces.

An analytic investigation was performed to clarify the roles of finite grad-λ and finite η, ν_0 in the plasma-perturbation interaction. Finite grad-λ alone increases the amplitude of the radial magnetic field at the resonant surface for both $m=0$ and $m=1$ modes. For $m=0$ modes, finite η, ν_0 act to form a "dissipative layer" which counteracts this effect.

Numerical simulations with an evolving equilibrium were also performed. The field errors at the boundary did not affect the final steady state, but did influence which resistive instabilities were important in producing it.

ACKNOWLEDGMENTS

How do I begin to thank all of the people who both helped me and just plain put up with me during the (seemingly) endless term of this project? I'll do my best...

To start, I want to thank Dr. Rick Nebel of the Theory Group of the Controlled Thermonuclear Research Division at the Los Alamos National Laboratory. He initiated the numerical studies that are the heart of this dissertation, tutored me in the strange ways of the DEBS code, answered endless questions, soothed me the dozens of times I was convinced that everything I had done was wrong, and — along the way — became a true friend. I also want to thank all the other members of the Theory Group for their warm hospitality and friendly conversation during my many summer visits, with a special mention of Dr. Ron Moses for the contribution of his model of field errors due to a "butt joint" gap.

I certainly cannot leave off the thanks due to the CTR division without expressing my great appreciation for the efforts of Jim Melton, who saved me from a horrible fate (I'm told) by running the EFFI code to obtain the ZT-40M and ZT-H toroidal field coil errors. I am also indebted to Joe DiMarco and Al Haberstich for information about the ZT-H design. Thanks are due to Warren Quinn and the CTR management for their financial support of my summer stays.

Closer to home, I want to express my appreciation to my advisor, Dr. Jim Callen. It was his urging and his influence that put me on the road to Los Alamos that spring of 1985, a road that had this dissertation at the other end. I am truly grateful for the insight that caused him to suggest that I consider incompressible perturbations. This contribution rescued my analytic efforts from a swamp of algebra and led them toward their final 100 + page glory. Finally, I'm glad that he put up with my sense of humor.

If you think that this dissertation *looks* good, Eric Goetz must get the credit. He taught me everything I know about "desk top publishing," including terms like *font, smart quotes,* and *kerning*! He also helped take some of the pressure off by teaching me about sounds like "doiyng."

I owe a debt of thanks to Professors Prager, Sprott, and Dexter for their encouragement and the useful discussions that took place over the course of this work. In particular, Professor Dexter provided me with the design data on the holes in the MST shell. Credit is due to all my friends in the plasma group, especially my two officemates Jeff Beckstead and Saeed Assadi. It's tough to put up with someone who's on the verge of becoming a screaming maniac at any time over the period of a month. Special thanks to Tom Lovell for much appreciated assistance in the area of drafting and for physical insights on vertical fields.

Finally, on a more personal note, thanks to my parents for being a rock of steady support and love throughout the whole time I've been here in Madison. Thanks also to my wonderful friends, the Kelloggs and the Witzelings, for being there for me even when it seemed like I wasn't anywhere to be found. I'm so glad you're still here at the finish line!

Oh yeah, this work was financially supported by the U.S. Department of Energy. Thanks for your tax dollars!

CONTENTS

CHAPTER 1

INTRODUCTION

1.1 THE REVERSED FIELD PINCH CONFIGURATION

The use of the "pinch effect" to confine a plasma column is an idea with a long history in the plasma physics community. A good survey of this history is provided in "Reversed-Field-Pinch Research," a review paper by Bodin and Newton.[1] For the purposes of this work, the ideas leading up to the experimental and theoretical investigation of the reversed field pinch (RFP) will be summarized, with an emphasis on the importance of the region of reversed toroidal field.

The possibility of balancing the pressure forces within a current-carrying plasma column by compression from the self-generated magnetic field was first investigated by Bennett in 1934.[2] Early pinch experiments proved susceptible to fast magnetohydrodynamic (MHD) instabilities,[3] including current-driven kink modes.[4] Theoretical models using ideal (dissipationless) MHD by Rosenbluth,[5,6] Tayler,[7] and Shafranov[8,9] predicted that the addition of a magnetic field along the direction of the column (axial or toroidal field B_ϕ) of a comparable size to the self-generated field (azimuthal field B_θ) could stabilize azimuthally-symmetric ($m=0$) instabilities and retard kink-type ($m=1$) instabilities. Experimentally, such "stabilized pinches" exhibited

gross stability of position, but were subject to other instabilities and associated fluctuations. The previous theories had assumed that current was confined to a thin layer at the edge of the plasma column. As theory began to treat the instabilities associated with distributed currents via the "energy principle"[10] and its applications,[11,12] two approaches toward pinch stability developed. In the tokamak concept, $B_\phi \gg B_\theta$ was chosen. This gives stability to external kink modes by ensuring that the plasma current (related to B_θ) is less than the Kruskal–Shafranov limit (related to B_ϕ). If $q = r B_\phi / R B_\theta > 1$, then the tokamak (in periodic cylindrical geometry) is stable to ideal internal modes driven by both current and pressure.[13] In the RFP concept, $B_\phi \sim B_\theta$ was retained. However, the direction of B_ϕ was reversed at the edge of the plasma. (Hence, *reversed field* pinch.) The extra shear in the magnetic field thus created stabilizes ideal internal modes. Stability to external kink modes is provided by a conducting wall.[14]

The increased shear provided by the region of reversed field at the RFP edge has several practical advantages. The theoretical work of Robinson[15] shows that cylindrical pinch configurations with a minimum in pitch ($P = r B_\phi / B_\theta$) are subject to current–driven ideal instabilities localized about this minimum. This is especially important when the plasma column is surrounded by a small vacuum region, where $P \sim B_\phi r^2$, as is the case in many experiments. Unless the pitch profile in the plasma column rises monotonically, as in a tokamak, there will be a pitch minimum near the edge. In the RFP, stability is achieved by having $B_\phi < 0$

there. The pitch profile then falls through zero and can match to $P \sim -r^2$ in the vacuum, allowing a monotonic decrease. Such a profile also has a large slope, giving increased shear in the edge magnetic field. According to the analysis of Suydam,[16] shear can provide stability to localized pressure-driven ideal instabilitites. In principle, the large shear in an RFP can balance a considerable pressure gradient. Theoretical equilibria with values of β (ratio of particle energy to field energy) large compared to those for the relatively high-field tokamak have been found which are stable to ideal modes. Thus, the reversed field region makes it possible for an experimentally-attractive ideally stable, high-β configuration to exist, even in the presence of a small edge vacuum region.

The experimental realization of an ideally stable equilibrium with high β requires detailed programming of the pressure and magnetic field profiles. Given the technology to achieve this, a further difficulty arises from the tendency of a real plasma, which has small but finite dissipation, to evolve away from these profiles through resistive diffusion. Fortunately, the plasma has a tendency to generate profiles that have the proper shape (although perhaps not the theoretically optimum β). A well-known example is the ZETA experiment, which exhibited a spontaneous onset of toroidal-field reversal followed by an interval of quiescence.[17] This "quiet period" was characterized by a rise in electron temperature, β , and energy and particle confinement times which lasted as long as the reversed field was maintained. Edge fluctuations in electron temperature and electrostatic potential were greatly reduced. Theoretically,

this can be understood in terms of the stabilization of ideal pressure-driven modes. The Suydam criterion for stability was violated before the quiet period, but was later satisfied through the increase in shear brought about by reversal. In more modern RFP's, this reversal can be sustained.

A theory has been constructed to account for the appearance and sustainment of a reversed toroidal field. It asserts that experimental RFP states are near a minimum energy state, to which the plasma attempts to relax. The model, due to J. B. Taylor,[18,19] calculates the fully relaxed state of a non-ideal toroidal plasma in which the particle energy is negligible compared to the magnetic energy ($\beta=0$). The magnetic energy is minimized, subject to the constraint of constant total helicity, K_0. The total helicity is defined as $K_0=\int \mathbf{A}\cdot\mathbf{B}\,dV$, where $\mathbf{B}=\nabla\times\mathbf{A}$ and the integral is over the total plasma volume. The resulting fields are given by:

$$\nabla\times\mathbf{B} = \lambda\,\mathbf{B} \qquad \text{with} \qquad \lambda = \text{constant}. \qquad (1.1.1)$$

The value of λ is determined by the choice of K_0 and the toroidal flux $\Phi_T \equiv \int\int dA_\phi\, B_\phi = \pi a^2 (B_\phi)_{AVG}$, where the integral is over a poloidal cross-section and $(B_\phi)_{AVG}$ is the average toroidal field thus obtained. An axisymmetric minimum energy state with a reversed toroidal field, commonly called the "Taylor State," exists for $2.40 < \lambda a < 3.11$ (a = plasma minor radius). The field profiles are given by Bessel functions, and the model is also referred to as the Bessel Function Model (BFM). As the endpoint of a relaxation process, this state can be described in terms of global quantities — $F \equiv B_\phi(a) \,/\, (B_\phi)_{AVG}$, which measures the amount of

reversal, and the pinch parameter $\Theta \equiv B_\theta(a) / (B_\phi)_{AVG} = \mu_0 I a / 2\Phi_T$ — rather then initial conditions. Theory predicts a unique curve in F – Θ space. A plot of F versus Θ for several different RFP experiments forms a locus of points close to this curve, even though the final RFP state can arise from a variety of different initial conditions. Thus, relaxation theory appears to account for the experimentally – observed reversal.

The means by which the relaxation process proceeds has been a subject of active interest in the RFP theory community. A model which has enjoyed some success has been relaxation via the action of long – wavelength resistive MHD instabilities. As in the case of ideal modes, the region of reversed field at the edge of the plasma plays an important role. Numerical simulations of the force – free ($\beta = 0$) resisitive MHD equations have been performed.[20, 21] Results show that a steady state with a reversed axial field (on average) can be generated and sustained by the action of long – wavelength (poloidal mode number m = 1) resistive instabilities. However, the growth and overlap of magnetic islands formed by these instabilities leads to a region of stochastic magnetic field in the plasma core. This can be seen in Figure 1.1, in which puncture plots indicate the position of field lines in a plane of constant – θ at two different times.[22] As time progresses, the field lines wander throughout 90% of the plasma volume, *except* in the region of reversed field. The increased shear there prevents the growth of large magnetic islands whose overlap leads to stochasticization of the magnetic field. Good flux surfaces are maintained and act as barriers to the radial wandering of field lines from the core.

Thus, resistive instabilities can relax the plasma into an RFP state, with radial confinement provided by good flux surfaces in the reversal region.

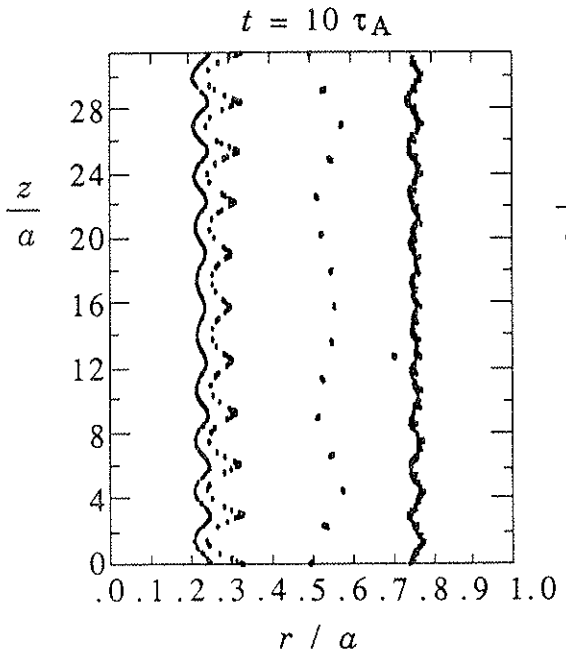

Figure 1.1 a Field–line puncture plot at $t = 10\ \tau_A$. Good flux surfaces still exist in the plasma core. Field lines wander somewhat.

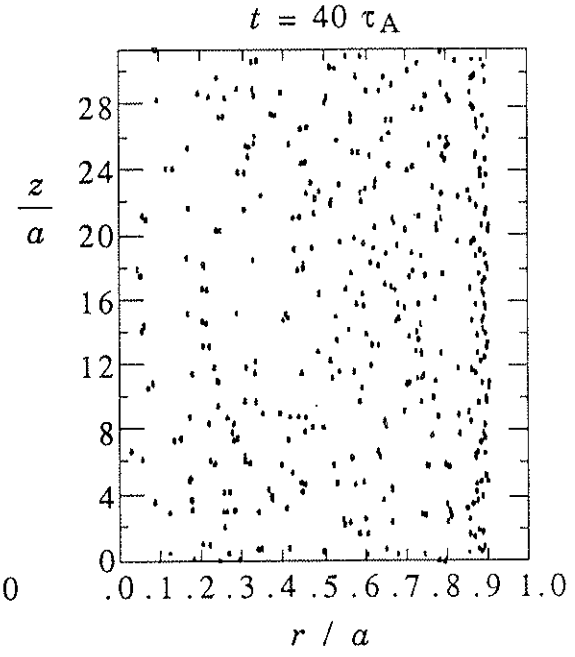

Figure 1.1 b Field–line puncture plot at $t = 40\ \tau_A$. Good flux surfaces are gone, except in the edge. Field lines wander throughout the core, but not in the reversal region.

The RFP configuration offers several features that make it attractive for study. On the practical side, the large magnetic shear is capable of supporting a high–β equilibrium and maintaining ideal MHD stability to internal ideal modes. With external ideal modes stabilized by a conducting wall, the current can be raised above the Kruskal–Shafranov limit,

promising high current density and efficient Ohmic heating. On the more abstract side, plasma relaxation and the sustainment of reversal against diffusion, along with the associated transport, are fascinating problems in fundamental plasma physics. As has been emphasized, all these features are linked to the presence of a region of reversed field at the plasma edge.

1.2 THE EFFECTS OF FIELD ERRORS

Any experimental device designed to produce an RFP plasma will have some limitations that give rise to magnetic "field errors." These are local or non-axisymmetric fields that are not part of the basic RFP configuration. For example, the toroidal field in the plasma is ordinarily produced by external coils made up of discrete windings. Moving along the torus, the magnitude of the field will fluctuate slightly as the various turns are passed. The net field consists of a toroidally-uniform B_ϕ with a slight "ripple" superimposed on it. This non-axisymmetric ripple is a "field error." Since the coils have poloidal symmety, the ripple will have Fourier components with $m = 0$, $|n| > 0$ (where m and n are the poloidal and toroidal mode numbers). Although an increase in the number of coils can decrease the size of the ripple, it can never be totally eliminated.

Field errors have the potential to harm an RFP plasma by disrupting the important reversal region at the edge. A theoretical picture of this can be sketched, based on the discussions in the previous section. Consider the effects of the ripple fields mentioned above. These introduce $m = 0$ field perturbations into the plasma which resonate with the RFP

fields at the toroidal-field reversal surface. The resonant radial perturbations form magnetic islands from the good flux surfaces in the reversal region. This leads to some loss of confinement, as the transport across an island is much faster than that across an intact flux surface. In addition, the formation of an m = 0 island forces the pitch to be close to zero in that area. This pitch-flattening reduces the shear in the reversal region, possibly leading to the onset of localized ideal instabilities and further loss of confinement. Finally, if the field errors are large enough, the m = 0 magnetic islands could interact with the stochastic core. In this case, good flux surfaces would be destroyed. Confinement would be lost through transport of plasma to the wall along stochastic field lines.

Other types of field errors can also be dangerous. Perturbations with m = 1 can spur the growth of plasma instabilities and increase the extent of the stochastic core, or initiate the above sequence of events by the non-linear production of m = 0 islands. Localized perturbations can divert the good flux surfaces in the edge towards the wall. Stochastic fields can then wander closer to the wall and increase transport in these regions.

In fact, experimental RFP devices experience better performance when field errors are corrected. The main effects observed are a decrease in the loop voltage (V_{LOOP}) needed to drive the toroidal plasma current (I), with a corresponding improvement in the global energy confinement time: $\tau_E \propto \beta_\theta I / V_{LOOP}$. The pulse duration ($\tau_{PULSE}$) also increases.[23] For example, in the HBTX1 device at Culham Laboratory in England, an

upgrade from HBTX1 – A to HBTX1 – B produced a factor of 5 reduction in field errors due to ripple and distortion around ports in the shell. When a steady vertical field was used to center the plasma and prevent flux surfaces from intersecting the wall, an increase in τ_E by up to a factor of 5 resulted, in discharges with sustained current and density.[24] In the TPE–1RM15 device at the Electrotechnical Laboratory in Japan, minimization of field errors was a specific aspect of the design. The application of a DC vertical field allowed an increase in τ_E by about a factor of 3. Use of a time–varying vertical field to control field errors at the gap (cut in the conducting shell) resulted in an increase in τ_{PULSE} by up to a factor of 8 (~ 1 to ~ 8 ms.).[25] An increase in τ_{PULSE} with a similar type of correction was also observed in the OHTE experiment at General Atomic.[26] At Los Alamos, the ZT–40M RFP was able to extend τ_{PULSE} by a factor of 3 (from 9 to 27 ms.) when large irregularities in the magnetic geometry were corrected.[27] Thus, field errors have a significant effect on experimental RFP performance.

1.3 MOTIVATION AND OUTLINE OF THE PRESENT WORK

Calculations of field errors produced by the physical "imperfections" necessary for a practical RFP experiment (ports in the conducting shell for diagnostic access, gaps in the shell for penetration of externally–generated fields, coils of finite extent) have been performed. The errors due to holes in the conducting shell have been investigated both analytically[28] and numerically.[29,30] A good survey, which includes analytic and empirical

expressions for field errors from a variety of sources and applies these expressions to various machines, has been given by Newton.[31]

One limitation of these calculations was that they did not include the response of the plasma. Recently, Pinsker and Reiman performed a field error calculation which included the effects of self-consistent plasma current.[32] They confined their attention to the important case of islands formed around the field reversal surface in the presence of external m = 0 field perturbations. As has already been mentioned, the ripple associated with the toroidal field coils produces perturbations of this kind. The model chosen to represent the self-consistent plasma fields and currents was the relaxed "Taylor State," described in equation (1.1.1). In the calculation, m = 0 plasma perturbations satisfying equation (1.1.1) were matched to m = 0 vacuum perturbations outside the plasma, across a free boundary. It was predicted that the resulting islands at the field reversal surface are amplified by the self-consistent response of the plasma, especially in the absence of a close-fitting conducting wall.

Obviously, field errors have been an important design consideration for the next generation of RFP devices, including ZT-H at Los Alamos and MST at the University of Wisconsin-Madison. Preliminary calculations of errors in the absence of plasma were performed and tolerances on "acceptable" error size were set.[33,34] However, the results of Pinsker and Reiman pointed to the importance of self-consistently evaluating the effects of field errors in the presence of a

plasma. The availability of a reliable 3-D MHD code at Los Alamos, with recent improvements designed to facilitiate the study of long-timescale resistive phenomena, led to a collaboration between Los Alamos and the University of Wisconsin-Madison. Over the course of several summers, I worked with Dr. Richard Nebel and other members of the Controlled Thermonuclear Research Division on applying this code to the self-consistent field error problem. A series of simulations was performed.

The treatment of Pinsker and Reiman was extended by assuming an RFP equilibrium and numerically calculating the relaxation of the perturbations caused by external field errors. Interactions between the plasma and the perturbations were modeled by the resistive MHD equations shown below:

$$\mathbf{E} = -\mathbf{V}\times\mathbf{B} + \eta\,\mathbf{J} \tag{1.3.1}$$

$$\frac{\partial \mathbf{B}}{\partial t} = -\nabla\times\mathbf{E} \tag{1.3.2}$$

$$\rho\left[\frac{\partial \mathbf{V}}{\partial t} + \left(\mathbf{V}\cdot\nabla\right)\mathbf{V}\right] = \mathbf{J}\times\mathbf{B} + \nu_0\nabla^2\mathbf{V} \tag{1.3.3}$$

$$\mu_0\,\mathbf{J} = \nabla\times\mathbf{B} \tag{1.3.4}$$

$$\nabla\cdot\mathbf{B} = 0 \quad . \tag{1.3.5}$$

In these equations, the displacement current is neglected in Ampere's Law, equation (1.3.4), since the low-frequency resistive evolution is of interest. In the expression for momentum balance, equation (1.3.3), the plasma

stress tensor is handled in a particular way. The diagonal terms, which give rise to pressure-gradient forces, are neglected. The off-diagonal terms, which give rise to various viscous stresses, are represented as a "fluid-like," or collisional, viscosity. Even with these approximations, the use of the given MHD equations to calculate the self-consistent plasma response has some advantages over the assumption of a totally-relaxed state. For example, experimental RFP plasmas are not totally relaxed. This model allows for the input of equilibrium profiles that more accurately represent them. Furthermore, the equations include resistivity, viscosity, and flow, which are important in understanding the evolution of an experimental plasma toward a relaxed state. All of these features will turn out to have significant effects.

The balance of this work deals with the results obtained from the MHD model. In Chapter 2, calculations of the field errors are described, and the results of the MHD simulations are presented. The effects produced by the features of the model mentioned above are considered in the next two chapters. Linear calculations of the profiles assumed by externally-induced perturbations in the presence of a fixed RFP equilibrium are presented. Perturbations with m = 1 are taken up in Chapter 3, and those with m = 0 in Chapter 4. Chapter 5 consists of a numerical examination, via the 3-D MHD code, of the effects of external field errors on an evolving RFP plasma. Finally, Chapter 6 contains some concluding remarks.

REFERENCES

[1] H. A. B. Bodin and A. A. Newton, Nucl. Fusion **20**, 1255 (1980).

[2] W. H. Bennett, Phys. Rev. **45**, 890 (1934).

[3] S. Glasstone and R. H. Lovberg, *Controlled Thermonuclear Reactions* (D. van Nostrand, Princeton, New Jersey, 1960).

[4] M. Kruskal and M. Schwarzschild, Proc. R. Soc. London Ser. A **223**, 348 (1954).

[5] (a) M. Rosenbluth , "Stability of the Pinch," LA – 2030, Los Alamos Scientific Laboratory, (1956).

(b) M. N. Rosenbluth, in *Proceedings of the Second International Conference on the Peaceful Uses of Atomic Energy*, (UN, Geneva, 1958), Vol. 31, p. 85.

[6] M. Rosenbluth, "Infinite Conductivity Theory of the Pinch," LA – 1850, Los Alamos Scientific Laboratory, (1956).

[7] R. J. Tayler, Proc. Phys. Soc. London B70 **31**, 1049 (1957).

[8] V. D. Shafranov, Sov. J. At. Energy **1**, 709 (1956).

[9] V. D. Shafranov, in *Plasma Physics and the Problem of Controlled Thermonuclear Reactions, Vol. 2*, edited by M. A. Leontovich (Pergamon Press, London, 1959), p. 197.

[10] I. B. Bernstein, E. A. Frieman, M. D. Kruskal, and R. M. Kulsrud, Proc. R. Soc. London Ser. A **244**, 17 (1958).

[11] W. A. Newcomb, Ann. Phys. **10**, 232 (1960).

[12] D. C. Robinson, Plasma Phys. **13**, 439 (1971).

[13] J. P. Freidberg, Rev. Mod. Phys. **54**, 801 (1982).

[14] *Ibid.*, pp. 874 – 877.

[15] D. C. Robinson, Plasma Phys. **13**, 439 (1971).

[16] B. R. Suydam, in *Proceedings of the Second International Conference on the Peaceful Uses of Atomic Energy*, (UN, Geneva, 1958), Vol. 31, p. 157.

[17]H. A. B. Bodin and A. A. Newton, Nucl. Fusion **20**, 1255 (1980).

[18] Original paper: J. B. Taylor, Phys. Rev Lett. **33**, 1139 (1974).

[19] Review paper: J. B. Taylor, Rev. Mod. Phys. **58**, 741 (1986).

[20]A. Y. Aydemir, D. C. Barnes, E. J. Caramana, A. A. Mirin, R. A. Nebel, D. D. Schanck, and A. G. Sgro, Phys. Fluids **28**, 898 (1985).

[21] D. D. Schnack, D. C. Barnes, Z. Mikic, D. S. Harned, and E. J. Caramana, J. Comp. Phys. **70**, 330 (1987).

[22] D. D. Schnack and R. A. Nebel, Phys. Fluids **28**, 321 (1985).

[23] A. A. Newton, in Physics of Mirrors, Reversed Field Pinches and Compact Tori, edited by S. Ortolani and E. Sindoni (Editrice Compositori, Bologna, 1988), p. 221.

[24] B. Alper, V. Antoni, M. K. Bevir, H. A. B. Bodin, C. A. Bunting, P. G. Carolan, J. Cunnane, D. E. Evans, A. R. Field, S. J. Gee, C. G. Gimblett, R. Hayden, T. R. Jarboe, P. Kirby, A. Manley, A. A. Newton, P. G. Noonan, A. Patel, R. S. Pease, M. G. Rusbridge, K. P. Schneider, D. P. Storey, H. Y. W. Tsui, S. Whitfield, and P. D. Wilcock, in *Proceedings of the Eleventh International Conference on Plasma Physics and Controlled Nuclear Fusion Research*, Kyoto, Japan (IAEA, Vienna, 1987), Vol. 2, p. 399.

[25] T. Shimada, Y. Hirango, Y. Yagi, A. A. Newton, and K. Ogawa, in *Proceedings of the Eleventh International Conference on Plasma Physics and Controlled Nuclear Fusion Research*, Kyoto, Japan (IAEA, Vienna, 1987), Vol. 2,
p. 453.

[26] R. J. LaHaye, G. L. Goforth, M. J. Jackson, M. J. Schaffer, and P. L. Taylor, Bull. Am. Phys. Soc. **26**, 1056 (1981).

[27] R. B. Howell and H. F. Vogel, J. Appl. Phys. **56**, 2017 (1984).

[28] J. W. Rudmin and J. R. Drake, Appl. Phys. **48**, 3 (1977).

[29] R. B. Howell and H. F. Vogel, J. Appl. Phys. **56**, 2017 (1984).

[30] R. Spencer, in Proceedings of the Reversed Field Pinch Theory Workshop, edited by H. R. Lewis (Los Alamos National Laboratory, Los Alamos, New Mexico, 1982), p. 129.

[31] A. A. Newton, in Physics of Mirrors, Reversed Field Pinches and Compact Tori, edited by S. Ortolani and E. Sindoni (Editrice Compositori, Bologna, 1988).

[32] R. I. Pinsker and A. H. Reiman, Phys. Fluids **29**, 782 (1986).

[33] For ZT-H, see: J. N. DiMarco in *Proceedings of the International Workshop on Engineering Design of Next Step Reversed Field Pinch Devices*, edited by D. B. Thomson (Los Alamos National Laboratory, Los Alamos, New Mexico, 1987), p.23.

[34] For MST, see: R. N. Dexter, D. W. Kerst, T. W. Lovell, S. C. Prager, J. C. Sprott, "MST Technical Design Considerations," PLP 965, University of Wisconsin-Madison (December, 1985). or

R. N. Dexter, D. W. Kerst, T. W. Lovell, S. C. Prager, and J. C. Sprott, "Madison Symmetric Torus," submitted to Fusion Technology, November 1989.

CHAPTER 2

NUMERICAL RESULTS FOR A STATIC RFP EQUILIBRIUM

2.1 INTRODUCTION

This chapter presents the results of numerical simulations of an RFP plasma in the presence of edge field errors. The simulations were designed to allow perturbations induced by the field errors to interact with a specified set of magnetic fields representing an RFP equilibrium. This interaction was brought about through the equations of nonlinear, three-dimensional magnetohydrodynamics (3-D MHD). The final state was then a plasma-perturbation mixture showing the effects of the equilibrium currents on the error-induced perturbations and the perturbed radial fields on the equilibrium field structure. The goal was to produce a picture that was self-consistent and included some realistic dynamics and plasma characteristics.

A general outline of the calculation is presented in Section 2.2 . The choice of a very particular sort of RFP equilibrium, one which was both stable and static, is motivated and the form of the equilibrium is given there. The way in which the field errors were imposed at the boundary of the plasma is detailed. In addition, the initial (non-self-consistent)

profiles of the perturbations within the plasma volume are derived. Finally, the interaction is described.

Section 2.3 contains information about the code used to perform the simulation. The equations and geometry are described. Values of various inputs, such as quantities characterizing the spatial grid and dimensionless physical parameters, are given. Some mention is made of the increases in computing power and advances in numerical algorithms which combined fortuitously to make a calculation of this type possible.

Field errors at the plasma edge arising from three different sources were studied. These errors, and the models used to calculate them, are described in Sections 2.4 – 2.6 . The sources were: the discreteness of the toroidal field coils and any asymmetry in their positioning (2.4), the flow of plasma – induced currents around holes in the conducting shell (2.5), and the flow of such currents around a "butt joint" gap in the shell (2.6) .

These sections also include the results of the numerical simulations. First, there is general information on the final plasma – perturbation state. Next, the effects of the plasma on the perturbations are detailed. Finally, the effects of the perturbations on the equilibrium flux surfaces are given for plasma parameters corresponding to an actual RFP device. Three different machines were considered: ZT – 40M, a device in operation at Los Alamos National Laboratory at the time that the simulations were performed; ZT – H, a device being designed at Los Alamos at that time; and MST, a device then under construction at the

University of Wisconsin-Madison. As outlined in Chapter 1, these "machine performance results" have important implications for the ability of these devices to perform as designed.

2.2 COMPUTATIONAL MODEL

The simulation was a time-dependent, boundary-value problem. As such, it required both initial conditions and boundary conditions. The most important initial condition was the specification of the equilibrium fields. The boundary conditions involved imposition of the field errors at the plasma edge. The special choices that went into both of these will be described below.

The model for the equilibrium fields was chosen to be a relaxed state which is characteristic of an experimental plasma. The Modified Bessel Function Model (MBFM)[1], developed at Los Alamos, is a modification of the minimum-energy state (Bessel Function Model) of the Taylor relaxation theory.[2] The change is necessary to reproduce the experimental results observed in ZT-40M. Essentially, the equilibrium current is allowed to vanish at the wall bounding the plasma. This is what would be expected in an experimental plasma with a cold, resistive edge in contact with a material boundary. In addition, with a proper choice of model parameters, the global quantities predicted by the model (toroidal and poloidal voltage, toroidal flux, F versus Θ) show excellent agreement with those observed in the experiment, as a function of time.[3] Over a large range of operating parameters and without reference to initial

conditions, the MBFM accurately represents a steady-state which exhibits reversal of the toroidal field for a time longer than that which would be required for such a field profile to diffuse away resistively.[4] Thus, even though this model is not a Taylor minimum-energy state, it is assumed to be a similar end-product of plasma relaxation. In this case, the experimental plasma it represents has additional features which do not conform to the assumptions of the original theory.

The relaxed state was taken to be force-free. This approximates the conditions in the low-beta plasmas observed experimentally. The fields are solutions of a steady-state force-balance equation from which the pressure term has been removed:

$$\mathbf{J}_0 \times \mathbf{B}_0 = 0 \ . \tag{2.2.1}$$

This equation has the general solution

$$\mathbf{J}_0 = \frac{\lambda(r)}{\mu_0} \mathbf{B}_0 \ . \tag{2.2.2}$$

The relaxed fields sought are of the form

$$\mathbf{B}_0(r) = B_{\theta 0}(r)\ \hat{\theta} + B_{z\,0}(r)\ \hat{z} \ . \tag{2.2.3}$$

The current can be eliminated from equation (2.2.2) by combining it with equation (1.3.4), which relates current to magnetic field. The equation for the magnetic fields then becomes:

$$\nabla \times \mathbf{B}_0 = \lambda(r)\mathbf{B}_0 \ . \tag{2.2.4}$$

All that remains is the selection of a profile for $\lambda(r)$ and an overall constant which gives the on-axis field strength.

The form of the $\lambda(r)$-profile is what gives the Modified Bessel Function Model its name. The profile is piece-wise linear. In the center of the plasma volume, $\lambda(r) = \lambda_0 = \text{constant}$. A value of λ which is constant across the entire plasma is what characterizes the Bessel Function Model. In this case, however, a modification occurs near the plasma edge, at a cutoff radius here called r_n. (Perversely, the "n" subscript stands for the "knee" in the λ-profile. The "k" is silent.) From this point to the edge, at radius $r = a$, the value of λ decreases linearly to zero. A picture of this profile is shown in Figure 2.1 below.

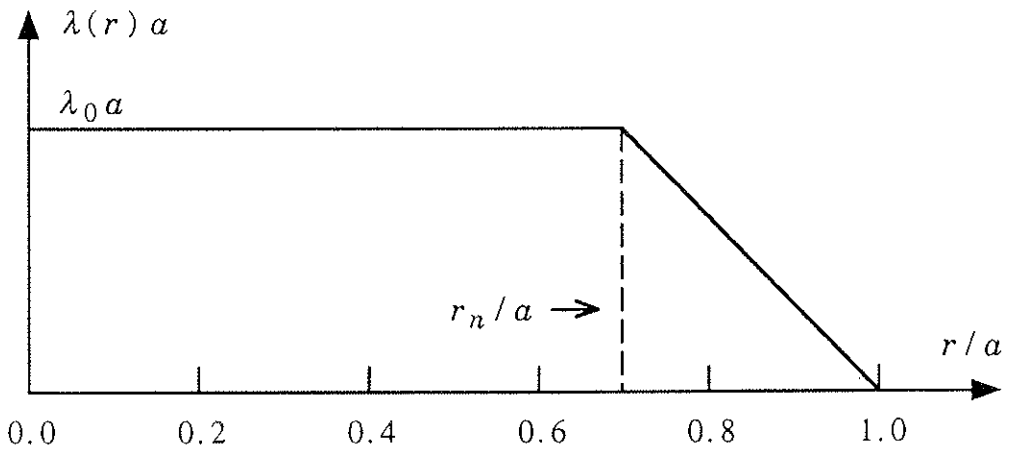

Figure 2.1 Radial profile of $\lambda(r)$ in the Modified Bessel Function Model.

The values of the parameters λ_0 and r_n are related to the values of Θ and $F(\Theta)$ produced by the profile. Given a value of Θ, corresponding values of $F(\Theta)$, λ_0 and r_n can be obtained. This can be done to find the

parameters which best model an actual ZT-40M discharge.[5] In obtaining the initial conditions for the simulation, however, the parameters were selected by requiring the resultant fields to satisfy a somewhat different condition. This will be discussed in the paragraphs that follow. In any case, a value of Θ corresponding to a "typical" low-theta experimental shot ($\Theta = 1.515$) was chosen. The other parameters have the following values:

$$F(\Theta) = -.1444\,, \qquad \lambda_0 = 2.950\,, \qquad r_n = 0.70\,a\,.$$

Figures 2.2 and 2.3 show the relaxed field and current profiles produced by (2.2.4) with a λ-profile using the above parameters. They represent the

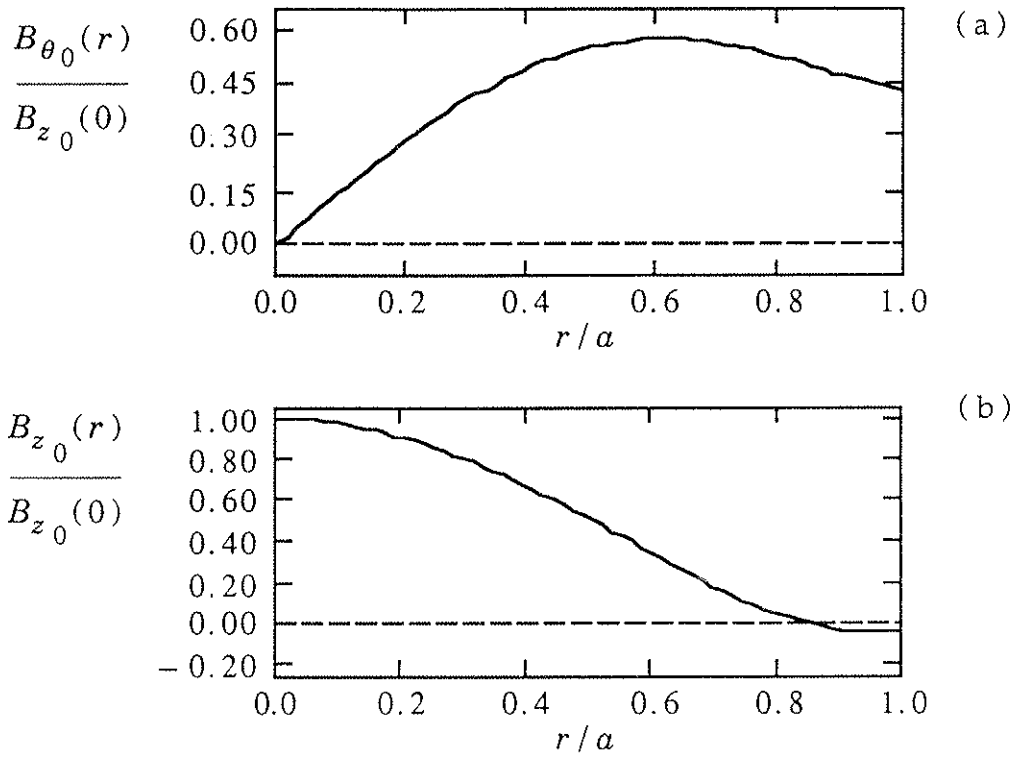

Figure 2.2 Poloidal (a) and axial (b) magnetic field profiles in the Modified Bessel Function Model.

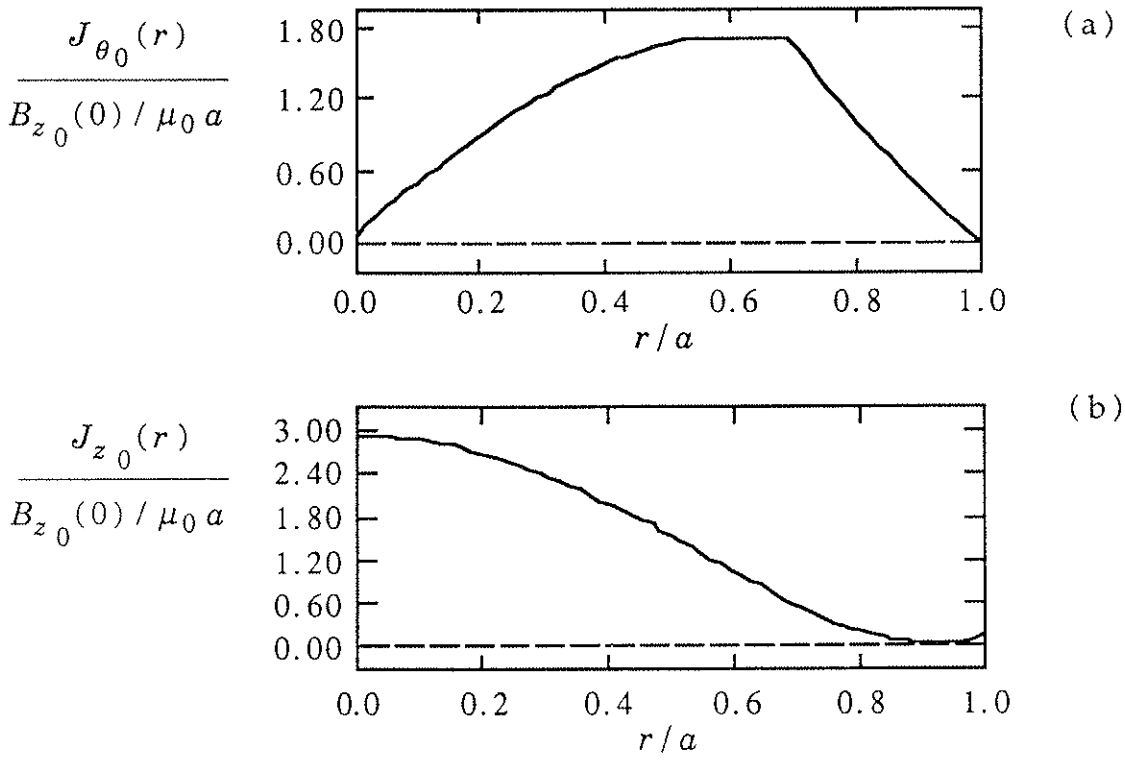

Figure 2.3 Poloidal (a) and axial (b) current profiles in the Modified Bessel Function Model.

RFP equilibrium used in the initialization of the simulation.

It was advantageous to use an equilibrium that was stable to resistive instabilities. These instabilities play an important role in the physics of the RFP. However, their role cannot be studied effectively in a device in which the RFP state is dominated by external influences, such as field errors. It was the object of this simulation to investigate the interaction of the equilibrium fields and currents with perturbations induced by edge field errors. The presence of additional perturbations

arising from plasma instabilities would only have masked the extent of the externally-produced effects. This is another reason why relaxed profiles were chosen as the equilibrium; if the plasma were truly relaxed, these profiles would be stable.

The model which was chosen, however, is not completely relaxed. As has already been pointed out, it is not a Taylor minimum-energy state. In theory, there is still "free energy" available to drive instabilities. Thus, although the model describes a state that is relaxed on the average, the plasma which is being represented can be made to oscillate about this state through the growth and interaction of instabilities. (There is some evidence for this in the experimental data.[6])

To prevent the growth of instabilities in the simulation, the values of λ_0 and r_n were chosen in a particular way. Initially, values characteristic of a typical 120 kA discharge from ZT-40M were chosen. A linear stability code[7] was used to test the stability of the resulting equilibrium field profiles. The values of λ_0 and r_n were then adjusted so as to produce stable profiles. Only profiles with values of Θ and $F(\Theta)$ close to what would be expected from experimental data were considered. Stable profiles were found for the values of the parameters given previously.[8] To prevent the plasma from evolving away from this initial state due to resistive diffusion, the resistivity was set to zero in the equilibrium evolution equation. Thus, it was possible to use stable profiles to characterize the RFP plasma for the entire simulation.

In this simulation, the RFP plasma described above was bounded by a perfectly conducting wall. This has been a good model for the conventional mode of operation of the present generation of RFP's. In these machines, the time constant associated with the penetration of a magnetic field through the conducting shell around the plasma is longer than the discharge time. This is the case with ZT-40M[9] and MST[10], and the simulation can be said to represent the plasma boundary in these machines fairly well.

Recently, a series of experiments has been performed on several machines[11,12,13] to investigate the behavior of an RFP in the presence of a resistive shell. The time constant for field penetration through a resisitive shell is comparable to the length of the discharge. Such a shell provides the advantage of external control of the global equilibrium position. For this reason, ZT-H has been designed with a resistive wall.[14] However, the introduction of such a shell also permits the growth of new plasma instabilities.[15,16] As was mentioned previously, such instabilities would mask the effects of the perturbations induced by field errors. As an externally-introduced influence, they are another source of concern, but this is a separate issue. Thus, ZT-H will also be modeled with a perfectly conducting wall boundary. The simulation can be thought of as examining the effects of error-induced perturbations on a time-scale shorter than a shell time.

The boundary condition at the wall was that the radial magnetic fields are given by the radial field errors. These fields are permitted even though the wall has been assumed to be a perfect conductor. In the case of stray fields from the toroidal field coils, it is assumed that the radial field errors have been present long enough to "soak through" the perfectly conducting wall. This is a reasonable approximation to an actual discharge, where the toroidal field coils are energized before the plasma current is initiated. In the other cases, radial field errors are produced when the plasma shifts its equilibrium position and induces currents in the wall. It is assumed that these currents sample non-conducting regions. Given these exceptions, the requirement of a perfectly conducting wall acts to limit the radial fields present at the boundary to the radial error fields.

These fields were also held fixed in time. For the stray fields from the toroidal coils, this is consistent with the conditions that allow them to penetrate the conducting-wall boundary. They are present on a very long time scale. An uncorrected shift in the equilibrium position of the plasma is caused by an error in the equilibrium-control system. This error is likely to persist for the duration of the discharge. In the case of the "butt joint" gap, however, the time dependence of the vertical fields involved in the equilibrium control is included in the field-error model. In this case, the simulation can be thought of as a "snap shot" of the plasma evolution at a particular point in time. In any event, the size of the field errors at the wall was held fixed throughout the simulation.

The equilibrium field profiles representing the RFP have been chosen and the field errors at the boundary have been described. All that remains in defining the simulation is an initial specification of the perturbation profiles associated with the edge field errors. Vacuum profiles were used. This choice is certainly appropriate in the case of the errors from the toroidal field coils, which are assumed to penetrate the wall before any plasma appears. In the other cases, it is just a simple initial assumption. In a vacuum, there is no current. Thus, equation (1.4.4) gives:

$$\nabla \times \mathbf{B} = 0 \ . \tag{2.2.5}$$

A general solution can be written in the form:

$$\mathbf{B} = -\nabla \Phi_M \ . \tag{2.2.6}$$

The form of the magnetic scalar potential Φ_M can be found by requiring (2.2.6) to satisfy equation (1.4.5):

$$\nabla \cdot \mathbf{B} = 0 \ . \tag{2.2.7}$$

Then, the vacuum profiles for **B** can be found from equation (2.2.6) with a magnetic scalar potential that satisfies

$$\nabla^2 \Phi_M = 0 \tag{2.2.8}$$

in the plasma volume, and the radial part of

$$\left[-\nabla \Phi_M \right]_{r=a} = \mathbf{B}_{\text{FIELD ERROR}} \tag{2.2.9}$$

at the plasma boundary. The specific form of these solutions for the geometry of the code used to perform the simulation will be given in the next section.

Viewed as a perturbation to a plasma, the vacuum profiles derived above lead to a time evolution. When added to an RFP equilibrium, they perturb only the magnetic fields and not the currents. Thus, the perturbations are not in force balance, and the plasma–perturbation combination will evolve in time. If fixed field errors at the boundary are added, this picture completely describes the simulation. The numerical code which carried forward the time evolution is described in the next section.

2.3 CODE DESCRIPTION

The simulation was performed by a code named DEBS.[17] This code is the implementation of the algorithm for solving the time–dependent, nonlinear, 3–D MHD equations described in the reference cited. The dependent variables are chosen to be the magnetic vector potential $\mathbf{A}$ ($\mathbf{B}=\nabla\times\mathbf{A}$) and the velocity $\mathbf{V}$. The algorithm is designed to focus attention on physical phenomena which evolve on long (resistive) time–scales, so the time variable (t) is scaled to the resistive diffusion time (τ_R). In an appropriate set of nondimensional variables, the equations to be solved are:

$$\frac{\partial \widetilde{\mathbf{A}}}{\partial \widetilde{t}} = S\,\widetilde{\mathbf{V}}\times\widetilde{\mathbf{B}} - \widetilde{\eta}\,\widetilde{\mathbf{J}} \tag{2.3.1}$$

$$\widetilde{\rho}\left(\frac{\partial \widetilde{\mathbf{V}}}{\partial \widetilde{t}} + S\,\widetilde{\mathbf{V}}\cdot\widetilde{\nabla}\,\widetilde{\mathbf{V}}\right) = S\,\widetilde{\mathbf{J}}\times\widetilde{\mathbf{B}} + \nu\,\widetilde{\nabla}^{2}\,\widetilde{\mathbf{V}} \tag{2.3.2}$$

$$\widetilde{\mathbf{J}} = \widetilde{\nabla}\times\widetilde{\mathbf{B}} \tag{2.3.3}$$

$$\widetilde{\mathbf{B}} = \widetilde{\nabla}\times\widetilde{\mathbf{A}}\ . \tag{2.3.4}$$

The gauge in which the gradient of the electrostatic potential is equal to zero has been chosen. Table 2.1 summarizes the relationships between physical and nondimensional (tilda-labeled) quantities.

Certain assumptions that go into the choice of the above equations are worthy of note. First, these equations do not contain the plasma pressure. This assumption of a zero-beta model approximates the experimental observation that RFP plasmas have low values of beta. It is consistent with the force-free relaxed state chosen to represent the RFP equilibrium. Second, the mass density is not evolved. Since the model does not contain pressure, it is reasonable to expect that large changes in mass density should not arise. However, the model is considered to be fully compressible, in the sense that $(\nabla\cdot\mathbf{V}) = 0$ is not imposed and that large-scale velocity perturbations can compress the magnetic field. It is assumed that any bunching of the mass density associated with this activity will not be important. A more recent version of the code, which includes mass density evolution, shows that these effects do not strongly

DIMENSIONAL QUANTITY	DIMENSIONLESS FORM	SCALE FACTOR
Density : ρ	$\tilde{\rho} = \rho / \rho_C$	Characteristic Density: $\rho_C = \rho(r=0)$
Resistivity : η	$\tilde{\eta} = \eta / \eta_C$	Characteristic Resistivity: $\eta_C = \eta(r=0)$
Distance : ∇	$\tilde{\nabla} = a \nabla$	Plasma radius: a
Time : t	$\tilde{t} = \frac{t}{\tau_R}$	Resistive Diffusion Time: $\tau_R = \frac{\mu_0 a^2}{\eta_C}$
Magnetic Field : $\mathbf{B}$	$\tilde{\mathbf{B}} = \mathbf{B}/B_C$	Characteristic Field Strength: $B_C = B_{z0}(r=0, t=0)$
Velocity : $\mathbf{V}$	$\tilde{\mathbf{V}} = \mathbf{V}/V_A$	Alfven Velocity: $V_A = \frac{B_C}{\sqrt{\mu_0 \rho_C}}$
Magnetic Vector Potential : $\mathbf{A}$	$\tilde{\mathbf{A}} = \mathbf{A}/A_C$	Characteristic Vector Potential: $A_C = B_C a$
Current : $\mathbf{J}$	$\tilde{\mathbf{J}} = \mathbf{J}/J_C$	Characteristic Current: $J_C = \frac{B_C}{\mu_0 a}$

Table 2.1

influence resistive evolution.[18] Third, the viscosity included in the model is a Navier–Stokes "fluid–like," or collisional, viscosity. It does not have the tensorial character which would be expected for a plasma in a magnetic field. This scalar viscosity is included for numerical stability. Nevertheless, it is assumed to provide a good first approximation to the cross–field viscosity that might be expected in a plasma. All of the above assumptions pertain to the set of equations used in the simulation. These were implemented in the version of DEBS available at the time. As alluded to above, upgraded versions containing pressure and mass density evolution are now operating succesfully. Work is under way on incorporating the full Braginski stress tensor as well.

The set of equations contains two static profiles and two dimensionless parameters. The static profiles are the nondimensional mass density and resistivity. For simplicity, they are set equal to one:

$$\tilde{\rho} = 1 \qquad \text{and} \qquad \tilde{\eta} = 1 \ , \tag{2.3.5}$$

or, equivalently, the mass density and resistivity are taken to be constant:

$$\rho = \rho_C \qquad \text{and} \qquad \eta = \eta_C \ . \tag{2.3.6}$$

The magnitude of the resistivity enters into the dimensionless parameter S, the Lundquist number. This parameter has the definition:

$$S = \frac{\tau_R}{(a / V_A)} \ , \tag{2.3.7}$$

and represents the ratio of the resistive–diffusion and Alfven time scales. In scaling studies, S is the resistivity "knob" in the code. Given the definition of τ_R in Table 2.1 and the value for η in (2.3.6),

$$S \sim \frac{1}{\eta} \tag{2.3.8}$$

is a useful rule of thumb for scaling purposes. The second dimensionless parameter, ν, is the dimensionless viscosity. It has the definition:

$$\nu = \frac{\tau_R}{\left(\rho_C a^2 \right) / \nu_0} , \tag{2.3.9}$$

where ν_0 is a characteristic dimensional viscosity. This parameter, the ratio of the resistive and viscous diffusion time scales, acts as the viscosity "knob" in the code. For numerical purposes, the dimensional viscosity is written in terms of the grid scales in the code and a variable magnitude:

$$\nu_0 = \rho_C \frac{(\text{rhocon})(\Delta r)^2}{(\Delta t)} , \tag{2.3.10}$$

so that:

$$\nu = \frac{(\text{rhocon}) \left(\Delta r / a \right)^2}{\left(\Delta t / \tau_R \right)} . \tag{2.3.11}$$

In scaling, the magnitude (rhocon) is varied. The numerical values of S and ν used in the simulation are summarized in the table that follows.

PARAMETER	DEFINITION	"BASE" CASE	RANGE
S	$S = \frac{\tau_R}{(a / V_A)}$	S = 1000	500 < S < 4000
ν	$\nu = \frac{(\text{rhocon})\left(\frac{\Delta r}{a}\right)^2}{\left(\frac{\Delta t}{\tau_R}\right)}$	rhocon = 2.0	0.5 < rhocon < 8.0

Table 2.2

It is interesting to compare the size of the numerical viscosity used in the simulation to the size of the cross-field viscosity which might be expected in the experimental plasma being simulated. The numerical viscosity used to provide stability in the algorithm is given by equation (2.3.11). This expression can be evaluated using the radial and time increments that appear in the code (see Table 2.3 b below) and the value of rhocon for a "base" case. The result is ν (code) = 2.52 . For comparison, a dimensionless viscosity can be defined for an experimental plasma using (2.3.9). A physically-motivated choice of ν_0 replaces that made in (2.3.10). Braginskii transport coefficients[19] were chosen; the cross-field ion viscosity coefficient $\eta_1{}^i$ is used as ν_0, and the parallel resistivity is used to calculate the resistive diffusion time. With "typical" ZT-40M data:[20]

$Z = 1$ $\qquad$ $m_i = m_{DEUTERIUM}$

$n_i = n_e = 5.00\ e\ 13\ cm^{-3}$ $\qquad$ $T_i = T_e = 200$ eV

$a = 20$ cm $\qquad$ $B_{TYPICAL} = 5000$ Gauss

the calculated result is ν(experiment) = 0.21 . For a given resistivity, the model in the code is about twelve times more viscous than the experimental plasma that it is intended to simulate. Given that some numerical viscosity is necessary, this is a reasonable order-of-magnitude approximation to the cross-field dynamics.

The DEBS code solves equations (2.3.1)-(2.3.4) in a periodic cylinder. This geometry is an approximation to a large-aspect-ratio torus. The cylinder has radius a and length $L = 2\pi R$, where R is the major radius of the equivalent torus. The equations are finite-differenced in the radial direction and Fourier-analyzed in the two periodic directions, θ and z. Fast Fourier Transform (FFT) routines are used to shuttle back and forth between Fourier and configuration space. The variables are stored in Fourier space, and each type of operation is performed where it can be done most simply. Linear terms are time-advanced in Fourier space, and derivatives are evaluated there. Nonlinear terms are evaluated by performing a simple product in configuration space. This type of an algorithm, called pseudospectral, has several advantages over a traditional spectral algorithm. The coded equations retain the simple appearance of their original forms, which greatly simplifies debugging. In addition, due to the efficiency of the available FFT's, the number of operations is actually reduced when complicated convolution sums are replaced by transforms and simple products.[21] (Simple products do create large-number modes not defined in the transforms. These act like, or "alias," small-number modes. Truncation at the top of the spectrum is used in "dealiasing."[22])

The quantities that characterized the spatial mesh in the various runs of the simulation are listed in the tables on the following pages. The number of grid points used to represent ZT-40M, ZT-H, and MST are given. The Fourier amplitudes are characterized by the poloidal mode number (m) and the toroidal mode number (n). As usual, these represent the harmonic of the smallest wave number. In normalized form, these fundamental wave numbers are:

$$k_\theta a = 1 \qquad k_z a = \frac{a}{R} = \text{inverse aspect ratio} .$$

The range of mode numbers used in each case, after dealiasing is taken into account, is also given below.

Now that the geometry and method of solution have been specified, some loose ends from the previous section can be tied up. Since each Fourier mode is evolved separately, the resisivity can be removed from the equilibrium (m = n = 0) component of Ohm's law, equation (2.3.1) . The equilibrium fields are protected against changes caused by resisitive diffusion, a situation which was considered to be desirable, while the pertubations induced by the field errors ($m, n \neq 0, 0$) undergo a fully resistive evolution.

It was also decided that the field errors should be fixed in time at the boundary of the plasma. Given the variables used in the simulation, only boundary conditions on **A** can be directly imposed. In the gauge used in the simulation, these boundary condition are:

CASE	a / R	Θ GRID	z GRID	m	n
ZT – 40 : COILS	0.1754	32	128	0 < m < 10	– 42 < n < 42
ZT – H : COILS	0.1778	16	256	0 < m < 5	– 85 < n < 85
ALL PORTS		64	128	0 < m < 21	– 42 < n < 42
GAP		8	512	0 < m < 2	| n | < 170
SINGLE PORT	2.1361 (short, fat cylinder)	128	64	0 < m < 42	– 21 < n < 21
DIAGNOSTIC SECTION		128	64	0 < m < 42	– 21 < n < 21
MST : ALL PORTS	0.3467	128	64	0 < m < 42	– 21 < n < 21
GAP		8	512	0 < m < 2	| n | < 170
SINGLE PORT	2.5964	128	64	0 < m < 42	– 21 < n < 21

Table 2.3 a

ADDITIONAL INFORMATION	
RADIAL GRID	Two staggered meshes, one with 64 divisions and one with 63 divisions: $\Delta r / a = 1 / 63 = 1.587\,e-2$
TIME INCREMENT	Normalized to Alfven time ($\tau_A = a / V_A$) : $\Delta t / \tau_A = 0.2$, a constant Normalized to Resistive Diffustion time : $\Delta t / \tau_R = 0.2 / S$

Table 2.3 b

$$\left[\hat{r} \times \frac{\partial \mathbf{A}(m,n)}{\partial t} \right]_a = -\left[\hat{r} \times \mathbf{E}(m,n) \right]_a . \qquad (2.3.12)$$

The requirement that the wall be a perfect conductor rules out tangential electric fields there. The tangential components of vector potential are fixed in time at the boundary. In Fourier space, B_r (m,n) is related to components of **A** in a solely algebraic way:

$$B_r(m,n) = -i \left[\frac{m}{r} A_z(m,n) - (n k_z) A_\theta(m,n) \right]. \qquad (2.3.13)$$

Thus, the presence of a perfectly-conducting wall requires that the radial magnetic field be held fixed in time at the boundary. In the simulation, the field errors at the plasma boundary were represented by a time-independent radial magnetic field.

The boundary condition on the velocity can also be addressed. It has been observed above that the presence of a perfectly conducting wall prevents any $m,n \neq 0,0$ tangential electric field from existing at the boundary. In addition, it was assumed that there is no resistance to the flow of equilibrium currents on the cylinder axis. Thus, there is no need to drive the plasma with an external $m = n = 0$ tangential electric field at the boundary. This means that the total electric field at the boundary is zero, and Ohm's law does not require an inward radial pinch velocity there. With viscosity present, this allowed the choice $\mathbf{V}(a) = 0$.

Finally, the form of the initial perturbation profiles can be specified. As stated in equation (2.2.6) , these can be found from a magnetic scalar potential:

$$B_r = -\frac{\partial \Phi_M(m,n)}{\partial r} \tag{2.3.14}$$

$$B_\theta = i\left(\frac{m}{r}\right)\Phi_M(m,n) \tag{2.3.15}$$

$$B_z = i\,(n\,k_z)\,\Phi_M(m,n)\ . \tag{2.3.16}$$

According to equation (2.2.8), this potential satisfies Laplace's equation. In this cylindrical geometry, the Fourier amplitudes obey the equation:

$$\frac{\partial^2 \Phi_M(m,n)}{\partial r^2} + \frac{1}{r}\frac{\partial \Phi_M(m,n)}{\partial r} - \left[(nk_z)^2 + \frac{m^2}{r^2}\right]\Phi_M(m,n) = 0\ . \tag{2.3.17}$$

The solutions are the well-known modified Bessel functions:[23]

$$\Phi_M(m,n) = \Phi_a \, I_m(n k_z r). \qquad (2.3.18)$$

One boundary condition has already been imposed through the exclusion of the modified Bessel function of the second kind (K_m), which has a singularity at the origin. The second boundary condition, imposed at the wall, determines the value of the constant Φ_a. Once this has been found, the profiles given by (2.3.14)-(2.3.16) can be used in the simulation as initial conditions for the magnetic perturbations within the plasma volume.

The appropriate boundary condition at the wall, given by the radial component of equation (2.2.9), is that the radial magnetic field is determined by the radial field errors. Since equation (2.2.9) is a vector equation, it reduces to three conditions: (2.3.14)-(2.3.16) evaluated at $r = a$, with the error fields on the left side. These equations show that the three components of a field error cannot be imposed independently, since only a single constant is available for matching. In the case of the errors associated with the toroidal field coils, it can be assumed that the coils are located at a small distance from the plasma. Then, the error fields at the wall are vacuum fields; their components are related in the same way as those on the right sides of (2.3.14)-(2.3.16). In this case, Φ_a can be found from the field errors via any of the equations. In the simulation, the axial equation was used. In the case of errors occuring directly at the plasma edge, those arising from holes or a gap in the conducting shell, only the

Fourier amplitudes associated with a radial field error were found. Matching was done using the radial equation at the plasma edge.

The simulation described in this section had large-scale requirements in terms of both memory size and computing time. Field errors, by nature, tend to give rise to fine-scale perturbations. To model them accurately, especially using realistic values of aspect ratio, a large grid was required to provide adequate resolution. Determining the response of the RFP plasma involved following the plasma-perturbation mixture for a considerable fraction of a resisitive diffusion time, since the resistivity often plays an important role in RFP dynamics. In an algorithm with an explicit time-advance, the size of the time-step is limited by the fastest physical phenomena in the code. In this case, these are the shear and compressional Alfven waves. To resolve these accurately would have required a time-step of order:

$$\Delta t = \frac{2\ \Delta r}{V_A} \qquad \text{or} \qquad \frac{\Delta t}{\tau_A} = 2\left(\frac{\Delta r}{a}\right) = 0.032\ ,$$

where ($2\,\Delta r$) is the shortest possible wavelength in the system. Then, the large separation between the resistive diffusion time-scale and the Alfven time-scale, measured by S, must be taken into account. Either a very large number of time steps or a very large implicit algorithm would have been required to follow any resistive dynamics.

Satisfying all these requirements would not have been possible, were it not for a combination of two advances which converged at just the

proper time. At the beginning of this project, a Cray II supercomputer became available for timesharing at the National Magnetic Fusion Energy Computer Center. The large amount of storage available on this machine was able to accomodate the large size of the code. In addition, a new algorithm, called the "semi-implicit method" was coming into use. The properties of this algorithm have been well-described elsewhere.[24,25,26] Suffice it to say that the method introduces additional dispersion into the equations, effectively "slowing down" the waves on the smallest scales until they are numerically stable at much larger time steps. Thus, a time-step much larger than the limiting time-step for an explicit method — specifically, $\Delta t / \tau_A = 0.2$, as quoted in Table 2.3 — can be used even though the Alfven waves are still present in the equations. The total number of time steps required to follow resistive evolution is greatly reduced. It should be noted that even with these advances, the simulation runs taxed the limits of available resources. The code was typically 12,000,000 words in length and required 1000 CPU minutes per run.

2.4 RESULTS ON ERRORS FROM THE TOROIDAL COIL SET

2.4a FIELD ERROR MODEL

The field errors produced by a set of toroidal field coils can be calculated with the aid of a code called EFFI.[27] As an input, the toroidal field coils, in full toroidal geometry, are modeled as a set of current elements. The code then uses the Biot-Savart law to integrate over these currents and find the magnetic fields produced at a position corresponding

to the edge of the plasma. The resulting fields must first be made compatible with the cylindrical geometry of the simulation. This is done by removing the (1 / R) dependence in the field magnitude. Next, the Fourier transform is taken and the m = n = 0 components subtracted out. The remaining $m,n \neq 0,0$ components can be used as the boundary conditions in equation (2.2.9); these are the field errors. As was stated before, only one component of the error field is needed as a boundary condition. For this study, the z-component was chosen, since it is believed to be less affected by the conversion from toroidal to cylindrical geometry. Equation (2.3.16) is then used to impose the error field at the boundary, and the resulting vacuum perturbations in the plasma can be calculated.

The procedure outlined above was used to obtain the field errors from the toroidal field coil sets of ZT-40M and ZT-H. (MST has an unusual design. It has no external coils; all of the currents which produce the equilibrium fields flow directly in the conducting shell. The field errors which arise from this situation will be taken up in the next two sections.) Figures 2.4 and 2.5 show some important energy spectra for the field errors in ZT-40M and ZT-H, respectively. What is presented is the energy in each Fourier mode with m=0 and m=1, as a function of n. Field errors with m=0 arise primarily from "ripple" in the toroidal field due to the discreteness of the coils. Errors with m = 1 result when coils are wound around ports on the outboard side of the torus. The ZT-40M spectra show that the largest modes have a value of n which is a multiple

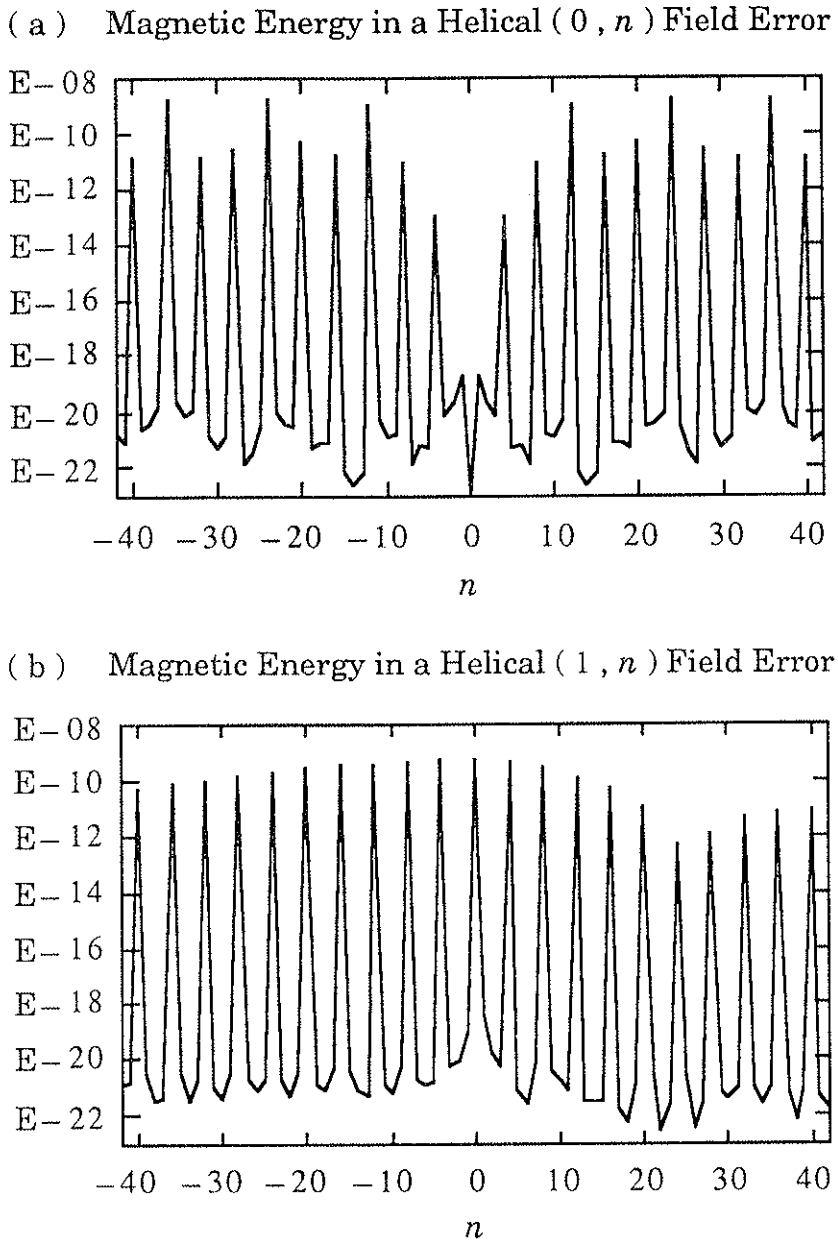

Figure 2.4 Plots of magnetic energy in an (m,n) Fourier mode as a function of n: (a) is for m=0 and (b) is for m=1. These Fourier modes are the coil errors for ZT40-M. For purposes of comparison to other plots, note that the quantity plotted is only *proportional* to magnetic energy.

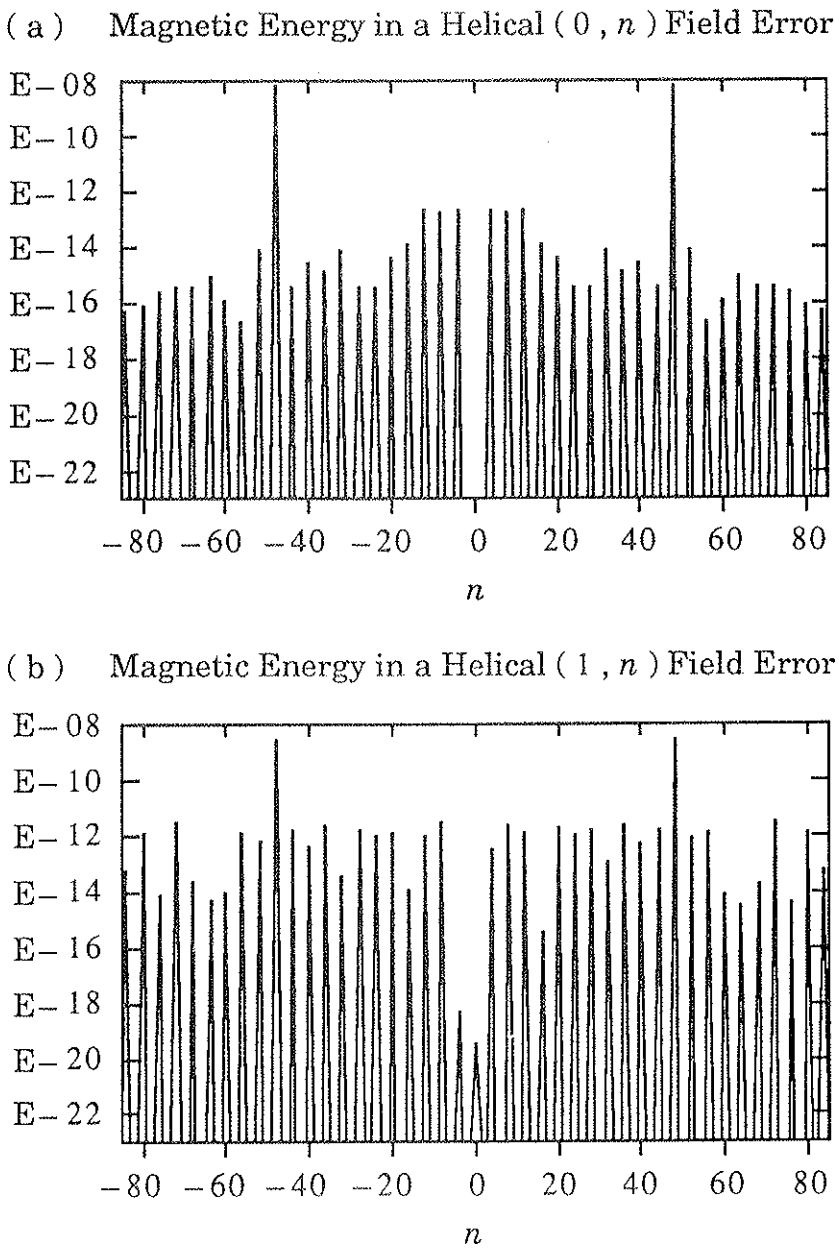

Figure 2.5 Plots of magnetic energy in an (m,n) Fourier mode as a function of n: (a) is for m=0 and (b) is for m=1. These Fourier modes are the coil errors for ZT–H. For purposes of comparison to other plots, note that the quantity plotted is only *proportional* to magnetic energy.

of four. This reflects the presence of the four pump ports equally spaced around the toroidal circumference. The winding of coils around ports that are spaced between twelve flux-transformer cores may make additional contributions to modes for which n is a multiple of twelve. In ZT-H, the basic n = 48 periodicity for the m = 0 modes comes from the number of toroidal field coils. The ZT-H design minimizes m = 1 errors. The magnitudes of the localized radial error fields described by these spectra, normalized to the poloidal field strength at the wall, are less than 3% in ZT-40M and less than 0.5% in ZT-H.

The field-error spectral components considered above have the most potential for influencing the physics of the RFP. As was mentioned in Chapter 1, modes with m=0 are important because they are resonant at the field-reversal surface. Modes with m=1 can affect the growth of the resistive instabilities that play a role in RFP sustainment. Therefore, attention will be focused on modes with these values of m in the simulation results which make up the rest of this section.

2.4b PLASMA-PERTURBATION STEADY-STATE

The first result from the simulation is that the plasma-perturbation combination settled down into a steady-state. Evidence for this can be seen in Figure 2.6, which plots the magnetic energy in the radial magnetic field components as a function of time. Since the radial magnetic field is entirely associated with the field errors, any change or

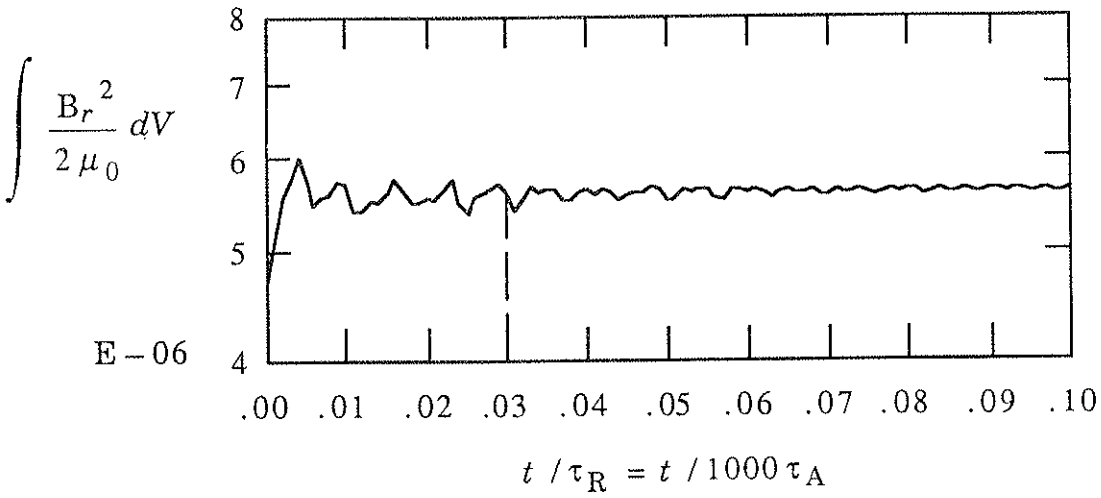

Figure 2.6 Plot of the magnetic energy in the radial magnetic field components as a function of time. Note that the time variation damps quickly after 30 τ_A.

growth in the perturbations would be reflected in this energy. The figure shows that the perturbations have basically finished changing after about 30 τ_A. The profiles presented in Figure 2.7 support this observation. These are profiles of the radial magnetic field for a (0,24) mode at two different times: 30 τ_A and 100 τ_A, the end of the simulation. They are identical.

The steady-state was independent of the choice of initial perturbation profiles. The original choice, as described in the previous section, was for the initial perturbations to be given by vacuum profiles. The code then calculated the magnetic vector potentials associated with these fields. As an alternative choice, the magnetic vector potentials calculated for the vacuum fields were weighted by a factor of $(r/a)^8$. New

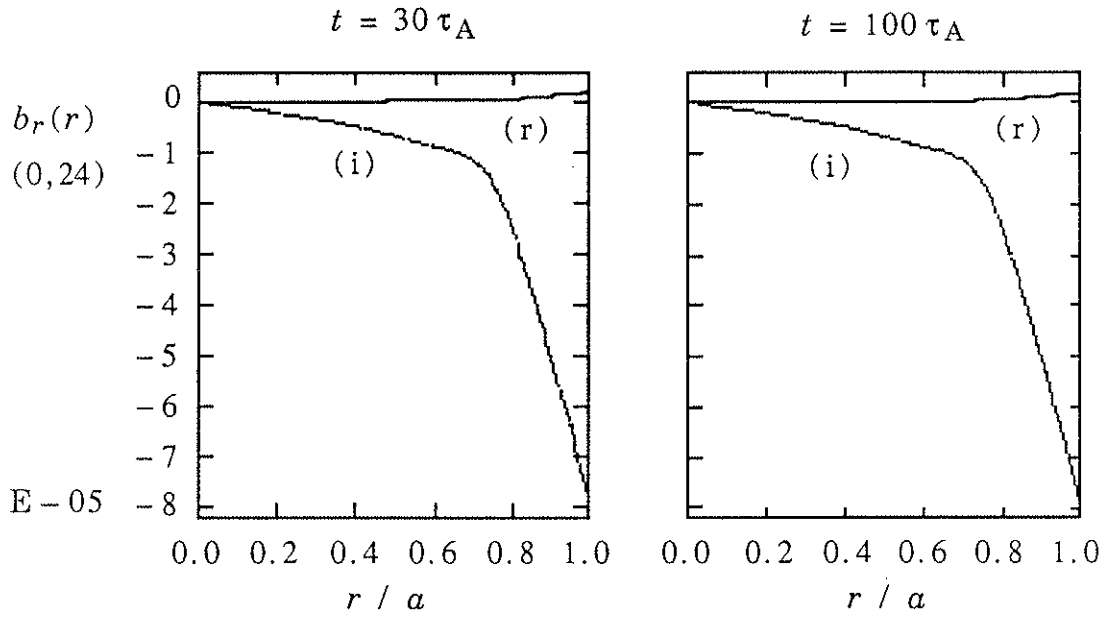

Figure 2.7 Radial profiles of $b_r(0,24)$ for two different times: $t = 30\,\tau_A$ and $t = 100\,\tau_A$. The radial profile does not change. (Note: (r) and (i) stand for real and imaginary parts of the complex b_r amplitude.)

magnetic fields were then calculated from these modified vector potentials. These were proper magnetic fields — they satisfied $\nabla \cdot \mathbf{B} = 0$, since they were obtained from a vector potential — but they now had currents associated with them. Figure 2.8 shows the profile of the (0,24) radial magnetic field given by each choice. A simulation was then performed for each set of initial profiles. A steady-state was reached in both cases. Figure 2.9 shows the profile of the (0,24) radial magnetic field at the conclusion of each simulation. The steady-state profiles are basically identical.

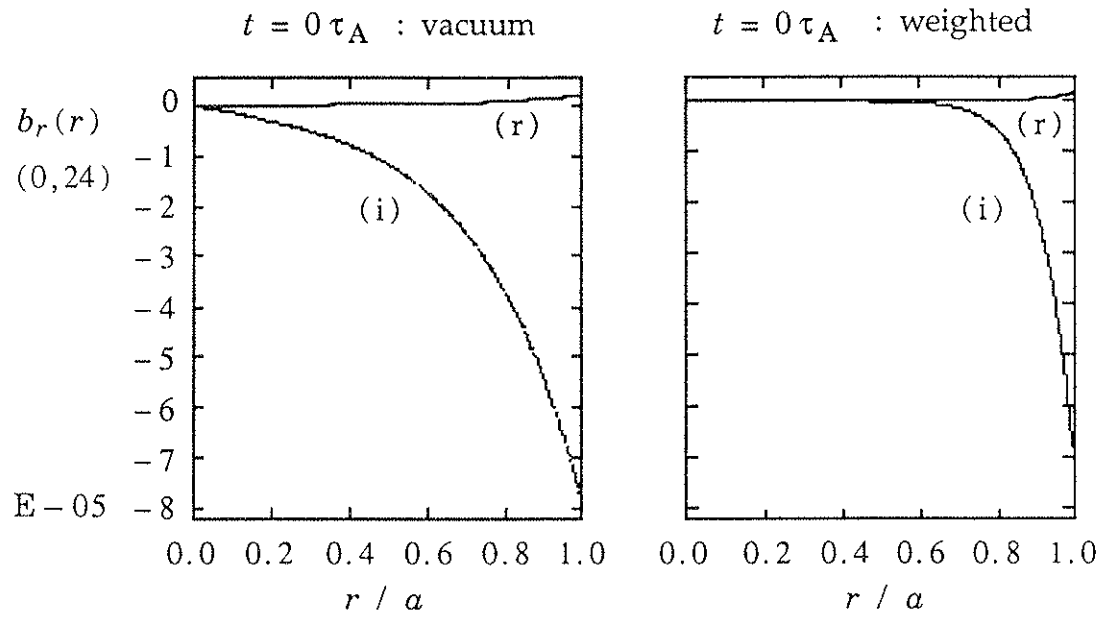

Figure 2.8 Radial profiles of $b_r(0,24)$ at $t = 0\,\tau_A$ showing two different initial conditions. ((r)–real, (i)–imaginary)

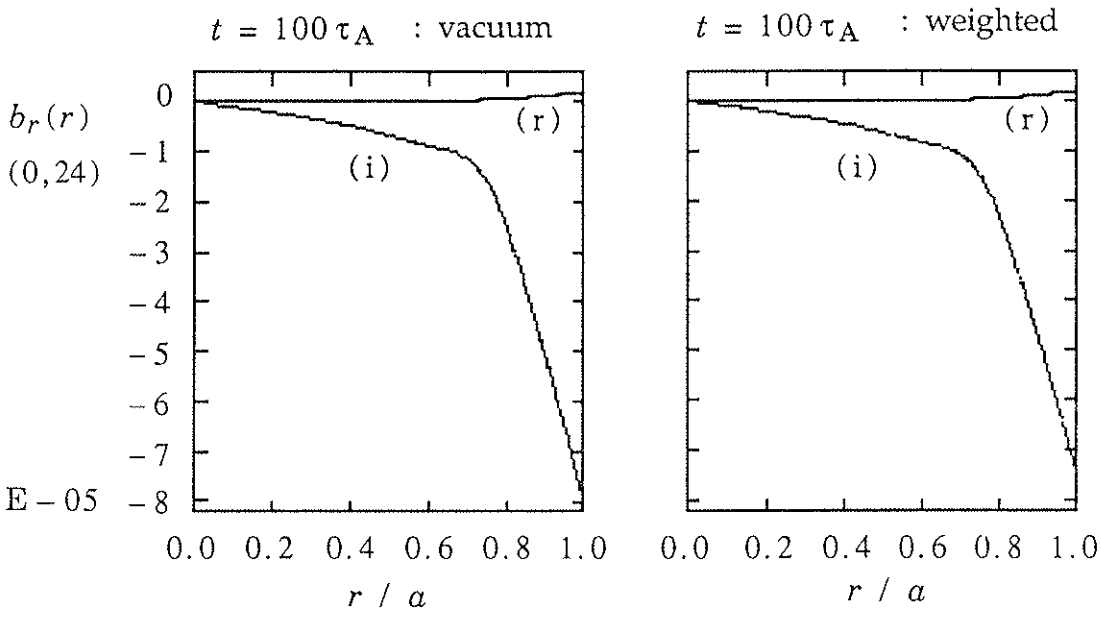

Figure 2.9 Radial profiles of $b_r(0,24)$ at $t = 100\,\tau_A$ showing that the final result is independent of initial conditions. ((r)–real, (i)–imag.)

The steady-state was linear in the size of the perturbation. The magnitude of the perturbations varied linearly with the size of the field error applied at the wall. Figure 2.10a shows the profile of the (0,24) radial magnetic field when the field error at the wall is the Fourier amplitude calculated for the ZT-40M toroidal field coil set. Figure 2.10b shows the same profile when this amplitude has been increased by a factor of four. The profiles are identical, except for an overall scale factor of four. Apparently, this linearity holds for errors whose Fourier amplitudes are in the range of the small values calculated for the toroidal field coil set. The extent to which this breaks down when the errors get larger will be discussed in the section on "butt joint" gap errors (Section 2.6).

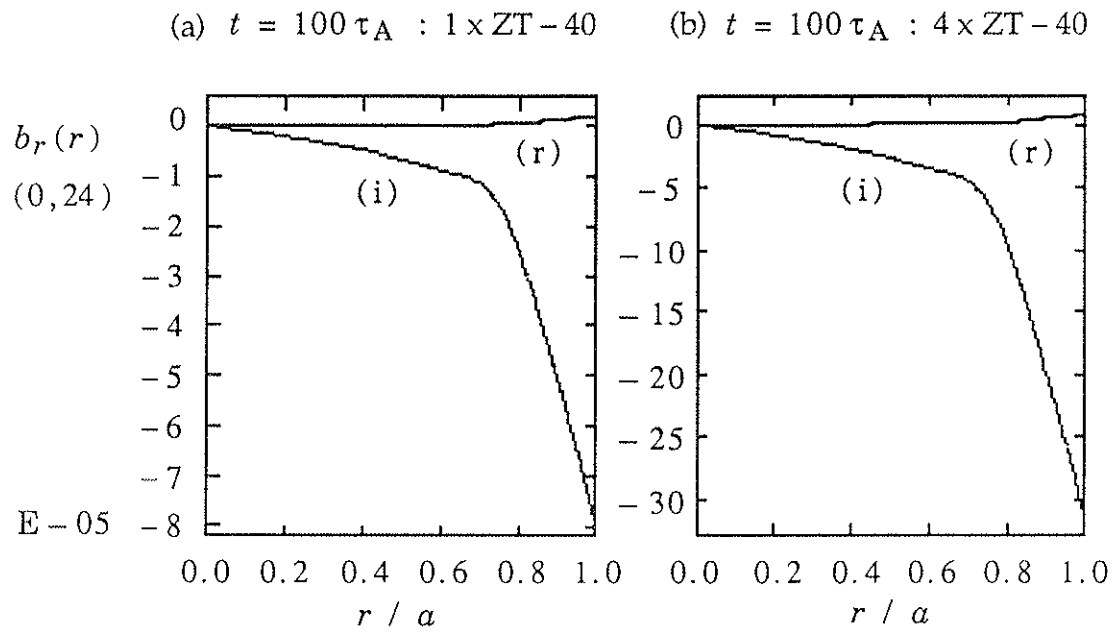

Figure 2.10 Radial profiles of $b_r(0,24)$ for two different levels of edge field error: (a) 1 x ZT-40M and (b) 4 x ZT-40M. The radial perturbation is linear in field-error amplitude. ((r)-real, (i)-imaginary)

2.4c PLASMA EFFECTS ON THE PERTURBATIONS

The next results from the simulation will illustrate the way in which the perturbation profiles were changed through their interaction with the plasma equilibrium fields. The mode numbers selected for study were the $(0,12)$, $(0,24)$, and $(1,-16)$ in ZT-40M and the $(0,48)$ in ZT-H. The reasons for selecting m = 0,1 have already been discussed. In general, these particular modes had the largest amplitudes. Attention will be focused on the radial magnetic field profiles. Radial fields with a particular mode number can cause magnetic islands to form around the resonant surface for that mode and thus have the most potential for affecting the RFP equilibrium.

The amplitude of a $(1,n)$ radial field perturbation at the $(1,n)$ resonant surface was <u>increased</u> (in absolute value) in the presence of the RFP equilibrium. Figure 2.11 shows the profile of the $(1,-16)$ radial magnetic field for the initial vacuum profile ($t = 0\ \tau_A$) and for the final profile ($t = 100\ \tau_A$), after interaction with the RFP equilibrium. The value of $|b_r|$ at the resonant surface ($r_s / a = 0.60$) increases by a factor of 2.95 . In this case, the presence of the plasma worsened the effects of the vacuum field errors.

The amplitude of m=0 radial field perturbations at the m=0 resonant surface was actually <u>decreased</u> (in absolute value) after the interaction with the RFP equilibrium fields. The presence of the plasma acted to <u>heal</u> the effects of the vacuum perturbations. Figure 2.12 compares

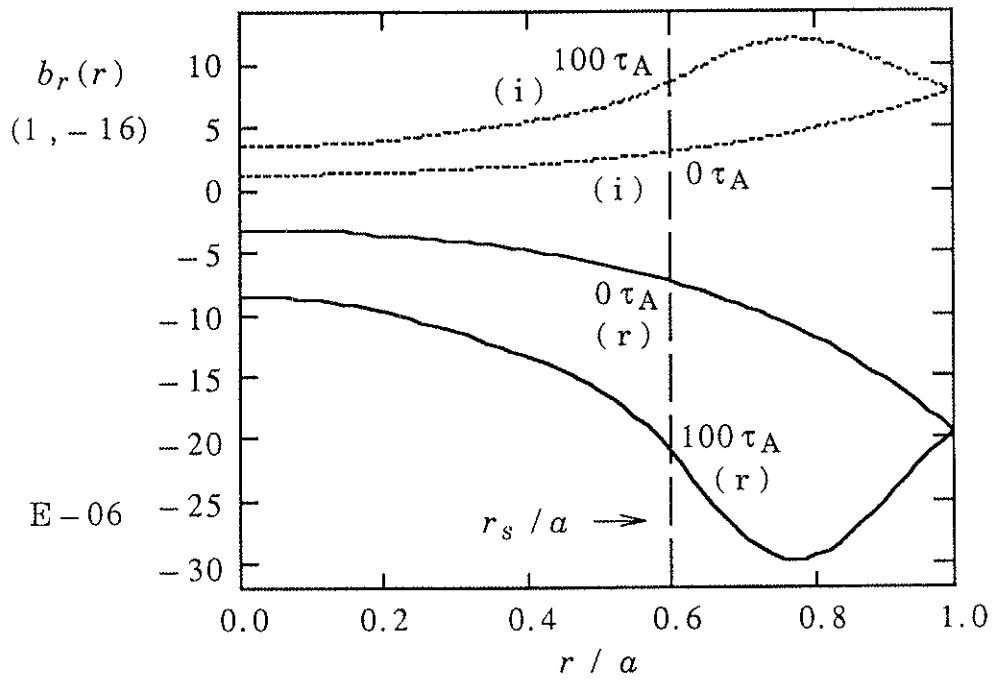

Figure 2.11 Radial profile of $b_r(1,-16)$ before ($t = 0\,\tau_A$) and after ($t = 100\,\tau_A$) interaction with the plasma. The value of $|b_r(r_s)|$ is increased. ((r) – real, (i) – imaginary)

the (0,24) radial magnetic field profiles before ($t = 0\,\tau_A$) and after ($t = 100\,\tau_A$) the interaction with the plasma. The decrease in the value of $|b_r|$ at the resonant surface ($r_s / a = 0.86$) is 22.3%. For the other modes, the values of this decrease were: 18.1% for (0,12) and 9.8% for (0,48).

The fact that the influence of the plasma caused the m = 0 radial field at the resonant surface to be smaller (in absolute value) than that for a vacuum profile is a remarkable result. It certainly contradicts the prediction of the analytic calculation cited in Chapter 1.[28] However, close

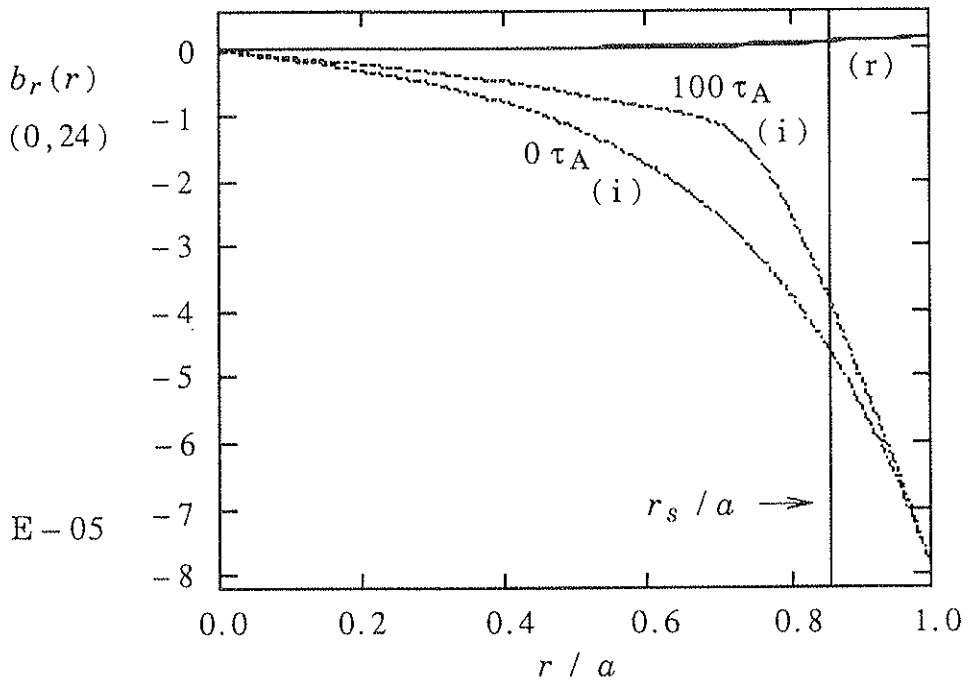

Figure 2.12 Radial profile of $b_r(0,24)$ before ($t = 0\ \tau_A$) and after ($t = 100\ \tau_A$) interaction with the plasma. The value of $|b_r(r_s)|$ is decreased. ((r) – real, (i) – imaginary)

comparison with that work must be done carefully since the model used in that paper differs from the model used in the simulation in several important ways. In particular, most of the amplification of the radial field that is predicted in the paper occurs for the case of an RFP plasma which is bounded by a perfectly conducting wall at a distance from the plasma edge, or which is not bounded by a perfectly conducting wall at all. However, even in the case of an RFP plasma bounded by a close-fitting, perfectly conducting wall, an amplification of some 21% is predicted for the (0,24) mode. It seems that additional features of the simulation, not included in

the analytic model, must cause the observed reduction of the m = 0 radial field.

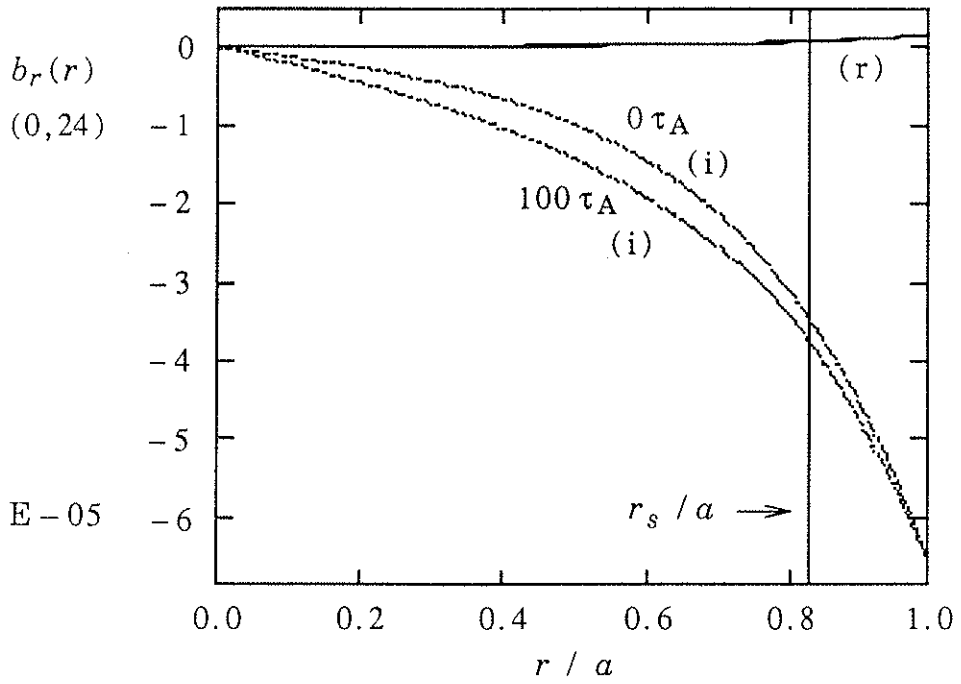

Figure 2.13 Radial profile of $b_r(0, 24)$ before ($t = 0\,\tau_A$) and after ($t = 100\,\tau_A$) interaction with a plasma represented by a Bessel Function Model equilibrium. The value of $|b_r(r_s)|$ is increased. ((r)-real, (i)-imaginary)

One feature that plays a role is the use of a relaxed equilibrium state in which λ is not a constant. When the gradient in λ was removed from the equilibrium fields, the reduction in the m = 0 radial field at the resonant surface disappeared. In fact, the m = 0 radial magnetic field was increased there. Figure (2.13) shows the same "before" and "after"

profiles as Figure (2.12). In this case, however, the RFP equilibrium fields were given by the Bessel Function Model, with $\lambda = \lambda_0 = 2.95 = \text{constant}$. The value of $|b_r|$ at the resonant surface ($r_s / a = 0.825$) after interaction with the plasma is increased by 8%. Thus, the removal of the finite gradient in λ reversed the way in which the radial magnetic field perturbation is affected by the RFP equilibrium. The fact that the 8% increase is less than the 21% predicted by the analytic model suggests that another important feature of the simulation — the use of non-ideal and non-force-free terms in the plasma-perturbation interaction — may be having an effect.

Non-ideal (finite η) and non-force-free (finite ν_0) terms do play a role in the linear steady-state reached in the simulation. In a force-free, linear steady-state, the perturbed magnetic forces produced by the plasma-perturbation interaction — $(\mathbf{J} \times \mathbf{B})_{1(m,n)} = \mathbf{J}_0 \times \mathbf{B}(m,n) + \mathbf{J}(m,n) \times \mathbf{B}_0$ — would go to zero. This means that the components of the perturbations perpendicular to the equilibrium fields would cancel each other out. By comparison, the components of the perturbed fields parallel to the equilibrium fields — $(\mathbf{J} \cdot \mathbf{B})_{1(m,n)} = \mathbf{J}_0 \cdot \mathbf{B}(m,n) + \mathbf{J}(m,n) \cdot \mathbf{B}_0$ — should be large. Figure (2.14) shows the radial profile of $|\mathbf{J} \times \mathbf{B}|_{1(0,24)}$ which is produced at the end of the simulation. The $(\mathbf{J} \cdot \mathbf{B})_{1(0,24)}$ profile is included for comparison. Over most of the radius, $|\mathbf{J} \times \mathbf{B}|_{1(0,24)} = 0$ and $(\mathbf{J} \cdot \mathbf{B})_{1(0,24)}$ is (relatively) large; the steady-state can be considered to be force-free. However, in the vicinity of two radial locations, the "knee" in λ at $r_n / a = 0.70$ and the m = 0 resonant surface at $r_s / a = 0.86$,

the value of $(\mathbf{J} \cdot \mathbf{B})_{1\,(0,24)}$ goes to zero and $| \mathbf{J} \times \mathbf{B} |_{1\,(0,24)}$ becomes significant. In the linear steady-state, the left side of equation (2.3.2) vanishes and the perturbed force must be balanced by the viscous term. The presence of the velocity in the steady-state momentum equation now couples it to Ohm's law and brings in the influence of the resistive term. Thus, non-force-free (finite ν_0) and non-ideal (finite η) terms are important around the m = 0 resonant surface, where the reduction in the m = 0 radial field occurs.

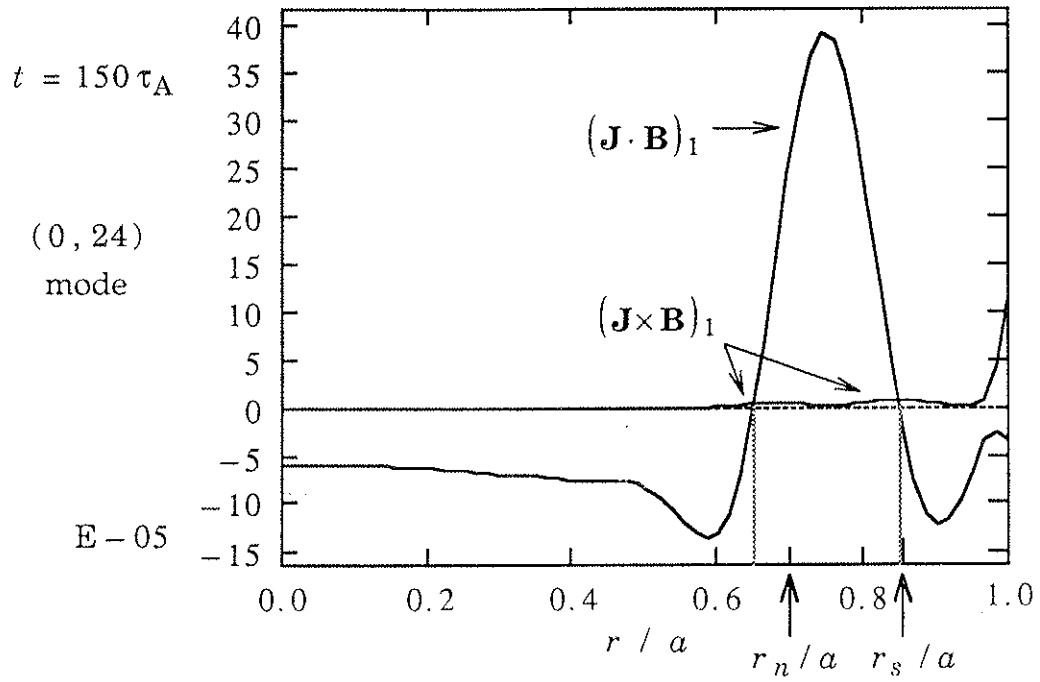

Figure 2.14 Radial profiles of the perturbed magnetic forces and parallel currents — $| \mathbf{J} \times \mathbf{B} |_{1\,(0,24)}$ and $(\mathbf{J} \cdot \mathbf{B})_{1\,(0,24)}$ — for a (0 , 24) mode. Note that $| \mathbf{J} \times \mathbf{B} |_{1\,(0,24)}$ peaks where $(\mathbf{J} \cdot \mathbf{B})_{1\,(0,24)}$ goes to zero, around $r_n / a = 0.70$ and $r_s / a = 0.86$.

In fact, the size of the viscosity and resistivity have a direct impact on the amount by which the m = 0 radial field is reduced. The results on this reduction quoted above were for simulations using the "base case" values of the dimensionless parameters. (See Table 2.2.) To test the persistence of the effect, scaling runs were performed for the case of the errors from the toroidal field coils of ZT-40M. (For the sake of completeness, a run was performed using values ν and S equal to those of the "base case," but with the number of radial divisions reduced by a factor of two. The results were identical to the "base case" results already presented, indicating that the solutions are radially converged.) Viscosity scaling was done by varying the value of rhocon at constant S, and resistivity scaling was done by varying the value of S at constant rhocon. (The dimensionless viscosity ν, given by equation (2.3.11), is proportional to S. It does not change during the S-scaling if rhocon is held constant, however, since all the other terms in equation (2.3.2) are also proportional to S.) The results are presented in Figures 2.15 and 2.16 in terms of the percentage of m = 0 radial field reduction at the m = 0 resonant surface:

$$\%\ \text{REDUCTION}\,(0,n) \equiv \frac{\left|b_r(r_s)_{(0,n)}\right|_{\text{VACUUM}} - \left|b_r(r_s)_{(0,n)}\right|_{\text{STEADY-STATE}}}{\left|b_r(r_s)_{(0,n)}\right|_{\text{VACUUM}}}$$

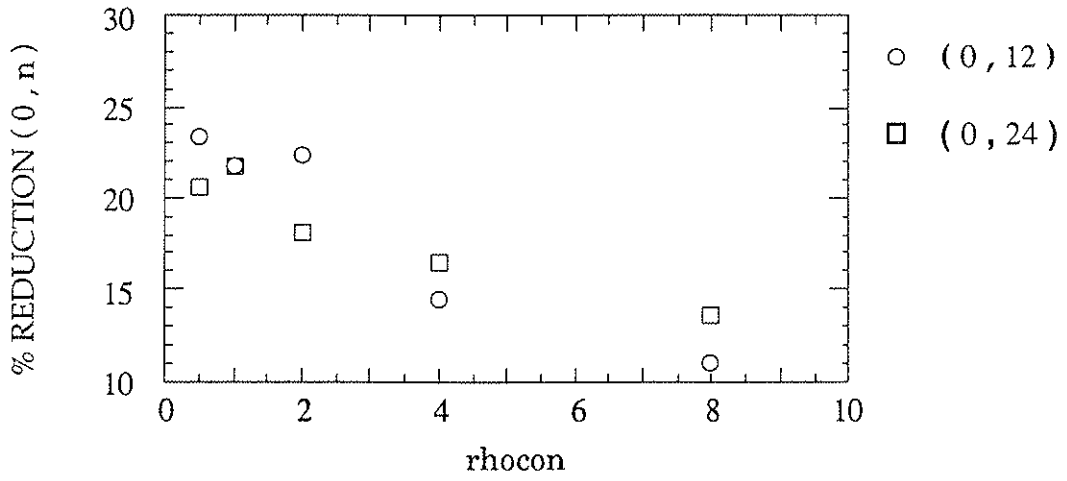

Figure 2.15 Plot of the percentage reduction in $|b_r(r_s)|$ for m = 0 modes as a function of rhocon (viscosity). For this (limited) range of parameters, the reduction persists as rhocon becomes small.

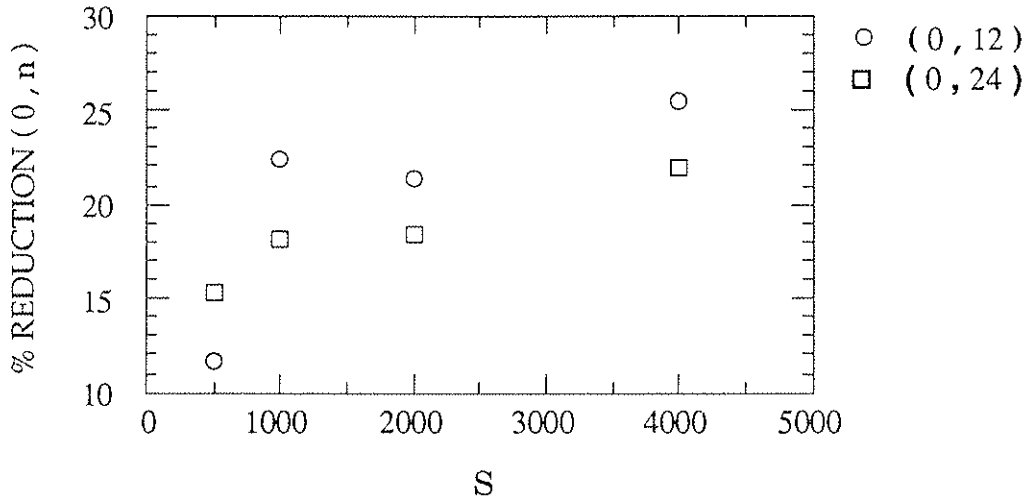

Figure 2.16 Plot of the percentage reduction in $|b_r(r_s)|$ for m = 0 modes as a function of S (resistivity). For this (limited) range of parameters, the the reduction persists as resistivity (~ 1 / S) becomes small.

The dependence on the viscosity and the resistivity does not scale out of the problem as these quantities become small. In fact, the percentage reduction becomes larger for the smaller resistivity (larger S) and smaller perdendicular viscosity (smaller rhocon) that would characterize a hot laboratory plasma. This result is intriguing, but must be taken with a very large grain of salt at this point. The scaling was performed over a very limited range of rhocon and S, and all of the values used were far from those that really characterize experimental plasmas.

The roles played by the important features of the simulation model mentioned above will be taken up analytically in Chapters 3 and 4. The presence of a non-zero gradient in λ and finite resistivity and viscosity will be considered. The goal will be an understanding of the physical mechanisms involved and, in the case of m = 0 perturbations, a more complete look at the scaling of the reduction in the radial field. These calculations will be pursued in some detail.

2.4d PERTURBATION EFFECTS ON THE EQUILIBRIUM: "MACHINE PERFORMANCE RESULTS"

The presence of a radial magnetic field with mode numbers (m,n) leads to the formation of a magnetic island around the resonant surface for that mode number. The extent to which perturbations induced by errors from the toroidal field coil set produce islands that affect the physical behavior of the RFP plasma will now be assessed. It has been shown that these perturbations are small enough to interact linearly with

the equilibrium fields. Thus, the linear island-width formula:[29]

$$\frac{W}{a} = 4\left(\frac{r_s}{a}\right)\sqrt{\frac{|b_r(r_s)|}{B_{\theta 0}(r_s)}\left[\left(\frac{r_s}{a}\right)\left|n\,\frac{\partial q}{\partial(r/a)}\right|_{r_s}\right]^{-1}}$$

will be used to calculate island sizes. Note that the island width is related to the square root of the radial magnetic field at the resonant surface.

The perturbations with m=1 did not produce appreciable magnetic islands. Figure 2.17 shows a plot of (1,-16) helical flux contours at the

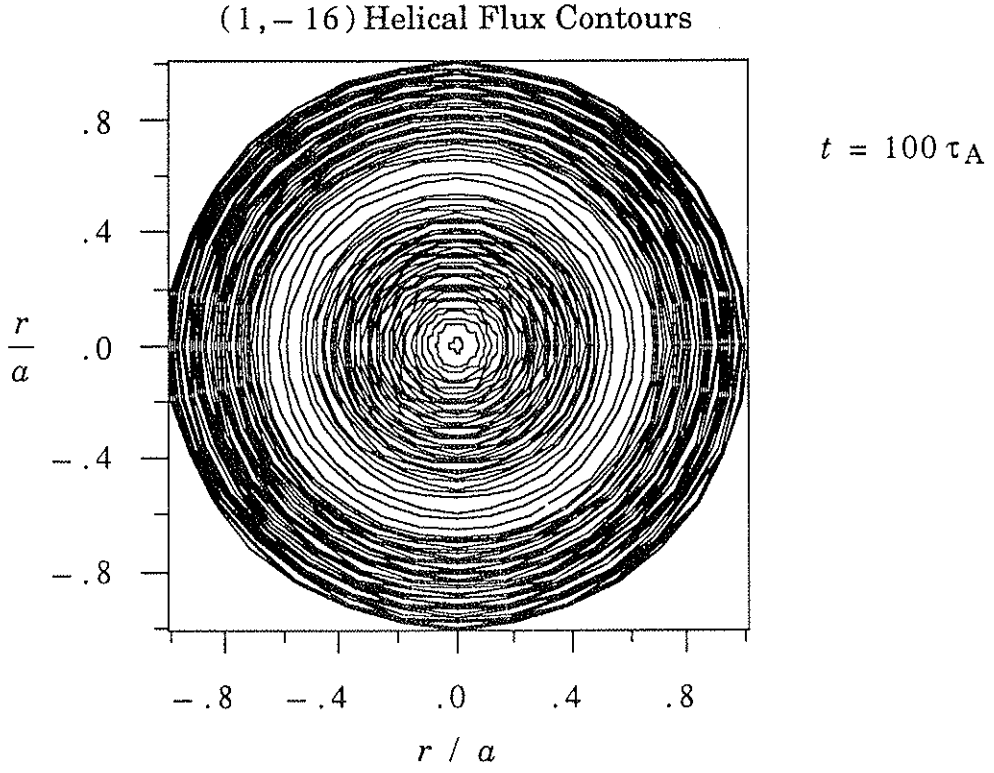

Figure 2.17 Plot of (1,-16) helical flux contours at the conclusion of a simulation using the coil errors from ZT-40M. No magnetic islands are apparent around the resonant surface $r_s / a = 0.60$.

end of a simulation using the coil errors from ZT-40M. The amount of flux through a helical ribbon defined by the magnetic axis (the line along the center of the cylinder) and a helix with $(1)\theta + (-16)\,k\,z = \text{constant}$ at radius r is plotted[30] for various values of r. A radial field of the same pitch would connect like-values of flux across the point of maximum flux, the resonant surface $r_s / a = 0.60$, creating a crescent-like "magnetic island." The plot shows no evidence of such an island. The linear island width is calculated to be $(W/a)_{(1,-16)} = 1.06\ e-2$, using information on the radial field and equilibrium fields from the simulation results. Even though the value of the radial field has been increased by a factor of 2.95 over the course of the simulation, with a corresponding increase of about 70% in island size, the islands were still too small to be resolved by the code. This indicates that, in ZT-40M at least, large m = 1 islands caused by field errors from the toroidal field coils should not mask the islands produced by the resisitive instabilities that are active in the RFP dynamics. It is possible that the radial field "seeds" provided by the field errors may "encourage" some modes to grow faster than others. (This point will be raised again in Chapter 5.)

The perturbations with m = 0 did produce some magnetic islands. On the whole, they are not significant. Calculations of the linear island width at the beginning of the simulation give: $(W/a)_{(0,24)} = 1.93\ e-2$ and $(W/a)_{(0,24)} = 1.68\ e-2$ for ZT-40M, and $(W/a)_{(0,48)} = 1.52\ e-2$ for ZT-H. At the end of the simulation, the reduction in radial field at the resonant surface has reduced the size of the islands some 10% in ZT-40M

and 5% in ZT-H. Figures 2.18 and 2.19 show (0,n) helical flux contours at the end of the simulations of ZT-40M and ZT-H, respectively. In this case, each contour represents the flux through a circle of radius r with z = constant — that is, the toroidal flux. Since every (0,n) mode is resonant at the same point, the m=0 resonant surface at $r_s/a=0.86$, islands aroundthis point are produced by the radial field components for all n. In the ZT-40M case, Figure 2.18 shows that the result of combining all the small islands, like those given above, was still an island chain of modest

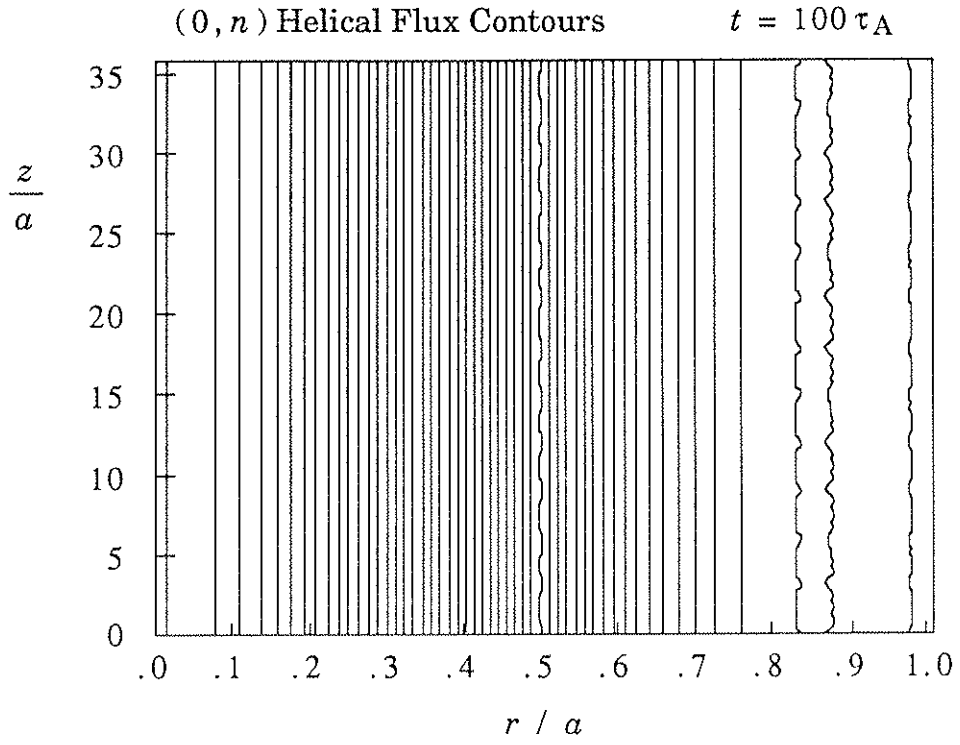

Figure 2.18 Plot of (0,n) helical flux contours at the conclusion of a simulation using the coil errors from ZT-40M. Modest islands with a periodicity of n = 24 are apparent around the resonant surface $r_s / a = 0.86$.

size. The shape of the islands can be seen and a characteristic n = 24 periodicity is evident. In the ZT-H case, the outcome was even better. The islands in Figure 2.19 are so small that their shape could not be resolved by the code. However, a perturbation with a periodicity of n = 48 can be seen on flux surfaces around the resonant surface.

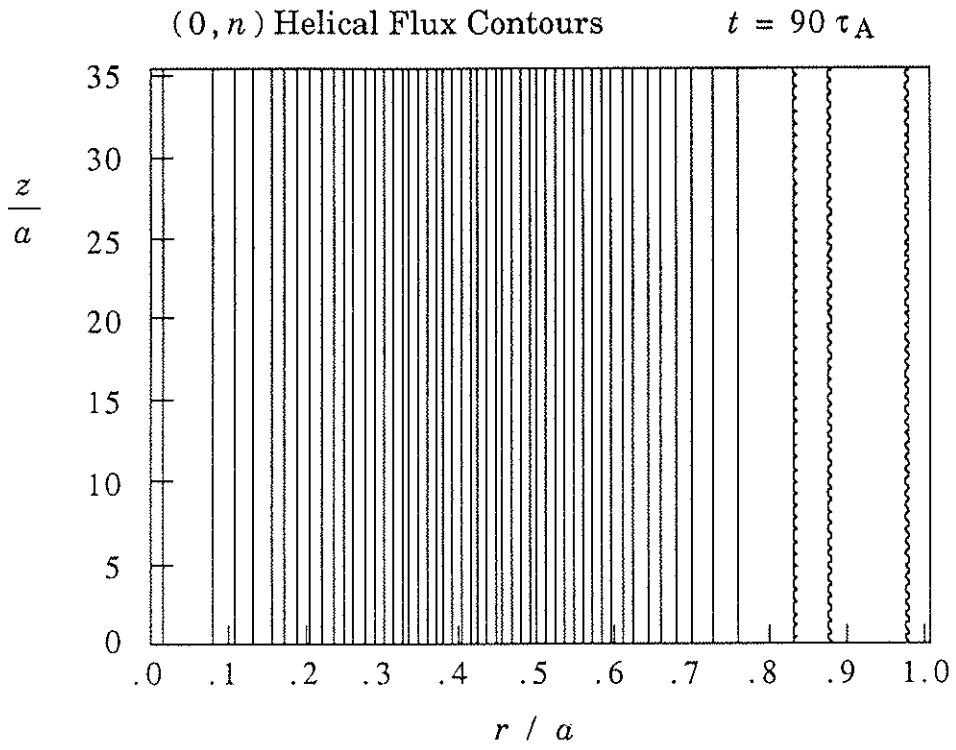

Figure 2.19 Plot of (0,n) helical flux contours at the conclusion of a simulation using the coil errors from ZT-H. No islands are apparent, but a perturbation with a periodicity of n = 48 can be seen around the resonant surface $r_s / a = 0.86$.

The above results show that the islands produced by m = 0 field errors from the toroidal field coils in ZT-40M and ZT-H should not

greatly alter the picture of the RFP dynamics. The islands are not big enough to disrupt the important edge region. This is especially important since m = 0 errors from coil discreteness cannot be avoided and can only be reduced by the expensive process of adding more coils. It appears that ZT-H, as now designed, will be able to study RFP confinement without undue influence from these field errors. A rough guide in the ZT-H design was that the "trouble point" for error-induced m = 0 islands would be if these islands extended halfway between the reversal surface and the wall. Figures 2.20 and 2.21 show plots of (0,n) flux contours from simulations

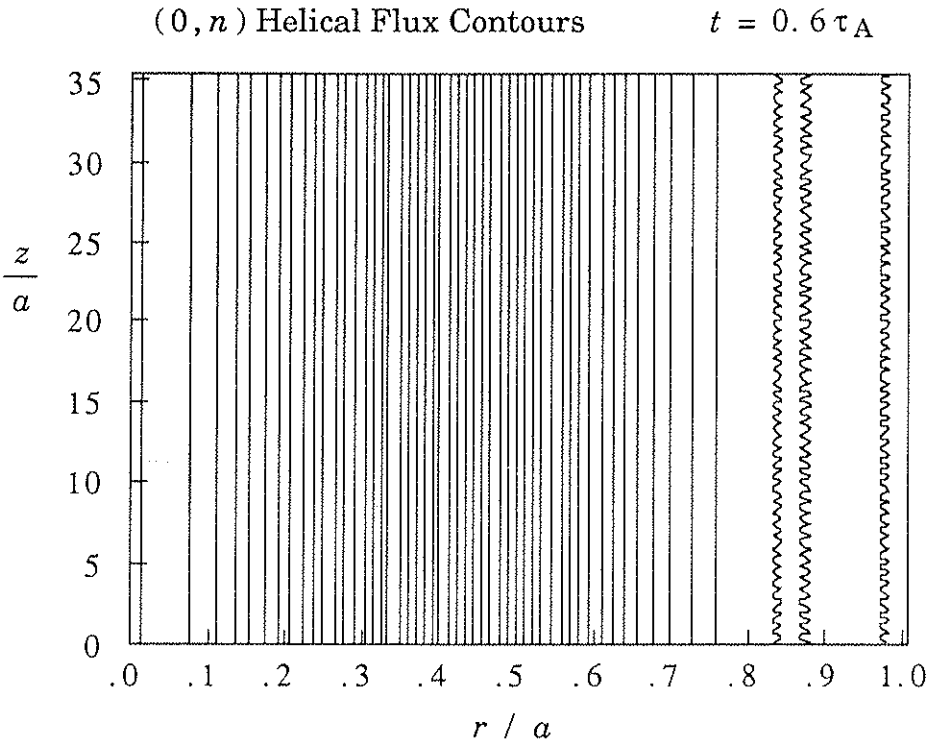

Figure 2.20 Plot of (0,n) helical flux contours at the start of a simulation using 4 x ZT-H coil errors. The islands (bounded by the "ruffled surfaces") do not extend halfway to the wall.

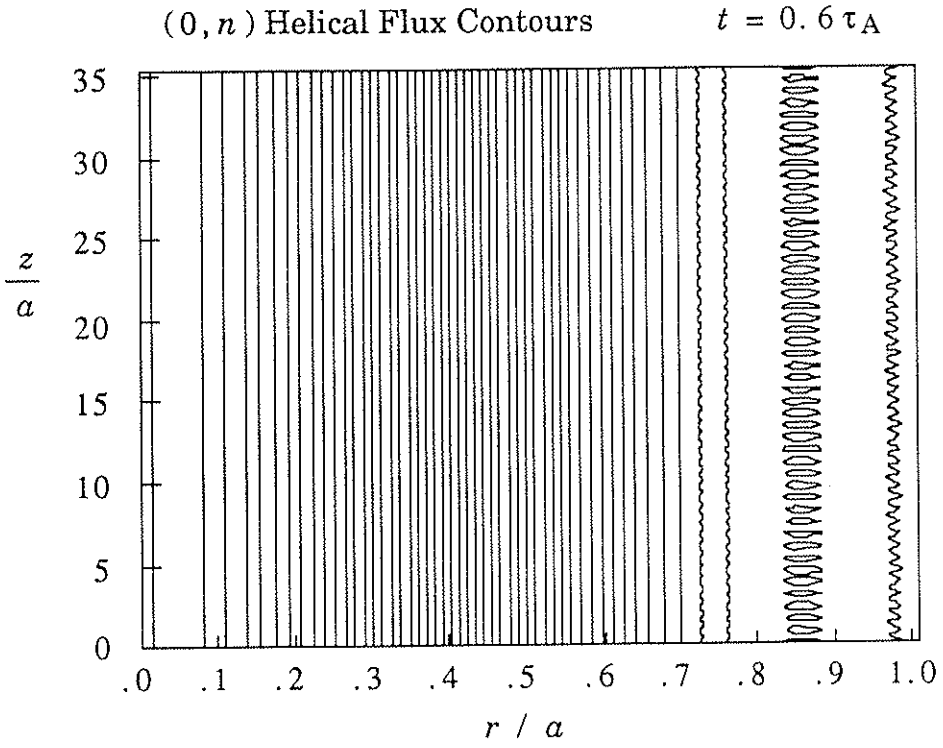

Figure 2.21 Plot of (0,n) helical flux contours at the start of a simulation using 8 x ZT-H coil errors. The islands (bounded by the "ruffled surfaces") extend more than halfway to the wall.

in which the size of the field errors from the ZT-H toroidal field coils was increased by a factor of 4 and 8, respectively. These plots are for the beginning of the simulation, before any island reduction. Given the above criterion, there is a safety factor of 5 to 8 in the size of the field error at the wall. (Note that this is an estimate. The size of each island must be interpolated, since the separatrix is not resolved by the code in either Figure 2.20 or Figure 2.21.)

2.5 RESULTS ON ERRORS FROM HOLES IN THE SHELL

2.5a FIELD ERROR MODEL

The field errors associated with holes in the conducting shell are caused by the flow of currents induced in the shell. These currents, whatever their source, are diverted around a hole and produce radial magnetic fields that bend the equilibrium field lines into and out of the hole. As another way to view this process, consider the shell as a perfectly conducting surface with no field on the inside and a uniform, tangential field on the outside. If a hole is introduced into the surface, the field will bend into the hole. This can be considered as a magnetostatic boundary value problem, and the radial fields can be calculated in terms of the field discontinuity across the surface. This discontinuity can be decomposed into two oppositely-directed fields, one on each side of the surface, added to a constant magnetic field, which cancels the field on the inside. The oppositely-directed fields play the major role in the boundary value problem, since the constant field can be added directly, by superposition. An application of Ampere's law across a surface shows that such oppositely-directed fields arise as the result of the current flowing in the surface. The relation between the field discontinuity (ΔB), the field on one side of the surface (B_s) and the surface current density (I_s) is:

$$\Delta B = 2B_s = \mu_0 I_s \quad . \tag{2.5.1}$$

Using equation (2.5.1), the physical origins of the hole errors can be discussed in terms of currents, while the solutions for the radial fields can be found from the related field discontinuities.

In ZT-H, and most conventional RFP's, the currents in the shell are associated with the creation of vertical fields. Equilibrium ($m = n = 0$) currents associated with the penetration of the equilibrium fields are prevented from flowing by the presence of insulated gaps in the conducting shell. However, a toroidal, current-carrying plasma requires a vertical field (B_v) for force balance along the major radius.[31] During the early phase of a discharge, the plasma shifts position. Toroidal image currents are induced in the wall. These flow in one direction on the "outboard" (large major radius) side of the torus, follow the poloidal gap (insulated poloidal ring allowing application of toroidal voltage) around to the other side, and return in the opposite direction on the "inboard" (small major radius) side. This pattern produces the $m = 1$ (or $cos\theta$) distribution necessary to generate a vertical field. At about this time, the external vertical field system is activated. This system is designed to provide an external source of vertical field for controlling the plasma equilibrium position. It induces currents in the wall which oppose those created by the plasma. If there is a mismatch between the external vertical field and that required by the plasma, perhaps due to a change in plasma profiles, or if no external vertical field system exists, net current will remain in the shell.

This current was taken as the source of the field errors in ZT–H due to the holes in the conducting shell . A "worst case scenario," the absence of an external vertical field system, was assumed. The net surface current density (I_v) was assumed to produce a vertical field (B_v) on the inside of the plasma vessel. The size of this vertical field, for a plasma with cylindrical cross–section and large aspect ratio (R / a), is:[32]

$$\frac{B_v}{B_{\theta 0}(a)} = \frac{1}{2}\left(\frac{a}{R}\right)\left[ln\left(8\frac{R}{a}\right) + \beta_{pol} + \frac{l_i}{2} - \frac{3}{2}\right]. \qquad (2.5.2)$$

The poloidal beta (β_{pol}) and the internal inductance (l_i), are defined by:

$$\beta_{pol} = \frac{\langle p \rangle - p(a)}{B_{\theta 0}(a)^2 / 2\mu_0} \qquad (2.5.3)$$

and

$$l_i = \frac{\langle B_{\theta 0}(r)^2 \rangle}{B_{\theta 0}(a)^2} , \qquad (2.5.4)$$

where p is the plasma pressure and $\langle ... \rangle$ stands for the average over a poloidal cross–section. The simulation modeled a plasma in which pressure has been neglected. Thus, $\beta_{pol} = 0$ was used. For the equilibrium profiles described in Section 2.2, the code calculated $l_i = 1.327$. Assuming that the conducting shell is a perfectly conducting surface, the field discontinuity produced by I_v is given by equation (2.5.1):

$$\Delta B = 2 B_v = \mu_0 I_v . \qquad (2.5.5)$$

The poloidal distribution must also be added, so that

$$\Delta B = 2 B_v \cos\theta . \qquad (2.5.6)$$

This value of field discontinuity was used to calculate the radial magnetic fields in the hole. (An external vertical field system can be included if ΔB is multiplied by a fraction representing the system–plasma mismatch.)

In the case of MST, the largest currents flowing in the conducting shell are those used to generate the equilibrium fields. As was mentioned in the last section, MST has no external coils. The m=n=0 toroidal current (I_z) is symmetrically routed away from the poloidal gap in a radial direction, bent around the iron core, and returned. This current produces the poloidal field at the edge of the plasma, $B_{\theta 0}(a)$, and equation (2.5.1) gives a field discontinuity across a perfectly conducting surface of

$$\Delta B_\theta = 2B_{\theta 0}(a) = \mu_0 I_z \ . \qquad (2.5.7)$$

(It should be noted that the toroidal current is not really routed away from the poloidal gap in a poloidally symmetric manner. Some m=1 component must be provided to create the needed vertical field. Using equation (2.5.2) and the stated values of β_{pol} and l_i, the size of the vertical field can be estimated at about 40% of $B_{\theta 0}(a)$. In this context, this smaller effect will be neglected.) A similar scenario allows the m=n=0 poloidal current (I_θ) to flow around the toroidal gap (insulated toroidal ring allowing application of poloidal voltage). This current produces the toroidal field at the edge of the plasma, $B_{z0}(a)$, and a field discontinuity:

$$\Delta B_z = 2B_{z0}(a) = \mu_0 I_\theta \ . \qquad (2.5.8)$$

When modeling the radial field-errors associated with the holes in MST, the calculation made use of these values for the field discontinuity.

The approximations that go into the radial-field calculation will now be presented. There are many holes in the shell of either ZT-H or MST. It was decided to treat each hole separately and then obtain the final result by superposition. This choice involves the implicit assumptions that all the holes are small — for a typical hole of radius r_h , $r_h / a \ll 1$ — and well-separated. If this is the case, the radial field in one hole can be calculated without regard to the radial fields in all the others, to a good approximation. In addition, the curvature of the cylindrical coordinate system would not be very apparent right around a small hole. The neighborhood of the hole could be represented by a flat plane. The assumption of small holes is basically a good one:

$$\left[\frac{r_h}{a}\right]_{MAX} = 0.134 \qquad \text{in ZT-H,}$$

and

$$\left[\frac{r_h}{a}\right]_{MAX} = 0.110 \qquad \text{in MST.}$$

The assumption that all of the holes are well-separated is not as good. The holes in diagnostic arrays are spaced rather closely, for example. However, the coupled-hole problem is a difficult one, and the approach taken above is reasonable and has a readily accessible solution.

The problem of finding the radial field in a single hole in a perfectly conducting plane has been solved as a problem in magnetostatics.[33] The geometry of this situation is illustrated in Figure 2.22 . Above the plane

$(r > a)$, there is a tangential magnetic field in the $y-$direction. It has uniform strength ΔB far from the hole. Below the plane $(r < a)$, the field away from the hole is zero. The hole itself has radius α, and is described by the polar coordinate $\rho^2 = y^2 + z^2$. The radial field in the hole $(r = a)$ given in terms of the field discontinuity across the hole (ΔB), is:

$$B_r(r=a, y, z) = \begin{cases} \left(\frac{2\Delta B}{\pi}\right)\left(\frac{y}{\sqrt{\alpha^2 - \rho^2}}\right) & \rho < \alpha \\ 0 & \rho > \alpha \end{cases} . \quad (2.5.9)$$

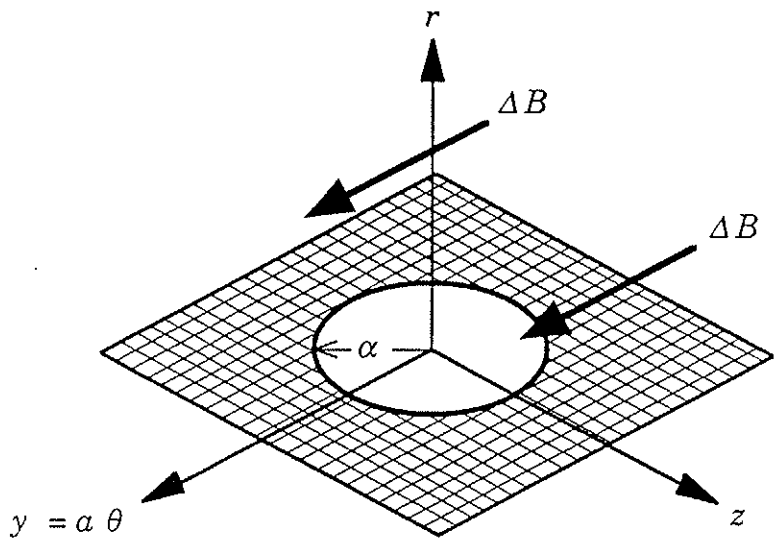

Figure 2.22 Geometry for the calculation of the radial field entering a hole in a perfectly conducting plane. The tangential magnetic field ΔB is uniform and constant away from the plane.

The real quantities of interest are the Fourier amplitudes obtained by taking the Fourier transform of the above radial field. To re-establish contact with the periodic geometry of the code, the y-direction in the plane is identified with the poloidal direction in the cylinder ($y = a\,\theta$), and the z-direction in the plane is identified with the (periodic) axial direction in the cylinder. Then, the limits on y and z are:

$-\pi a < y \leq \pi a$ where a = minor radius and

$-\pi R < z \leq \pi R$ where R = major radius (of an equivalent torus).

In a periodic geometry, the continuous wave numbers k_y and k_z take on the discrete values

$$k_y = \frac{m}{a} \qquad \text{and} \qquad k_z = \frac{n}{R} \; . \tag{2.5.10}$$

Under these conditions, the spectrum of Fourier amplitudes is given by:

$$[B_r(m,n)]_{r=a} =$$

$$\frac{i\,\Delta B}{\pi^2}\,\varepsilon\left(\frac{\alpha}{a}\right)^2 \sum_{s=1}^{\infty} \frac{(-1/2)^s}{(s-1)!}\left(m\,\frac{\alpha}{a}\right)^{2s-1} \frac{j_s\left(n\,\frac{\alpha}{a}\,\varepsilon\right)}{\left(n\,\frac{\alpha}{a}\,\varepsilon\right)^s} \; . \tag{2.5.11}$$

In the above expression, ε is the inverse aspect ratio ($\varepsilon = a / R$) and j_s is the spherical Bessel function of the first kind, of order "s".[34] For all values of m and n used in the code, the series converges adequately for a maximum value of s equal to 50.

The spectrum for a single hole given by equation (2.5.11) is quite broad in both m and n. This can be seen in the following figures, which present a sample m-spectrum and n-spectrum for a large hole that might be "typical" of ZT-H or MST ($\alpha/a = 1/8$). The ZT-H aspect ratio is used. Figure 2.23 shows a graph of Fourier amplitude as a function of $|m|$ at $|n| = 1$, approximately the peak of the n-spectrum. Figure 2.24 shows a similar plot of Fourier amplitude versus $|n|$ at $|m| = 16$, the peak of the m-spectrum. (The Fourier amplitudes are odd in m and even in n,

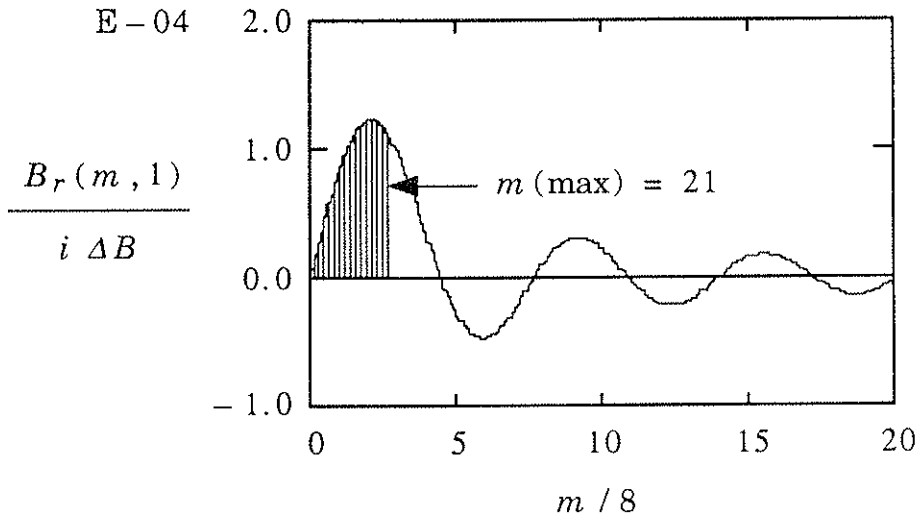

Figure 2.23 Plot of Fourier amplitude as a function of $|m|$ at $|n| = 1$ for the radial field in a single hole, as calculated from equation (2.5.11). The maximum value of m used in the simulation is indicated. (The spectrum is odd in m.)

as can be inferred from equation (2.5.11).) Even using the maximum number of modes permitted by machine storage (see Table 2.3), only about

half of the largest peak from each spectrum could be included in the simulation. (Included modes are shown in the shaded regions.)

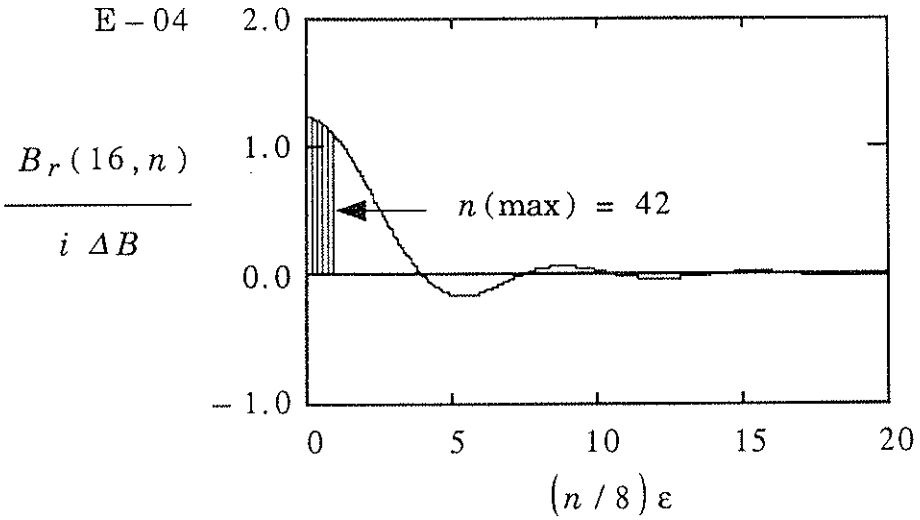

Figure 2.24 Plot of Fourier amplitude as a function of |n| at |m| = 16 for the radial field in a single hole, as calculated from equation (2.5.11). The maximum value of n used in the simulation is indicated. (The spectrum is even in n.)

The radial fields given by such a spectrum are not likely to create large magnetic islands. With so many modes excited, even the largest ones have rather small amplitudes — a typical value of $B_r / \Delta B \sim 10^{-1}$ gives a maximum amplitude of $B_r(m,n) / \Delta B \sim 10^{-4}$. Moreover, the modes with the largest amplitudes are non-resonant: $m/n \neq q$ anywhere in the plasma. The spectra tend to peak at small |n| and large |m| — around $|m|(\alpha/a) \sim 2$. Thus, the largest radial fields have $|m/n| \gg 1$ while the RFP equilibrium has $|q| \ll 1$. Other modes with smaller amplitude but

larger values of |n| might be candidates for resonance, but they don't penetrate into the plasma. The modified Bessel function solutions for the initial vacuum profiles (see equation (2.3.18)) fall off more quickly away from the boundary as n is increased. Under these conditions, the exclusion of weaker modes that are more non-resonant (larger m) or less penetrating (larger n) from the simulation, as shown in the spectra above, becomes less serious. No single mode from an individual hole is likely to give rise to a large magnetic island.

The most serious threat for island formation comes from the constructive interference of radial fields from more than one hole. The simulation included the effects of all the holes in the conducting shell, within the limits of the approximations in the model. The shape of the spectrum was the same for each hole, with the magnitude for each m and n determined by the hole size. This single-hole spectrum was given by equation (2.5.11), which neglects the effects of radial field in other holes. Interaction between holes was allowed, however, through the inclusion of phase factors that took into account the position of a hole in the shell. The geometry of Figure 2.22 centers the hole at $\theta = 0$ and $z = 0$, and this choice is implicit in the spectrum of equation (2.5.11). Given a Fourier decomposition of the form

$$B_r\,(r=a) \;=\; [B_r\,(m\,,n)\,]_{r\,=\,a}\;\; e^{\,-i\,(\,m\theta\,+\,nkz\,)}, \qquad (2.5.12)$$

the multiplication of each Fourier amplitude, B_r(m,n) , by a phase factor

$$e^{+i(m\theta_0 + nkz_0)} \qquad (2.5.13)$$

changes the spectrum to be that for a hole at $\theta = \theta_0$ and $z = z_0$. All the actual values of poloidal angle θ_0 and toroidal angle $\phi_0 = z_0 / R$ from ZT-H and MST were used in calculating these phase factors. Then, a summation over the holes was performed. Radial fields with the same periodicity as the hole separation could thus be reinforced.

(Determining the actual hole positions in the shell was somewhat more subtle than simply measuring angular positions in a toroidal coordinate system. As described in the beginning of Section 2.5a, a toroidal plasma will shift outward along the major radius. If the diagnostic chords are to intersect the center of the shifted plasma, the origin of the poloidal coordinate system describing the holes must be displaced outward relative to the center of the shell. Such a displacement is included in the design of both ZT-H and MST. Although such a plasma shift is a toroidal effect that will not occur in a cylindrical simulation, it was decided that the actual hole positions should be represented. Thus, the design displacement — 2.22 cm. for ZT-H and 6.00 cm. for MST — was included. This has one disadvantage. As seen from the plasma center, the holes are pushed towards the outer mid-plane. Any prediction of mode reinforcement via constructive interference may be reduced by this change in the poloidal spacing. On the other hand, the removal of holes from the exact top and bottom of the shell enhanced the prospects for mode reinforcement. Given the $cos\theta$ dependence of the current, the holes at $\theta = 90^\circ$ or $\theta = 270^\circ$

would not otherwise contribute. Thus, although the difference between including and neglecting the shift has not been explored, it is thought to be small.)

The radial magnetic fields described by the Fourier amplitudes and phase factors calculated above constitute the field errors. Once the proper value of field discontinuity was selected, equation (2.3.14) was used to impose these fields at the wall. Then, the initial vacuum profiles for the simulation were found.

2.5b PLASMA – PERTURBATION STEADY – STATE

The plasma – perturbation combination reached a steady – state similar to that decribed in Section 2.4 b .

2.5c PLASMA EFFECTS ON THE PERTURBATIONS

Given linear perturbations and resistive MHD, these effects are the same as those described in Section 2.4 c .

2.5d PERTURBATION EFFECTS ON THE EQUILIBRIUM: "MACHINE PERFORMANCE RESULTS"

i ZT – H

ZT – H is designed with a total of 120 holes in the shell. They range in size from 4 3/4″ (12.07 cm.) – diameter pump ports to 2 1/8″ (5.40 cm.) – diameter diagnostic ports.[35] Figure 2.25 is a top – view schematic of the device, showing the toroidal distribution of the poloidal arrays of

holes. The position of the holes in each array are indicated on a corresponding poloidal cross-section. The position of every hole shown went into the calculation of the phase factors of equation (2.5.13).

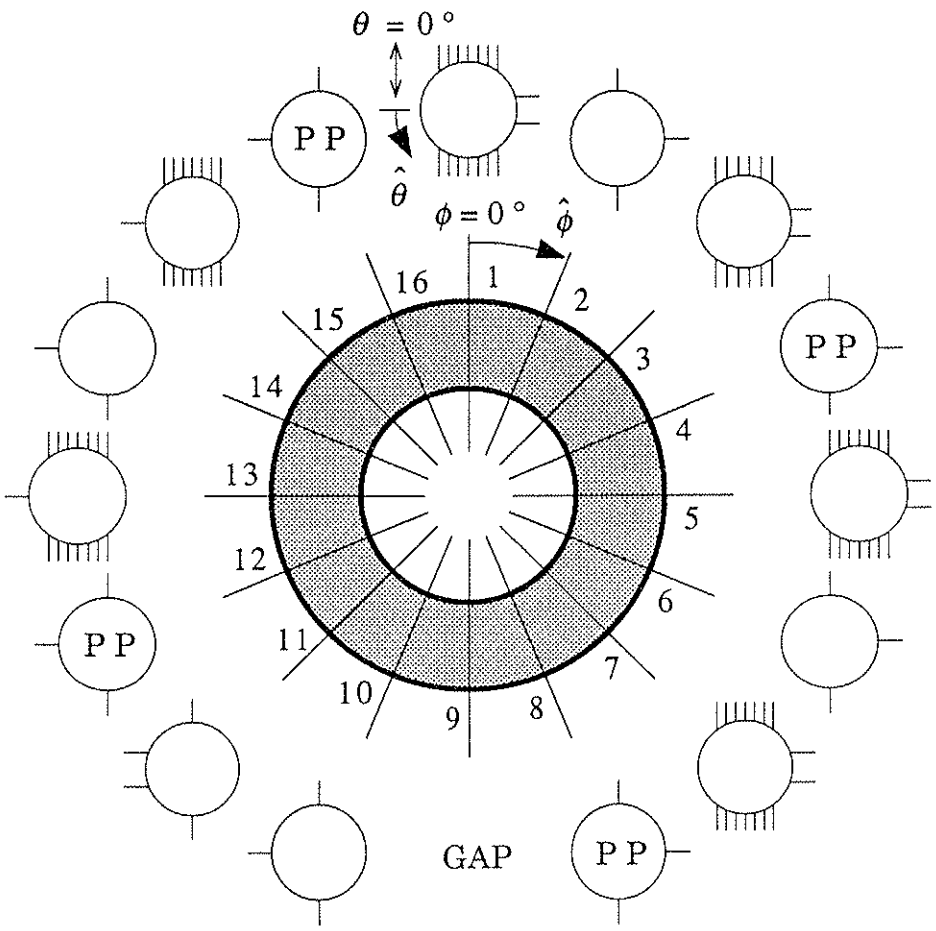

Figure 2.25 ZT-H holes: The shaded ring represents a top view of the torus. Each numbered line represents the toroidal position of an array of holes. An array is represented by a poloidal cross-section at the end of its line, and the lines on these represent the hole positions. (PP = pump port)

The value of field discontinuity (ΔB) used to evaluate the spectrum of equation (2.5.11) was that associated with the creation of a vertical field. The fact that the field in the hole model is assumed to be in the $y = a\,\theta$ direction is perfectly consistent with this. A vertical field can be viewed as a poloidal field with an m = 1 or $cos\theta$ poloidal dependence. This was taken into account in equation (2.5.6), which, along with equation (2.5.2), gave the numerical value of ΔB.

The largest magnetic islands should be caused by resonant modes with mode numbers that coincide with the periodicity of the holes. As before, modes with m = 1 are considered. (Note that the spectrum given by equation (2.5.11) has no m = 0 modes.) The value of n that is most likely to be reinforced by constructive interference is n = 16. There are sixteen equally-spaced toroidal locations for hole arrays, even though one of these is actually empty. Thus, attention is focused on the resonant (1, -16) mode. Even this mode did not produce a magnetic island of any considerable size. The linear island width is calculated to be $(W/a)_{(1,-16)}$ = 1.59 e - 2. Figure 2.26 shows a plot of (1, -16) helical flux contours at the end of the simulation. The area around the resonant surface at $r_s / a = 0.60$ shows that this island was too small to be resolved by the code. This result obtains for the case of the current in the shell providing 100% of the vertical field required for the plasma to be in force balance. In the simulation, the amount of vertical field could be increased through an increase in ΔB. When ΔB is increased by a factor of 100, the calculated linear island width at the beginning of the simulation becomes:

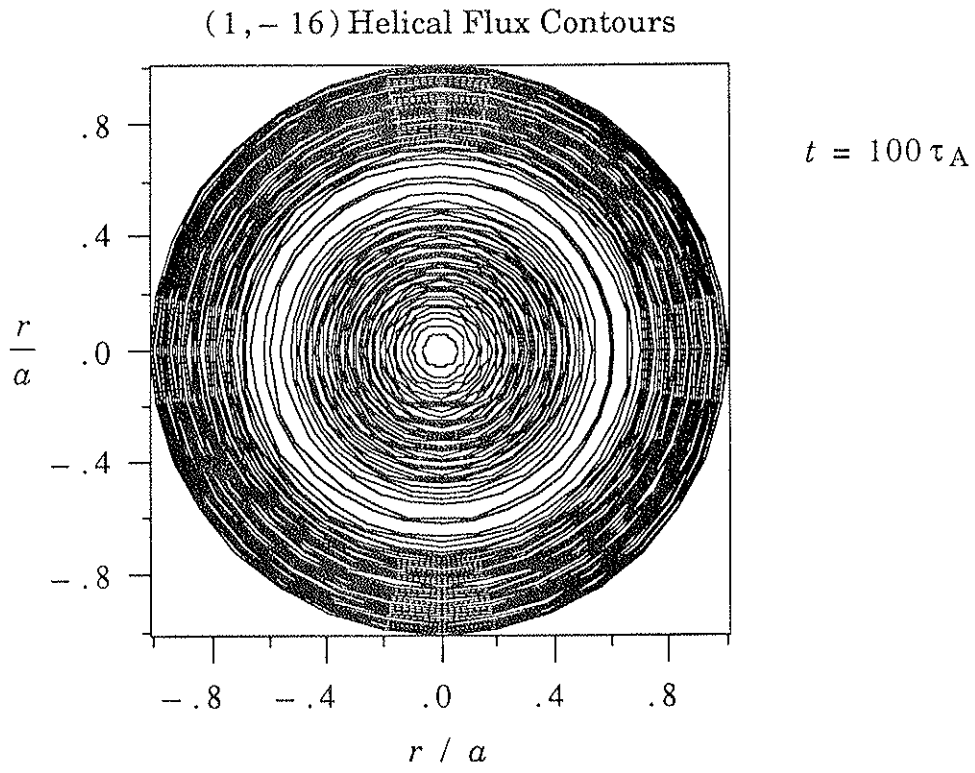

Figure 2.26 Plot of (1, – 16) helical flux contours at the conclusion of a simulation using the shell errors from ZT–H and ΔB for a current providing 100% of the vertical field. Any magnetic island around the resonant surface $r_s / a = 0.60$ could not be resolved by the code.

$(W/a)_{(1,-16)} = 9.32\ e-2$. This island did appear on a plot of (1, – 16) helical flux contours, as shown in Figure 2.27. Even so, at only about 9% of the minor radius, the island is rather small. Thus, the ZT–H plasma is not likely to be hurt by magnetic islands produced by holes in the conducting shell. For the reasonable value of 10% vertical field mismatch,

there is a safety margin of about 1000, or 10 to reach 100% mismatch and another 100 to produce a noticeable island.

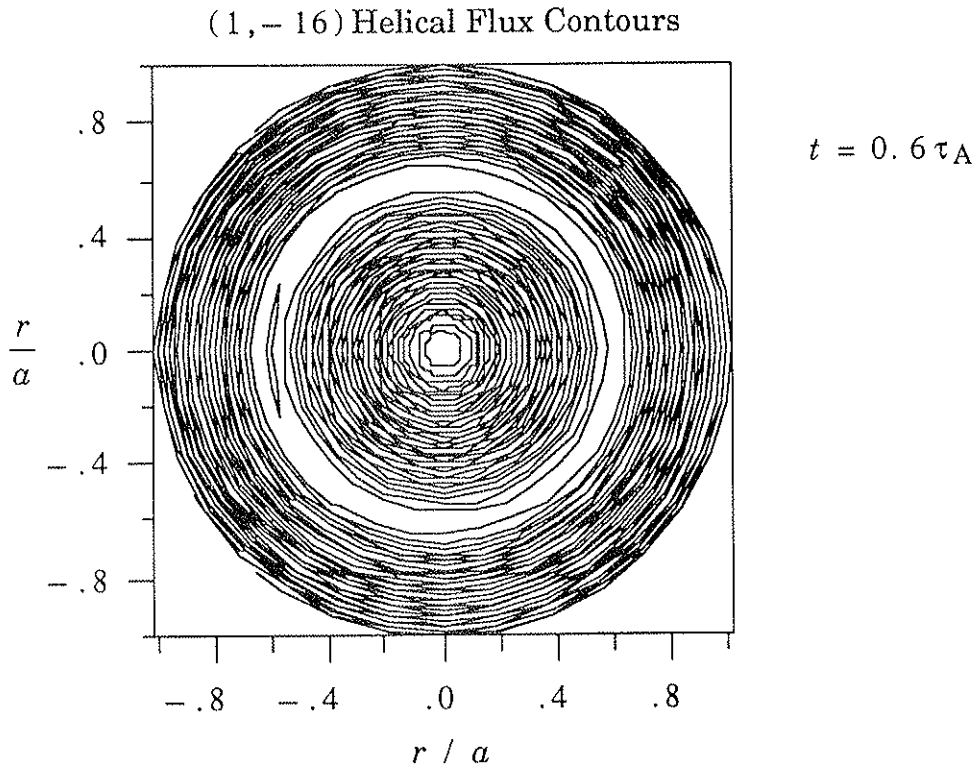

Figure 2.27 Plot of (1, − 16) helical flux contours at the conclusion of a simulation using the shell errors from ZT − H and ΔB for a current providing 100 x 100% of the vertical field. A small magnetic island is evident around the resonant surface $r_s / a = 0.60$.

Aside from causing the formation of magnetic islands, radial fields associated with holes in the shell can divert field lines near the edge of the

plasma. The simulation results show that this is not a major source of trouble either. Figure 2.28 is a field-line puncture plot. It shows a view of the mid-plane of the cylinder, along the axial direction. Field lines at various radial positions are tagged and then followed, as they trace out curves around the cylinder. Each time they cross the mid-plane, the crossing position is marked. The figure shows that the field lines receive a radial "kick" around the location of a hole, but generally remain well-confined. (The eight-fold periodicity is due to the eight toroidal locations that have three holes poloidally.) The field lines do not intersect the wall.

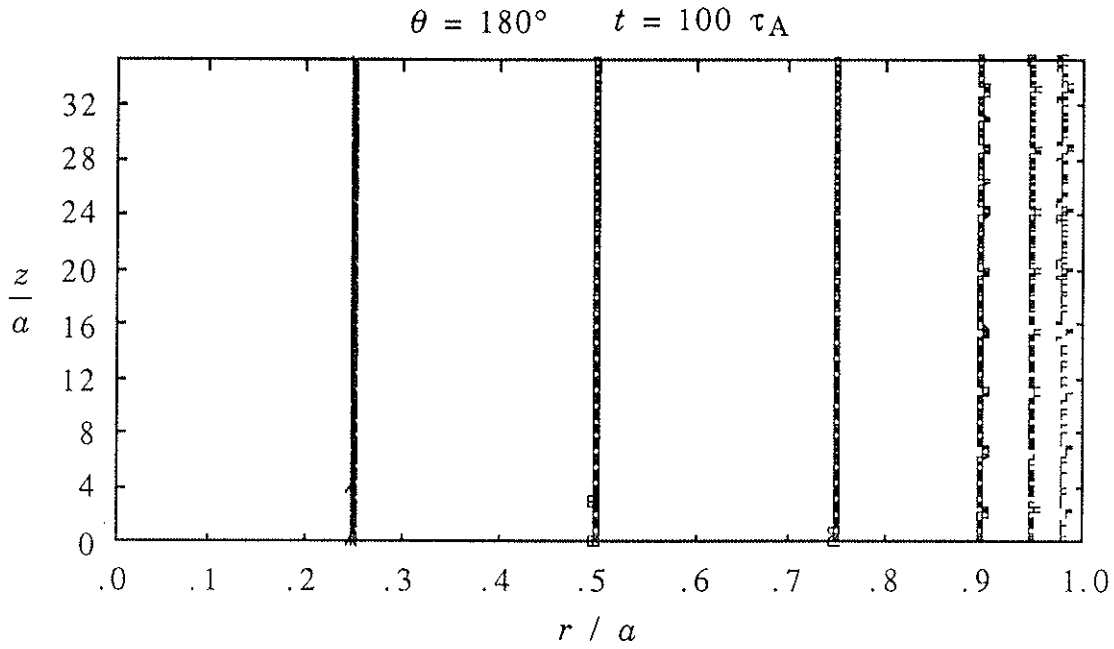

Figure 2.28 Field-line puncture plot showing the intersection of field lines with the r-z plane at $\theta = 180°$. The n = 8 radial departure of the field lines near the edge is an indication of the influence of the holes.

The amount of field line deviation caused by a single hole was studied more precisely by increasing the resolution of the code. This was done by reducing the length of the cylinder relative to its minor radius. The hole then occupied a greater fraction of the length and was more easily "seen" by modes with lower values of n. For a fixed value of n_{max}, more of the B_r-spectrum describing the hole could be included. The radial fields from the hole fall off to a background level at an axial distance of approximately five hole widths (10α). Thus, the length of the cylinder was chosen to be $L = 2\pi R = 22\alpha$ (2α for the hole and 10α on either side). For a hole with $\alpha/a = 0.1337$, the inverse aspect ratio is now $\varepsilon = a/R = 2.136$. This is an increase by a factor of 12. Figure 2.24 shows that the amount of n-spectrum covered increases by the same factor, for a fixed value of n_{max}. Part of this increase in toroidal resolution was passed on to the poloidal resolution: n_{max} was halved and m_{max} was doubled. The net result was that, for each spectrum, the entire first peak and half of the next was included in the simulation.

The results show that the amount of field line deviation produced by a single hole is well within the design tolerance. The size of the hole quoted above is that for the largest in the device — the 4 3/4"-diameter pump port. Figure 2.29 is a field-line puncture plot that shows the amount of deviation. A field line near the edge remains well-confined, but is "pulled" 15.9 mm. towards the wall by the hole. Figure 2.30 is a puncture plot that shows field lines in the vicinity of a poloidal cross-section containing a pump-port-sized hole and two diagnostic arrays

(see location 13 on Figure 2.22). Again, a field line is basically well-confined. The deviation towards the large hole is only 14.2 mm. in this case, perhaps due to interference from the diagnostic arrays. These results correspond to a "worse case" scenario, in which 100% of the vertical field is provided by currents in the shell. Given an anticipated vertical field mismatch of 10%, the deviations would be reduced to 1.59 mm. and 1.42 mm. These are well within the design criterion of 5 mm.[36]

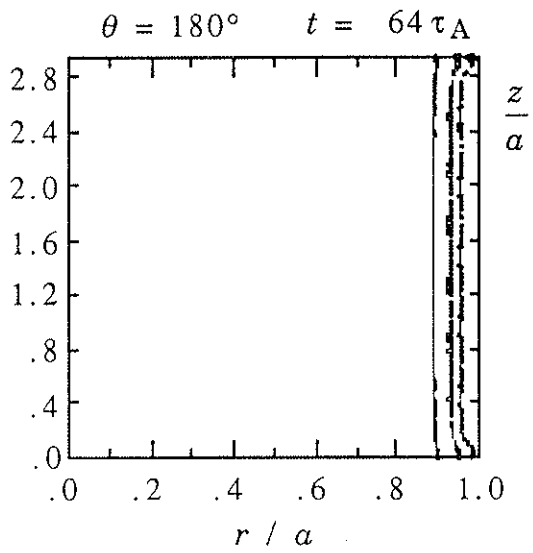

Figure 2.29 Field-line puncture plot for the r-z plane at θ = 180°. Field lines at the edge are pulled towards the single 4 3/4" -diameter pump port at z/a = 0 = 2.94.

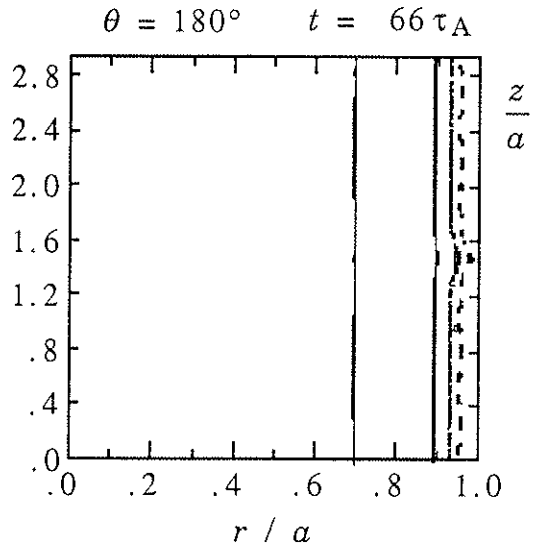

Figure 2.30 Field-line puncture plot for the r-z plane at θ = 180°. Field lines at the edge are pulled towards the single 4 3/4" -diameter pump port at z/a = 1.47 and nearby dignostic arrays. (See location 13 on Figure 2.22.)

ii MST

At the time of the simulation, the MST design included a total of 368 holes in the shell.[37] Of these, 175 are intended for diagnostic access. The largest are four 4 1/2″(11.43 cm.)-diameter ports and the remainder are mostly 1 1/2″(3.81 cm.)-diameter ports. These diagnostic ports are shown in Figure 2.31. As before, a top view of the device indicating the toroidal distribution of the poloidal arrays is presented. The remaining 193 holes are 1 1/2″-diameter ports that are used for pumping out the chamber. They are arranged in seven rows along the bottom of the device, within a poloidal arc from $\theta = -109^\circ$ to $\theta = -57^\circ$. Four rows of 28 holes each (spaced every 10° toroidally from $\phi = 45^\circ$ to $\phi = 315^\circ$) alternate with three rows of 27 holes each (spaced every 10° toroidally from $\phi = 50^\circ$ to $\phi = 310^\circ$). The "empty" toroidal locations (except for the poloidal gap at $\phi = 0^\circ$) are occupied by "blind" holes that are not completely drilled through. These account for another 56 holes which can be included in the simulation. The phase factor for each of these holes was calculated from equation (2.5.13), and a sum over holes was performed.

The field discontinuity (ΔB) came from the shell currents that generate the equilibrium fields. Equations (2.5.7) and (2.5.8) show that both poloidal and toroidal field discontinuities arise outside each hole, because the shell currents act to create an equilibrium field in both directions. The field in the hole model is assumed to be in the poloidal direction, and the poloidal discontinuity given by equation (2.5.7) can be used to find the Fourier amplitudes from the spectrum of equation (2.5.11). To make use of

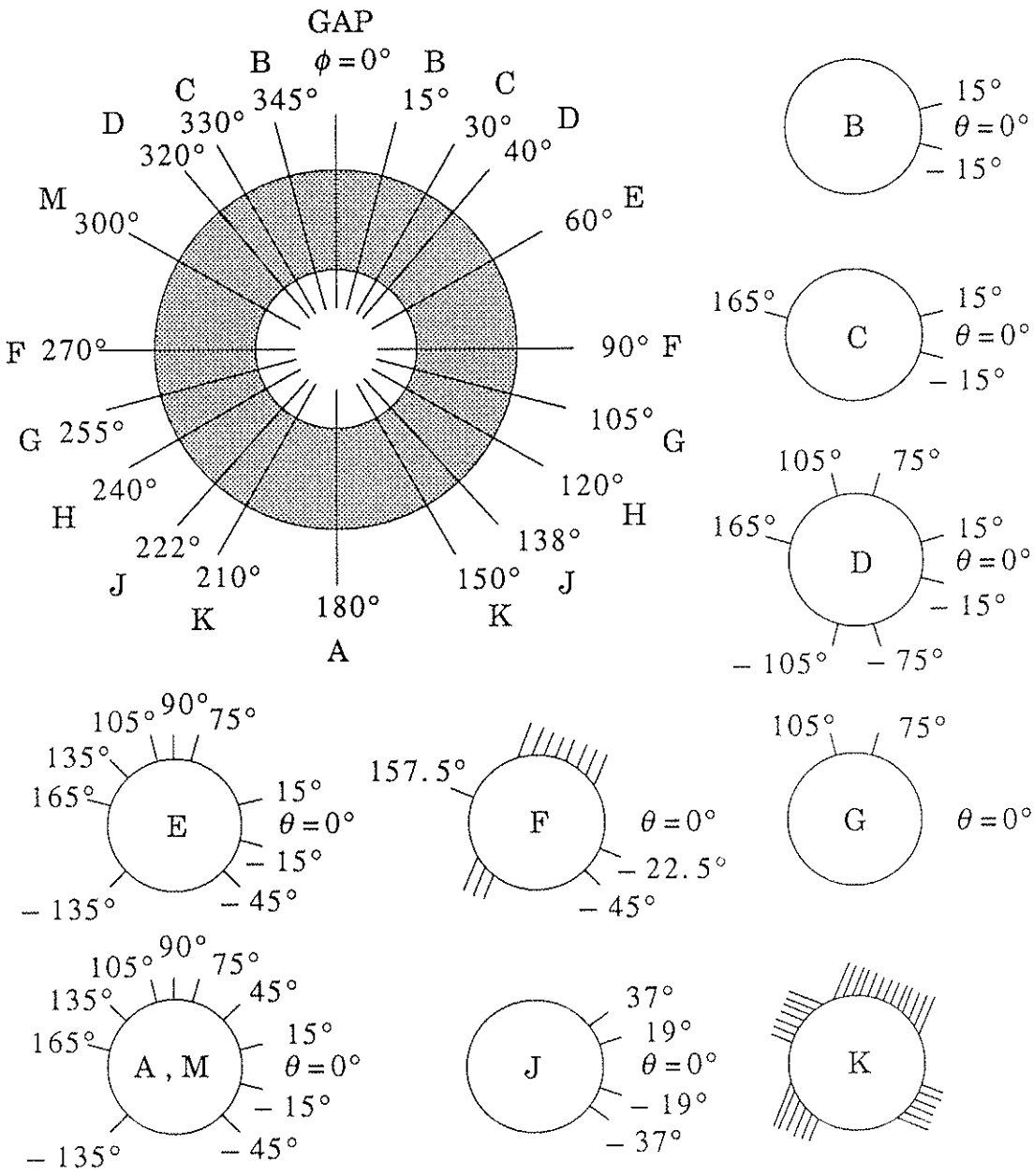

H is the same as A and M without the hole at 90°

Figure 2.31 MST holes: The shaded ring is a top view of the torus with the toroidal position of each labeled hole array indicated. Each array is shown as a poloidal cross-section, and the lines are the hole positions.

the toroidal discontinuity of equation (2.5.8), the y and z-directions in the model must be interchanged. This can be done by exchanging the roles played by k_y and k_z from (2.5.10) in the spectrum of (2.5.11). The given ΔB_z can then be used to find the Fourier amplitudes from this new spectrum. (Note that m=0 modes are included in this "interchanged" spectrum, as the m-spectrum is now given by Figure 2.24 .) The Fourier amplitude used as the field error for each mode consisted of the sum of the poloidal and toroidal contributions.

Three types of modes are most likely to produce problems. As before, modes with m=0 are a source of concern because of their effect on the reversal surface. Resonant modes with n numbers that are the same as the periodicity of the hole separation are likely to cause magnetic island formation. Finally, the array of pumping holes along the bottom of the device may produce radial fields that have up-down asymmetry. This would show up as a shift of the plasma — a (1,0) mode. Each of these potential problems will be considered.

Modes with m=0 do not pose a significant threat. Figure 2.32 shows (0,n) helical flux contours at the conclusion of a simulation run. There are no resolvable magnetic islands around the resonant surface at r_s / a = 0.86. The radial perturbations do "wiggle" the flux surfaces, however. Certain larger indentations can be observed at the two indicated axial locations — z/a = 6.91 and z/a = 11.18 . These correspond to toroidal locations of $\phi = 137^\circ$ and $\phi = 222^\circ$, just the positions of the large 4 1/2"-

diameter ports. This (0,n) flux plot includes the effects of all modes with m = 0. Since the "interchanged" m-spectrum associated with ΔB_z peaks at m = 0 (see Figure 2.24), the largest holes can be resolved somewhat by the summation over n. Their radial fields can be observed acting in a more localized fashion. These local effects are more properly observed in a field-line puncture plot, where all modes contribute, and will be sought there later.

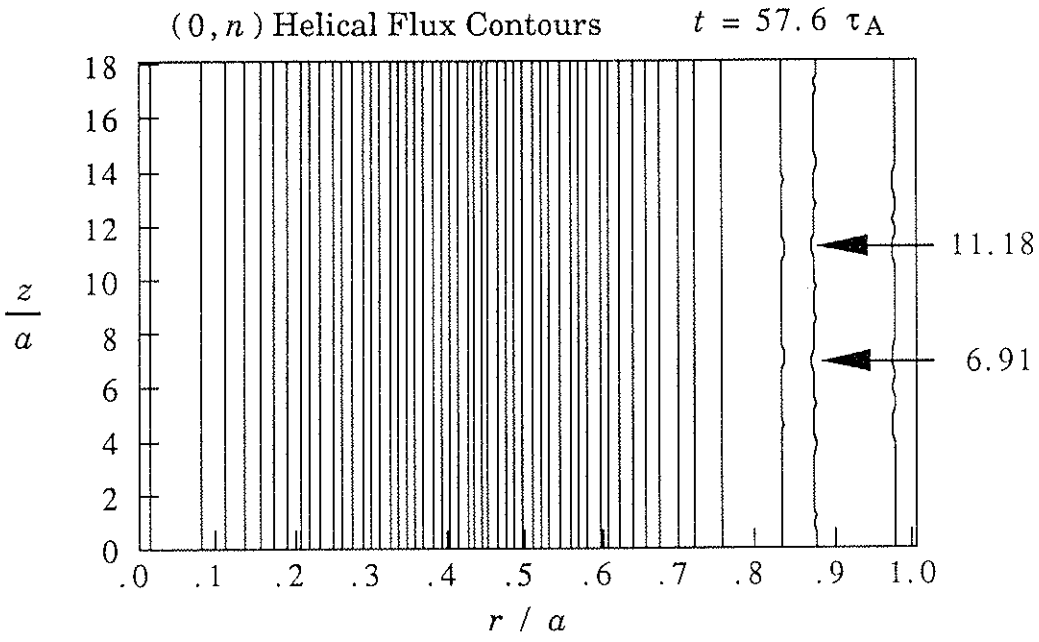

Figure 2.32 Plot of (0,n) helical flux contours at the conclusion of a simulation using the shell errors from MST. No islands can be observed around the resonant surface $r_s / a = 0.86$. The influence of the holes can be seen in the radial excursions of the flux surfaces near the indicated toroidal locations.

No large m = 1 magnetic islands arose. Experience has shown that equilibrium profiles like those of Figure 2.2 are most sensitive to resonant perturbations with $|k\,a| = |n\,\varepsilon| \sim 2$. For MST, $\varepsilon = a/R = 0.3467$ and $|n| \sim 6$, making the resonant (1, −6) mode the most likely to cause island formation. Moreover, there are two different groups of hole arrays with six members spaced equally around the toroidal direction. $\phi = 30^\circ, 90^\circ, 150^\circ, 210^\circ, 270^\circ, 330^\circ$ and $\phi = 60^\circ, 120^\circ, 180^\circ, 240^\circ, 300^\circ$ (the poloidal gap is in the remaining spot at $\phi = 0^\circ$). This six-fold symmetry will increase the size of

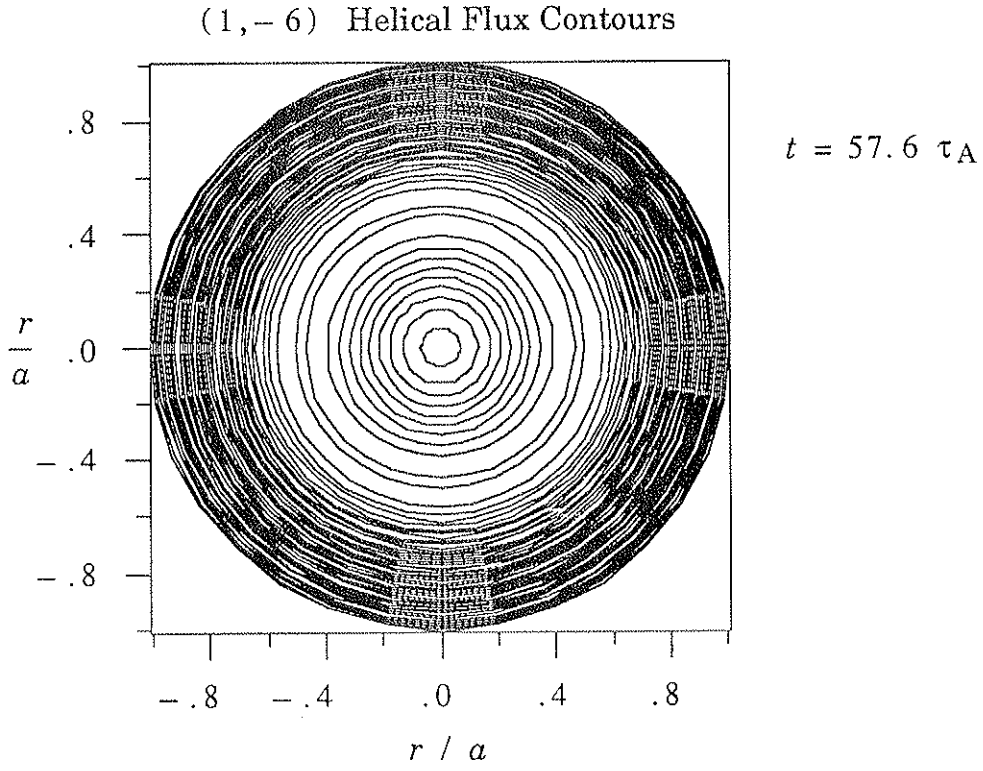

Figure 2.33 Plot of (1, −6) helical flux contours at the conclusion of a simulation using the shell errors from MST. No magnetic islands are apparent around the resonant surface $r_s / a = 0.48$.

a (1,−6) perturbation through constructive interference. Even so, this mode did not produce a magnetic island that could be resolved by the code. Figure 2.33 shows a plot of (1,−6) helical flux contours at the end of the simulation. The area around the resonant surface at $r_s / a = 0.48$ shows no evidence of an island. An increase in ΔB by a factor of 50 did produce a (1,−6) magnetic island whose width was less than 10% of the plasma radius. Thus, MST is safe from magnetic islands produced by holes in the conducting shell, with a safety factor of about 50 in shell current.

MST should also be safe from a shift caused by the fields around the fairly localized array of pumping holes. The radial fields from a localized array are strong at one poloidal location; they have a (1,0) character. Field lines are bent in one direction in the vicinity of the holes, and in the opposite direction 180° away poloidally. If the holes are localized to the bottom of the plasma, this produces a sideways shift. Figure (2.34) shows contours of (1,0) helical flux at the end of the simulation. These are basically contours of constant poloidal flux which are concentric about the magnetic axis. No appreciable shift of this axis is evident, even though both "real" and "blind" holes were included in the simulation to give the proper n=0 symmetry. Localized radial fields from the pumping holes are not large in MST.

Finally, the amount of field line deviation produced by the holes in MST was considered. Figure 2.35 is a field−line puncture plot showing the behavior of the field lines in the presence of all the holes (including the

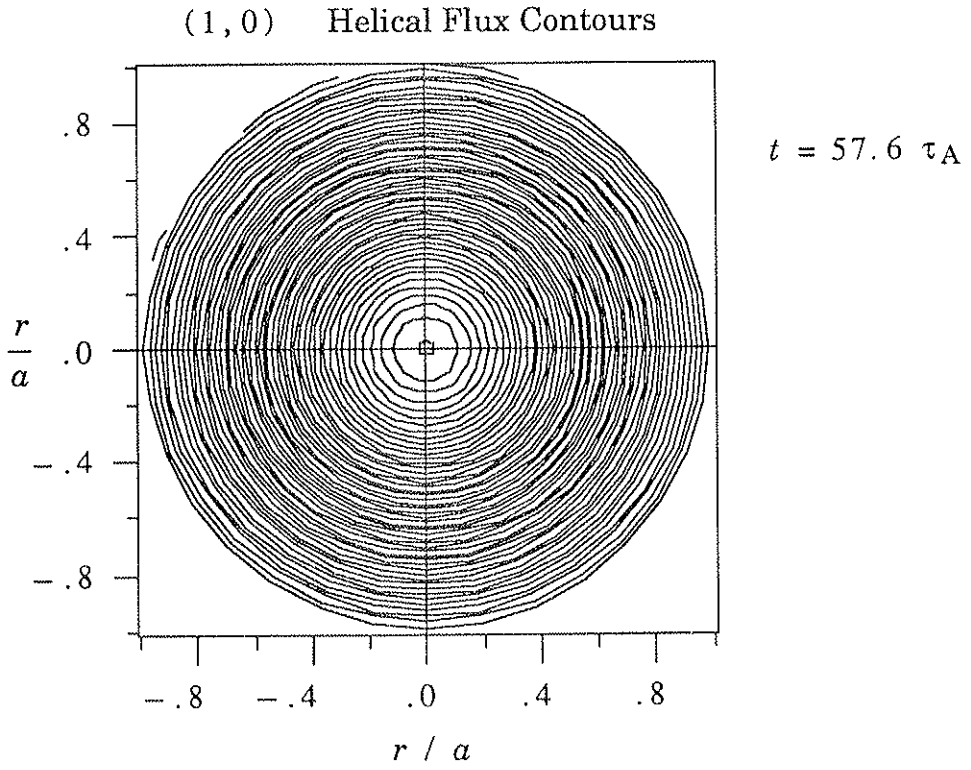

Figure 2.34 Plot of (1,0) helical flux contours at the conclusion of a simulation using the shell errors from MST. There is a slight outward shift of the magnetic axis, but it is very small.

"blind" holes). The field lines are well-confined, but receive small radial kicks from the holes. The presence of a hole array at a particular toroidal location is less apparent here than it was in the ZT-H case. It may be that the variety of poloidal spacings in each array provide for a "de-phasing" between toroidal locations. Figure 2.36 is a puncture plot that shows the behavior of the field lines in the vicinity of a single 4 1/2"-diameter port. The resolution of the hole has been increased by reducing the length of the

cylinder in the same manner as was described for ZT-H. The field line is "pulled" 21.3 mm. toward the wall. Thus, the field lines in MST remain basically well-confined in the presence of radial fields from holes in the shell, although their deviation around the four largest ports may be a source of concern.

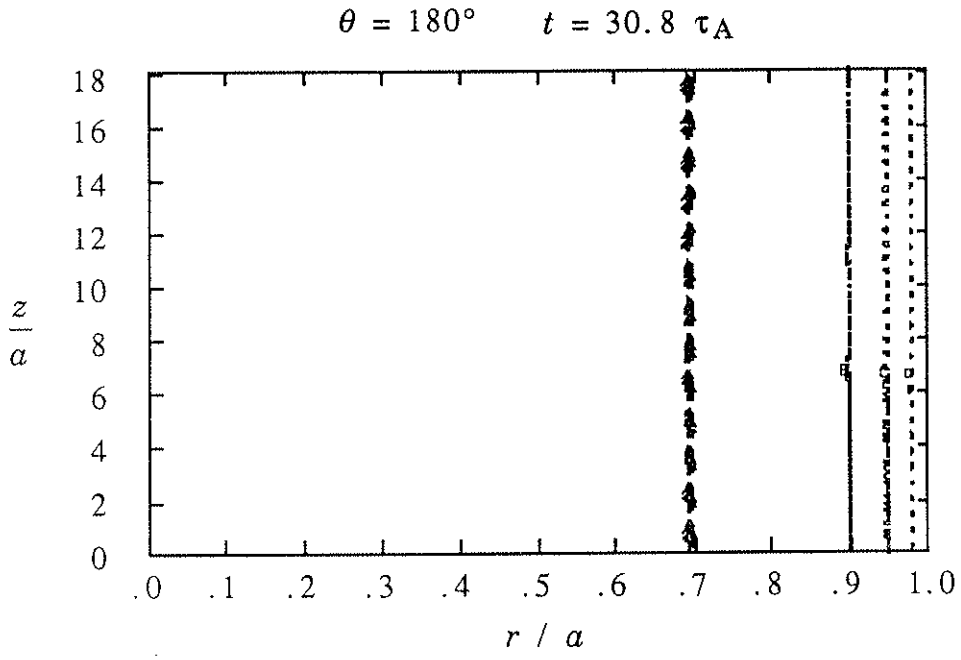

Figure 2.35 Field-line puncture plot showing the intersection of field lines with the r-z plane at $\theta = 180°$. The influence of a hole array at a particular toroidal location is more difficult to discern than it was in the ZT-H case, except for the two arrays with the large holes at $z/a = 6.91$ and $z/a = 11.18$.

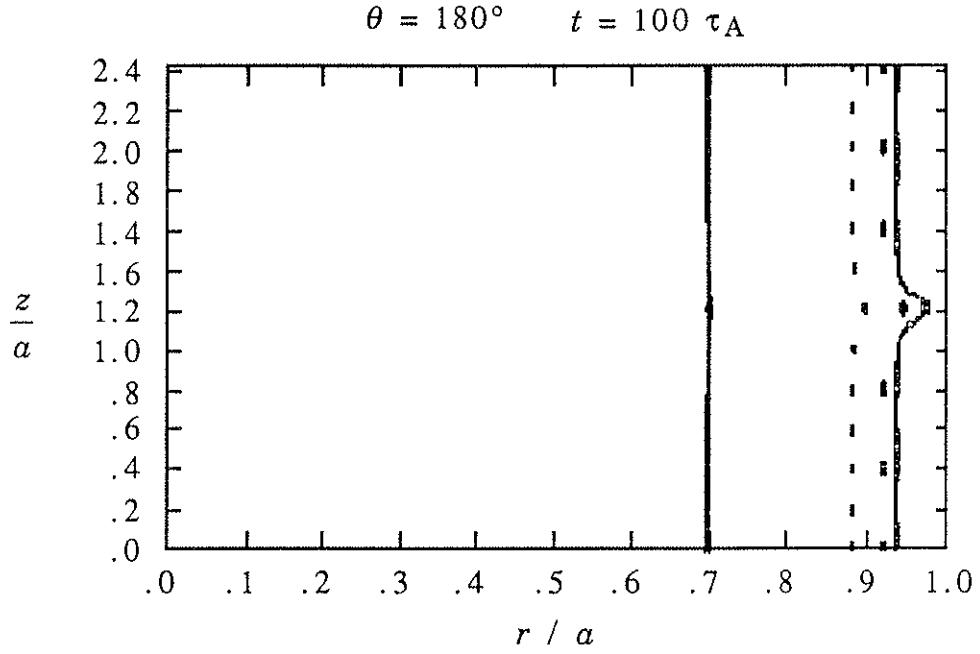

Figure 2.36 Field – line puncture plot for the r – z plane at θ = 180°. Field lines at the edge are pulled towards the single 4 1/2″ – diameter port at z / a = 1.21.

2.6 RESULTS ON ERRORS FROM A GAP IN THE SHELL

2.6a FIELD ERROR MODEL

Like the field errors associated with holes in the shell, the field errors arising from a gap are caused by interrupted current flow. In the model to be presented, the currents in the shell are those associated with the penetration of an external vertical field (B_v). The process is similar to that described in Section 2.5a: induced toroidal currents approach the poloidal gap, are diverted around it, and return in the opposite direction.

The emphasis in this case is on the "diverted" currents flowing poloidally. These give rise to radial fields that enter through the gap.

This model includes more realistic effects than that used to describe the holes. This time, the shell is not assumed to be a perfect conductor; it has a small, but non-zero, resistivity (η_{sh}) associated with it. This allows the radial magnetic field to "soak" into the shell on a resistive diffusion time scale (τ_0, to be defined later), as well as entering through the gap. The model is also time-harmonic, with a time dependence given by $\exp(i\omega t)$. The value of $\tau_{\mathrm{RISE}} \sim 1/\omega$ characterizes the time-scale on which the vertical field is applied. Thus, the model contains both the rise of the vertical field (τ_{RISE}) and the "soak in" (τ_0), with the measure of their relative importance given by the characteristic parameter $\omega\tau_0 = \tau_0/\tau_{\mathrm{RISE}}$.

A simple picture of the calculation is presented below. Both the idea and its mathematical execution are the product of Dr. R. Moses of the Theory Group (CTR-6) of the Controlled Thermonuclear Reseach Division at the Los Alamos National Laboratory.[38] Figure 2.37 shows the model geometry. The wall of the cylindrical chamber that will contain the plasma now has a thickness (Δa) and a finite resistivity (η_{sh}). At z = 0, there is a poloidally-symmetric break in the wall — the poloidal gap. The break is assumed to have an infinitesimal extent in z, but to be insulated, so that electric fields can extend across it while currents cannot. A time-harmonic vertical field is applied from the outside:

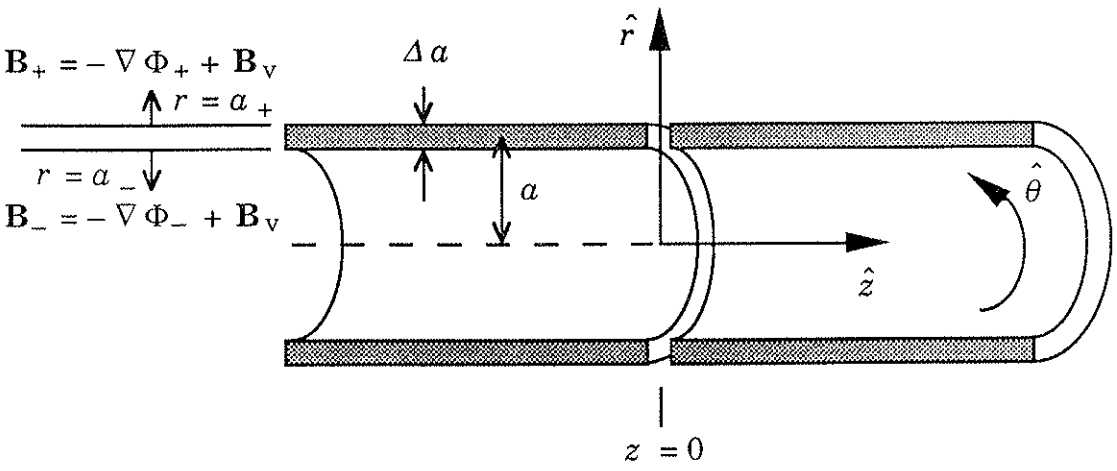

Figure 2.37 Geometry for the calculation of the radial field entering a gap in a conducting cylinder during the penetration of a vertical field. The form of the field on either side of the wall of the cylinder is indicated.

$$\mathbf{B}_V = B_v \left(\hat{\theta}\, \cos\theta + \hat{r}\, \sin\theta \right) e^{i\omega t} , \qquad (2.6.1)$$

where B_v is given by equations (2.5.2) – (2.5.4). The time – variation of this field causes currents in the shell. These, in turn, produce fields inside the shell and alter the vertical field outside. For the purposes of calculation, the field on either side of the shell ("+" for just outside $r = a$ and "–" for just inside $r = a$) is given by $\mathbf{B}_V$ plus a vacuum solution. In this cylindrical geometry, the magnetic scalar potentials (Φ) associated with the vacuum solutions (see equations (2.2.5) – (2.2.8)) can be given in terms of modified Bessel functions (see equations (2.3.17) – (2.3.18)). A $\sin\theta$ (m = 1) dependence is chosen to correspond to that of the applied field. Then:

$$\Phi_- = \sum_{n=0}^{\infty} b_n \left[\frac{I_1(n k_z r)}{(n k_z)\, I_1'(n k_z a)} \right] \sin\theta \cos(n k_z z)\, e^{i\omega t} \tag{2.6.2}$$

$$\Phi_+ = \sum_{n=0}^{\infty} b_n \left[\frac{K_1(n k_z r)}{(n k_z)\, K_1'(n k_z a)} \right] \sin\theta \cos(n k_z z)\, e^{i\omega t} \tag{2.6.3}$$

These scalar potentials represent the fields produced by the shell currents.

The mathematical procedure goes as follows. The scale length across the shell is assumed to be much smaller than the shortest scale length along the shell: $(\Delta a) / a \ll 1$. Then, the current in the shell is given by:

$$\mathbf{J}_{SH} = \frac{1}{\mu_0} \nabla \times \mathbf{B} \tag{2.6.4}$$

$$= \frac{1}{\mu_0 \Delta a} \left[-(B_{z+} - B_{z-})\, \hat{\theta} + (B_{\theta+} - B_{\theta-})\, \hat{z} \right] ,$$

to a good approximation. (No radial current is permitted in the thin shell.) This current gives rise to electric fields in the (somewhat) resistive shell:

$$\mathbf{E}_{SH} = \eta_{sh}\, \mathbf{J}_{SH} . \tag{2.6.5}$$

In turn, these produce the time-varying magnetic fields which create the differences in the "+" and "−" magnetic fields across the shell:

$$\nabla \times \mathbf{E}_{SH} = -i\omega \mathbf{B} . \tag{2.6.6}$$

Thus, the self-continuity loop is closed.

The presence of a gap introduces a discontinuity in the z – direction. The axial current must go to zero at the location of the gap:

$$J_z = \frac{1}{\mu_0 \Delta a} \left(B_{\theta +} - B_{\theta -} \right) = 0 \qquad \text{at z} = 0. \qquad (2.6.7)$$

Reference to Figure 2.37 and equations (2.6.2) – (2.6.3) shows that this condition is a constraint which links the coefficients b_n. A purely n = 0 response to the vertical field, which is a valid solution to equations (2.6.4) – (2.6.6), cannot satisfy this constraint. Terms involving b_n with n > 0 must appear in the magnetic scalar potentials. These give rise to (1, n) radial magnetic fields that may be resonant in the plasma.

Equations (2.6.4) – (2.6.6) can be solved for the b_n, subject to the constraint of (2.6.7). To express the solution, first define $f(n)$ and D :

$$f(n) = \frac{1 + (n k_z a)^2}{2 (n k_z a)} \left[\frac{I_1 (n k_z a)}{I_1{}' (n k_z a)} - \frac{K_1 (n k_z a)}{K_1{}' (n k_z a)} \right] \qquad (2.6.8)$$

$$\frac{B_v}{D} = 1 + \sum_{n=1}^{\infty} \left(\frac{2}{1 + (n k_z a)^2} \right) \left[\frac{1 - \left(\frac{i}{\omega \tau_0} \right)}{\frac{1}{f(n)} - \left(\frac{i}{\omega \tau_0} \right)} \right] \qquad (2.6.9)$$

with $$\tau_0 \equiv \frac{\mu_0 a (\Delta a)}{2 \eta_{sh}} .$$

Then, the solutions are:

$$b_0 = \frac{B_v - D}{1 - \left(\frac{i}{\omega \tau_0}\right)} , \qquad b_n = \frac{-2D}{1 - f(n)\left(\frac{i}{\omega \tau_0}\right)} . \tag{2.6.10}$$

When equation (2.3.14) is used to obtain the radial fields from the magnetic scalar potentials, it becomes apparent that b_n is the Fourier amplitude of the (1,n) radial magnetic field at the wall. Thus, the b_n = $B_r(1,n)$ were the field errors used in the simulation. The initial magnetic field profiles were found from equations (2.3.14)–(2.3.16) using the scalar potential of (2.6.2). Figure 2.38 shows a graph of $| b_n(\text{real}) / B_v |$ versus n for $\omega\tau_0 = 10$ (ZT–H parameters). The spectrum is broad and, unlike the hole case, each component is large. The values of n that are resonant in the plasma are likely to cause considerable magnetic islands to form .

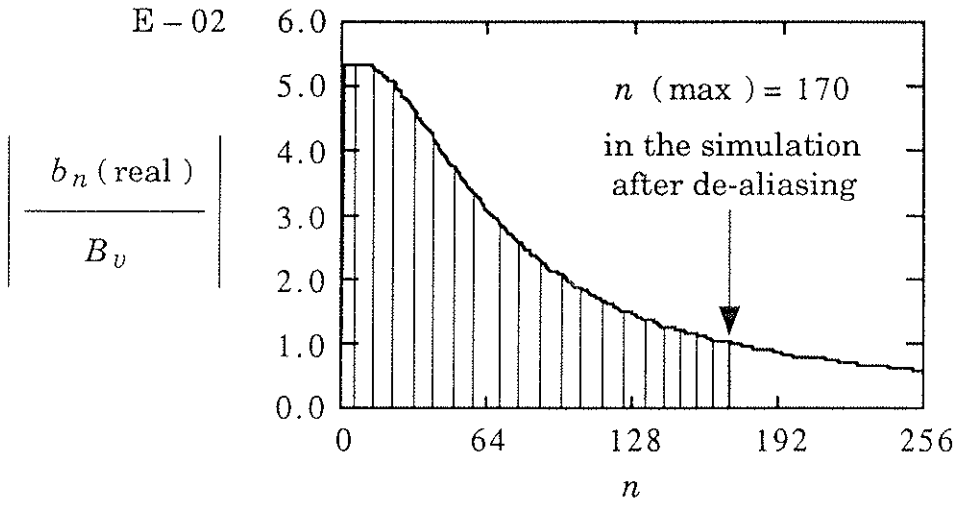

Figure 2.38 Plot of (1,n) Fourier amplitude for the radial field in the gap (real part) as a function of n, for $\omega\tau_0 = 10$ (ZT–H parameters).

2.6b PLASMA – PERTURBATION STEADY – STATE

The plasma – perturbation combination did reach a steady – state. However, this state is now one in which nonlinear effects are important. The figures that follow show the initial and final energy spectra for m = 0 modes from a gap case using ZT–H parameters:

$\tau_0 = 50$ msec. $\quad \tau_{RISE} \sim 1/\omega = (1/4)$ RAMP TIME $= 5$ msec.

so that $\quad \omega\tau_0 = 10$.

The field errors fixed at the plasma edge were those found in the previous section, modes with m = 1 only. This fact is reflected in the initial m = 0 energy spectrum shown in Figure 2.39 . The only mode containing energy

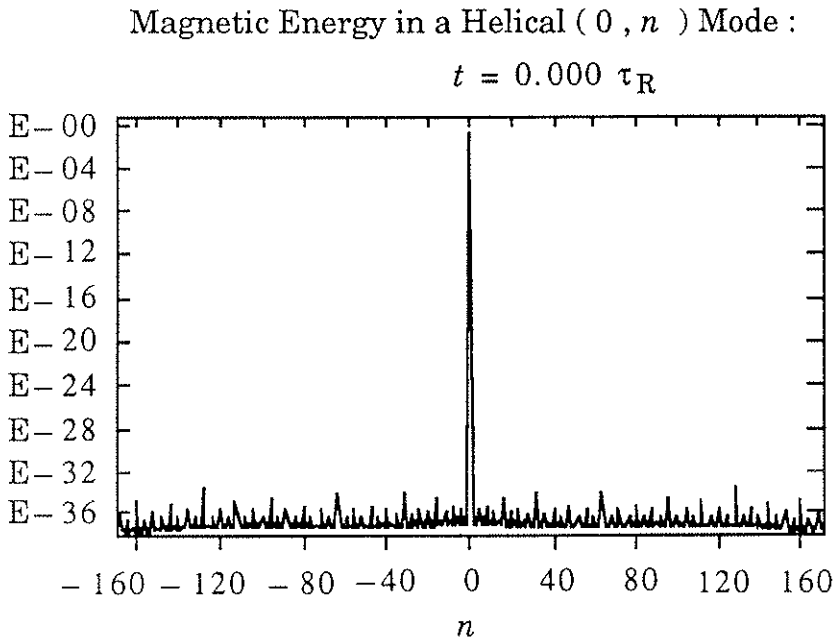

Figure 2.39 Plot of magnetic energy in an (0, n) Fourier mode as a function of n at the start of a ZT–H gap case. Only the equilibrium (n = 0) is initialized.

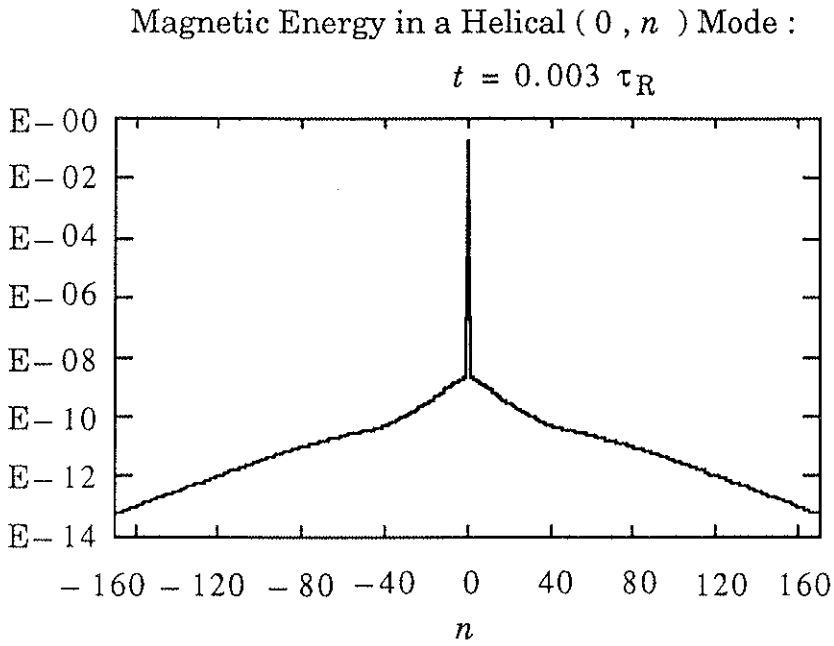

Figure 2.40 Plot of magnetic energy in an (0,n) Fourier mode as a function of n at the conclusion of a ZT-H gap case. A broad range of modes has been excited.

above the noise level at the beginning of the simulation was the equilibrium (n=0). However, by the end of the simulation, a broad spectrum of modes with m=0 had been excited. This is illustrated in Figure 2.40 . Since these modes were not initially present, and the chosen equilibrium was stable, they must have arisen from nonlinear interaction between the large m=1 modes which were initialized.

This observation sets a limit on the size of the field-error perturbations that will interact with the RFP equilibrium to form a linear steady state, as described in Section 2.4b. The spectrum of Figure 2.38

shows that a radial magnetic field amplitude of $| B_r(1,n) / B_v | \sim 5 \times 10^{-2}$ produced the observed nonlinear interactions. In Section 2.4, a magnetic field perturbation amplitude of $| b_r(1,n) / B_{z\,0}(0) | \sim 2 \times 10^{-5}$ from field errors associated with the toroidal field coils interacted with the plasma in a linear fashion. (See Figure 2.11, for example. The normalization is that for magnetic fields in the 3-D MHD code.) In order to compare the two expressions precisely, some normalization factors must be given. First, the relationship between B_v and $B_{\theta\,0}(a)$ is given by equation (2.5.2). Using ZT-H parameters gives $B_v / B_{\theta\,0}(a) \sim 0.26$. For the equilibrium profiles used in the simulation, $B_{\theta\,0}(a) / B_{z\,0}(0) \sim 0.44$. Finally, in the case under consideration it was assumed that only 10% of the vertical field needed to maintain the plasma position created current in the shell. The remaining current was assumed to have been canceled by current induced by the plasma. Thus, B_v must be multiplied by 0.10. Assembling all these factors gives $| B_r(1,n) / B_{z\,0}(0) | \sim 2 \times 10^{-4}$. Although the phase-correlation of the radial fields at the gap likely played an important role in the nonlinear interaction of the gap errors, it appears that the size of the field errors due to the toroidal field coils can only be increased by a factor of ten before nonlinear effects should at least become a concern.

2.6c PERTURBATION EFFECTS ON THE EQUILIBRIUM: "MACHINE PERFORMANCE RESULTS"

It may be expected that perturbations which are large enough to undergo nonlinear interactions will affect the plasma equilibrium in a

negative way. This did turn out to be the case. The nonlinearly-generated m = 0 modes produced large magnetic islands. In the ZT-H case mentioned previously, the amplitudes of the perturbations were only about ten times those in the toroidal-field-coil case. However, since these modes were produced by m = 1 modes with neighboring values of n, they were primarily n = 1, rather than n ~ 10. Using both of these factors, the linear island-width formula (see the start of Section 2.4 d) predicts an island width 10 times larger in the gap case: $(W/a)_{(n=0)} \sim 0.15$. (Compare

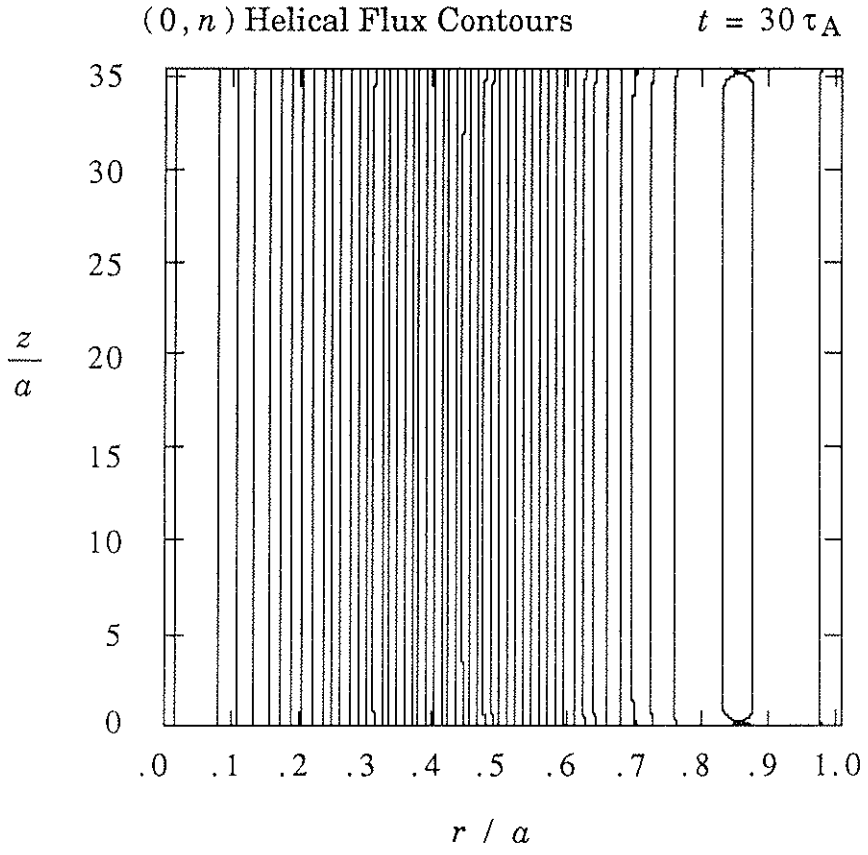

Figure 2.41 Plot of (0, n) helical flux contours at the end of a ZT-H run using the gap errors from 10% B_v. Note the large island about $r_s / a = 0.86$.

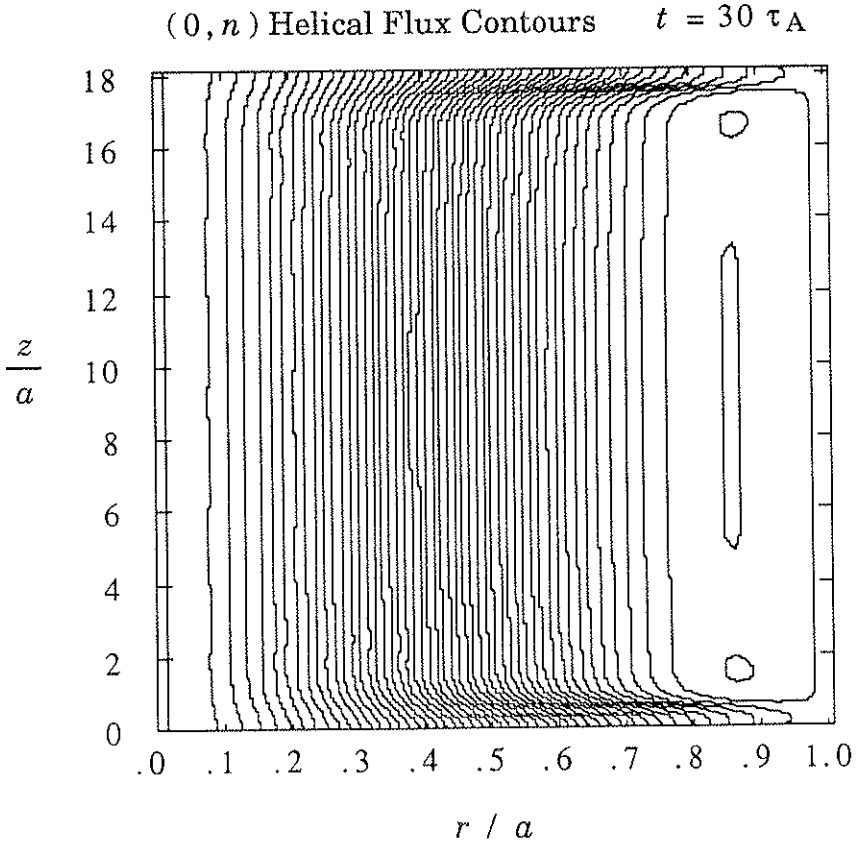

Figure 2.42 Plot of (0, n) helical flux contours at the end of a MST run using the gap errors from 100% B_v. Note the larger island.

with the results of the toroidal-field-coil case in Section 2.4d.) An island of this size can be observed in Figure 2.41. Figure 2.42 is for MST parameters:

$\tau_0 = 233$ msec. $\quad \tau_{RISE} = (\pi/2)(1/\omega) = 15$ msec.

so that $\omega\tau_0 = 24.4$.

In this case, it was assumed that 100% of the vertical field necessary for plasma positioning was produced by currents induced in the shell by the

plasma, since MST has no external vertical field system. The m=0 islands are correspondingly worse. Their influence extends well within the plasma. (In both of the above cases, S = 10,000 and rhocon = 20.)

The m=1 radial magetic field perturbations also had a negative impact on field lines in the plasma core. Figures 2.43 and 2.44 show field-line puncture plots for the ZT-H and MST cases mentioned above. For ZT-H parameters, with 10% B_v penetration modeled, the radial magnetic perturbations caused islands. With MST parameters and 100% penetration

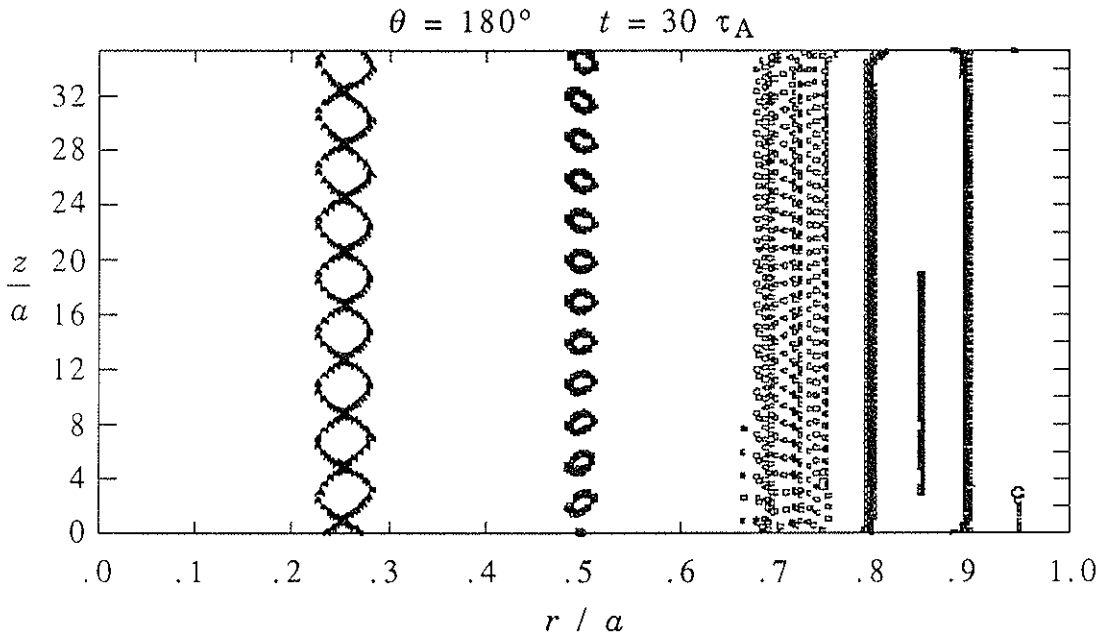

Figure 2.43 Field-line puncture plot showing the intersection of field lines with the r-z plane at θ = 180°. This is the ZT-H case, with 10% B_v penetration modeled. Islands have formed in the core.

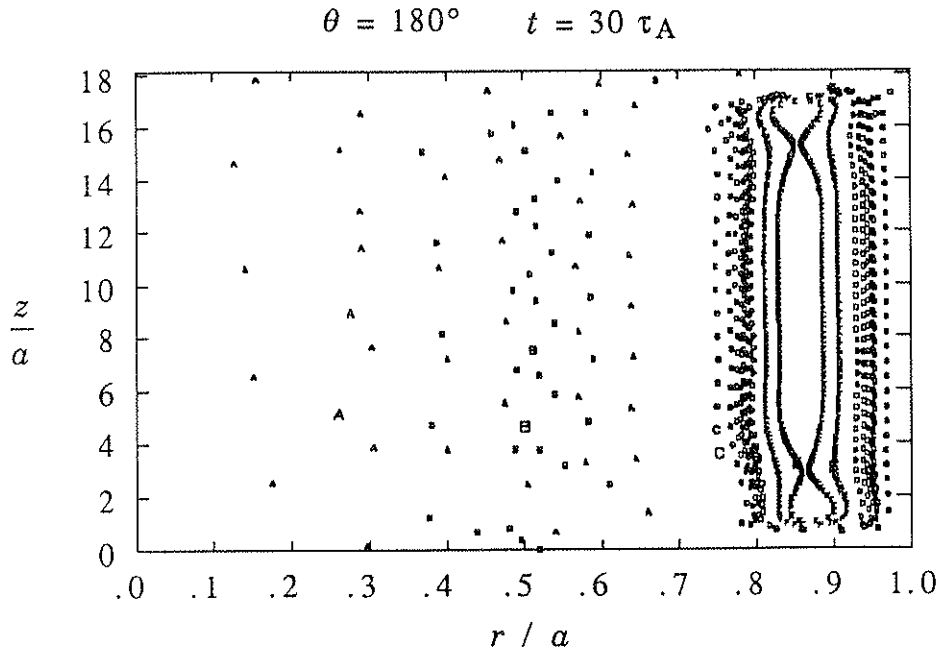

Figure 2.44 Field-line puncture plot showing the intersection of field lines with the r – z plane at θ = 180°. This is the MST case, with 100% B_v penetration modeled. The core is stochastic; note the wandering of the field line labeled "A."

of B_v modeled, the effects of the m = 1 field-error perturbations look like those created by plasma instabilities. A large edge m = 0 island and a stochastic core are present, even though there are no unstable modes in the plasma. Any attempt to understand the physics of the RFP in a device with such gap errors would be quite difficult. The attention in the designs of both ZT-H and MST to the compensation of these errors by preventing the flow of current around the gap seems to have been well worth the effort involved.

REFERENCES

[1] K. F. Schoenberg, R. F. Gribble, and J. A. Phillips, Nucl. Fusion **22**, 1433 (1982).

[2] J. B. Taylor, Phys. Rev. Lett. **33**, 1139 (1974).

[3] K. F. Schoenberg, R. F. Gribble, and J. A. Phillips, Nucl. Fusion **22**, 1433 (1982).

[4] E. J. Caramana and D. A. Baker, Nucl. Fusion **24**, 423 (1984).

[5] K. F. Schoenberg, R. F. Gribble, and J. A. Phillips, Nucl. Fusion **22**, 1433 (1982).

[6] *Ibid.*, p. 1437.

[7] J. P. Freidberg and D. W. Hewett, J. Plasma Phys. **26**, 177 (1981).

[8] R. A. Nebel (private communication).

[9] R. S. Massey, R. G. Watt, P. G. Weber, G. A. Wurden, D. A. Baker, C. J. Buchenauer, L. C. Burkhardt, T. Cayton, J. N. DiMarco, J. N. Downing, R. M. Erickson, R. F. Gribble, A. Haberstich, R. B. Howell, J. C. Ingraham, E. M. Little, G. Miller, C. P. Munson, J. A. Phillips, M. M. Pickrell, K. F. Schoenberg, A. E. Schofield, and D. M. Weldon, "Status of the ZT-40M RFP Experimental Program," presented at the Sixth ANS Topical Meeting on the Technology of Fusion Energy, San Francisco, California, March, 1985. Also: LA-UR-85-420, Los Alamos National Laboratory (1985).

[10] R. N. Dexter, D. W. Kerst, T. W. Lovell, S. C. Prager, J. C. Sprott, "MST Technical Design Considerations," PLP 965, University of Wisconsin-Madison (December, 1985). or

R. N. Dexter, D. W. Kerst, T. W. Lovell, S. C. Prager, and J. C. Sprott, "Madison Symmetric Torus," submitted to Fusion Technology, November 1989.

[11] T. Tamano, W. D. Bard, C. Chu, Y. Kondoh, R. J. LaHaye, P. S. Lee,

M. T. Saito, M. J. Schaffer, and P. L. Taylor, Phys. Rev. Lett. **59**, 1444 (1987).

[12] B. Alper, in *Proceedings of the IEEE International Conference on Plasma Science*, Seattle, Washington, 1988 (IEEE, New York, 1988) paper No. 5P17.

[13] S. Robertson and P. Schmid, Phys. Fluids **30**, 884 (1987).

[14] J. N. DiMarco in *Proceedings of the International Workshop on Engineering Design of Next Step Reversed Field Pinch Devices*, edited by D. B. Thomson (Los Alamos National Laboratory, Los Alamos, New Mexico, 1987), p.23.

[15] C. G. Gimblett, Nucl. Fusion **26**, 617 (1986).

[16] Y. L. Ho, Ph. D. thesis, University of Wisconsin-Madison, 1988.

[17] D. D. Schnack, D. C. Barnes, Z. Mikic, D. S. Harned, and E. J. Caramana, J. Comp. Phys. **70**, 330 (1987).

[18] D. D. Schnack (private communication).

[19] S. I. Braginskii, in *Reviews of Plasma Physics*, edited by M. A. Leontovich (Consultants Bureau, New York, 1965), Vol. 1, p.205.

[20] R. S. Massey, R. G. Watt, P. G. Weber, G. A. Wurden, D. A. Baker, C. J. Buchenauer, L. C. Burkhardt, T. Cayton, J. N. DiMarco, J. N. Downing, R. M. Erickson, R. F. Gribble, A. Haberstich, R. B. Howell, J. C. Ingraham, E. M. Little, G. Miller, C. P. Munson, J. A. Phillips, M. M. Pickrell, K. F. Schoenberg, A. E. Schofield, and D. M. Weldon, "Status of the ZT-40M RFP Experimental Program," presented at the Sixth ANS Topical Meeting on the Technology of Fusion Energy, San Francisco, California, March, 1985. Also: LA-UR-85-420, Los Alamos National Laboratory (1985).

[21] D. D. Schnack, D. C. Baxter, and E. J. Caramana, J. Comp. Phys. **55**, 485 (1984).

[22] *Ibid.*, pp. 496-497.

[23] M. Abramowitz and I. A. Stegun, *Handbook of Mathematical Functions* (Dover, New York, 1965), p. 374.

[24] D. D. Schnack, D. C. Barnes, Z. Mikic, D. S. Harned, and E. J. Caramana, J. Comp. Phys. **70**, 330 (1987).

[25] D. S. Harned and W. Kerner, J. Comp. Phys. **60**, 62 (1985).

[26] D. S. Harned and D. D. Schnack, J. Comp. Phys. **65**, 57 (1986).

[27] S. J. Sackett, "EFFI – A Code for Calculating the Electromagnetic Field, Force, and Inductance in Coil Systems of Arbitrary Geometry; User's Manual," UCID – 17621, Lawrence Livermore National Laboratory (1977).

[28] R. I. Pinsker and A. H. Reiman, Phys. Fluids **29**, 782 (1986).

[29] G. Bateman, *MHD Instabilities* (MIT Press, Cambridge, Massachusetts, 1978), p.197.

[30] R. B. White, in *Handbook of Plasma Physics, Vol. I*, edited by A. A. Galeev and R. N. Sudan (North – Holland, New York, 1983), pp. 631 – 632.

[31] G. Bateman, *MHD Instabilities* (MIT Press, Cambridge, Massachusetts, 1978), p.79.

[32] V. D. Shafranov, in *Reviews of Plasma Physics*, edited by M. A. Leontovich (Consultants Bureau, New York, 1966), Vol. 2, p.103.

[33] J. D. Jackson, *Classical Electrodynamics*, 2nd. ed. (John Wiley and Sons, New York, 1975), pp. 201 – 204.

[34] M. Abramowitz and I. A. Stegun, *Handbook of Mathematical Functions* (Dover, New York, 1965), p. 437.

[35] A. Haberstich (private communication).

[36] J. N. DiMarco in *Proceedings of the International Workshop on Engineering Design of Next Step Reversed Field Pinch Devices*, edited by

D. B. Thomson (Los Alamos National Laboratory, Los Alamos, New Mexico, 1987), p.24.

[37] R. N. Dexter (private communication).

[38] R. W. Moses (private communication).

CHAPTER 3

LINEAR BEHAVIOR OF m = 1 MODES FOR THE "NO DYNAMO" MODEL

3.1 INTRODUCTION

In the previous chapter, the interaction of a plasma and a set of magnetic perturbations induced by edge field errors was studied by numerical solution of the time-dependent, non-linear MHD equations. The RFP plasma was modeled by a relaxed, but static, equilibrium. The perturbations eventually settled into a steady-state in which their amplitudes were linearly dependent on the amplitudes of the field errors at the plasma edge. This combination of time-independence and linearity can be exploited to gain some insight into the plasma-perturbation interaction. A simplified set of equations — the time-independent, linearized MHD equations — can be solved to find radial profiles of the perturbations. These can be used in a study of the way in which certain features of the plasma model alter the perturbations. Such a study constitutes the subject of the next two chapters.

Two separate features of the plasma are under consideration here. Each has been included in the model because it is important in a realistic RFP. The first is the presence of a finite-gradient region in the profile of λ ($\equiv J/B$ in the equilibrium), near the plasma edge. Although the totally-

relaxed Taylor state requires λ = constant, this finite-gradient region allows the current to go to zero at the plasma edge while the field remains finite. As has already been mentioned, such a current profile is closer to that expected for a typical RFP experiment with a cold edge and a high edge resistivity. The second feature is the inclusion of finite dissipation: resistivity (η) and viscosity (ν_0). It is important to include resistivity when using MHD to model an RFP. Resistive instabilities play a role in the "dynamo effect,"[1,2] which maintains the RFP in its relaxed state. Even when the resistive evolution of the equilibrium is prohibited, as it is here, it is important to keep resistivity in the perturbation dynamics, in order to be consistent with a relaxed equilibrium state.

This chapter is concerned with perturbations with m=1. Section 3.2 examines which of the features mentioned above — hereafter referred to as finite grad-λ and finite η, ν_0 — has the most influence on the radial profile of an m=1 perturbation. Section 3.3 describes the profile changes observed in the 3-D MHD simulation after the perturbation and plasma interact and offers a simple physical interpretation in terms of the important feature identified previously. Section 3.4 presents the derivation of the particular set of time-independent, linearized MHD equations used to perform the detailed calculation. Section 3.5 exhibits perturbation profiles obtained by solving the equations in two different ways. Comparisons are made and differences are interpreted in terms of the roles played by finite grad-λ and finite η, ν_0.

3.2 FINITE GRAD – λ VERSUS FINITE η, ν_0

To judge the effects of finite grad – λ and finite η, ν_0 on a perturbation profile, it is useful to solve for a profile with constant – λ and $\eta = \nu_0 = 0$ first. The time – independent, linearized MHD equations can be readily solved in this case.

The first simplification occurs by choosing $\eta = \nu_0 = 0$. Using the MHD equations from Chapter 1, take $\partial/\partial t = 0$ and $\eta = \nu_0 = 0$:

$$\mathbf{E} = -\mathbf{V}\times\mathbf{B} \tag{3.2.1}$$

$$\nabla\times\mathbf{E} = 0 \tag{3.2.2}$$

$$\rho\left(\mathbf{V}\cdot\nabla\right)\mathbf{V} = \mathbf{J}\times\mathbf{B} \tag{3.2.3}$$

$$\mu_0\,\mathbf{J} = \nabla\times\mathbf{B} \tag{3.2.4}$$

$$\nabla\cdot\mathbf{B} = 0 \tag{3.2.5}$$

These equations can be linearized by representing the variables as follows:

VARIABLE		EQUILIBRIUM		PERTURBATION
$\mathbf{J}$	=	$\mathbf{J}_0$	+	$\mathbf{j}$
$\mathbf{B}$	=	$\mathbf{B}_0$	+	$\mathbf{b}$
$\mathbf{V}$	=	$\mathbf{0}$	+	$\mathbf{v}$
$\mathbf{E}$	=	$\mathbf{0}$	+	$-\nabla\phi$

Terms to first order in the perturbation are retained. The left side of (3.2.3) is second-order in $\mathbf{v}$; it can thus be neglected. The magnetic perturbation decouples from the velocity perturbation.

The magnetic perturbation — $\mathbf{b}$ — can be found from a smaller set of equations. The starting point is the right side of (3.2.3):

$$\mathbf{J}\times\mathbf{B} = 0 \ . \tag{3.2.6}$$

The general solution to this equation can be written as

$$\mathbf{J} = (\varpi)\mathbf{B} \ . \tag{3.2.7}$$

However, an acceptable solution must also satisfy the constraints represented by equation (3.2.5) and equation (3.2.4), here rewritten as:

$$\nabla \cdot \mathbf{J} = 0 \ . \tag{3.2.8}$$

Taking the divergence of (3.2.7), and using (3.2.8) and (3.2.5), the constraint condition becomes:

$$\mathbf{B} \cdot \nabla \varpi = 0 \ . \tag{3.2.9}$$

The equation for $\mathbf{b}$ can be derived from the parts of (3.2.7) and (3.2.9) which are first-order in perturbation amplitude. For the purposes of linearization, the equations can be rewritten to show the equilibrium quantities and perturbations explicitly:

$$(\mathbf{J}_0 + \mathbf{j}) = (\varpi)(\mathbf{B}_0 + \mathbf{b}) \tag{3.2.10}$$

and $$(\mathbf{B}_0 + \mathbf{b}) \cdot \nabla \varpi = 0 \ . \qquad (3.2.11)$$

The requirement of constant-λ is now used to choose ϖ and separate the equilibrium and perturbation equations. By definition, λ is an equilibrium quantity. The choice $\varpi = (\lambda / \mu_0) = \text{constant}$ in (3.2.10) gives the expected equilibrium equation,

$$\mathbf{J}_0 = \left(\frac{\lambda}{\mu_0}\right)\mathbf{B}_0 \ , \qquad (3.2.12)$$

and the perturbation equation:

$$\mathbf{j} = \left(\frac{\lambda}{\mu_0}\right)\mathbf{b} \ . \qquad (3.2.13)$$

This is the proper equation, provided that the constraint represented by equation (3.2.11) can be satisfied. (This point will become important when the case of finite grad-λ is considered later.) Constant-ϖ does satisfy (3.2.11). Thus, recalling that the equilibrium and perturbed currents must solve the linear equation (3.2.4) separately, the equation for $\mathbf{b}$ can be written from (3.2.13) and (3.2.4):

$$\nabla \times \mathbf{b} = \lambda \mathbf{b} \ . \qquad (3.2.14)$$

The eigenfunction solutions to this equation are the well-known Chandrasekhar-Kendall functions.[3]

The perturbation profiles found above for constant-λ and $\eta = \nu_0 = 0$ can now be used as a base case against which profiles with constant-λ,

finite η, ν_0 and finite grad$-\lambda$, finite η, ν_0 can be compared. The Chandrasekhar–Kendall function associated with the axial magnetic perturbation in the constant$-\lambda$, $\eta = \nu_0 = 0$ case is the easiest one to use as a basis for comparison; its radial behavior is given by a Bessel function. For perturbations with poloidal mode number m=1 and toroidal mode number n, in a periodic cylinder of length $2\pi R$, the form is:

$$b_z = C\, J_1(\gamma r)\, \cos(\theta + nkz)\,, \qquad (3.2.15)$$

where $k = 1/R$ is the basic axial wavenumber, $\gamma^2 = \lambda^2 - (nk)^2$, J_1 is the first order Bessel function of the first kind,[4] and C is a constant. The radial part of (3.2.15) is plotted in Figure 3.1, with $C = b_z(a)/J_1(\gamma a)$ and the $b_z(a)$

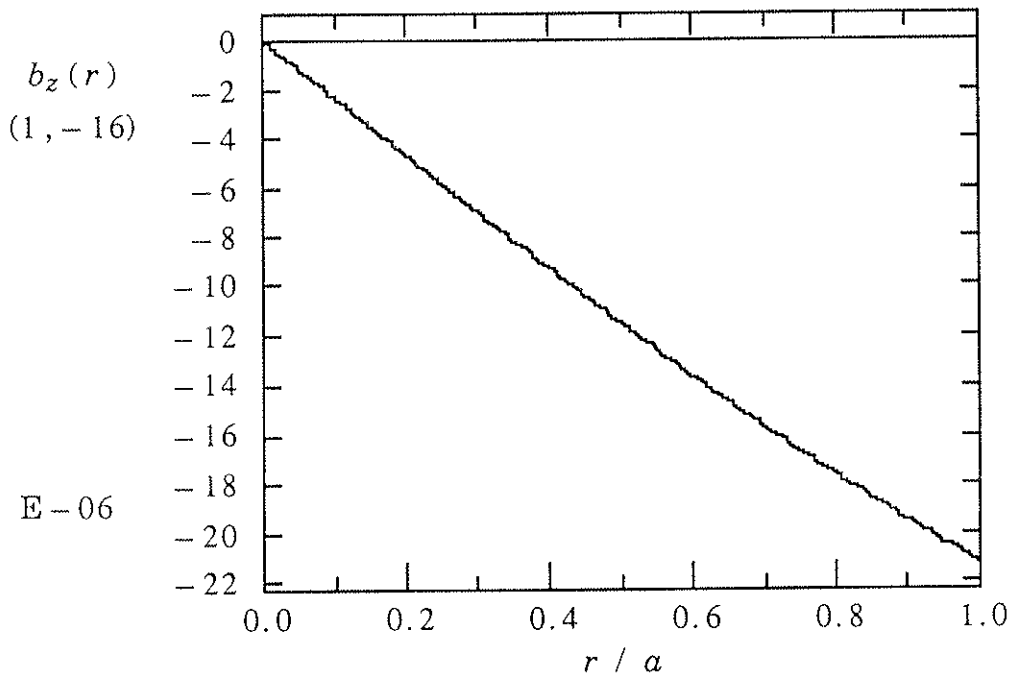

Figure 3.1 Radial profile of an m = 1 axial magnetic perturbation in the constant$-\lambda$, $\eta = \nu_0 = 0$ case (imaginary part of $b_z(a)$ used).

given by the amplitude of the axial field error at the wall. For comparison, the effect of finite η, ν_0 is shown in Figure 3.2, where the radial profile of b_z for a case with constant$-\lambda$ and finite η, ν_0 is plotted. In Figure 3.3, the effect of finite grad$-\lambda$ is added; the radial profile of b_z for a case with both finite grad$-\lambda$ and finite η, ν_0 is shown. Both of these latter profiles come from 3-D MHD code results for a ZT-40M "coil" case.

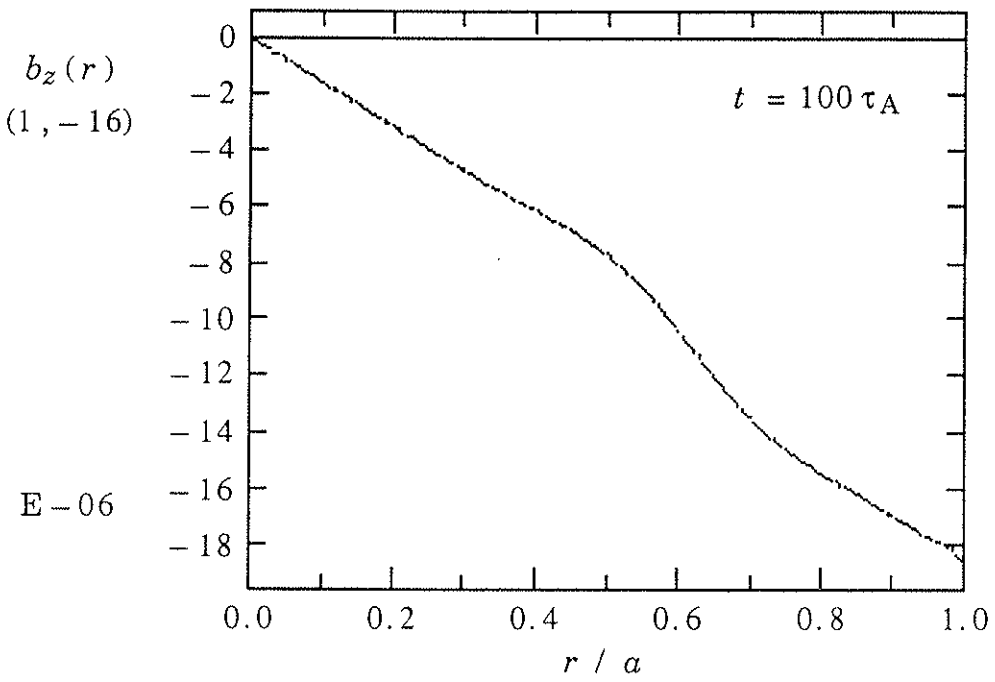

Figure 3.2 Radial profile of an m=1 axial magnetic perturbation (imaginary part) in the constant$-\lambda$, finite η, ν_0 case.

The presence of finite grad$-\lambda$ has the most influence on the radial profile of the m=1 perturbation. Comparing Figure 3.2 to Figure 3.1 shows that the addition of finite η, ν_0 puts a "bump" in the profile. However,

the general profile shape is still close to the original $-J_1(\gamma r)$; for example, it is still concave with respect to the line $b_z = 0$. Also, note that the change in the value of $b_z(a)$ is relatively small. The fact that there is a change is not really important in itself; after all, it is the radial error field at the edge that is the fixed boundary condition and not the axial magnetic perturbation. The fact that the change is small implies that the relationship between these components is not greatly affected. It is the addition of finite grad$-\lambda$ that makes the real difference. Figure 3.3 shows that the value of $b_z(a)$ changes sign in this case. The equations governing

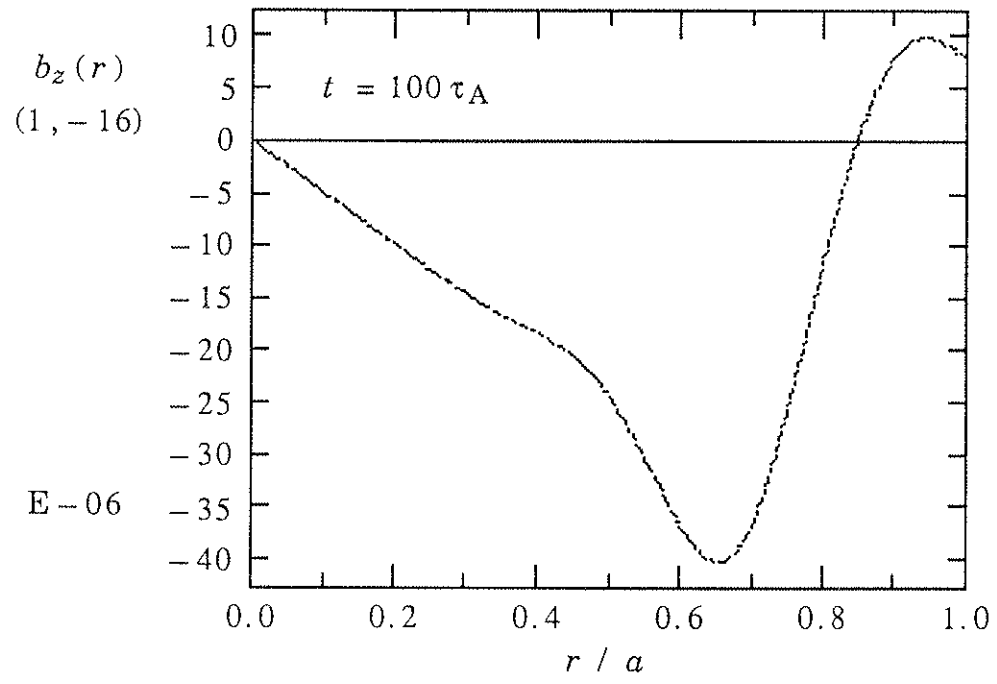

Figure 3.3 Radial profile of an m = 1 axial magnetic perturbation (imaginary part) in the finite grad$-\lambda$, finite η, ν_0 case.

the relationships between the magnetic perturbations in different directions have changed considerably. In addition, the profile reaches a minimum, increases and crosses the $r-$axis, and then reaches a maximum. This cannot be attributed to some rescaling of the $-J_1(\gamma r)$ profile due to the different boundary conditions. A $-J_1(\gamma r)$ profile would reach its first zero at $\gamma r_{zero} = 3.83$.[5] For the ZT-40M case, the relevant parameters are $\lambda a = 2.95$, $n = -16$, $k a = 0.1754$, and $\gamma a = 0.91$. This results in a value of $r_{zero}/a = 4.21$. The profile in Figure 3.3 passes through zero at a much smaller value of r/a. This is a major change from $-J_1(\gamma r)$ behavior. Thus, it is the introduction of finite grad-λ that has the most important effect on a magnetic perturbation with m=1.

3.3 PHYSICAL INTERPRETATION

As observed above, a magnetic perturbation induced by an edge radial field error is changed by the presence of an RFP plasma. The most important result may be the change in the radial profile of the perturbed radial magnetic field — b_r . The resonant surface for mode (m,n) is defined as the magnetic surface, at radius r_s, on which

$$F \equiv \mathbf{k}\cdot\mathbf{B}_0 = \frac{m}{r} B_{\theta 0} + nk B_{z 0} = 0 . \qquad (3.3.1)$$

The presence of a non-vanishing b_r on this surface gives rise to an (m,n) magnetic island there. The size of this island depends on the size of $|b_r|$ at the resonant surface. When the radial b_r-profile is altered, the size of the island may be increased or decreased.

In the case of perturbations with m = 1, the 3-D MHD code results show an increase in $|b_r|$ at the resonant surface. Figure 3.4 shows the radial profile of b_r for the (1, -16) mode before and after its interaction with the plasma, as simulated by the 3-D MHD code. Before, the profile is that of a vacuum field with the given error-field amplitude at the boundary. After, the profile is a solution to the time-independent, linearized MHD equations. Note that the value of $|b_r(r_s)|$ is increased by about a factor of 3. This indicates that the size of an island produced by the error-induced perturbations is greatly increased due to the presence of the

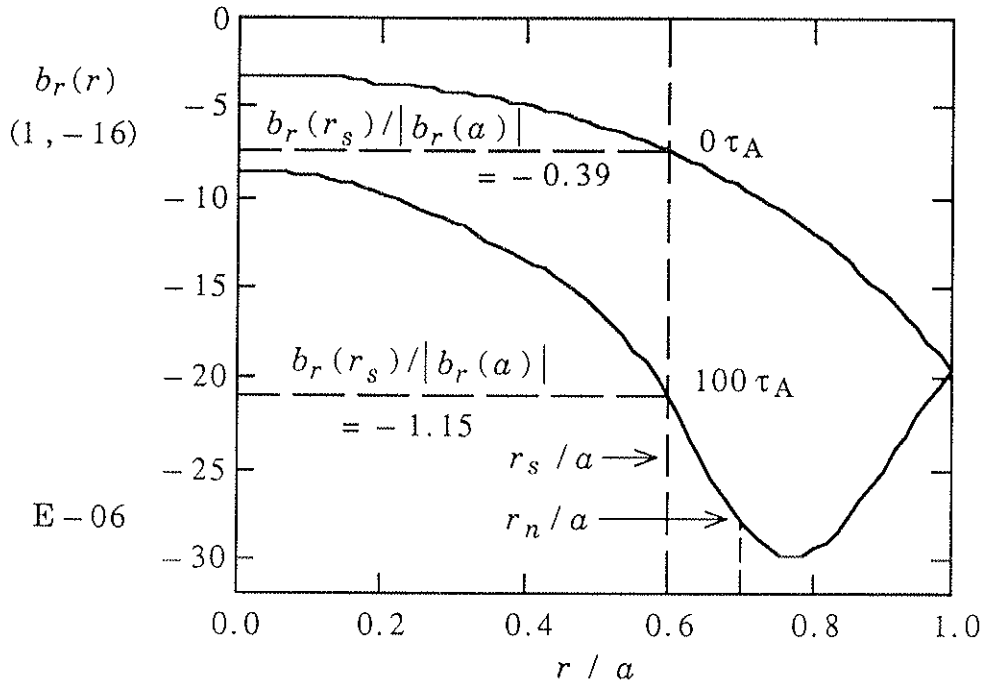

Figure 3.4 Radial profile of a (1, -16) b_r perturbation (real part), before ($t = 0\ \tau_A$) and after ($t = 100\ \tau_A$) interaction with the plasma. The value of $|b_r(r_s)|$ is increased.

plasma. In the case of constant-λ, the increase is only 33% for $\eta = \nu_0 = 0$ and 11% for finite η, ν_0. It appears that finite grad-λ is most important in producing this effect, as was suggested in the previous section . It can be shown that finite grad-λ gives rise to perturbed currents flowing along equilibrium magnetic field lines. It is then possible to attribute the increase in the value of $|b_r(r_s)|$ to the action of these perturbed currents.

When there is a finite grad-λ, or $\lambda = \lambda(r)$, the equation for the magnetic perturbation is no longer correctly given by (3.2.13). This is because

$$\mathbf{j} = \left(\frac{\lambda(r)}{\mu_0}\right)\mathbf{b} \tag{3.3.2}$$

no longer satisfies the constraint represented by equation (3.2.11). For the present choice of $\varpi = [\lambda(r)/\mu_0]$, this equation reads:

$$(B_{r\,0} + b_r)\left(\frac{\partial \lambda}{\partial r}\right) = 0 \ . \tag{3.3.3}$$

In the equilibrium, $B_{r\,0} \equiv 0$. This implies that $b_r \equiv 0$. Obviously, the trivial solution is not of interest; it doesn't even satisfy the boundary condition. The importance of the constraint equation in this finite grad-λ case was suggested before. Here it is apparent that it makes the choice $\varpi = [\lambda(r)/\mu_0]$ no longer valid.

Another choice for ϖ must be made in (3.2.10) and (3.2.11) to separate the equilibrium and perturbation equations. A more general

choice can be made as follows: $\varpi = [\,\lambda(r) + g(r,\theta,z)\,]/\mu_0$, where λ is an equilibrium quantity and g is a perturbed quantity. Equation (3.2.10) becomes:

$$(\mathbf{J}_0 + \mathbf{j}) = \left(\frac{\lambda(r)+g}{\mu_0}\right)(\mathbf{B}_0+\mathbf{b}) \tag{3.3.4}$$

and the constraint equation, (3.2.11), becomes:

$$(\mathbf{B}_0+\mathbf{b})\cdot\nabla\left(\frac{\lambda(r)+g}{\mu_0}\right) = 0\ . \tag{3.3.5}$$

The equilibrium equation is then:

$$\mathbf{J}_0 = \left(\frac{\lambda(r)}{\mu_0}\right)\mathbf{B}_0\ , \tag{3.3.6}$$

with the constraint:

$$B_{r\,0}\left(\frac{\partial\lambda}{\partial r}\right) = 0\ . \tag{3.3.7}$$

This constraint is satisfied for the finite grad$-\lambda$ case because $B_{r\,0} \equiv 0$. Equation (3.3.6) can be used as the proper equilibrium equation. In the case of the perturbations, the equation is:

$$\mathbf{j} = \left(\frac{\lambda(r)}{\mu_0}\right)\mathbf{b} + \left(\frac{g}{\mu_0}\right)\mathbf{B}_0\ , \tag{3.3.8}$$

with the constraint:

$$\mathbf{b} \cdot \nabla \left(\frac{\lambda(r)}{\mu_0} \right) + \mathbf{B}_0 \cdot \nabla \left(\frac{g}{\mu_0} \right) = 0 \ . \qquad (3.3.9)$$

Equations (3.3.8) and (3.3.9) are the proper equations for **b** in the finite grad – λ case.

The equation for **j** now has two terms. The first is the same as that in equation (3.3.2), a current perturbation caused by the diversion of equilibrium current (λ) along a perturbed field line. The new term represents the flow of perturbed current (g) along an equilibrium field line. The origin of this perturbed current in the finite grad – λ case can be understood by a simple physical argument based on equation (3.3.9). First, recall that this equation originally comes from equation (3.2.8), here reproduced as:

$$\nabla \cdot \mathbf{j} = 0 \ . \qquad (3.3.10)$$

Simply put, this says that there are no sources of perturbed current. If a net amount of perturbed current leaves a flux surface at one point and enters again at another, there must be a flow of perturbed current within the flux surface between these points. To emphasize the role of finite grad – λ , consider (3.3.9) in the following form:

$$\frac{b_r}{\mu_0} \left(- \frac{\partial \lambda}{\partial r} \right) = \mathbf{B}_0 \cdot \nabla \left(\frac{g}{\mu_0} \right) . \qquad (3.3.11)$$

The fact that λ depends on radius means that as an equilibrium field line is made to "flutter" in and out to different values of radius by a radial

magnetic perturbation (b_r), it samples different values of λ . This is equivalent to saying that b_r "transports" parallel equilibrium current in and out of the flux surface. The left side of (3.3.11) is precisely the net amount of equilibrium current (λ) "transported" across a flux surface (from smaller to larger r) by b_r. (See Figure 3.5.) As was already stressed

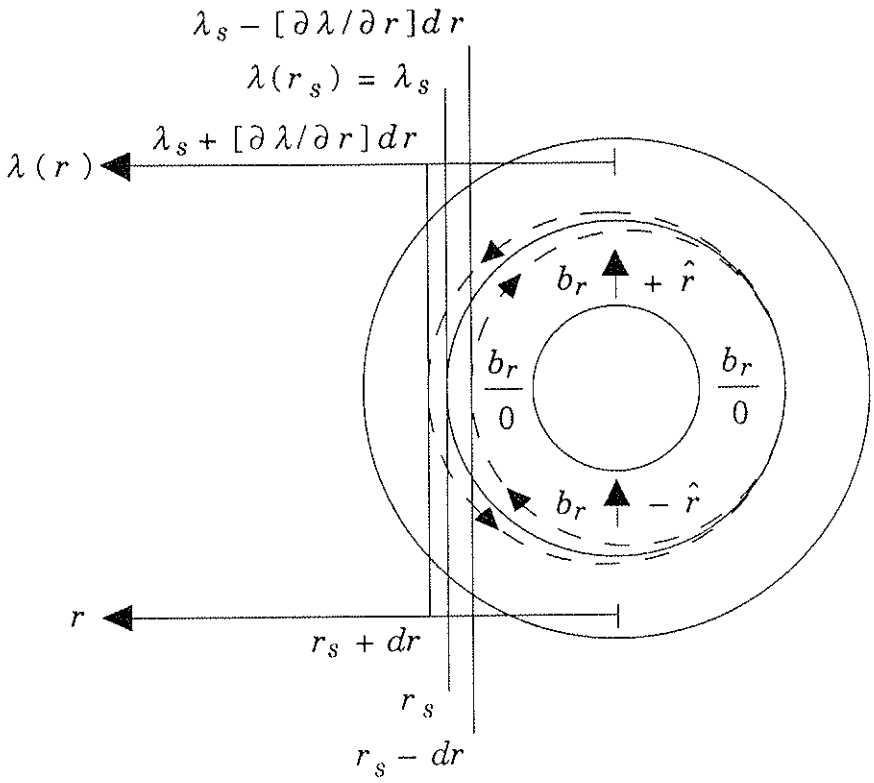

Figure 3.5 The dashed line indicates the path traced by the intersections of an equilibrium field line with a poloidal plane in the presence of an m=1 radial magnetic perturbation (b_r). The field line samples different values of λ along its length, and this difference is the radial transport of parallel current.

above, this flow across the flux surface must be balanced by a flow within the flux surface. A perturbed current must flow along the equilibrium field lines to connect the points of equilibrium current entrance and exit. This perturbed current is just g. The flow along an equilibrium field line is described by the parallel derivative of g on the right side of (3.3.11). In this way, finite grad$-\lambda$ leads to an extra current perturbation.

This additional current perturbation has an effect on the radial profile of b_r. The perturbed parts of equations (3.2.4) and (3.2.5) combine to yield the following approximate relation:

$$\mu_0 j_\theta \sim \left(\frac{i}{nk} \right) \frac{\partial^2 b_r}{\partial r^2} . \qquad (3.3.12)$$

This suggests that a change in the poloidal current perturbation would change the curvature of the radial b_r profile. Would this change increase or decrease $|b_r(r_s)|$? No definitive answer can be given on the basis of such a sketchy relation. However, it is worthwhile to note that the equilibrium is not in a minimum energy state, as long as $\lambda = \lambda(r)$. There is "free energy" available to go into the perturbations. In that case, the radial integral of ${b_r}^2$ would increase. The profile of b_r would show a greater increase of $|b_r|$ with r, leading to a larger value of $|b_r(r_s)|$. Thus, it is possible to attribute the observed behavior of the radial b_r-profile to the additional current perturbation described above. Of course, this speculation must be tested by actually solving the equations for the radial b_r-profile. This will be done in the next two sections.

3.4 TIME – INDEPENDENT, LINEARIZED MHD EQUATIONS

Much of the work of deriving the equations needed to solve for the vector magnetic perturbation — **b** — has already been done. Recall equation (3.3.8):

$$\mathbf{j} = \left(\frac{\lambda(r)}{\mu_0} \right) \mathbf{b} + \left(\frac{g}{\mu_0} \right) \mathbf{B}_0 \ . \tag{3.4.1}$$

The perturbed current can be eliminated using equation (3.2.4):

$$\mu_0 \, \mathbf{j} = \nabla \times \mathbf{b} \ . \tag{3.4.2}$$

The resulting equation is:

$$\nabla \times \mathbf{b} = \lambda(r) \, \mathbf{b} + g \, \mathbf{B}_0 \ . \tag{3.4.3}$$

The other necessary equation is (3.3.11):

$$\frac{b_r}{\mu_0} \left(- \frac{\partial \lambda}{\partial r} \right) = \mathbf{B}_0 \cdot \nabla \left(\frac{g}{\mu_0} \right) . \tag{3.4.4}$$

These last two form the set that will be solved.

The spatial behavior of the magnetic perturbations must now be specified precisely. In the preceding general discussions, mode numbers (m , n) have been mentioned in relation to the perturbations. These arise when considering a plasma confined in a periodic cylinder. The equations in the 3 – D MHD code were solved in this geometry, and the same will be done here. More specifically, the perturbations are Fourier analyzed in the

two periodic directions, θ and z . The spatial dependence of the vector $\mathbf{b}$ is then given by

$$\mathbf{b}(\mathbf{r}) = \mathbf{b}(r)\, e^{-i(m\theta + nkz)}, \tag{3.4.5}$$

where (m,n) are the poloidal and toroidal mode numbers. The wavenumber k is the axial fundamental: $k = 1/R$, where $2\pi R$ is the length of the cylinder. A useful relation arises from the spatial dependence taken above. For an equilibrium field given by

$$\mathbf{B}_0(r) = B_{\theta 0}(r)\,\hat{\theta} + B_{z 0}(r)\,\hat{z}\,, \tag{3.4.6}$$

the parallel derivative is

$$\mathbf{B}_0 \cdot \nabla = -iF\,, \tag{3.4.7}$$

where F is the same as in (3.3.1).

The equation for the radial profile of the radial magnetic perturbation can now be found. After some algebra, the equation is found to be:[6]

$$(r b_r)'' + \frac{1}{r}\left(\frac{m^2 - n^2k^2r^2}{m^2 + n^2k^2r^2}\right)(r b_r)' + \left[\left(\lambda^2 - n^2k^2 - \frac{m^2}{r^2} + \frac{2nkm\lambda}{m^2 + n^2k^2r^2}\right) - \left(\frac{m B_{z0} - nkrB_{\theta 0}}{rF}\right)\lambda'\right](r b_r) = 0\,, \tag{3.4.8}$$

where $'$ stands for $\partial/\partial r$. In this chapter, the focus is on modes with m = 1, so the equation takes the form:

$$(r b_r)'' + \frac{1}{r}\left(\frac{1-n^2k^2r^2}{1+n^2k^2r^2}\right)(r b_r)' + \left[\left(\lambda^2 - n^2k^2 - \frac{1}{r^2} + \frac{2nk\lambda}{1+n^2k^2r^2}\right) - \left(\frac{B_{z0} - nkrB_{\theta 0}}{rF}\right)\lambda'\right](r b_r) = 0 \ . \tag{3.4.9}$$

The problem has been reduced from a vector partial differential equation to a scalar ordinary differential equation. Before the process of solution can continue, however, some information on the equilibrium fields must be obtained.

The equilibrium fields are the solutions of equation (3.3.6), given the desired profile of $\lambda(r)$. Combining (3.3.6) and (3.2.4) gives the equation totally in terms of $\mathbf{B}_0$:

$$\nabla \times \mathbf{B}_0 = \lambda(r)\mathbf{B}_0 \ . \tag{3.4.10}$$

Since the object of solving for the fields is to gain some insight into the results of the 3-D MHD code, the $\lambda(r)$-profile of interest is the piecewise-linear one that was used in the code. This can be represented as follows:

$$\lambda(r) = \left\{ \begin{array}{ll} \lambda_0 & 0 \le r \le r_n \\ \lambda_0\left(\frac{a-r}{a-r_n}\right) & r_n < r \le a \end{array} \right\}, \tag{3.4.11}$$

with

$$\lambda' = \begin{cases} 0 & 0 \le r \le r_n \\ -\left(\dfrac{\lambda_0}{a - r_n}\right) & r_n < r \le a \end{cases} . \qquad (3.4.12)$$

Once λ_0, r_n and $B_{z\,0}(r = 0)$ — or Θ, $F(\Theta)$ and toroidal flux Φ_T — are chosen, the equilibrium fields can be found by numerical integration.

However, solving the above equations for the individual field components is not really necessary. The equilibrium fields can be eliminated from the perturbation equation in favor of the "safety factor," q. The definition of q is as follows:

$$q = \frac{rB_{z\,0}}{RB_{\theta\,0}} = \frac{krB_{z\,0}}{B_{\theta\,0}} . \qquad (3.4.13)$$

With this definition, the term in equation (3.4.9) which depends on the equilibrium fields can be rewritten in terms of q :

$$-\left(\frac{B_{z\,0} - nkrB_{\theta\,0}}{rF}\right)\lambda' \equiv \frac{\lambda'}{nkr}\left(\frac{n^2k^2r^2 - nq}{1 + nq}\right) . \qquad (3.4.14)$$

This form has certain advantages. It is easier to find where $(1+nq)=0$, given a knowledge of the $q-$profile, than where $F=0$, given a knowledge of the equilibrium field components. For the case of $n=-16$ from the 3-D code, a glance at the numerical $q-$profile indicates that $(1+nq)=0$ at a resonant surface $r_s = 0.60$, in the constant-λ region. Thus, $(1+nq)\neq 0$ where there is a finite grad-λ, and the denominator of (3.4.14) does not

contribute a singularity to the equation for b_r. Another advantage to using the right side of (3.4.14) is that an analytic expression for q can be found quite accurately for the MBFM equilibrium fields given above.

A differential equation for q can be found, and solved analytically to a good approximation, using the $\lambda(r)$-profile of (3.4.11). Differentiating (3.4.13) with respect to r, and using (3.4.10) to eliminate the derivatives of the equilibrium fields in favor of $\lambda(r)$, the following differential equation for $q(r)$ can be found:

$$q' = \left(\frac{2}{r}\right) q - (k r)\lambda\left[1 + \left(\frac{q}{k r}\right)^2\right]. \qquad (3.4.15)$$

Although (3.4.15) is a non-linear differential equation, it can be simplified using a little input from the 3-D MHD code results, to which comparisons will be made. In the region where λ is a constant, the equilibrium fields are given by Bessel functions,[7] and q can easily be expressed without solving this equation. It is the region of finite grad-λ that proves troublesome. However, for the case in the code, $(k r)_{\min} = 0.1228$ and $|q|_{\max} = 0.04$ in this region. Thus, $(q/k r)^2{}_{\max} = 0.106 \ll 1$. To reproduce the q-profile found in the code in the finite grad-λ region, the second term in the square brackets in (3.4.15) can be neglected. Then:

$$q' - \left(\frac{2}{r}\right) q \cong -(k r)\,\lambda(r)\ . \qquad (3.4.16)$$

This is a linear, first-order differential equation. It can easily be solved by finding an integrating factor.[8] The solution in the finite grad-λ region is:

$$q(r) \equiv r^2 \left[\frac{q(r_0)}{r_0^2} - \int_{r_0}^{r} \left(\frac{dx}{x} \right) k \, \lambda(x) \right] . \qquad (3.4.17)$$

For the $\lambda(r)$-profile of (3.4.11), this becomes:

$$q(r) \equiv r^2 \left[\frac{q(r_0)}{r_0^2} - \left(\frac{k \lambda_0}{1-(r_n/a)} \right) \left(ln\left(\frac{r}{r_0}\right) - \frac{r-r_0}{a} \right) \right] , \qquad (3.4.18)$$

where $r_n < r \leq a$ and $r_n < r_0 \leq a$. This expression can be matched to the Bessel function expression in the constant-λ region ($0 \leq r \leq r_n$) at r_n by choosing $r_0 = r_n$. The q-profile thus created, although obtained in part from an approximate differential equation, agrees well with that found by a direct integration of equation (3.4.15) over the range $r_n \leq r \leq a$. This is shown in Figure 3.6 .

Some useful information about equilibrium fields can be obtained from equation (3.4.18). Suppose that experimental information on F and Θ is available and it is desired to find the equilibrium force-free fields that best correspond to this data. The Modified Bessel Function Model, which consists of equation (3.4.10) and a $\lambda(r)$-profile like that in (3.4.11), can be used to obtain force-free field profiles that match experimentally-observed, global parameters. Given Θ, for example, two parameters of the model — λ_0 and r_n — can be found.[9] The advantage of knowing equation (3.4.18) as well is that it provides the radius at which the toroidal field reverses (r_{rv}), without requiring that the field equations be solved.

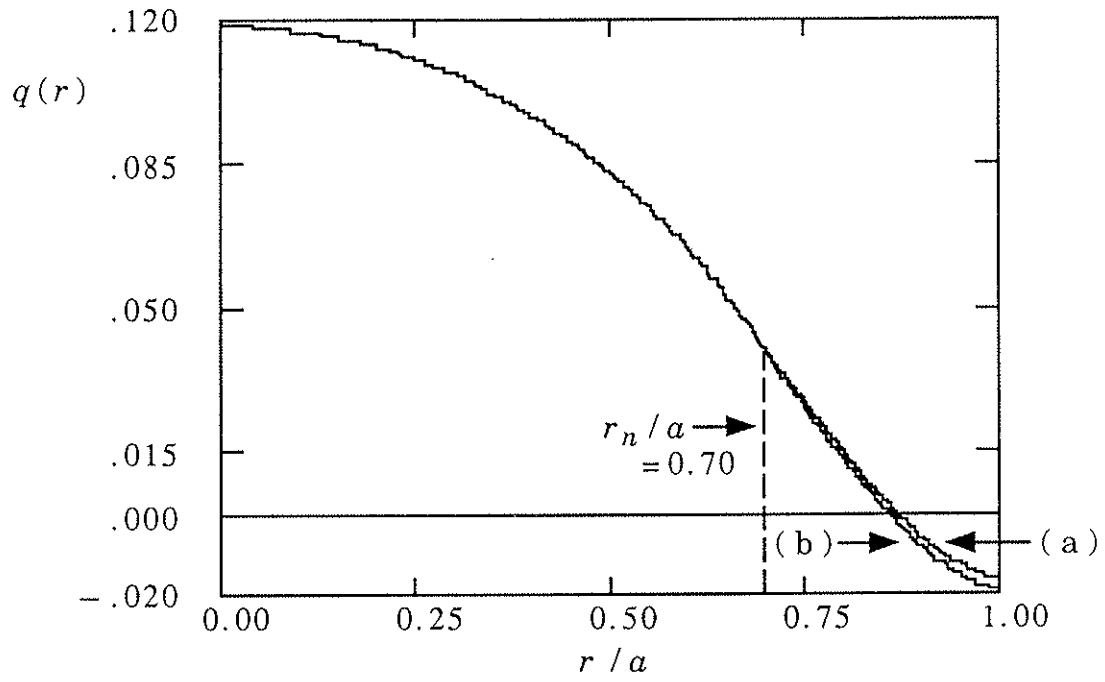

Figure 3.6 The q – profile found from equation (3.4.18) — (a) — agrees reasonably well with that obtained from an integration of equation (3.4.15) over the range $r_n \leq r \leq a$ — (b).

In general, r_{rv} is the radius where $q = 0$; however, a simple approximate expression can be derived. It is generally known from experience that the reversal point lies near the edge of the plasma, $r = a$. To take advantage of this, take $r_0 = a$ and expand (3.4.18) around a, using the distance from the edge $\rho = 1 - (r/a)$ as a small parameter ($\rho \ll 1$). The result, to lowest order for the term in brackets, is:

$$q(\rho) = q(a)\left(1-\rho\right)^2\left(1 - \frac{\Omega}{2}\rho^2\right) \qquad (3.4.19)$$

with

$$\Omega = \frac{(k a)(\lambda_0 a)}{\left(1 - \frac{r_n}{a}\right)|q(a)|} . \qquad (3.4.20)$$

According to (3.4.19), there are two zeros for $q(\rho)$. One is at $\rho = 1$, or $r = 0$. This clearly violates the assumption of small ρ, and calls the expansion into question. In fact, (3.4.18) is not valid for $r \leq r_n$. This solution can be ignored. The other zero is:

$$\rho_{rv} = \sqrt{\frac{2}{\Omega}} . \qquad (3.4.21)$$

This can be rewritten in terms of the global parameters F and Θ , and the model parameters λ_0 and r_n found from Θ . The definitions of q , F, and Θ lead to the relationship: $|q(a)|/(k a) = |F|/\Theta$. Using this expression, equation (3.4.20), and the definition $\rho_{rv} = 1 - (r_{rv}/a)$ in (3.4.21) gives:

$$\frac{r_{rv}}{a} = 1 - \left[\left(\frac{2}{\lambda_0 a}\right)\left(\frac{|F|}{\Theta}\right)\left(1 - \frac{r_n}{a}\right)\right]^{\frac{1}{2}} \qquad (3.4.22)$$

for the reversal radius. This is a useful expression involving quantities that are readily available from experiment or easily calculated. (Of course, the ρ_{rv} calculated from (3.4.22) must satisfy the assumption $\rho \ll 1$. This can be checked *a posteriori*.) As an example, consider the equilibrium fields used in the 3 – D MHD code. For this case $\lambda_0 a = 2.95$, $|F| = 0.1444$, $\Theta = 1.515$, and $r_n/a = 0.70$, and equation (3.4.22) yields a value of $r_{rv}/a =$

0.86. This is precisely the value obtained from the code results by measuring the point at which the profile of B_{z0} goes through zero.

All the information necessary to solve for the radial b_r profile is now available. The solution of equation (3.4.9), with the $\lambda(r)-$profile of (3.4.11), will reveal whether the presence of a finite grad$-\lambda$ actually has the effect of increasing $|b_r(r_s)|$, as was suggested in the previous section.

3.5 SOLUTIONS AND CONCLUSIONS

The structure of the $\lambda(r)-$profile suggests that the solution for b_r be sought in two separate regions and then matched at their boundary. The two regions will be referred to as the "constant$-\lambda$ region" ($0 \le r \le r_n$) and the "finite grad$-\lambda$ region" ($r_n < r \le a$) . This approach was used at the end of the previous section in describing the solution of (3.4.15) for the $q-$profile. The presence of a constant$-\lambda$ in a particular region resulted in a known solution in terms of Bessel functions in this region. The same is true in this case. The solutions for b_r in the case of constant$-\lambda$ have already been derived in Section 3.3. They are the Chandrasekhar$-$Kendall functions, whose radial parts are given by combinations of Bessel functions. These solutions will be used in the constant$-\lambda$ region. In the finite grad$-\lambda$ region, the equation will be solved in two different ways.

The values of the various parameters in the equation are chosen to correspond to those used in the 3$-$D MHD code. They are summarized below:

PARAMETER	VALUE
$\lambda(r)$ – profile	
$\lambda_0 a$	2.95
r_n / a	0.70
Axial Dependence	
$k a$	0.1754
n	– 16
Boundary Condition	
$b_r(a)$	– 1.87 e –5
Important Radii	
r_s / a	0.60
r_{rv} / a	0.86

Table 3.1

It has already been noted that, with these parameters, equation (3.4.9) does not have a singularity due to the λ'/F term. It is worth pointing out that there is a discontinuity in λ' at $r = r_n$ which will affect the solutions.

The solution in the constant – λ region is given by the following expression

$$b_r(r) = b_r(r_n)\left[\frac{\left(\frac{\lambda_0 - nk}{\gamma_0 r}\right)J_1(\gamma_0 r) + nkJ_0(\gamma_0 r)}{\left(\frac{\lambda_0 - nk}{\gamma_0 r_n}\right)J_1(\gamma_0 r_n) + nkJ_0(\gamma_0 r_n)}\right] \qquad (3.5.1)$$

for $0 \le r \le r_n$,

with $\gamma_0{}^2 = \lambda_0{}^2 - n^2k^2$.

The quantity $b_r(r_n)$ will be determined from matching to the solution in the finite grad$-\lambda$ region. The equation in the finite grad$-\lambda$ region — equation (3.4.9) — is second-order in r. Two constants of integration must be provided to completely specify the solution before any matching can take place. One will be the value of $b_r(a)$ given above. Since $b_r(r_n)$ has yet to be defined, the ratio of slope to value at $r = r_n$ —that is, $b_r'(r_n)/b_r(r_n)$ as calculated from (3.5.1)— will be given as the second constant. These two boundary conditions will allow $b_r(r_n)$ to be determined as a part of the solution in the finite grad$-\lambda$ region. This value will then be used in (3.5.1) as well.

The simplest way to solve for b_r in the finite grad$-\lambda$ region is just to numerically integrate. This was done, using equation (3.4.9) for b_r, equation (3.4.11) for the λ-profile, and equation (3.4.15) for the q-profile. The numerical method used is called "invariant imbedding."[10] It involves a Ricatti transformation which converts a system of linear, first-order equations subject to boundary conditions to a system of nonlinear, first-order equations subject to initial conditions. Initial value equations

are generally easier to deal with numerically. A detailed description of the "invariant imbedding" technique, which will also be called upon in Chapter 4, will be reserved for the Appendix. For now, suffice it to say that the IMSL routine DVERK [11] — a Runge-Kutta-Verner fifth and sixth order method — was used to integrate the initial value equations.

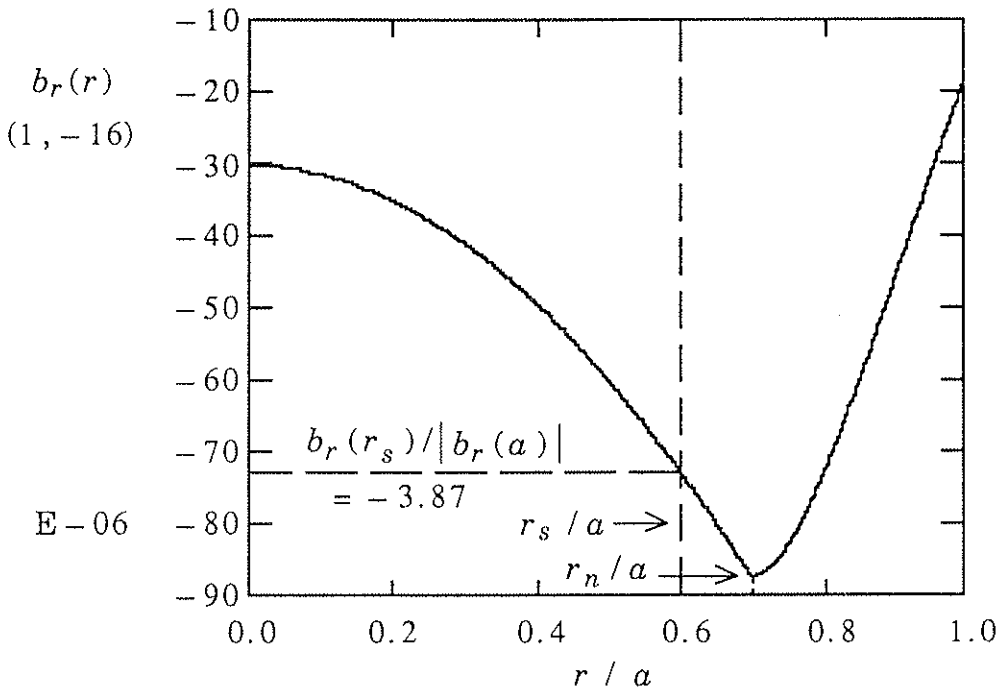

Figure 3.7 Radial profile of a (1 , − 16) b_r perturbation found by direct integration. There is an increase in $|b_r(r_s)|$ which is more than a factor of 3 greater than that in the 3 − D code results.

The results of the numerical integration are shown in Figure 3.7 . Note that the effect of finite grad − λ is indeed to increase the value of $|b_r(r_s)|$. The value shown represents an increase of about a factor of 10

over the value for a vacuum profile. Thus, the additional current perturbation introduced by the presence of finite grad$-\lambda$ enhances the radial field. This is quite apparent near $r = r_n$, where the profile in the constant$-\lambda$ region is sharply "pulled down" to match the steeply falling profile in the finite grad$-\lambda$ region. The sharp change in slope in this area corresponds to the discontinuity in λ' at $r = r_n$.

A second approach to finding b_r in the finite grad$-\lambda$ region lies in ordering equation (3.4.9) in terms of some small parameter, identifying the lowest order equation and then solving this approximate equation. It is hoped that a solution in terms of simple, tabulated functions can be found. Such a solution might lend some insight into the quantitative effect of λ' on $|b_r(r_s)|$, without requiring that many numerical integrations be performed. To this end, consider a form of (3.4.9) which has been rewritten in terms of dimensionless parameters:

$$y''a^2 + \frac{1}{\left(\frac{r}{a}\right)}\left(\frac{1-\nu^2\left(\frac{r}{a}\right)^2}{1+\nu^2\left(\frac{r}{a}\right)^2}\right)y'a + \left[\left((\lambda a)^2 - \nu^2 - \frac{1}{\left(\frac{r}{a}\right)^2}\right) - \frac{2\nu(\lambda a)}{1+\nu^2\left(\frac{r}{a}\right)^2} + \Lambda\frac{\nu\left(\frac{r}{a}\right)}{(1+nq)}\left(1-\frac{nq}{\nu^2\left(\frac{r}{a}\right)^2}\right)\right]y = 0\ , \tag{3.5.2}$$

where $y \equiv (r\,b_r)$. The parameters and their numerical values, as well as the values of functions of r, are given in the table below.

PARAMETER	DEFINITION	VALUE
Λ	$\lvert \lambda' a^2 \rvert$	9.83
ν	$\lvert n k a \rvert$	2.81
λa	See (3.4.11)	$0.00 \le \lambda a \le 2.95$
r/a	—	$0.70 \le r/a \le 1.00$
$n q$	See (3.4.13)	$-0.64 \le n q \le 0.27$

Table 3.2

Since Λ and ν are the largest parameters, it is logical to factor them out and then expand the remaining terms in powers of $(1/\Lambda)$ and $(1/\nu)$.

A more formal ordering can be defined. The small parameter is $\delta \equiv (1/\Lambda)$, which has the value $\delta = 0.102$. Since there is no *a priori* relationship between $(1/\Lambda)$ and $(1/\nu)$, the choice $(1/\nu) = O(\delta^{1/2})$ is made on the basis of the numerical values for this case ($\delta = 0.102$ and $(1/\nu) = 0.356$). As can be seen above, the departure of (r/a) from unity is also $O(\delta^{1/2})$. In order to exploit this relatively small variation, the radius variable is transformed to the form $\rho = 1 - (r/a)$, with $\rho = O(\delta^{1/2})$. The various functions of radius specified in the table above can now be rewritten and ordered. In particular, $q(r)$ can be expanded using (3.4.18). The choice $r_0 = r_{r\upsilon}$ is made, and the expansion is performed around this point. There are two advantages to this. The first is that $q(r_{r\upsilon}) = 0$, which simplifies

the expression. The second is that this radius lies approximately in the center of the finite grad$-\lambda$ region, so that the appropriate expansion variable — $(r - r_{rv})/a = \{ [\, 1 - (r_{rv}/a) \,] - \rho \}$ — has its minimum possible excursion. Thus, the expansion can be kept fairly accurate with a small number of terms. Since $q(r_{rv}) = 0$, one power of the expansion variable can be factored out directly. In what remains, terms second order and higher in the expansion variable are neglected. With this, the expansion should be accurate to around 10%. The expression for $n\,q(\rho)$ is:

$$n\,q \;=\; (\delta v)\,\sigma_0 (1 - \sigma_1 \rho)(1 + \sigma_2 \rho)\,, \tag{3.5.3}$$

$$\text{with} \qquad \sigma_0 = \left(\frac{1 - \frac{r_{rv}}{a}}{\delta} \right)^2 \left(\frac{3}{2} - \frac{r_{rv}}{a} \right)\,, \tag{3.5.4}$$

$$\text{and} \qquad \sigma_1 \;=\; \frac{1}{\left(1 - \frac{r_{rv}}{a} \right)}\,, \tag{3.5.5}$$

$$\text{and} \qquad \sigma_2 \;=\; \frac{\left(4\,\frac{r_{rv}}{a} - 3 \right)}{\left(3 - 2\,\frac{r_{rv}}{a} \right)\left(1 - \frac{r_{rv}}{a} \right)}\,. \tag{3.5.6}$$

The new forms of the other functions of radius are shown below:

$$\frac{r}{a} \;=\; 1 - \rho \qquad \text{and} \qquad \lambda\, a \;=\; \frac{\rho}{\delta}\,.$$

Finally, the ordering is summarized in the following table. Given the small value $\delta = 0.102$:

$O(\delta)$	$O(\delta^{1/2})$	$O(1)$	$O(\delta^{-1/2})$	$O(\delta^{-1})$
δ	$\delta\nu$		ν	Λ
	ρ (max)		λa (max)	
	nq (max)	σ_0	σ_1, σ_2	

Table 3.3

Using the above ordering , equation (3.5.2) can be approximated. The first step is to divide each term through by the largest parameter. The resulting expressions are then grouped according to size, largest first, using appropriate combinations of δ and ν as indicators. The result is:

$$\frac{\partial^2 y}{\partial \rho^2} + \left(\frac{1}{1-\rho}\right)\left[\frac{(1-\rho)^2 - \left(\frac{1}{\nu}\right)^2}{(1-\rho)^2 + \left(\frac{1}{\nu}\right)^2}\right]\frac{\partial y}{\partial \rho} +$$

$$\left(\frac{\nu}{\delta}\right)\left\{\left(\frac{1-\rho}{1+nq}\right)\left[1 - \left(\frac{\delta}{\nu}\right)\frac{(nq/\delta\nu)}{(1-\rho)^2}\right] - (\delta\nu)\left[1 - \left(\frac{\rho}{\delta\nu}\right)^2\right]\right.$$

$$\left. - \left(\frac{\delta}{\nu}\right)\left[\frac{1}{(1-\rho)^2} + \frac{2(\rho/\delta\nu)}{(1-\rho)^2 + \left(\frac{1}{\nu}\right)^2}\right]\right\} y = 0 . \qquad (3.5.7)$$

Next, the smallest terms are eliminated. A balance must be struck between the desire for a simple solution, which would mean dropping most terms, and an accurate solution, which would mean keeping more terms. Given that terms of $O(\delta^{1/2})$ and terms of $O(1)$ are not really that

well separated, it was decided that the lowest-order equation should include terms up to $O(\delta)$. This yields coefficients of y and its derivatives that are accurate to about 10% . After some algebra, the equation can be written:

$$\frac{\partial^2 y}{\partial \rho^2} + \left[b_0 + b_1 \rho + b_2 \rho^2 \right] \frac{\partial y}{\partial \rho} + \left(\frac{\nu}{\delta} \right) \left[c_0 + c_1 \rho + c_2 \rho^2 + c_3 \rho^3 + c_4 \rho^4 \right] y = 0 , \tag{3.5.8}$$

with:

$$b_0 = \frac{1 - \left(\frac{1}{\nu} \right)^2}{1 + \left(\frac{1}{\nu} \right)^2} \qquad O(1)$$

$$b_1 = b_0 \left[1 - \left(\frac{4 \left(\frac{1}{\nu} \right)^2}{1 - \left(\frac{1}{\nu} \right)^4} \right) \right] \qquad O(1)$$

$$b_2 = b_0 \left[1 - \left(\frac{2 \left(\frac{1}{\nu} \right)^2}{1 - \left(\frac{1}{\nu} \right)^4} \right) \left(\frac{5 + \left(\frac{1}{\nu} \right)^2}{1 + \left(\frac{1}{\nu} \right)^2} \right) \right] \qquad O(1)$$

and:

$$c_0 = \left[1 - (\delta \nu)\left(1 + \sigma_0\right) + (\delta \nu)^2 \sigma_0{}^2 \right] \qquad O(1)$$

$$c_1 = -\left[\left(1-(\delta\nu)\sigma_0\right) + (\delta\nu)\,\sigma_0(\sigma_2-\sigma_1)\left(1-2(\delta\nu)\sigma_0\right) \right] \qquad O(1)$$

$$c_2 = (\delta\nu)\,\sigma_0\,\sigma_1\sigma_2\left[\left(1-4(\delta\nu)\sigma_0\right) + \left(\frac{\sigma_2-\sigma_1}{\sigma_2\,\sigma_1}\right) \right. \qquad O(\delta^{-1/2})$$

$$\left. + (\delta\nu)\sigma_0\left(\frac{\sigma_2{}^2+\sigma_1{}^2}{\sigma_2\,\sigma_1}\right) \right] + \frac{1}{(\delta\nu)}$$

$$c_3 = -(\delta\nu)\,\sigma_0\,\sigma_1\sigma_2\left[\ 1 + 2\,(\delta\nu)\sigma_0(\sigma_2-\sigma_1)\ \right] \qquad O(\delta^{-1/2})$$

$$c_4 = (\delta\nu)^2\,\sigma_0{}^2\,\sigma_1{}^2\,\sigma_2{}^2, \qquad O(\delta^{-1})$$

where σ_0, σ_1, and σ_2 are defined in equations (3.5.4)–(3.5.6) above. (Note that the ordering sizes given at the right are formal orderings only. Numerical coefficients are treated as $O(1)$, and groups of terms of the same order are treated as being of that order. This is a somewhat naive approach, but it was desired to obtain a result not overly dependent on the specific numbers chosen.)

Although equation (3.5.8) does not have a simple solution, it can be solved. The chosen compromise between accuracy and simplicity has forced the consideration of a complicated equation. Unfortunately, the goal of finding a solution in terms of simple, tabulated functions cannot be met. However, a series solution of equation (3.5.8) can be obtained. The solution takes the following form:

$$y = \sum_{k=0}^{\infty} A_k \rho^k \quad , \tag{3.5.9}$$

with A_0 and A_1 as the two undetermined constants of integration, and the remaining coefficients given by the recursion relation:

$$A_k = -\left(\frac{b_0}{k}\right) A_{k-1} - \left[\frac{\left(\frac{\nu}{\delta}\right) c_0 + (k-2)\, b_1}{k\,(k-1)}\right] A_{k-2}$$
$$- \left[\frac{\left(\frac{\nu}{\delta}\right) c_1 + (k-3)\, b_2}{k\,(k-1)}\right] A_{k-3} - \left[\frac{c_2}{k\,(k-1)}\right] A_{k-4}$$
$$- \left[\frac{c_3}{k\,(k-1)}\right] A_{k-5} - \left[\frac{c_4}{k\,(k-1)}\right] A_{k-6} \tag{3.5.10}$$

for $k \geq 2$. (For terms with $k < 6$, set A's with negative indices to zero.) The A's can be separated into parts that depend on A_0 and A_1 separately. Thus, equation (3.5.9) can be rewitten as:

$$y = A_0\, y_0(\rho) + A_1\, y_1(\rho) \quad , \tag{3.5.11}$$

where y_0 is an infinite series in ρ beginning with 1 (or ρ^0) so that $y_0(0) = 1$, and y_1 is an infinite series in ρ beginning with ρ^1, so that $y_1(0) = 0$. The constants of integration can be found by applying the boundary conditions, as described in the paragraph following equation (3.5.1) . (Remember, $y \equiv (rb_r)$.) A radial profile calculated from this series solution is shown in Figure 3.8.

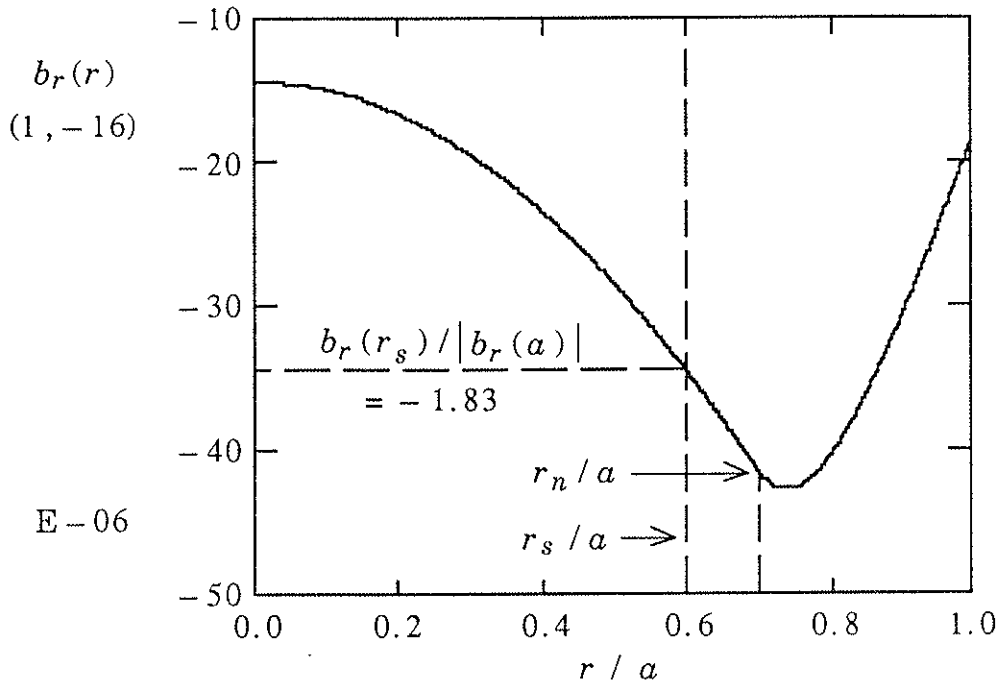

Figure 3.8 Radial profile of a (1 , – 16) b_r perturbation found by series solution. The increase in $|b_r(r_s)|$ is more moderate than in the case of the numerical integration.

The series solution of (3.5.8) does yield some useful information. Figure 3.8 shows that the value of $|b_r(r_s)|$ is only increased by a factor of 4.7 over the value for a vacuum profile. This is certainly a significant increase, but it is a factor of 2 less than that observed in the case of the numerical integration. In addition, the profile in the series case falls less steeply in the finite grad–λ region, and the sudden change in slope around $r = r_n$ is less pronounced. All these observations can be understood as the effects of approximating the coefficient of (rb_r) in equation (3.5.2). Consider the change in slope. This comes from a

discontinuity in $(rb_r)''$. Equation (3.5.2) connects $(rb_r)''$ to the product of (rb_r) and a coefficient. This coefficient depends on $\Lambda \equiv \lambda' a^2$, which has a discontinuity at $r = r_n$. (See equation (3.4.12).) The fact that the sharpness of the change in $(rb_r)'$, and thus the discontinuity in $(rb_r)''$, is reduced in the series solution suggests that the approximation process has "smoothed out" the jump in this coefficient. A look at the numbers shows that this does indeed occur. The jump in curvature — which is defined as $[(rb_r)''/(rb_r)]_{r_n +} - [(rb_r)''/(rb_r)]_{r_n -}$ — has a value of ($62.76/a^2$) in the numerical integration case and ($51.07/a^2$) in the series case. In addition to the effect on the slope, this reduction of the jump in curvature is accompanied by a reduction in $|b_r(r_s)|$. This observation is important. It suggests that in a real plasma, where the natural smoothing of λ will reduce any jump in λ' and $(rb_r)''/(rb_r)$, the amplifying effect of finite grad$-\lambda$ on $|b_r(r_s)|$ will be reduced as well.

The effect of introducing finite resistivity and viscosity (η, ν_0) is to produce a more physical case which more closely resembles the real plasma described above. In this case, a connection between a reduced jump in $(rb_r)''/(rb_r)$ and a smaller amplification of $|b_r(r_s)|$ can actually be observed. The result of adding finite η, ν_0 to finite grad$-\lambda$ can most easily be examined in the results of the 3-D MHD code. Finite dissipation can be expected to "smooth out" rapid changes in spatial field profiles. In particular, finite resistivity should diffuse away any sharp changes in the equilibrium currents and smooth out the effects of discontinuities in λ'. Thus, any jump in $(rb_r)''/(rb_r)$ should be small. Figure 3.4 shows that

this is indeed the case. There is very little evidence for a sharp change in slope around $r = r_n$ in this profile, compared to the profile produced by numerical integration of equation (3.4.9). Along with this, the increase in $|b_r(r_s)|$ over the value for a vacuum profile should be smaller than the factor of 10 observed in the case of the numerical integration. In fact, $|b_r(r_s)|$ is only increased by a factor of 3 . This is consistent with what is expected.

In summary, finite grad$-\lambda$ has the most important effect on the interaction between a magnetic field perturbation induced by a field error and an RFP plasma, for the case of m=1. In the presence of finite grad$-\lambda$ an additional current perturbation, one along equilibrium field lines, is produced. The effect of this current perturbation is to change the curvature of the profile of the radial magnetic field perturbation. As a result, the value of radial magnetic field at the m=1 resonant surface (r_s) is increased. It is this radial magnetic field which causes a magnetic island to form at the resonant surface. This increase in $|b_r(r_s)|$ can be reduced by the introduction of finite η, ν_0 , or any other physical effect which acts to remove sharp changes in the $\lambda-$profile.

REFERENCES

[1] A. Y. Aydemir and D. C. Barnes, Phys. Rev. Lett. **52**, 930 (1984).

[2] D. D. Schnack, E. J. Caramana, and R. A. Nebel, Phys. Fluids **28**, 321 (1985).

[3] S. Chandrasekhar and P. C. Kendall, Astrophys. J. **126**, 457 (1957).

[4] M. Abramowitz and I. A. Stegun, *Handbook of Mathematical Functions* (Dover, New York, 1965), p. 358.

[5] *Ibid.*, p. 409.

[6] See also: J. P. Goedbloed, Physica **53**, 501 (1970).

[7] J. B. Taylor, Phys. Rev. Lett. **33**, 1139 (1974).

[8] G. F. Simmons, *Differential Equations with Applications and Historical Notes* (McGraw – Hill, New York, 1972), pp. 47 – 48.

[9] K. F. Schoenberg, R. F. Gribble, and J. A. Phillips, Nuclear Fusion **22**, 1433 (1982).

[10] M. R. Scott, in *Numerical Solutions of Boundary Value Problems for Ordinary Differential Equations*, edited by A. K. Aziz (Academic Press, New York, 1975), p.89.

[11] IMSL products and documentation are subject to periodic updates. Routines are often renamed. DVERK was described in the June, 1982 version of the IMSL manual. For further information on IMSL products, contact:

IMSL
Customer Relations
2500 ParkWest Tower One
2500 CityWest Boulevard
Houston, Texas 77042 – 3020

CHAPTER 4

LINEAR BEHAVIOR OF m = 0 MODES FOR THE "NO DYNAMO" MODEL

4.1 INTRODUCTION

This chapter continues the study of the ways in which certain features of the plasma model — a finite gradient in $\lambda \equiv J/B$ (grad $-\lambda$) and finite resistivity and viscosity (η, ν_0) — alter a magnetic field perturbation induced by an edge field error. The focus here will be on perturbations with poloidal mode number m = 0. As was mentioned in Chapter 2, this case is of particular interest. The results from the 3-D MHD code belie the expectations raised by the previous look at the interaction of such a perturbation with an RFP plasma.[1] The size of the radial field perturbation at the location of the m = 0 resonant surface in the presence of the plasma is reduced from its value in a vacuum, rather than increased. This promises less disruption of flux surfaces due to island formation around this resonant surface—in this case, the important field-reversal surface. The important consequences for stability and transport which may be expected from this have already been discussed in Chapter 1. As this result must arise from the more realistic description of the RFP plasma used in the 3-D code, it is important to understand the roles played by each of the features mentioned above.

As in the last chapter, the study of the roles of finite grad$-\lambda$ and finite η, ν_0 is undertaken in a systematic manner. In Section 4.2, the relative importance of these features is assessed. Section 4.3 contains an examination of the results from the 3-D code. These include the change in the shape of the radial magnetic perturbation profile and the scaling of the magnitudes of various magnetic and velocity perturbations with η and ν_0. A simple physical picture based on the one developed in Chapter 3, Section 3.3, is used to explain these results in terms of the features of the model being studied. The physical picture suggested must be supported by actual solutions for the profile of the radial magnetic field perturbation. The set of time-independent, linearized MHD equations used in this case are derived in Section 4.4. In Section 4.5, the methods of solution are described and the solutions presented. Finally, in Section 4.6, the results are compared to those of the 3-D MHD code and conclusions are drawn about the applicability of the results to an actual plasma device.

4.2 FINITE GRAD$-\lambda$ VERSUS FINITE η, ν_0

Sorting out the individual roles of finite grad$-\lambda$ and finite η, ν_0 is more difficult in the case of m=0 perturbations than it was for perturbations with m=1; however, a heuristic approach is still useful. As was the case with m=1 perturbations, it is easiest to start by looking at radial profiles of perturbations with constant-λ and $\eta = \nu_0 = 0$. The effects can then be added one-by-one: first finite η, ν_0 and then finite η, ν_0 and finite grad$-\lambda$. Also, in this context it is useful to continue looking at axial

magnetic field perturbations (b_z). The solutions for the case with constant-λ and $\eta = \nu_0 = 0$ have a simple radial behavior which makes comparison easier. Some information on radial magnetic field perturbations (b_r) will also be considered. The profile changes which will be pointed out are most easily observed for the perturbations with toroidal mode number n = 12. Profiles of these modes will be shown here, although analytic calculations done later will use n = 24.

The profiles of magnetic perturbations in a plasma with constant-λ and $\eta = \nu_0 = 0$ have already been found in Chapter 3, Section 3.2; they are given by the Chandrasekhar-Kendall functions.[2] The form of the axial magnetic field perturbation for the case of poloidal mode number m=0 and toroidal mode number n, in a periodic cylinder of length $2\pi R$, is:

$$b_z = C\, J_0(\gamma r)\cos(n k z)\ , \qquad (4.2.1)$$

The various terms are defined as follows: $k = 1/R$ is the fundamental axial wavenumber, $\gamma^2 = \lambda^2 - (n k)^2$, J_0 is the Bessel function of the first kind of order zero,[3] and C is a constant. The values of the parameters are chosen to be the same as those used in the 3-D MHD code for a ZT-40M "coil" case: $\lambda a = 2.95$, $n = 12$, $k a = 0.1754$, and $\gamma a = 2.07$. In this way, a comparison can be made to the code-generated profiles which include the effects of finite η, ν_0 and finite grad-λ, finite η, ν_0. The radial part of (4.2.1) is plotted in Figure 4.1, with $C = b_z(0)$. To facilitate comparison with the profile for constant-λ, finite η, ν_0, the value of $b_z(0)$ is taken from the 3-D MHD code results for that case.

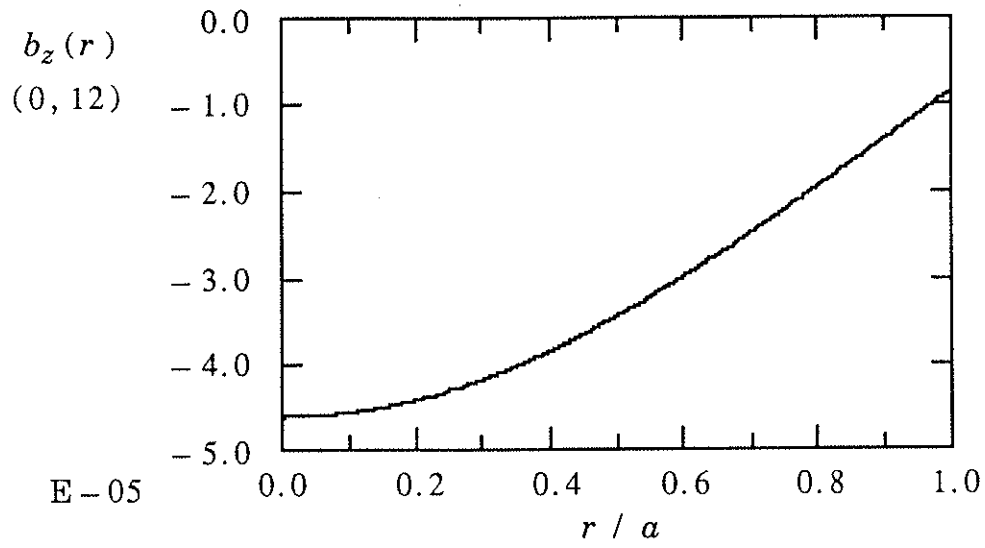

Figure 4.1 Radial profile of an m = 0 axial magnetic perturbation in the constant− λ , $\eta = \nu_0 = 0$ case (real part of $b_z(0)$ used).

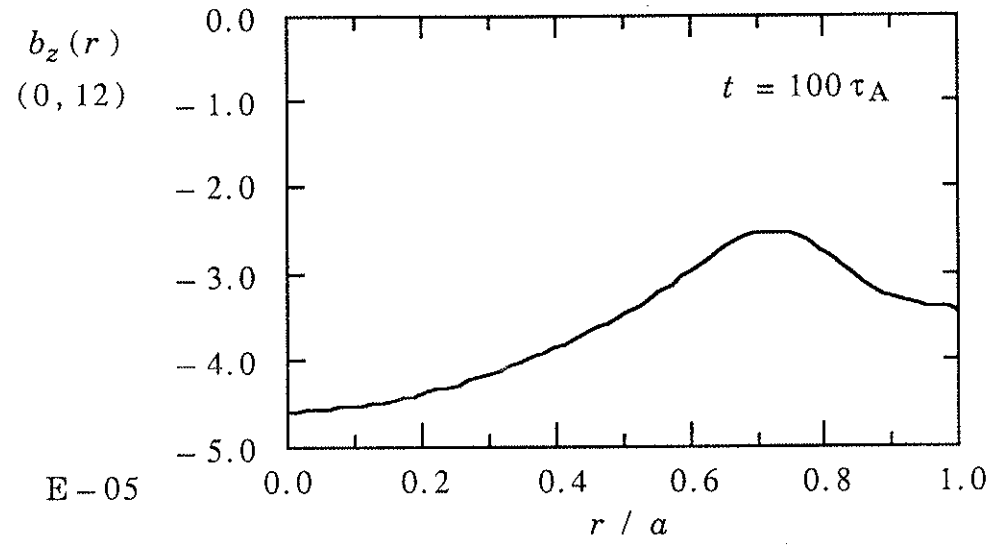

Figure 4.2 Radial profile of an m = 0 axial magnetic perturbation (real part) in the case of constant− λ , finite η , ν_0 case.

The addition of finite η, ν_0 greatly changes the character of the perturbation profile. The radial profile of b_z calculated by the 3-D MHD code for a case with finite η, ν_0 is shown in Figure 4.2 . The deviation from a profile given by $-J_0(\gamma r)$, illustrated in Figure 4.1, is apparent. Unlike a J_0 function, the absolute value of b_z decreases to a minimum and begins to increase again without first having gone through zero.

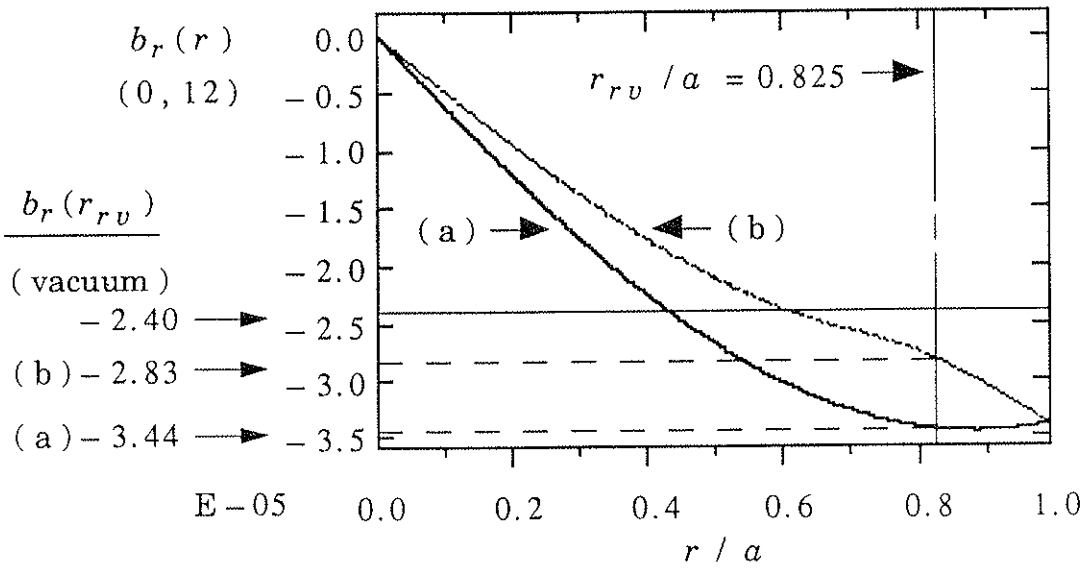

Figure 4.3 Radial profiles of an m = 0 radial magnetic perturbation (imaginary part) in the constant-λ case. Profile (a) is for $\eta = \nu_0 = 0$ and profile (b) is for finite η, ν_0.

It is worthwhile to note the corresponding changes in the b_r profile. These are illustrated below in Figure 4.3 . The profile with finite η, ν_0 has smaller values of $|b_r|$ near the edge of the plasma. Most importantly, the value of $|b_r|$ at the m = 0 resonant surface (the reversal surface r_{rv}) is

reduced from its value in the case of $\eta = \nu_0 = 0$. The reduction is by a factor of approximately 18%. This is an important result, but it is not identical to the reason for all the interest in modes with m=0, as cited in Section 4.1. There, it was observed that the value of $|b_r(r_{rv})|$ in the presence of a plasma with both finite η, ν_0 and finite grad$-\lambda$ is reduced below the value it would have for a perturbation in vacuum. The very presence of such a plasma provides some "healing" effects. In the case shown above, although the value of $|b_r(r_{rv})|$ is reduced for a plasma with finite η, ν_0 as compared to a plasma with $\eta = \nu_0 = 0$, the value in both cases is greater than that for a vacuum profile. Thus, although the introduction of finite η, ν_0 plays an important role, it does not constitute the whole story.

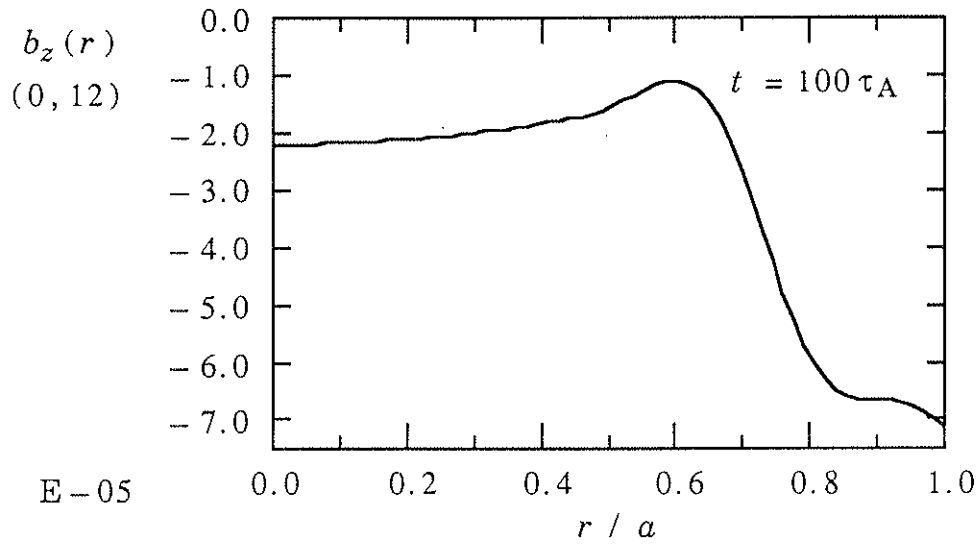

Figure 4.4 Radial profile of an m=0 axial magnetic perturbation (real part) in the finite grad$-\lambda$, finite η, ν_0 case.

The role of finite grad$-\lambda$ must also be taken into account. Figure 4.4 shows the radial profile of b_z calculated by the 3-D MHD code for a case including finite η, ν_0 and finite grad$-\lambda$. In general, the features resemble those of the profile in Figure 4.2: the absolute value of b_z initially decreases, reaches a minimum at $r/a \sim 0.7$, and increases as r/a approaches unity. However, notice the change in scale. The central part of the profile is "pulled down" (in absolute value), while the edge of the profile is "pulled up." In the process, the "turn over" in the profile, which was the signature of finite η, ν_0, has been greatly enhanced. This observation can also be applied to the case of the b_r profile. It might be expected that the signature of finite η, ν_0 in that case — reduction of $|b_r(r_{rv})|$ — would be enhanced upon the introduction of finite grad$-\lambda$. As was already noted at the end of the last paragraph, this is precisely the difference between having just finite η, ν_0 and both finite η, ν_0 and finite grad$-\lambda$ in the 3-D MHD code.

The relative roles of finite η, ν_0 and finite grad$-\lambda$ can now be assigned. Finite η, ν_0 produces the basic change in the b_r profile which causes some reduction of $|b_r(r_{rv})|$. The introduction of finite grad$-\lambda$ causes the profile to be "pulled down" (in absolute value) at the center (the value of $b_r(a)$ is now fixed by the field error) in such a way that the reduction of $|b_r(r_{rv})|$ is enhanced — the value of $|b_r(r_{rv})|$ is reduced below that for a vacuum profile.

4.3 PHYSICAL INTERPRETATION

The changes in the profile of the magnetic perturbation which have been alluded to above will now be explored in more detail, with an eye towards explaining the roles of finite grad$-\lambda$ and finite η, ν_0. The emphasis has been on the reduction of the radial magnetic perturbation at the resonant surface for m = 0 modes. This surface is defined in equation

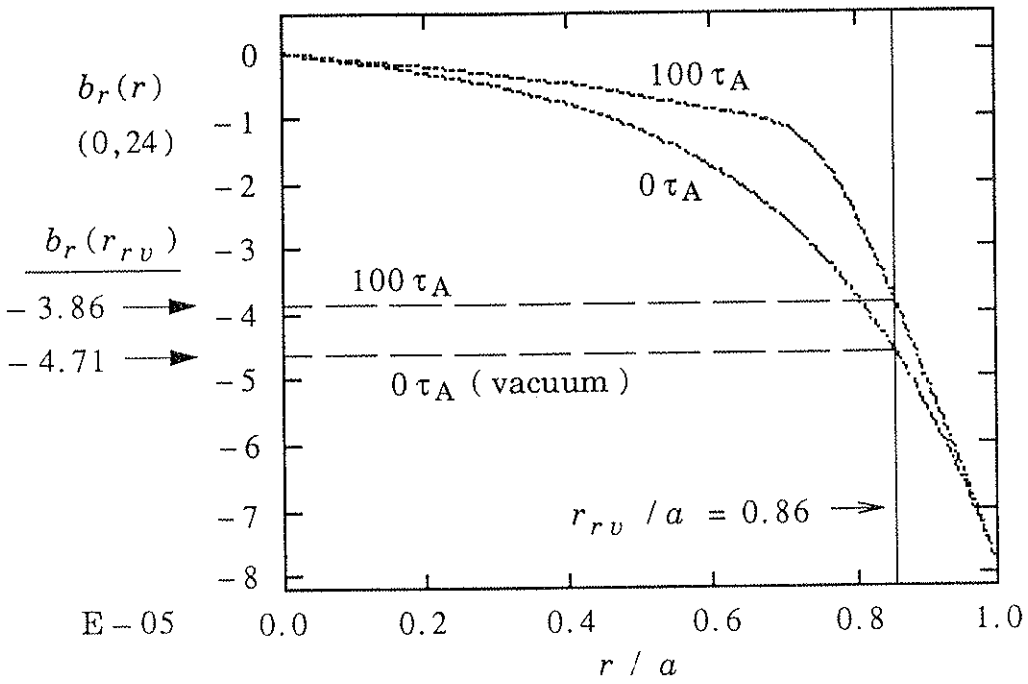

Figure 4.5 Radial profile of a (0 , 24) b_r perturbation (imaginary part), before ($t = 0\ \tau_A$) and after ($t = 100\ \tau_A$) interaction with the plasma. The value of $|b_r(r_{rv})|$ is decreased.

(3.3.1). For modes with m = 0, it is the magnetic surface, at radius r_s, where

$$F = \mathbf{k} \cdot \mathbf{B}_0 = nkB_{z0} = 0 \ . \qquad (4.3.1)$$

This is obviously the radial location of the reversal surface r_{rv}, where B_{z0} goes through zero. Thus, for the remainder of this chapter, $r_s = r_{rv}$. Figure 4.5 shows the radial profile of b_r for a perturbation with toroidal mode number n = 24 before the introduction of the plasma (vacuum profile) and after. The reduction at the reversal surface is indicated. The value of this reduction, in the case shown, is about 18%. As indicated in Chapter 2, the amount of this reduction varies with the value of η and ν_0.

The behavior of the perturbations as η and ν_0 are varied is an important source of information on the profile changes caused by finite η, ν_0. During the work on the scaling of the reduction in $|b_r(r_{rv})|$ for Chapter 2, it became apparent that as η and ν_0 were varied the shapes of the profiles of magnetic field and velocity perturbations remained basically the same, while the amplitudes of these perturbations varied. To be more specific, in all the cases, the general shape of the profile— the number of peaks and valleys and their relative positions and sizes — remained the same. The magnitude of the perturbation at a specific point, and the radial location of this point, did change as η and ν_0 were varied. An example of this is shown in Figure 4.6, which compares profiles of $b_\theta(0,24)$ for cases in which ν_0 differs by a factor of sixteen.

These observations show that it is reasonable to assume that the velocity and magnetic field perturbation profiles have a self-similar form. That is, it is consistent with the data to represent a general perturbation as

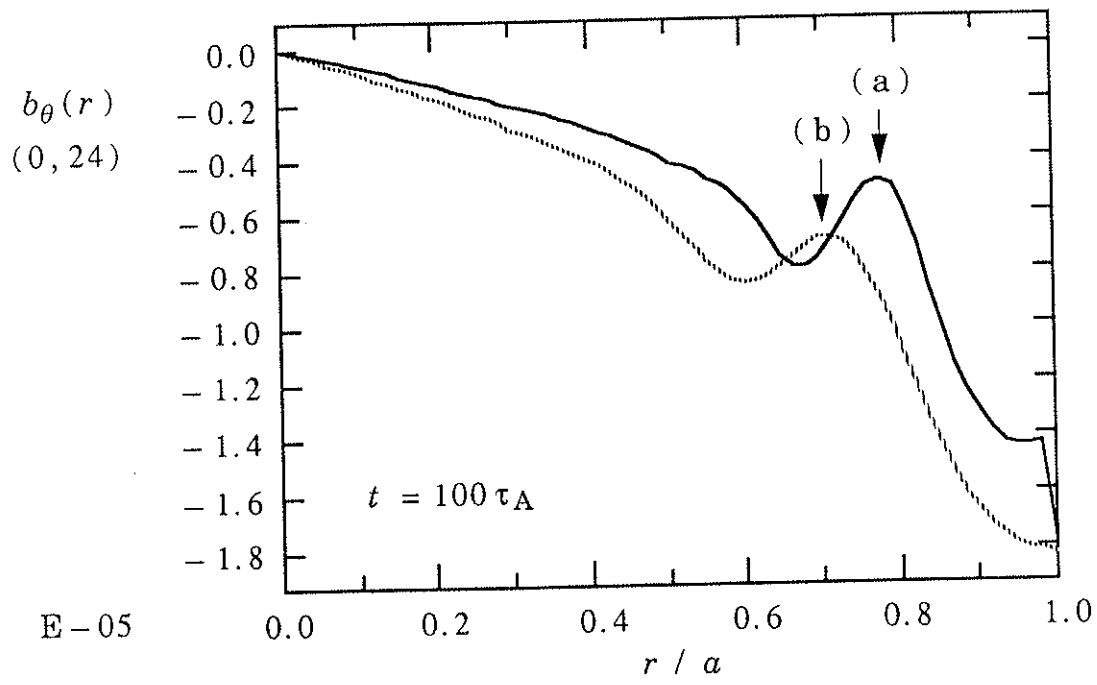

Figure 4.6 Radial profiles of a (0 , 24) b_θ perturbation (real part) for two different values of ν_0. Profile (a) is for rhocon = 0.5 and profile (b) is for rhocon = 8. (Equation (2.3.10) shows the linear relationship between rhocon and ν_0.) The profiles exhibit the same general features.

$$p_{m,n}(r\,;\eta,\nu_0) = P_{m,n}(\eta,\nu_0)\, f\left(\frac{r}{\Re}\right), \qquad (4.3.2)$$

where $P_{m,n}(\eta,\nu_0)$ is an amplitude function that carries the scaling information, f is an invariant profile shape, and $\Re = \Re_{m,n}(\eta,\nu_0)$ is a variable scale length that determines the radial location of the profile

features. Thus, the use of finite η, ν_0 changes the perturbation profiles by introducing a physical effect which occurs on a particular length scale.

An analysis of the computer results was performed to identify the amplitude functions for the various perturbations. The simplest kind of power law was sought: $B_{m,n}(\eta, \nu_0) = S^a \nu_0{}^b$ for magnetic perturbations, and $V_{m,n}(\eta, \nu_0) = S^c \nu_0{}^d$ for velocity perturbations. The quantity $S \sim 1/\eta$ was used as the resistivity variable because that was the "knob" available in the 3-D MHD code. A single point that could be readily identified as S and ν_0 changed was chosen for each perturbation profile. For the profile of b_r, the point $r = r_{rv}$ was chosen, since $|b_r(r_{rv})|$ is the quantity of interest. For the profiles of the other components of b, the relative minimum in absolute value was chosen. (These profiles show a general increase in absolute value with r.) For all the components of v, the point of maximum absolute value was used. The value of the perturbation at this point was then recorded for the computer runs in which S was varied at fixed ν_0. These values were then plotted as a function of S on a log-log plot. The slope of that plot was identified as the exponent "a," for a magnetic perturbation, and "c," for a velocity perturbation. The same analysis was performed on the data from the runs in which ν_0 was varied at fixed S to find the exponents "b" and "d." The results for both magnetic and velocity perturbations are given in tables on the following two pages.

Table 4.1: $B_{m,n}(\eta, \nu_0) = S^a \nu_0{}^b$				
m , n	COMPONENT	a	b	| (a + b) / b |
0 , 12	r	– 0.071	0.058	22.4 %
	θ	– 0.223	0.229	2.6 %
	z	– 0.331	0.312	6.1 %
0 , 24	r	– 0.039	0.030	30.0 %
	θ	– 0.159	0.148	7.4 %
	z	– 0.163	0.111	46.8 %

The results summarized in the tables illustrate that the physical effect introduced by finite η, ν_0 also imposes a particular relationship between the velocity and magnetic fields. The amplitude function for each type of perturbation depends on both η and ν_0. The role that velocity plays in the physical effect determining these functions is represented by viscosity, since viscosity acts to damp velocity. The same can be said for the magnetic field and the resistivity. Table 4.2 shows that even though the scaling exponents for resistivity and viscosity vary with the component of the velocity perturbation and the mode number, they always add up to –1 for velocity perturbation amplitudes, to within a few percent. Table 4.1 shows shows that, with somewhat less accuracy, a similar statement can be

Table 4.2: $V_{m,n}(\eta, \nu_0) = S^c \nu_0{}^d$				
m , n	**COMPONENT**	**c**	**d**	**c + d**
0 , 12	r	– 0.397	– 0.604	– 1.001
	θ	– 0.538	– 0.492	– 1.030
	z	– 0.292	– 0.707	– 0.999
0 , 24	r	– 0.348	– 0.642	– 0.990
	θ	– 0.472	– 0.562	– 1.034
	z	– 0.250	– 0.747	– 0.997

made about the scaling exponents for magnetic field perturbation amplitudes summing to zero. These relationships between the dissipation coefficients are evidence of a physical mechanism linking velocity to magnetic field in a particular way.

The physical effects brought into play by the inclusion of finite grad$-\lambda$ and finite η, ν_0 can be explored using the picture developed previously in Chapter 3, Section 3.3 . Recall that the presence of finite grad$-\lambda$ changes the current perturbation to include perturbed current flowing along equilibrium field lines. The current perturbation is related to the second derivative of the radial magnetic field (see equation

(3.3.12)), and the addition further bends the radial magnetic field profile, causing an increase in $|b_r(r_{rv})|$. The relevant equations are (3.3.8), which gives the current perturbation and is here reproduced as

$$\mathbf{j} = \left(\frac{\lambda(r)}{\mu_0}\right)\mathbf{b} + \left(\frac{g}{\mu_0}\right)\mathbf{B}_0 , \tag{4.3.3}$$

and (3.3.9), which defines the additional perturbed current—g —and is here given as

$$\mathbf{b}\cdot\nabla\left(\frac{\lambda(r)}{\mu_0}\right) + \mathbf{B}_0\cdot\nabla\left(\frac{g}{\mu_0}\right) = 0 . \tag{4.3.4}$$

These two can be combined using equation (3.4.7):

$$\mathbf{j} = \left(\frac{\lambda(r)}{\mu_0}\right)\mathbf{b} - i\,b_r\left(\frac{\lambda'}{\mu_0 F}\right)\mathbf{B}_0 . \tag{4.3.5}$$

The difference between the case of a perturbation with m = 1 and the case of the perturbations with m = 0 lies in the function F. In Section 3.3, it was stated that the resonant surface for the m=1 mode under consideration — that is, the place where $F = 0$ — lay outside of the region of finite λ'. In the case of the m=0 modes, it was stated in the beginning of this section that F has a zero at the reversal surface. For the values given in Table 3.1, $r_n < r_{rv} < a$ and the reversal surface lies in the region of finite λ'. (See (3.4.12) for λ'.) It appears that the additional perturbed current has a singularity at $r = r_{rv}$. Equation (4.3.1) can be used to clarify this point. Substituting for F in (4.3.5) gives:

$$\mathbf{j} = \left(\frac{\lambda(r)}{\mu_0}\right)\mathbf{b} \; - \; i\,b_r \left(\frac{\lambda'}{\mu_0 n k}\right)\frac{\mathbf{B}_0}{B_{z\,0}} \; . \qquad (4.3.6)$$

The $z-$component of this equation is finite, since the dependence on $B_{z\,0}$ cancels out. The $\theta-$component has a term $B_{\theta_0}/B_{z\,0}$. This component does have a singularity at $r = r_{rv}$, since $B_{z\,0}$ goes to zero there and B_{θ_0} does not. Thus, as r approaches r_{rv}, the additional perturbed current introduced by finite grad$-\lambda$ goes to infinity; the profile of b_r is very strongly bent away from $b_r = 0$. This accounts for the bending and stretching of the profile with the introduction of finite grad$-\lambda$ that was referred to in Section 4.2. Obviously, an infinite current cannot be permitted. Another source of perturbed current near $r = r_{rv}$ must be found to resolve the singularity.

Physical effects introduced by finite η provide the new perturbed current which is needed. A simple description of the physical process can be sketched using the linearized form of some of the MHD equations from Chapter 1. It is useful to restate the problem here: the $\theta-$component of the perturbed current,

$$j_\theta \; = \left(\frac{\lambda(r)}{\mu_0}\right) b_\theta \; - \; i\,b_r \left(\frac{\lambda'}{\mu_0 n k}\right)\frac{B_{\theta\,0}}{B_{z\,0}} \; , \qquad (4.3.7)$$

has a singularity at $r = r_{rv}$, where $B_{z\,0}$ goes to zero. The effect of a finite resistivity can be found by looking at a slightly rearranged form of the $\theta-$component of the linearized Ohm's law:

$$j_\theta = \frac{e_\theta - v_r B_{z0}}{\eta} . \tag{4.3.8}$$

In steady state, it should be noted that:

$$e_\theta = -(\nabla \phi)_\theta = \left(\frac{im}{r} \phi\right) = 0 , \tag{4.3.9}$$

for modes with m=0. So, for the situation being considered, a radial velocity perturbation gives rise to a current perturbation:

$$j_\theta = \frac{- v_r B_{z0}}{\eta} . \tag{4.3.10}$$

Associated with this current perturbation is a perturbed force which opposes the radial velocity perturbation:

$$f_r\,(restoring) = j_\theta B_{z0} = \frac{- v_r B_{z0}^2}{\eta} . \tag{4.3.11}$$

In the case of $\eta = 0$, any radial velocity perturbation encounters an infinite force pushing back on it. The only possible outcome is $v_r = 0$ and $j_\theta = 0$. However, if $\eta \to 0$, the restoring force is still large enough to force v_r to zero, except in a region around the point where B_{z0} goes to zero. Here, the effect of the small denominator is balanced by a small numerator to make this restoring force finite. A finite force can be overcome, and a radial velocity perturbation can exist in this region. Equation (4.3.10) shows that j_θ can exist there as well. Thus, a small, but finite, resistivity permits an additional perturbed current in the θ-direction in the vicinity of $r = r_{rv}$.

This is precisely what is needed to smooth out the singularity in j_θ indicated in equation (4.3.7). As a result, the bending of the b_r profile is reduced, resulting in the observed reduction in $|b_r(r_{rv})|$ cited at the beginning of this section. In addition, since the effect is only important in a region of a certain size, a length scale is introduced into the problem. This is consistent with the observation made in the scaling analysis after equation (4.3.2).

The role of finite ν_0 lies in providing the force which drives the radial velocity perturbation mentioned above. The v_r needed to provide j_θ is opposed by the force given in equation (4.3.11). This force must be balanced by a force which can drive v_r, or else the velocity perturbation will be stopped and the current perturbation lost. This force is provided in the following rather roundabout way. There are axial velocity perturbations (v_z) which arise in conjunction with the radial velocity perturbations. (For example, only incompressible perturbations will be considered later.) The r-component of the steady-state, linearized momentum equation with finite ν_0 gives:

$$j_r = -\nu_0 \left(\frac{\nabla^2 v_z}{B_{\theta 0}} \right) . \qquad (4.3.12)$$

The effect of this current must be considered in light of equation (3.3.10). Recall that the interpretation of this equation was that there are no sources of perturbed current. Thus, the flow of perturbed current off of equilibrium field lines represented by equation (4.3.12) must be balanced by

the flow of current along equilibrium field lines. In particular, an axial current perturbation (j_z) is created. This results in a force

$$f_r\,(driving\,) \;=\; -j_z\,B_{\theta 0} \qquad (4.3.13)$$

which then can drive the radial velocity perturbation. There is a delicate balance between current perturbations (or magnetic field perturbations, by (3.4.2)) and velocity perturbations. This makes for the particular relationship between the magnetic and velocity fields reflected in the behavior of the scaling exponents in the perturbation amplitudes, as mentioned after Table 4.2 .

The discussion of the physical effects introduced by finite η, ν_0 presented in the above two paragraphs is based directly on a similar discussion about the physical mechanisms involved in finite-resistivity instabilities. The notions of restoring forces which become finite in a region around a field null and of driving forces which balance them come from Section VI of the classic paper by Furth, Killeen, and Rosenbluth.[4] Here, they have been applied to a steady-state case, where viscosity couples the linearized momentum equation to the linearized Ohm's law, rather than an instability growth rate. Some justification for using such an argument in this case may perhaps be found in the appearance of the fractional scalings in Tables 4.1 and 4.2 . Fractional scalings appear in the expressions for the growth rates and length scales of resistive instabilities.

In summary, the physical picture which has been developed to this point can be used to explain the observed behavior of the 3-D MHD code results. It was observed at the end of Section 4.2 that the introduction of finite η, ν_0 alters the magnetic perturbation profiles, and that the further introduction of finite grad-λ amplifies the effect. This can be explained as follows. The use of finite η, ν_0 allows the generation of additional perturbed currents around the reversal surface. These change the ways in which the magnetic field perturbation profiles bend, causing the b_z profile to "turn over" and the b_r profile to change in such a way as to produce a modest reduction of $|b_r(r_{rv})|$. The further addition of finite grad-λ introduces a singularity in the θ-component of the perturbed current at the reversal surface. The magnetic field profiles bend drastically in response. The smoothing effect of finite η, ν_0 on these profiles is now much more dramatic. A small bend in a magnetic field perturbation profile in the middle of a region of very large slope (the current is the curl of the field) can greatly change the profile shape. An effect such as this can account for the enhanced reduction of $|b_r(r_{rv})|$. Once again, the physical picture used to explain these results must be backed up by the actual solution of the equations to verify that the suggested "bending" occurs in the proper way. This will be taken up in the following sections.

4.4 TIME-INDEPENDENT, LINEARIZED MHD EQUATIONS

The new importance of finite η, ν_0, as well as finite grad-λ, requires the return to the MHD equations of Chapter 1. In this way, the

new terms can be properly incorporated into the derivation of the necessary equations. At this point, the only approximation which is used is that of time-independence.

The time-independent resistive MHD equations with finite fluid (ion) viscosity are:

$$\mathbf{E} = -\mathbf{V}\times\mathbf{B} + \eta\,\mathbf{J} \tag{4.4.1}$$

$$\nabla\times\mathbf{E} = 0 \tag{4.4.2}$$

$$\rho\left(\mathbf{V}\cdot\nabla\right)\mathbf{V} = \mathbf{J}\times\mathbf{B} + \nu_0\nabla^2\mathbf{V} \tag{4.4.3}$$

$$\mu_0\,\mathbf{J} = \nabla\times\mathbf{B} \tag{4.4.4}$$

$$\nabla\cdot\mathbf{B} = 0\ . \tag{4.4.5}$$

These equations can now be linearized. As in Chapter 3, Section 3.2, the variables are first decomposed into equilibrium parts and perturbed parts.

VARIABLE		EQUILIBRIUM		PERTURBATION
$\mathbf{J}$	=	$\mathbf{J}_0$	+	$\mathbf{j}$
$\mathbf{B}$	=	$\mathbf{B}_0$	+	$\mathbf{b}$
$\mathbf{V}$	=	$\mathbf{0}$	+	$\mathbf{v}$
$\mathbf{E}$	=	$\mathbf{0}$	+	$-\nabla\phi$

(Note that the choice $\mathbf{e} = -\nabla\phi$ for the electric field perturbation solves equation (4.4.2) and removes this equation from further consideration.) Terms to first order in the perturbation are retained. The left side of (4.4.3) is second-order in $\mathbf{v}$ and is thus be neglected. Equilibrium currents can be removed from the problem in favor of the λ-profile by using the equilibrium relation for the case of finite grad-λ, given in equation (3.3.6). That is,

$$\mathbf{J}_0 = \left(\frac{\lambda(r)}{\mu_0}\right)\mathbf{B}_0 \ . \tag{4.4.6}$$

Using (4.4.6), the momentum equation — (4.4.3) — can be written in linear form as

$$\left(\mathbf{j} - \frac{\lambda(r)}{\mu_0}\mathbf{b}\right) \times \mathbf{B}_0 + \nu_0 \nabla^2 \mathbf{v} = 0 \tag{4.4.7}$$

and Ohm's law — (4.4.1) — can be written as:

$$\nabla\phi = \mathbf{v} \times \mathbf{B}_0 - \eta\,\mathbf{j} \ . \tag{4.4.8}$$

The other equations necessary are the equilibrium and perturbed parts of (4.4.4):

$$\mu_0 \mathbf{J}_0 = \nabla \times \mathbf{B}_0 \tag{4.4.9}$$

$$\mu_0 \mathbf{j} = \nabla \times \mathbf{b} \tag{4.4.10}$$

and the equilibrium and perturbed parts of (4.4.5):

$$\nabla \cdot \mathbf{B}_0 = 0 \tag{4.4.11}$$

$$\nabla \cdot \mathbf{b} = 0 \, . \tag{4.4.12}$$

Equations (4.4.6) – (4.4.12) can be combined to produce two coupled equations for **b** and **v**. The perturbed current can be replaced in (4.4.7) using (4.4.10). This yields the first of the two equations, which is the final form of the original momentum equation:

$$\frac{1}{\mu_0} \left(\nabla \times \mathbf{b} - \lambda(r)\, \mathbf{b} \right) \times \mathbf{B}_0 = -\nu_0 \nabla^2 \mathbf{v} \, . \tag{4.4.13}$$

The second equation can be found from (4.4.8) by the elimination of the electrostatic potential ϕ . Taking the curl of (4.4.8), and using (4.4.10) – (4.4.12) and some vector identities, yields:

$$-\mathbf{B}_0 \left(\nabla \cdot \mathbf{v} \right) + \left(\mathbf{B}_0 \cdot \nabla \right) \mathbf{v} - \left(\mathbf{v} \cdot \nabla \right) \mathbf{B}_0 = -\left(\frac{\eta}{\mu_0} \right) \nabla^2 \mathbf{b} \, . \tag{4.4.14}$$

This is the final form of the original Ohm's law. Equations (4.4.13) and (4.4.14) will be used in what follows to find the perturbed fields and velocities. Once **b** and **v** have been found, the electrostatic potential can be found. For completeness, the equation for ϕ will be given. Taking the divergence of equation (4.4.8), and using (4.4.6), (4.4.9), (4.4.10), and some more vector identities, gives:

$$\nabla^2 \phi = \left(\nabla \times \mathbf{v} - \lambda(r)\, \mathbf{v} \right) \cdot \mathbf{B}_0 \, . \tag{4.4.15}$$

The two coupled vector equations for **b** and **v** derived above are equivalent to a set of six coupled scalar equations for the components of these vectors. To derive the scalar equations, the spatial behavior of the perturbed quantities and the equilibrium fields must be specified. The geometry chosen is again that of a periodic cylinder of length $2\pi R$. The spatial dependence of a perturbation in the two periodic directions, θ and z, can then be Fourier analyzed, and the individual Fourier modes found separately. The perturbations of interest in this chapter have poloidal mode number m = 0, and can be described by:

$$\mathbf{b}(\mathbf{r}) = \mathbf{b}(r)\, e^{-inkz} \tag{4.4.16}$$

and

$$\mathbf{v}(\mathbf{r}) = \mathbf{v}(r)\, e^{-inkz} , \tag{4.4.17}$$

where n is the toroidal mode number and the wavenumber k is the axial fundamental: $k = 1/R$. The equilibrium fields are given by

$$\mathbf{B}_0(r) = B_{\theta 0}(r)\,\hat{\theta} + B_{z0}(r)\,\hat{z} , \tag{4.4.18}$$

and obey an equation found by combining (4.4.6) and (4.4.9):

$$\nabla \times \mathbf{B}_0 = \lambda(r)\, \mathbf{B}_0 . \tag{4.4.19}$$

It is also useful to make the following definitions:

$$' \equiv \frac{\partial}{\partial r} \qquad \text{and} \qquad \nabla^2 \equiv \frac{1}{r}\frac{\partial}{\partial r}\left(r \frac{\partial}{\partial r} \right) - n^2 k^2$$

and keep in mind the definition of F from equation (4.3.1) . With this information, the six coupled scalar equations are found to be:

$$iF v_r = \frac{\eta}{\mu_0}\left[\nabla^2 b_r - \frac{b_r}{r^2}\right] \tag{4.4.20}$$

$$B_{\theta 0} v_z - B_{z 0} v_\theta = \left(\frac{B_{\theta 0}}{ink}\right) v_r' + \frac{1}{ink}\left[-\frac{B_{\theta 0}}{r} + \lambda B_{z 0}\right] v_r - \frac{\eta}{ink\mu_0}\left[\nabla^2 b_\theta - \frac{b_\theta}{r^2}\right] \tag{4.4.21}$$

$$\frac{1}{r}(r b_r)' = ink\, b_z \tag{4.4.22}$$

$$-iF b_r - \left[\frac{B_{\theta 0}}{r}(r b_\theta)' + B_{z 0}\lambda b_\theta\right] - \left[B_{z 0} b_z' - \lambda B_{\theta 0} b_z\right] = -\mu_0 \nu_0\left[\nabla^2 v_r - \frac{v_r}{r^2}\right] \tag{4.4.23}$$

$$-B_{z 0}\left[ink\, b_\theta - \lambda b_r\right] = -\mu_0 \nu_0\left[\nabla^2 v_\theta - \frac{v_\theta}{r^2}\right] \tag{4.4.24}$$

$$B_{\theta 0}\left[ink\, b_\theta - \lambda b_r\right] = -\mu_0 \nu_0\left[\nabla^2 v_z\right]. \tag{4.4.25}$$

The first equation is the r-component of the curl of Ohm's law, (4.4.14), and the second equation is the θ-component. The z-component of (4.4.14) is a linear combination of the r-component and the relation $\nabla \cdot \mathbf{b} = 0$. Of the r-component, z-component and $\nabla \cdot \mathbf{b} = 0$, only two are independent. The simpler expression — $\nabla \cdot \mathbf{b} = 0$ — was chosen over the z-component and is shown as the third equation. The last three

equations are the r, θ, and z–components of the momentum equation, (4.4.13), respectively.

This set of equations can be simplified greatly by assuming that the velocity perturbations are incompressible. This assumption can be justified for the case of the computer results under consideration in an *ad hoc* way. The code simulates a zero–beta plasma. That is, the particle pressure of the plasma is neglected. After being exposed to the perturbed magnetic fields arising from field errors, and thus perturbed forces, the plasma settles back down into force balance. In the absence of plasma pressure, the velocity perturbations that have arisen cannot couple to sound waves that compress the plasma. It may thus be reasonable to assume that the velocity perturbations are incompressible.

The best way to confirm the assumption of incompressibility is to perform a numerical test. An incompressible velocity perturbation obeys the equation:

$$\nabla \cdot \mathbf{v} = 0 \ . \tag{4.4.26}$$

For a perturbation with m = 0, this can be written as:

$$v_z = \frac{1}{ink}\left(v_r' + \frac{v_r}{r}\right) . \tag{4.4.27}$$

Equation (4.4.27) expresses a simple relationship between v_z and v_r. A look at equations (4.4.20)–(4.4.25) shows that the coupling between all the variables is quite involved. No relation between v_z and v_r as simple as

(4.4.27) is apparent. A logical test of the incompressibility assumption would be to use the values of v_r in the code results to calculate v_z from (4.4.27). This result would then be compared to the v_z produced by the code, presumably obtained by solving (4.4.20) – (4.4.25). If the two agree reasonably well, then the velocity perturbations can be taken to be incompressible. The results of such a test are shown below, in Figure 4.7 .

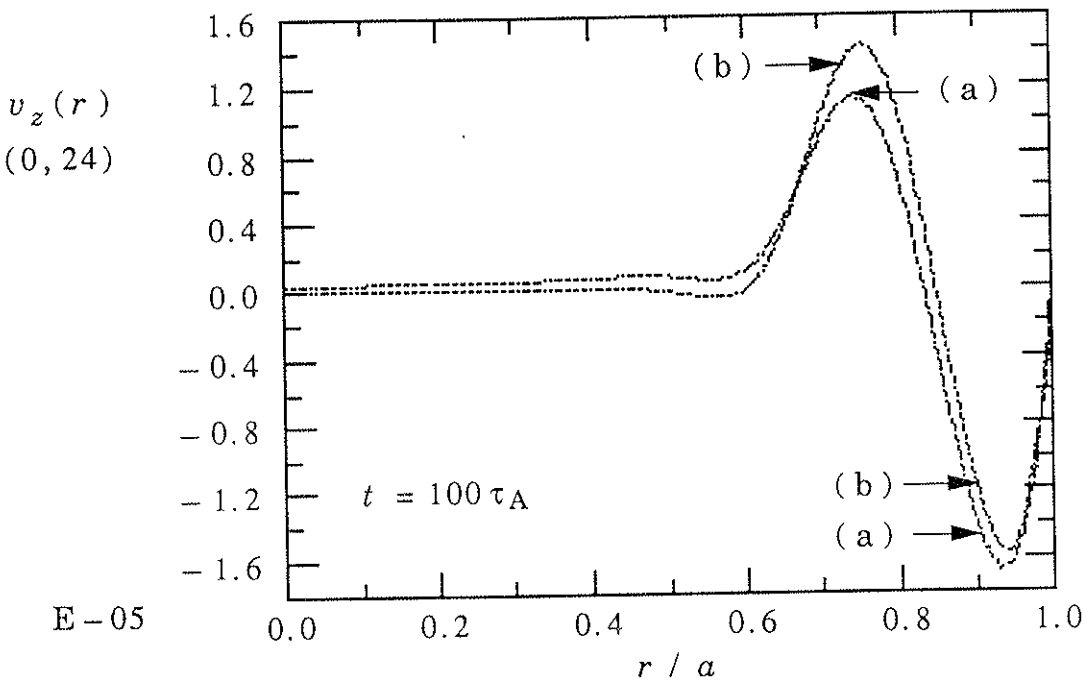

Figure 4.7 Radial profiles of a (0, 24) v_z perturbation (imaginary part) calculated as a test of the incompressibility assumption. Profile (a) was calculated from the full set of equations in the 3 – D MHD code and profile (b) was calculated using $\nabla \cdot \mathbf{v} = 0$. The good agreement between the profiles indicates that incompressibility is a reasonable assumption.

There is good agreement between the profiles. The values agree to within 20%, on the average. Thus, incompressibility will be considered a good assumption.

The mathematical statement of incompressibility, equation (4.4.27), can be added to the set of equations to be solved, and another equation can be removed. This greatly simplifies matters. The addition of an explicit relationship between v_z and v_r decouples v_θ from the problem. The largest terms in equation (4.4.21) near the reversal surface, where the velocity is expected to be important, are those proportional to $B_{\theta 0}$. When (4.4.27) is added to the set of equations, these largely cancel out. Some residual terms remain, including one involving v_θ. The numerical test performed above shows that these terms don't play a great role. Thus, equation (4.4.21) can be ignored and v_θ can be determined entirely from v_z through a combination of equations (4.4.24) and (4.4.25).

With the changes outlined above, and some judicious rearranging, the set of coupled equations can be written in the following instructive form:

$$iF v_r = \frac{\eta}{\mu_0}\left[\nabla^2 b_r - \frac{b_r}{r^2}\right] \tag{4.4.28}$$

$$-iF b_r - \left[\frac{B_{\theta 0}}{r}(r b_\theta)' + B_{z0}\lambda b_\theta\right] - \left[B_{z0} b_z' - \lambda B_{\theta 0} b_z\right] = -\mu_0 v_0\left[\nabla^2 v_r - \frac{v_r}{r^2}\right] \tag{4.4.29}$$

$$b_\theta = \left(\frac{\lambda}{ink}\right) b_r - \left(\frac{\mu_0 v_0}{ink B_{\theta 0}}\right) \nabla^2 v_z \tag{4.4.30}$$

$$v_z = \frac{1}{ink}\left(v_r' + \frac{v_r}{r}\right) \tag{4.4.31}$$

$$b_z = \frac{1}{ink}\left(b_r' + \frac{b_r}{r}\right) \tag{4.4.32}$$

$$\nabla^2 v_\theta - \frac{v_\theta}{r^2} = -\left(\frac{B_{z0}}{B_{\theta 0}}\right) \nabla^2 v_z \, . \tag{4.4.33}$$

When equations (4.4.30) – (4.4.32) are substituted into equation (4.4.29), the five coupled equations (4.4.28) – (4.4.32) reduce to two coupled equations for v_r and b_r. These are precisely the quantities that are of interest. The behavior of the radial magnetic field perturbation has been the motivation for the entire study. It was shown in the previous section that the presence of a finite radial velocity perturbation near the reversal surface allows a perturbed current to flow and that this current has a strong effect on the profile of the radial magnetic field. Once v_r and b_r have been found, the other perturbed quantities can be derived from equations (4.4.30) – (4.4.33).

The problem of solving the time – independent, linearized, resistive MHD equations has now been reduced to the problem of solving two coupled ordinary differential equations. The first of these equations for v_r and b_r is equation (4.4.28). The second can be found from equations (4.4.29) – (4.4.32). The set of equations which finally emerges, after a large

amount of algebra, is given below. (Note that a superscript in parenthesis stands for the number of derivatives with respect to r : ${v_r}^{(4)} \equiv {v_r}''''$.)

$$
\begin{aligned}
{b_r}^{(2)} + \frac{1}{r}\,{b_r}^{(1)} + \left[\left(\lambda^2 - n^2 k^2 - \frac{1}{r^2} \right) - \left(\frac{\lambda' F'}{\lambda F} \right) \right] b_r \qquad (4.4.34) \\
= \frac{\mu_0 v_0}{iF} \left[{v_r}^{(4)} + \frac{4}{r}\,{v_r}^{(3)} + \left(\frac{1}{r^2} - 2n^2 k^2 \right) {v_r}^{(2)} + \right. \\
\left. \left(\frac{1}{r^3} - \frac{4n^2 k^2}{r} \right) {v_r}^{(1)} + \left(n^4 k^4 + \frac{n^2 k^2}{r^2} - \frac{1}{r^4} \right) v_r \right]
\end{aligned}
$$

$$
v_r = \frac{\eta}{iF\mu_0} \left[{b_r}^{(2)} + \frac{1}{r}\,{b_r}^{(1)} - \left(n^2 k^2 + \frac{1}{r^2} \right) b_r \right] \qquad (4.4.35)
$$

Although these equations only involve the perturbations of interest, the system is still sixth order, equivalent to the original six equations — (4.4.28) through (4.4.33). In order to make progress towards a solution, some approximations must be made to reduce the order to a manageable number.

The most useful assumption is that of small resistivity and viscosity. At the temperatures of most laboratory plasmas, the resistivity is small enough to ensure that the resistive evolution of magnetic field profiles occurs on a time scale much longer (six to eight orders of magnitude) than any changes due to convection. For a viscosity which represents the rate of momentum transport across field lines, the rate of viscous evolution of velocity profiles is also many orders of magnitude slower than the rate of change caused by magnetic forces. If the fluid viscosity in the code is interpreted as a rate of momentum transport across

field lines, an assumption of small η, ν_0 is reasonable. Given such an assumption, the right sides of equations (4.4.34)–(4.4.35) can be ignored, for the most part. These terms are proportional to (η/F) or (ν_0/F), however, and do become important in a region around $r = r_{rv}$, where $F \to 0$. Since η, ν_0 are small, this region should also be small. This behavior is evident in the profile of $v_r(0,24)$ calculated by the 3–D MHD code, shown in Figure 4.8. As predicted by equation (4.4.35), the value of v_r is zero except in a region centered about $r = r_{rv}$. This region is rather large, since the values of η, ν_0 used in the code are relatively large. To facilitate the calculation, however, the values of η, ν_0 will be assumed to be small enough to be considered to lowest order. Then, their effects are limited to a

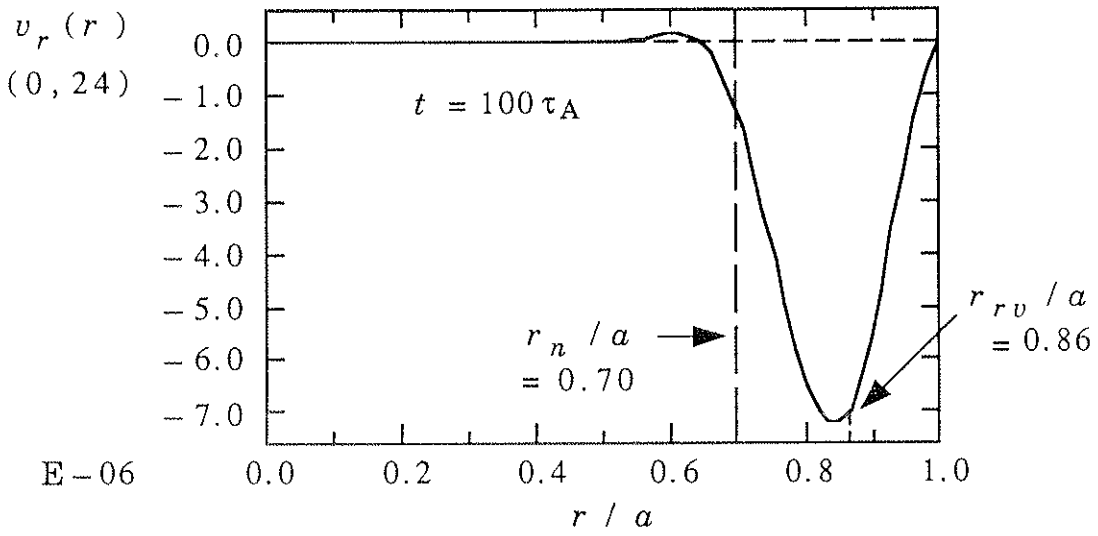

Figure 4.8 Radial profile of a (0, 24) v_r perturbation (real part). The perturbation is only non–zero in a limited region centered near the reversal surface ($r = r_{rv}$).

very thin "dissipative layer" (so called because of the importance of the small, but finite, dissipation — η, ν_0), within which they are constant. By this assumption, the problem is divided into two parts: the equations in the region where η, ν_0 can be ignored and the equations in the "dissipative layer."

4.4a Equations in the "Outer Region"

The region in which η, ν_0 can be ignored will be referred to as the "outer region." This is in keeping with the terminology of boundary layer theory and asymptotic matching,[5,6] which will be used in Section 4.5 to solve the complete problem. "Outer" basically means that the plasma acts under the simple influence of convection and force balance, and is "outside" the influence of the more complex dissipation processes.

The equations in the "outer region" are given by (4.4.34) – (4.4.35) with the right sides neglected. They are reproduced as follows:

$$b_r^{(2)} + \frac{1}{r} b_r^{(1)} + \left[\left(\lambda^2 - n^2 k^2 - \frac{1}{r^2} \right) - \left(\frac{\lambda' F'}{\lambda F} \right) \right] b_r = 0 \qquad (4.4.36)$$

$$v_r = 0 \, . \qquad (4.4.37)$$

The approximation of small η, ν_0 has reduced the order of the equations to two in this region. Equation (4.4.36) is precisely equation (3.4.8) for a force-free perturbation with: m = 0, F given by equation (4.3.1), and F' found from equation (4.4.19). The mathematical difficulties, and interesting physical effects, are contained in the last term in the bracket.

The behavior of this term divides the "outer region" itself into two sub-regions, depending on whether or not $\lambda' = 0$.

The sub-region in which $\lambda' = 0$ is called the constant-λ region. According to (3.4.12), this region consists of $0 \le r \le r_n$. Table 3.1 shows that the reversal surface does not lie in this range. Thus, the (λ'/F) term is everywhere determined and equal to zero. The equation for b_r in this region is:

$$b_r^{(2)} + \frac{1}{r} b_r^{(1)} + \left[\lambda_0^2 - n^2 k^2 - \frac{1}{r^2} \right] b_r = 0 . \qquad (4.4.38)$$

The sub-region in which $\lambda' \neq 0$ is called the finite grad-λ region. According to (3.4.12), this region consists of $r_n < r \le a$. The reversal surface does lie within this range, and the behavior of the solution is governed by the (λ'/F) singularity. It turns out that it is simpler to first solve the equation for b_z in this region and then relate this perturbation to b_r. The relevant equations follow:

$$b_z^{(2)} + \left[\frac{1}{r} - \frac{\Xi'}{\Xi} \right] b_z^{(1)} + \Xi b_z = 0 , \qquad (4.4.39)$$

with

$$\Xi = \lambda(r)^2 - n^2 k^2 + \left(\frac{k r}{q} \right) \lambda' \qquad (4.4.40)$$

$$b_r = \left(\frac{i n k}{\Xi} \right) b_z^{(1)} , \qquad (4.4.41)$$

and q defined in equation (3.4.13).

4.4b Equations in the "Inner Region"

The "inner region" refers to the area "inside" the dissipative layer, where the effects of finite η, ν_0 are important. The perturbations inside the layer are described by equations (4.4.34)–(4.4.35), in their entirety. These can be simplified somewhat by using (4.4.35) to remove the higher derivatives of b_r in (4.4.34). The resulting equations are:

$$\frac{\mu_0 \nu_0}{iF}\left[\left(v_r^{(4)} + \frac{F^2}{\nu_0 \eta} v_r\right) + \frac{4}{r} v_r^{(3)} + \left(\frac{1}{r^2} - 2n^2k^2\right) v_r^{(2)} + \left(\frac{1}{r^3} - \frac{4n^2k^2}{r}\right) v_r^{(1)} + \left(n^4k^4 + \frac{n^2k^2}{r^2} - \frac{1}{r^4}\right) v_r\right] = \left[\lambda^2 - \left(\frac{\lambda' F'}{\lambda F}\right)\right] b_r \tag{4.4.42}$$

$$v_r = \frac{\eta}{iF\mu_0}\left[b_r^{(2)} + \frac{1}{r} b_r^{(1)} - \left(n^2k^2 + \frac{1}{r^2}\right) b_r\right] \tag{4.4.43}$$

It has been assumed that the layer is very thin. Inside such a layer, the radius variable r can be replaced by a small variable representing the distance from the center of the layer: $x = r - r_s$. (The center of the layer is the resonant surface (r_s) for m = 0 modes, where $F = 0$. As was pointed out at the beginning of Section 4.3, this surface is also the reversal surface (r_{rv}), where $B_{z0} = 0$.) The functions of radius can be expanded in x. The advantage of a very thin layer is that the coefficients in the equations will

not vary appreciably and only the lowest order term in their expansion need be kept. As a result:

$$\begin{aligned} F \rightarrow \left(F'(r_s)\right)x &= F_s' x \\ r &\rightarrow r_s \\ \lambda \rightarrow \lambda(r_s) &= \lambda_s \end{aligned} \qquad (4.4.44)$$

Before introducing this expansion into the equations, it is useful to do some dimensional analysis. Using b for magnetic field, v for velocity, l for a length scale, and $F = lF_s'$:

equation (4.4.42) gives $$\frac{b}{v} \sim \frac{\mu_0 \nu_0}{\left(F_s'\right) l^3} \qquad (4.4.45)$$

and equation (4.4.43) gives $$\frac{b}{v} \sim \frac{\mu_0 \left(F_s'\right) l^3}{\eta} \; . \qquad (4.4.46)$$

Multiplying equations (4.4.45) and (4.4.46) produces the relative scaling of the magnetic and velocity perturbations:

$$b \sim \left(\frac{\nu_0}{\eta}\right)^{\frac{1}{2}} (\mu_0 v) \; . \qquad (4.4.47)$$

Dividing equation (4.4.45) by equation (4.4.46) yields the length scale for the equations:

$$l \sim \left[\frac{\nu_0 \eta}{\left(F_s'\right)^2}\right]^{\frac{1}{6}} \; . \qquad (4.4.48)$$

The information in (4.4.47) and (4.4.48) can be used to simplify the coupled equations. Relation (4.4.47) can be used to express each of the variables in terms of the same dimensional unit. Magnetic field is taken to be the basic unit, and the variables are redefined as follows:

$$\mathrm{B} = b_r \qquad \text{and} \qquad \mathrm{V} = \left(\frac{\nu_0}{\eta}\right)^{\frac{1}{2}} (\mu_0 v_r) \ .$$

The dimensional relation expressed in (4.4.48) is used to define the "layer width" (l), the characteristic size of the dissipative layer:

$$l = \left[\frac{\nu_0 \eta}{|F_s'|^2}\right]^{\frac{1}{6}} = \left[\frac{\nu_0 \eta}{\left(\lambda_s n k B_{\theta 0}(r_s)\right)^2}\right]^{\frac{1}{6}} , \qquad (4.4.49)$$

with $F_s' = -\lambda_s n k B_{\theta 0}(r_s)$ from (4.3.1) and (4.4.19).

The lengths in the problem can be normalized to this basic length. Also, since it contains the small parameters η, ν_0, it can be used as a small parameter for the purposes of expansion.

The coupled equations (4.4.42) – (4.4.43) can now be expanded about the resonant surface, according to the discussion preceding (4.4.44), and written in terms of a single dimensional unit, according to the discussion of the preceding paragraph. The variables and parameters which appear in the equations are defined in the following table.

EXPRESSION	DEFINITION	DIMENSION
Magnetic Field Variable	$B = b_r$	Magnetic Field
Velocity Variable	$V=\left(\frac{\nu_0}{\eta}\right)^{\frac{1}{2}}(\mu_0 v_r)$	Magnetic Field
Layer Position	$x = r - r_s$	Length
Layer Width	$l = \left[\frac{\nu_0 \eta}{\lvert F_s' \rvert^2}\right]^{\frac{1}{6}}$	Length
Normalized Layer Position	$\zeta = x / l$	None
Normalized Layer Width	$l_s = l / r_s$	None
Normalized Axial Scale	$\nu_s = n k r_s$	None
Normalized λ'	$\Lambda_s = \frac{\lvert \lambda' \rvert r_s}{\lambda_s}$	None

Table 4.3

The equations, with dependent variables in terms of magnetic field and dimensionless parameters, are given below:

$$\left(\frac{\partial^4 V}{\partial \zeta^4} + \zeta^2 V \right) + 4 l_s \frac{\partial^3 V}{\partial \zeta^3} + l_s^2 \left(1 - 2 \nu_s^2 \right) \frac{\partial^2 V}{\partial \zeta^2} + l_s^3 \left(1 - 4 \nu_s^2 \right) \frac{\partial V}{\partial \zeta} + l_s^4 \left(\nu_s^4 + \nu_s^2 - 1 \right) V = -i l_s B \left[\Lambda_s + l_s \zeta \left(\lambda_s r_s \right)^2 \right] \quad (4.4.50)$$

$$\frac{\partial^2 B}{\partial \zeta^2} + l_s \frac{\partial B}{\partial \zeta} - l_s^2 \left(1 + \nu_s^2 \right) B = -i \zeta V \quad (4.4.51)$$

These equations are still sixth order, but the presence of a small parameter (l_s) makes an order-reducing expansion possible.

4.5 SOLUTIONS

The attempt to solve for m=0 perturbations by assuming small η, ν_0 has focused attention on two distinct region of solution: the "outer region" and the "inner region." The equations appropriate to each of these regions can be solved separately, within the region. In the "outer region," the equation is a second-order ordinary differential equation. There are many techniques available for studying such a problem. Ironically, the presence of the (λ' / F) singularity greatly aids matters, since an expansion about the point where this term goes to infinity allows many terms to be neglected. In the "inner region," there are two coupled equations, but they can be expanded in terms of the small parameter l_s so that a simplified set can be solved at each order. Once the solutions in the

two regions have been found, they must be joined in such a way as to satisfy all the boundary conditions.

This approach is an application of boundary layer theory.[7] When integrating the equations for the "outer" solution out from the origin and in from the edge, there comes a point at which the simple model of the physics in this region becomes inadequate. This is indicated by the presence of a singularity in the equations, in this case the (λ'/F) singularity. The singularity is resolved by solving a set of more complicated equations, which include physical effects that may normally be small, in a small boundary layer. In this case, the boundary layer is the dissipative layer. These solutions are then joined to the "outer" solution as follows. The distance from the center of the layer to a point past the outside edge is small, in the distance units of the outer region, but quite large when normalized to the width of the very thin dissipative layer. Thus, the solution in the "outer region" is expanded near the layer edge in terms of a variable which goes to zero and the solution in the "inner region" is expanded near the layer edge in terms of a normalized variable which goes to infinity. The simplified forms of these expansions can be matched, to some order in the expansion parameter. This process is known as asymptotic matching. The matched solutions must obey the appropriate boundary conditions.

In what follows, the solutions in each region will be descibed first and unspecified constants of integration will be included. Then, the

matching process will be given and the values of the constants will be found. At the end of the entire affair, the profiles of v_r and b_r will have been found. The results can be compared to those of the 3-D MHD code and to the physical picture put forward in Section 4.3 .

4.5a Solutions in the "Outer Region"

The first part of the "outer region," the constant-λ region, has the simplest solutions. The equations in this region are given by:

$$b_r{}^{(2)} + \frac{1}{r}\, b_r{}^{(1)} + \left[\lambda_0{}^2 - n^2 k^2 - \frac{1}{r^2} \right] b_r = 0 \qquad (4.5.1)$$

$$v_r = 0 \,. \qquad (4.5.2)$$

Equation (4.5.1) is easily recognised as the Bessel equation of order one. The solution is given by :[8]

$$b_r(r) = b_r(r_n) \left[\frac{J_1(\gamma_0 r)}{J_1(\gamma_0 r_n)} \right] \qquad (4.5.3)$$

for $0 \le r \le r_n$, with $\gamma_0{}^2 = \lambda_0{}^2 - n^2 k^2$.

(If $\gamma_0{}^2 < 0$, the Bessel function J_1 is replaced by the modified Bessel function I_1 .) It is also useful to define the following quantity:

$$\beta = \left[\frac{\gamma_0 \, J_1'(\gamma_0 r_n)}{J_1(\gamma_0 r_n)} \right] . \qquad (4.5.4)$$

This represents the ratio of slope to value at the edge of the constant-λ region, $r = r_n$, and will be useful in imposing boundary conditions.

Equation (4.5.1) requires two boundary conditions. One has been imposed implicitly in (4.5.3) by writing the solution only in terms of the Bessel function of the first kind. A general solution would include the Bessel function of the second kind (Y_1) , which diverges at the origin. It has been excluded to ensure a regular solution there. The second boundary condition involves specifying the value of b_r at the point where the constant$-\lambda$ region meets the finite grad$-\lambda$ region: $b_r(r_n)$. Actually, two boundary conditions must be imposed at $r = r_n$, one from the constant$-\lambda$ region and one from the finite grad$-\lambda$ region. These conditions are satisfied by requiring that b_r and its first derivative be continuous at $r = r_n$. The ratio of slope to value as $r \rightarrow r_n$ in the finite grad$-\lambda$ region is matched to the parameter β, defined in (4.5.4) . This serves as the boundary condition for this region. Using this condition and the value of the field error at the plasma edge, the solution in the finite grad$-\lambda$ region can be completely specified. The value of $b_r(r_n)$ which results is then used in (4.5.3), by the continuity of b_r.

Before tackling the solution of the equations in the finite grad$-\lambda$ region, it is useful to exploit the presence of the singularity to make an expansion which simplifies the problem. The singularity appears in the quantity Ξ, which is defined in equation (4.4.40). The last term, which is inversely proportional to q, becomes large near the resonant surface for m $=0$ modes, where q approaches zero. This suggests that the essential features of the equation can be given by low$-$order terms in an expansion around the resonant surface (r_s). Start by expanding in $x = r - r_s$:

$$q(r) = q(r_s) + q'(r_s)\,x + \cdots \approx q'(r_s)\,x \qquad \text{and} \qquad r \approx r_s + x \ .$$

Then, using $q'(r_s) = -(k r_s)\,\lambda(r_s)$ from equation (3.4.15),

the equation for Ξ becomes:

$$\Xi = \lambda(r_s + x)^2 - n^2 k^2 + \Lambda_s \left(\frac{1}{r_s{}^2}\right)\left(\frac{r_s}{x} + 1\right) . \qquad (4.5.5)$$

(The parameter Λ_s is the same normalized λ' as was defined in Table 4.3.) The third term dominates the maximum value of the first two terms for: $|x/r_s| \ll \Lambda_s/(n k r_s)^2 = 0.469$, using parameters appropriate to the 3-D MHD code results for n = 24. Since $|x/r_s|_{\max} = 0.186$ in the finite grad-λ region, it will be assumed that Ξ can be adequately given by this lowest-order term. Then, only terms of the lowest order will be included in the expansion, as was the case with q above. Thus, equation (4.5.5) gives:

$$\Xi = \left(\frac{\Lambda_s}{r_s}\right)\left(\frac{1}{x}\right) \qquad \text{and} \qquad \frac{\Xi'}{\Xi} = -\left(\frac{1}{x}\right) . \qquad (4.5.6)$$

These expressions greatly simplify equations (4.4.39)-(4.4.41) for the magnetic perturbations in the finite grad-λ region.

With the simplifications made above, the equations in the finite grad-λ region can now be solved. The equations to be used are (4.4.39)-(4.4.41), expanded to lowest order in $x = r - r_s$. This means that Ξ and its derivative are given by (4.5.6), $r = r_s$, and $\lambda(r) = \lambda(r_s) = \lambda_s$. The proper dimensionless variables and parameters for this expansion are summarized in the following table:

EXPRESSION	DEFINITION
Normalized Position	$\xi = -x/r_s = (r_s - r)/r_s$
Normalized Derivative	$\frac{\partial}{\partial \xi} = -r_s\ (\ )^{(1)}$
Normalized λ'	$\Lambda_s = \frac{\lvert\lambda'\rvert r_s}{\lambda_s}$

Table 4.4

The equations, in terms of these normalized variables and parameters, are:

$$\xi \frac{\partial^2 b_z}{\partial \xi^2} + (1 - \xi)\frac{\partial b_z}{\partial \xi} - \Lambda_s b_z = 0 \tag{4.5.7}$$

$$b_r = \left(\frac{ink r_s}{\Lambda_s}\right) \xi \frac{\partial b_z}{\partial \xi} \tag{4.5.8}$$

$$v_r = 0 \ . \tag{4.5.9}$$

Equation (4.5.7) has a solution in terms of tabulated functions:

$$b_z(\xi) = a^* M(\Lambda_s, 1; \xi) + b^* U(\Lambda_s, 1; \xi) \ , \tag{4.5.10}$$

for $r_n < r \le a$ or, in normalized units, $\xi_a \le \xi < \xi_n$,

where $\xi_n = -\frac{x_n}{r_s}$ and $x_n = r_n - r_s$ at $r = r_n$ (4.5.11)

and $\xi_a = -\frac{x_a}{r_s}$ and $x_a = a - r_s$ at $r = a$. (4.5.12)

The functions M and U are Kummer's functions and a^* and b^* are arbitrary constants of integration. The Kummer's functions can be found in tables or can be calculated by means of a series representation.[9] Using (4.5.10) in (4.5.8) and some differential properties of the Kummer's functions, the radial magnetic perturbation can be found:

$$b_r(\xi) = A^* \xi M(\Lambda_s + 1, 2; \xi) + B^* \xi U(\Lambda_s + 1, 2; \xi) . \quad (4.5.13)$$

The constants in the expression for b_r in equation (4.5.8) have been absorbed into the arbitrary constants A^* and B^*.

The boundary conditions at the ends of the finite grad$-\lambda$ region provide relations between the constants A^* and B^*. At $r = r_n$, the ratio of b_r' to b_r is set equal to the value obtained from the solution in the constant$-\lambda$ region, as was mentioned previously. This value is given by the parameter β in equation (4.5.4). At $r = a$, the value of b_r is set equal to the value of the field error imposed at the wall: $b_r(a)$. The mathematical statements of these boundary conditions are given below:

$$\left(-\frac{1}{r_s}\right)\left[\frac{\partial b_r}{\partial \xi}\right]_{\xi_n} - \beta\, b_r(\xi_n) = 0 \quad \text{at } r = r_n \qquad (4.5.14)$$

and

$$b_r(\xi_a) = b_r(a) \qquad \text{at } r = a . \qquad (4.5.15)$$

If the expression for b_r in (4.5.13) is to satisfy these two equations, the constants A^* and B^* must be related in a particular way. Evaluation of (4.5.14) leads to:

$$A_L^* = \frac{B_L^*}{\Gamma(\Lambda_s + 1)} K_L \tag{4.5.16}$$

with

$$K_L = \Gamma(\Lambda_s + 1)\left[\frac{\Lambda_s U(\Lambda_s + 1, 1; \xi_n) + \beta x_n U(\Lambda_s + 1, 2; \xi_n)}{M(\Lambda_s + 1, 1; \xi_n) - \beta x_n M(\Lambda_s + 1, 2; \xi_n)}\right], \tag{4.5.17}$$

for the part of the finite grad$-\lambda$ region which includes $r = r_n$. The "L" subscript indicates the part of the finite grad$-\lambda$ region to the left of the dissipative layer at $r = r_s$. The quantities x_n and ξ_n have been defined in (4.5.11) and the function Γ is the Gamma function.[10] Evaluation of (4.5.15) leads to:

$$A_R^* = \frac{b_r(a)}{\xi_a M(\Lambda_s + 1, 2; \xi_a)} - \frac{B_R^*}{\Gamma(\Lambda_s + 1)} K_R \tag{4.5.18}$$

with

$$K_R = \Gamma(\Lambda_s + 1)\left[\frac{U(\Lambda_s + 1, 2; \xi_a)}{M(\Lambda_s + 1, 2; \xi_a)}\right], \tag{4.5.19}$$

for the part of the finite grad$-\lambda$ region which includes $r = a$. Here, the "R" subscript indicates the part of the finite grad$-\lambda$ region to the right of the dissipative layer at $r = r_s$. The quantities x_a and ξ_a have been defined in equation (4.5.12). In the presence of a dissipative layer, the relation on the left will be joined to the relation on the right via the equations in the layer. In the absence of a layer, "left" and "right" lose their meaning. The continuity of the b_r profile then requires $A_L^* = A_R^* = A^*$ and $B_L^* = B_R^* = B^*$. Using (4.5.16) and (4.5.18), A^* and B^* can be found and the profile

completely specified. It is worth noting that, in this case, the important value of b_r at the resonant surface, $r = r_s$ or $\xi = 0$, is given by:

$$\frac{[b_r(r_s)]_{\text{NO LAYER}}}{b_r(a)} = \frac{B^*/b_r(a)}{\Gamma(\Lambda_s+1)} \qquad (4.5.20)$$

$$= \left[(K_R + K_L)\,\xi_a\, M(\Lambda_s+1, 2; \xi_a) \right]^{-1}$$

4.5b Solutions in the "Inner Region"

The equations in the "inner region" can be simplified via an expansion in small layer width. The full coupled equations in the dissipative layer, which are sixth order in the variable, are:

$$\left(\frac{\partial^4 V}{\partial \zeta^4} + \zeta^2 V \right) + 4 l_s \frac{\partial^3 V}{\partial \zeta^3} + l_s^2 \left(1 - 2\nu_s^2\right) \frac{\partial^2 V}{\partial \zeta^2} + l_s^3 \left(1 - 4\nu_s^2\right) \frac{\partial V}{\partial \zeta} + l_s^4 \left(\nu_s^4 + \nu_s^2 - 1\right) V = -i l_s B \left[\Lambda_s + l_s \zeta (\lambda_s r_s)^2 \right] \qquad (4.5.21)$$

$$\frac{\partial^2 B}{\partial \zeta^2} + l_s \frac{\partial B}{\partial \zeta} - l_s^2 \left(1 + \nu_s^2\right) B = -i \zeta V \qquad (4.5.22)$$

The small parameter is the normalized layer width l_s. The key feature which makes an expansion attractive is the fact that B enters the right side of equation (4.5.21) multiplied by l_s. The B term affects the V term which is one order higher in l_s than itself. Thus, it should be possible to solve for the lowest order V alone, using a form of (4.5.21) that is uncoupled from

(4.5.22) . The lowest order B can then be found using (4.5.22), where V and B are of the same order. This B can then be used in (4.5.21) to find the next order V , which can then be used in (4.5.22) to find the next order B . The values of V and B to various orders in l_s can thus be found alternately, by solving uncoupled equations which are less than sixth order in either variable.

The process outlined above can be illustrated more concretely by considering the lowest order equations. The ordering parameter l_s is shown explicitly in equations (4.5.21)–(4.5.22). All normalized variables and parameters are taken to be $O(1)$. The lowest order equations are those for $O(l_s{}^0)$, or $O(1)$. These are given below, with the 0 subscript representing $O(l_s{}^0)$.

$$\left(\frac{\partial^4 V_0}{\partial \zeta^4} + \zeta^2 V_0 \right) = 0 \tag{4.5.23}$$

$$\frac{\partial^2 B_0}{\partial \zeta^2} = -i \zeta V_0 \tag{4.5.24}$$

The ordering has indeed uncoupled the equations.

Some knowledge of the behavior of V aids in finding a solution. A useful piece information can be gained from the computer–generated solutions. Figure 4.8 shows that the radial velocity perturbation profile is basically symmetric about the resonant surface. If this symmetry is to obtain in this expansion, it must be applied to the lowest order terms.

Thus, the region of solution can be confined to one half of the layer and the following boundary conditions can be applied at the layer center ($\zeta = 0$):

$$\left[\frac{\partial^3 V_0}{\partial \zeta^3}\right]_{\zeta=0} = \left[\frac{\partial V_0}{\partial \zeta}\right]_{\zeta=0} = 0 . \qquad (4.5.25)$$

Past the edge of the layer, in the finite grad$-\lambda$ region, the radial velocity perturbation goes to zero, as shown in equation (4.5.9) . The transition to the finite grad$-\lambda$ region occurs at a distance from the center of the layer which is large compared to the layer width: $\zeta \rightarrow \infty$, in this very small layer case. In this limit, the lowest order value of B must remain finite, so that it can be joined to the value in the finite grad$-\lambda$ region. Thus, the conditions:

$$V_0 \rightarrow 0$$

$$B_0 \text{ finite} \qquad \text{as} \qquad \zeta \rightarrow \infty \qquad (4.5.26)$$

can be added to the boundary conditions.

The obvious solution to equation (4.5.23), subject to (4.5.25) and (4.5.26), is $V_0 = 0$. This is reasonable: to $O(l_s{}^0)$, there is no layer and the velocity perturbation remains zero. As a double-check, the equations were integrated numerically, with the same result. The equation for B_0 is:

$$\frac{\partial^2 B_0}{\partial \zeta^2} = 0 , \qquad (4.5.27)$$

with solution: $B_0 = c^* + d^* \zeta$. (4.5.28)

Applying (4.5.26) forces $d^* = 0$. Thus, the lowest order solutions in the layer can be summarized as follows:

$$O(l_s{}^0) \qquad V_0 = 0 \qquad B_0 = C^* = \text{constant} . \tag{4.5.29}$$

The way in which solutions for V and B alternate is evident in the equations for the next order in the expansion: $O(l_s{}^1)$. The equation for V_1 only depends on B_0; it is uncoupled from the equation for B_1. To be more specific, the first order equations are:

$$\frac{\partial^4 V_1}{\partial \zeta^4} + \zeta^2 V_1 = -i l_s \Lambda_s B_0 \tag{4.5.30}$$

and

$$\frac{\partial^2 B_1}{\partial \zeta^2} + l_s \frac{\partial B_0}{\partial \zeta} = -i \zeta V_1 . \tag{4.5.31}$$

The solution for V_1 can be found from (4.5.30) alone. Given this solution, B_1 can be found from (4.5.31).

First, focus attention on equation (4.5.30) . This can be made to look simpler by redefining the velocity variable, using (4.5.29) for B_0. Defining:

$$\chi_1 = \frac{i V_1}{l_s \Lambda_s C^*} , \tag{4.5.32}$$

produces

$$\frac{\partial^4 \chi_1}{\partial \zeta^4} + \zeta^2 \chi_1 = 1 . \tag{4.5.33}$$

Since χ_1 will be the lowest-order non-zero solution for the radial velocity perturbation, the comments about the symmetry of the solution made before equation (4.5.25) still hold. The solution must be symmetric about the point $\zeta = 0$, so that only one half of the layer need be considered and:

$$\left[\frac{\partial^3 \chi_1}{\partial \zeta^3}\right]_{\zeta=0} = \left[\frac{\partial \chi_1}{\partial \zeta}\right]_{\zeta=0} = 0 . \qquad (4.5.34)$$

In the area past the edge of the layer, χ_1 must go to zero. Equation (4.5.33) suggests that:

$$\chi_1 \rightarrow \frac{1}{\zeta^2} \qquad \text{as} \qquad \zeta \rightarrow \infty . \qquad (4.5.35)$$

Equations (4.5.33)-(4.5.35) form a system which completely describes χ_1. An attempt was made to find an analytic solution, but equation (4.5.33) does not fall into any simple class of equations.[11] Numerical results will be described later, in **4.5d**.

Assuming that the solution for χ_1 is known, the solution for B_1 can be found by integrating equation (4.5.31) . Using (4.5.29) and (4.5.32), this equation can be written:

$$\frac{\partial^2}{\partial \zeta^2}\left(\frac{B_1}{l_s \Lambda_s C^*}\right) = -\zeta \chi_1 . \qquad (4.5.36)$$

The formal solution can be expressed as:

$$\left[\frac{B_1}{l_s \Lambda_s C^*} \right]_\zeta = d^* \zeta - \int_0^\zeta dw \int_0^w du \, (u \, \chi_1(u)) \, . \tag{4.5.37}$$

An additional constant of integration could be added, in principle. However, such a constant would be absorbed into the constant zeroth-order term $B_0 = C^*$ during the matching process. Thus, such a constant is taken to be zero in this and higher orders. This simplification has an additional advantage. Given that χ_1 has been chosen to be even in ζ, the double integral is odd in ζ, as is the linear term. The entire B_1 is odd in ζ. Since this function is used on the right side of the equation for V_2, the solution for V_2 should be odd. This alternation in symmetry with the order of the expansion allows definite boundary conditions to be imposed at the layer center in each order, as will be seen below. With the above specification of the magnetic perturbation in this order, the cycle of solution can begin again in the next higher order.

Now that the solution process has been sketched out for the first two orders in the expansion, the higher order equations and solutions will be summarized in tabular form. The tables will consist of orders from $l_s{}^1$ to $l_s{}^4$. The expanded solution to this order was found to give reasonable convergence to the actual solution in the asymptotic matching region.

$$\text{For} \quad O(l_s{}^k) \, , \quad \text{define} \quad \chi_k = \frac{i \, V_k}{(l_s{}^k) \, \Lambda_s \, C^*} \, . \tag{4.5.38}$$

Then, the equation for χ_k is given by:

$$\frac{\partial^4 \chi_k}{\partial \zeta^4} + \zeta^2 \chi_k = R_k(\chi) + S_k(\mathrm{B}) , \tag{4.5.39}$$

where the functions on the right are defined in Table 4.5 below.

k	$R_k(\chi)$	$S_k(\mathrm{B})$
1	0	1
2	$-4\frac{\partial^3 \chi_1}{\partial \zeta^3}$	$\Lambda_s\left(\frac{\mathrm{B}_1}{l_s \Lambda_s \mathrm{C}^*}\right) + (\lambda_s r_s)^2 \zeta\left(\frac{1}{\Lambda_s}\right)$
3	$-4\frac{\partial^3 \chi_2}{\partial \zeta^3} + (2\nu_s^2 - 1)\frac{\partial^2 \chi_1}{\partial \zeta^2}$	$\Lambda_s\left(\frac{\mathrm{B}_2}{l_s^2 \Lambda_s \mathrm{C}^*}\right) + (\lambda_s r_s)^2 \zeta\left(\frac{\mathrm{B}_1}{l_s \Lambda_s \mathrm{C}^*}\right)$
4	$-4\frac{\partial^3 \chi_3}{\partial \zeta^3} + (2\nu_s^2 - 1)\frac{\partial^2 \chi_2}{\partial \zeta^2} + (4\nu_s^2 - 1)\frac{\partial \chi_1}{\partial \zeta}$	$\Lambda_s\left(\frac{\mathrm{B}_3}{l_s^3 \Lambda_s \mathrm{C}^*}\right) + (\lambda_s r_s)^2 \zeta\left(\frac{\mathrm{B}_2}{l_s^2 \Lambda_s \mathrm{C}^*}\right)$

Table 4.5

After χ_k has been found, the magnetic perturbation B_k can be generated from:

$$\frac{\partial^2}{\partial \zeta^2}\left(\frac{B_k}{(l_s{}^k)\,\Lambda_s\,C^*}\right) = T_k(B) - \zeta\,\chi_k \quad , \tag{4.5.40}$$

where the function on the right is defined below in Table 4.6.

k	$T_k(B)$
1	0
2	$-\frac{\partial}{\partial\zeta}\left(\frac{B_1}{l_s\,\Lambda_s\,C^*}\right) + \left(1+\nu_s{}^2\right)\left(\frac{1}{\Lambda_s}\right)$
3	$-\frac{\partial}{\partial\zeta}\left(\frac{B_2}{l_s{}^2\,\Lambda_s\,C^*}\right) + \left(1+\nu_s{}^2\right)\left(\frac{B_1}{l_s\,\Lambda_s\,C^*}\right)$
4	$-\frac{\partial}{\partial\zeta}\left(\frac{B_3}{l_s{}^3\,\Lambda_s\,C^*}\right) + \left(1+\nu_s{}^2\right)\left(\frac{B_2}{l_s{}^2\,\Lambda_s\,C^*}\right)$

Table 4.6

The general solution of equation (4.5.40) is:

$$\left[\frac{B_k}{(l_s{}^k)\,\Lambda_s\,C^*}\right]_\zeta = \int_0^\zeta dw \int_0^w du\,\left(T_k(u) - u\,\chi_k(u)\right) . \tag{4.5.41}$$

The linear term $d^* \zeta$ only appears for $k = 1$, since any arbitrary linear term in a higher order would only be lumped into $d^* \zeta$ during the matching process.

Although the specification of the equations is now complete, the boundary conditions on χ_k must be given before any solutions can actually be found. The first useful fact is that the solutions for χ_k and B_k have definite symmetry about $\zeta = 0$. The solution need only be found on one side of the layer, from $\zeta = 0$ to $\zeta \to \infty$. It has already been pointed out that χ_1 is even and B_1 is odd. A look at the $k = 2$ row of Table 4.5 shows that the right side of equation (4.5.39) is odd for $k = 2$. The operator on the left is even. Thus, χ_2 must be odd. The $k = 2$ row of Table 4.6 and equation (4.5.41) show that B_2 is even. The symmetry of χ_k and B_k alternates with order. The type of symmetry determines the boundary behavior at $\zeta = 0$.

ORDER (k)	SYMMETRY	BOUNDARY CONDITION
1 , 3	χ_k even B_k odd	$\left[\frac{\partial^3 \chi_k}{\partial \zeta^3}\right]_{\zeta=0} = \left[\frac{\partial \chi_k}{\partial \zeta}\right]_{\zeta=0} = 0$
2 , 4	χ_k odd B_k even	$\left[\frac{\partial^2 \chi_k}{\partial \zeta^2}\right]_{\zeta=0} = \chi_k(0) = 0$

Table 4.7

The behavior at the other end of the layer, $\zeta \to \infty$, is given by the asymptotic form of χ_k . Equation (4.5.40) suggests that

$$\frac{\partial^2}{\partial \zeta^2}\left(\frac{B_k}{\left(l_s{}^k\right) \Lambda_s \, C^*} \right) \sim O\left(\zeta \chi_k\right) \ .$$

If χ_k asymptotically obeys a power law, as is the case for χ_1, then

$$\left(\frac{B_k}{\left(l_s{}^k\right) \Lambda_s \, C^*} \right) \sim \zeta^3 \chi_k$$

and

$$\left(\frac{B_k}{\left(l_s{}^k\right) \Lambda_s \, C^*} \right) \gg \chi_k \qquad \text{as} \qquad \zeta \to \infty \ . \tag{4.5.42}$$

Applying this to (4.5.39) gives

$$S_k(B) \gg R_k(\chi) \qquad \text{as} \qquad \zeta \to \infty \ ,$$

which can be verified by using (4.5.42) in Table 4.5 . Also

$$\frac{\partial^4 \chi_k}{\partial \zeta^4} \sim \frac{\chi_k}{\zeta^4} \ll \zeta^2 \chi_k \qquad \text{as} \qquad \zeta \to \infty \ .$$

Thus, the asymptotic form of χ_k that is obtained from equation (4.5.39) is:

$$\chi_k \to \frac{\left[S_k(B)\right]_{\zeta \to \infty}}{\zeta^2} \qquad \text{as} \qquad \zeta \to \infty \ . \tag{4.5.43}$$

In principle, the problem can now be solved for the χ_k , and then the B_k . This would involve finding the asymptotic form of the B_k's to

use in (4.5.43) and then performing a numerical integration. However, information about the profiles within the layer is not strictly necessary to find the important value $b_r(r_s)$, or $B(\zeta = 0) = B_0 = C^*$. This can be found from matching the solution for B to the solution outside the layer, and will be done first. In the process, the asymptotic form of the B_k's will be found so that the numerical integration can eventually be done.

4.5c Matching of the "Outer" and "Inner" Solutions

The matching process was described in the early part of this section. It involves the behavior of the radial magnetic perturbation in the region where the distance $x = r - r_s$ is small, but finite. From the perspective of the "inner region," this is the distance from the center of the dissipative layer. For a small layer, the normalized distance $\zeta = x/l$ becomes large. The form of the solution for $B = b_r$ as $\zeta \to \infty$ can be used. From the perspective of the "outer region," $x = r - r_s$ is the distance from the point of singularity. In the normalized units of this region, $\xi = -x/r_s$ is small. The form of the solution for b_r as $\xi \to 0$ can be used. The goal is that these simpler forms will be similar enough to join together with the number of arbitrary constants available.

The way in which the asymptotic form of the solution in the "inner region" can be obtained is illustrated using the first order solution, B_1. The functional form of B_1 is given by the integral expression in equation (4.5.37). The key to evaluating this expression in the limit as $\zeta \to \infty$ is the simple form assumed by χ_1, shown in equation (4.5.35) . When this form

is used in equation (4.5.37), the integrations can be performed. In this limit, B_1 takes on the following functional form:

$$\left[\frac{B_1}{l_s \Lambda_s C^*}\right]_{\zeta \to \infty} = d^* \zeta + 0.07 \zeta - \zeta ln|\zeta| \ . \tag{4.5.44}$$

The numerical term, 0.07ζ, arises from the part of the integral for which χ_1 is not yet in its asymptotic form. It was obtained from a numerical integration; the problem describing χ_1 is completely given by equations (4.5.33) – (4.5.35), without any arbitrary constants. This term is retained, and not lumped in with $d^* \zeta$, because it is a linear term which is proportional to C^*. Since d^* is truly arbitrary, it can absorb C^* and remain an independent constant. This allows for two independent constants in the solution, and will be an important feature of the matching. In higher orders, terms which arise in this way will be ignored, since they would be small corrections to this term.

In going to higher orders in B, a similar process can be used to obtain the form in the limit as $\zeta \to \infty$. For a particular B_k, use the limiting forms of the lower order B's in equation (4.5.43) and Table 4.5 to find the limiting form of χ_k. Then, use the same form of the lower order B's in Table 4.6 to find T_k. Combine this information in equation (4.5.41) and perform the integrations. The results are summarized below.

For ease of presentation, some new parameters are defined:

$m_1 = 1$ and

$$m_k = \frac{\left[1 + \frac{1}{\Lambda_s}\right]\left[1 + \frac{2}{\Lambda_s}\right]\cdots\left[1 + \frac{(k-1)}{\Lambda_s}\right]}{k!\,(k-1)!} \qquad 2 \le k \le 4 . \tag{4.5.45}$$

In addition, define the following, based on equation (4.4.44) and Table 4.3 :

k	M_k	U_k
1	1	-0.07
2	1	$U_1 + \frac{\left[1 - (\lambda_s r_s)^2 + \nu_s{}^2\right]}{\Lambda_s(\Lambda_s + 1)} + \frac{1}{\Lambda_s + 1} - \frac{3}{2}$
3	$1 + \frac{2\left[1 - (\lambda_s r_s)^2 + \nu_s{}^2\right]}{(\Lambda_s + 1)(\Lambda_s + 2)}$	$U_2 + U_1(M_3 - 1) + \frac{1}{\Lambda_s + 2} - \frac{5}{6} M_3$
4	$M_3 + \frac{6\left[1 - (\lambda_s r_s)^2 + \nu_s{}^2\right]}{(\Lambda_s + 2)(\Lambda_s + 3)}$	$U_3 + U_2(M_4 - M_3) + \frac{M_3}{\Lambda_s + 3} - \frac{7}{12} M_4$

Table 4.8

Then, using the quantities identified above, the form of B_k as $\zeta \to \infty$ is:

$$\left[\frac{B_k}{\left(l_s{}^k\right)\Lambda_s\, C^*}\right]_{\zeta\to\infty} = \frac{m_k\left(-\Lambda_s\,\zeta\right)^k}{\Lambda_s}\left[-d^*M_k + U_k + M_k\, ln\left|\zeta\right|\right]$$

$$\text{for} \qquad 1 \le k \le 4 . \qquad (4.5.46)$$

(Note: Earlier, an asymptotic power-law form for χ_k was assumed to justify the approximations made in obtaining equation (4.5.43). Using the form of the B_k from (4.5.46) in (4.5.43) and Table 4.5 produces an asymptotic form for χ_k which is indeed a power law, to within a ln term. Thus, the original assumption is at least self-consistent.)

The total solution for $B = b_r$ in the "inner region," as $\zeta \to \infty$, can now be assembled. The dimensionless variable ζ will be rewritten in terms of the common length in the matching region, $x = r - r_s$. Recall that:

$$\frac{x}{r_s} = \zeta\, l_s \quad , \qquad \text{from Table 4.3 .}$$

The solution will include two arbitrary constants, C^* and D^*. The second constant comes from d^*:

$$D^* = \Lambda_s\, C^*\left(d^* + ln\, l_s\right) . \qquad (4.5.47)$$

The ln term has been included to change the dimension of the argument of the ln term in (4.5.46). Then, to order $l_s{}^4$, the solution for $B = b_r$ is:

$$B = B_0 + \sum_{k=1}^{4} B_k \qquad \text{or}$$

$$b_r = C^* \left(1 + \sum_{k=1}^{4} \left(-\Lambda_s \frac{x}{r_s} \right)^k m_k \left[U_k + M_k \ln \left| \frac{x}{r_s} \right| \right] \right)$$

$$+ D^* \left(\frac{x}{r_s} \right) \left(1 + \sum_{k=2}^{4} \left(-\Lambda_s \frac{x}{r_s} \right)^{k-1} m_k M_k \right) . \qquad (4.5.48)$$

The asymptotic form of the solution for b_r in the "outer region" can be obtained from equation (4.5.13) by using the series solution for the Kummer's functions as $\xi \to 0$. Again, the dimensionless variable — ξ, in this case— will be rewritten in terms of the common length in the matching region, $x = r - r_s$. Recall that:

$$\xi = -\frac{x}{r_s} , \qquad \text{from Table 4.4 .}$$

The series contains a certain combination of Digamma (or ψ) functions.[12] These will be represented as:

$$P_k = \psi(\Lambda_s + k) - \psi(k) - \psi(k+1) . \qquad (4.5.49)$$

With these conditions, the series solution can be written:

$$b_r = \frac{B^*}{\Gamma(\Lambda_s + 1)} \left(1 + \sum_{k=1}^{4} \left(-\Lambda_s \frac{x}{r_s} \right)^k m_k \left[P_k + \ln \left| \frac{x}{r_s} \right| \right] \right)$$

$$- A^* \left(\frac{x}{r_s} \right) \left(1 + \sum_{k=2}^{4} \left(-\Lambda_s \frac{x}{r_s} \right)^{k-1} m_k \right) , \qquad (4.5.50)$$

where the m_k are the same as those used previously (defined in equation (4.5.45)) and Γ represents the Gamma function. The distance x is supposed

to be small, comparable to a few layer widths. The expansion has thus been continued to terms of the fourth order in x, in order to be consistent with the solution in the "inner region."

The solutions in the two regions, equations (4.5.48) and (4.5.50), are quite similar functions of x. It should be possible to match the "inner region" solution to the "outer region" solution through a proper choice of the arbitrary constants. The matching must be done at both ends of the dissipative layer. This means that there are six constants available:

C^*, D^* from the "inner region" solution,

A_L^*, B_L^* from the "outer region" solution on the LEFT side of the layer ($x < 0$),

and

A_R^*, B_R^* from the "outer region" solution on the RIGHT side of the layer ($x > 0$).

There should be six corresponding matching conditions. Four arise from matching like functions of x from (4.5.48) and (4.5.50), specifically:

equating the lowest-order-constant functions whose coefficients are:

B_L^* and C^* at the LEFT side of the layer ($x < 0$)

and B_R^* and C^* at the RIGHT side of the layer ($x > 0$)

and

equating the lowest-order-linear functions whose coefficients are:

$A_L{}^*$ and D * at the LEFT side of the layer ($x < 0$)

and $A_R{}^*$ and D * at the RIGHT side of the layer ($x > 0$) .

The final two conditions are provided by the relationship between $A_L{}^*$ and $B_L{}^*$, equation (4.5.16), and the relationship between $A_R{}^*$ and $B_R{}^*$, equation (4.5.18). With these, enough information exists to make a successful match.

The matching will be done at a value of x which is equal to several layer widths. This position can be defined as:

$$x_w = w l \quad . \tag{4.5.51}$$

For very small l and fairly large w, a small value of x_w can satisfiy both of the necessary requirements: $\xi = -x / r_s \rightarrow 0$ and $\zeta = x / l \rightarrow \infty$. The precise value of w will be determined later, by looking at the numerical integration of the χ_k. The value of ζ at which they reasonably approach their asymptotic form will be chosen as w. Of course, matching occurs at both $\pm x_w$.

The matching problem now consists of a set of six equations in six unknowns, the arbitrary constants listed previously. After some algebra, all the constants can be eliminated in favor of C *. A look at the "inner region" solution, equation (4.5.48), shows that this is the value of b_r at the center of the dissipative layer, $x = 0$. In other words, this is the important quantity $b_r(r_s)$, which has been the object of this study. Before presenting the expression for C *, a number of definitions will be made. The variable

which appears in the expressions for b_r is $\Lambda_s\ (x/r_s)$. At the matching points, the absolute value of x is given by (4.5.51), and we define the variable which will be used in the expressions to be:

$$\omega = \Lambda_s \frac{x_w}{r_s} = \Lambda_s\ w\ l_s\ . \tag{4.5.52}$$

Now, define the following, using Table 4.8 and equations (4.5.45) and (4.5.49):

$$u_k = m_k\ (\ U_k + M_k\ ln|w\ l_s|\ ) \tag{4.5.53}$$

$$p_k = m_k\ (\ P_k + ln|w\ l_s|\ ) \tag{4.5.54}$$

$$\begin{aligned} N^T = 1 &- \omega^2[\ {p_1}^2 - 2p_2 + {m_2}^2 - m_3(M_3 + 1)\ ] \\ &+ \omega^3[\ m_4(M_4 - 1) - m_2\, m_3(M_3 - 1)\ ] \\ &+ \omega^4\{\ {p_2}^2 - 2p_1p_3 + 2p_4 \\ &\quad + (\ {p_1}^2 - 2p_2)[\ {m_2}^2 - m_3(M_3 + 1)] \\ &\quad + {m_3}^2 M_3 - m_2\, m_4(M_4 + 1)\ \} \end{aligned} \tag{4.5.55}$$

$$N_1{}^B = 1 + \omega^2\left[p_2 + u_2 - p_1 u_1 - m_2{}^2 + m_3(M_3 + 1) \right]$$

$$+ \omega^4 \{ p_4 + u_4 - u_1 p_3 + u_2 p_2 - u_3 p_1$$

$$- (p_2 + u_2 - p_1 u_1)\left[m_2{}^2 - m_3(M_3 + 1)\right]$$

$$+ (p_1 - u_1)\left[m_4(M_4 - 1) - m_2 m_3(M_3 - 1) \right]$$

$$+ m_3{}^2 M_3 - m_2 m_4(M_4 + 1) \} \qquad (4.5.56)$$

$$N_2{}^B = (p_1 - u_1) \qquad (4.5.57)$$

$$+ \omega^2 \{ p_3 - u_3 - u_1 p_2 + u_2 p_1$$

$$- (p_1 - u_1)\left[m_2{}^2 - m_3(M_3 + 1)\right]$$

$$+ m_4(M_4 - 1) - m_2 m_3(M_3 - 1) \}$$

Then, using (4.5.52) – (4.5.57) , the expression for C * is:

$$\frac{C^*}{b_r(a)} = \frac{[b_r(r_s)]_{\text{NO LAYER}}}{b_r(a)} \left[\frac{N^T}{N_1{}^B + \omega\left(\frac{K_R - K_L}{K_R + K_L}\right) N_2{}^B} \right] . \qquad (4.5.58)$$

The K's are defined in equations (4.5.17) and (4.5.19) . The "NO LAYER" term is defined in equation (4.5.20) , and represents the value of the solution in the finite grad$-\lambda$ region in the absence of a dissipative layer. The term in the brackets represents the effect of a finite dissipative layer.

The solution process is complete. Now that C* has been found, it can be used to find D*, A_L*, A_R*, B_L*, and B_R*. Equation (4.5.47) can be used to find d*. Then, the asymptotic values of the B_k and χ_k can be specified via equations (4.5.46) and (4.5.43) so that the numerical integration of the "inner region" profiles can proceed. Finally, the matching constants listed above can be used to join these profiles to those in the "outer region," giving the complete solution.

4.5d Results

After this extensive solution process, the time has come to use some numbers in the equations that have been derived and look at some actual profiles. To this end, numerical values for the various parameters are given. First, there are those which characterize the equilibrium fields:

EQUILIBRIUM PARAMETERS	NUMERICAL VALUES
$r_s / a = r_{rv} / a$	0.86
r_n / a	0.70
$\lambda_0 a$	2.950
$\lambda_s a$	1.377
Λ_s	6.141
$B_{\theta_0}(r_s) / B_{z_0}(0)$ (from 3 – D code)	0.491

Table 4.9

Then, there are those parameters which characterize the perturbations:

PERTURBATION PARAMETERS	NUMERICAL VALUES	
	n = 12	n = 24
$n\,k\,a$	2.105	4.210
ν_s	1.810	3.620
$\dfrac{[b_r(r_s)]\ \text{NO LAYER}}{b_r(a)}$	3.497	3.305
$b_r(a)$	− 4.00 e − 5	− 7.71 e − 5

Table 4.10

The first solution to be presented will be a profile of b_r for a case in which λ is constant over the entire radius and $\eta = \nu_0 = 0$. This will serve as a basis against which to judge the effects of finite grad$-\lambda$. These effects, as well as the effects of finite η, ν_0, are qualitatively similar for n = 12 and n = 24. Thus, only n = 24 will be used in what follows. The b_r-profile for an equilibrium with λ constant to $r = a$, instead of $r = r_n$, and $\eta = \nu_0 = 0$ is given by equation (4.5.3), with the replacement $r_n \rightarrow a$. The result is shown in Figure 4.9 . The value of $|\,b_r\,|$ at the resonant surface is increased by 21% (that is, a factor of 1.21) over the value for a vacuum profile. (Note that in this case the position of the resonant surface is slightly different from that given in Table 4.9. The equilibrium field profiles with a constant λ are different from those with finite grad$-\lambda$.)

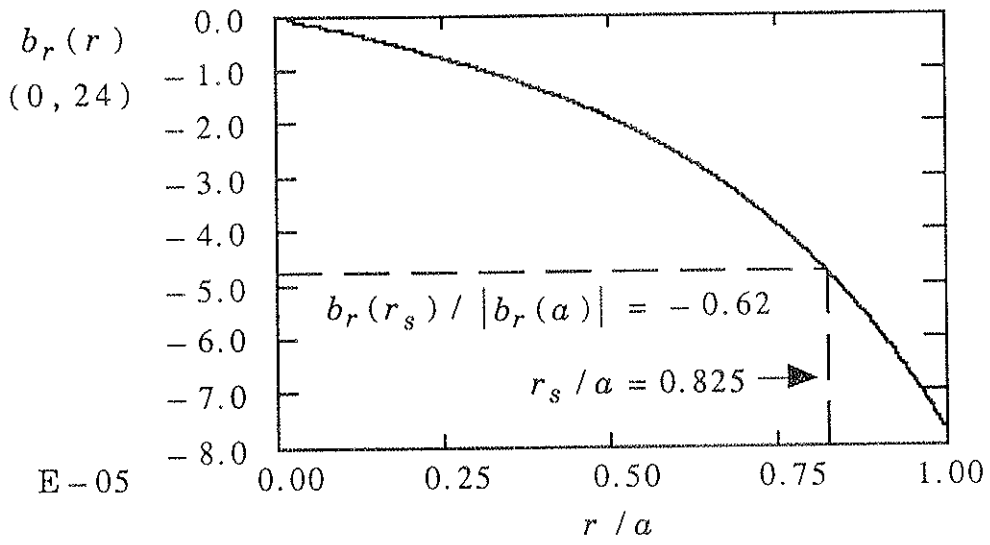

Figure 4.9 Radial profile of a $(0, 24)$ b_r perturbation (imaginary part) for constant-λ. The value of $|b_r(r_s)|$ is 21% greater than in the vacuum.

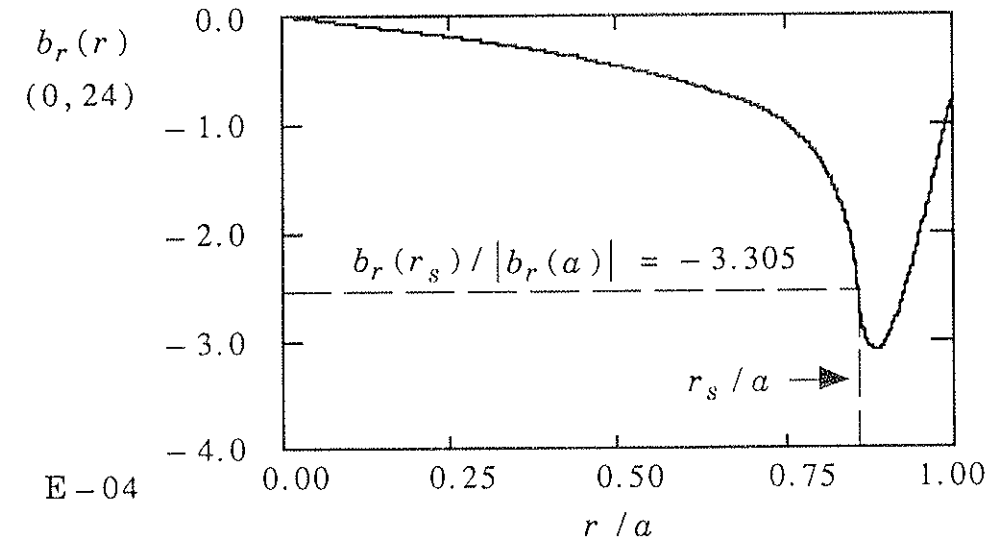

Figure 4.10 Radial profile of a $(0, 24)$ b_r perturbation (imaginary part) for finite grad-λ. The value of $|b_r(r_s)|$ is 5.38 times the vacuum value.

Next consider the solution for the profile of b_r in a case where the equilibrium has finite grad$-\lambda$. This is the solution in the "outer region," in the absence of a dissipative layer. In the finite grad$-\lambda$ region, it is given by equation (4.5.13). Using the parameter β from (4.5.4), the constants A^* and B^* can be found from equations (4.5.16) and (4.5.18) by ignoring the distinctions between "L" and "R." Once the value of this solution at $r = r_n$ has been obtained, it can be used in equation (4.5.3) to provide the solution in the constant$-\lambda$ region. The resulting profile is shown in Figure 4.10 .

The value of b_r at the resonant surface — $[b_r(r_s)]_{\text{NO LAYER}}$ — is quite large (in absolute value). It is greatly increased over that in the previous constant$-\lambda$ case. The presence of the additional perturbed current, which is singular at the resonant surface, causes the profile to bend sharply away from $b_r = 0$ in this vicinity. This confirms the speculations made about the role of finite grad$-\lambda$ in Section 4.3 (after equation (4.3.6)). As in the results for m=1 modes in the previous chapter, the bending of the profile greatly increases the value of $|b_r(r_s)|$ over the value for a vacuum profile. In this case, the increase amounts to a factor of 5.41 .

The next step is to consider the effect of introducing a dissipative layer. The easiest way to do this is to neglect the profiles for the moment and concentrate on the value of $b_r(r_s)$ in the presence of such a layer predicted by equation (4.5.58). Most of the information needed to evaluate

this equation has been given. The one piece that remains to be specified is the value of w in the expression for ω, equation (4.5.52). As was said earlier, the value of ζ at which the χ_k reasonably approach their asymptotic form will be chosen as w. To judge this, the set of equations for χ_1, (4.5.33) – (4.5.35), are integrated.

The method of integration chosen is called "invariant imbedding." It was described briefly in Chapter 3, Section 3.5 . Its principal utility here is that it avoids the necessity of using a "shooting method" to satisfy the boundary conditions. Only one initial–value integration need be performed. The boundary equations and integrated solutions then form a linear system of equations which is solved by matrix methods to find the solution satisfying the boundary conditions. This is described in more detail in the Appendix. Four boundary conditions are required for this problem, which is fourth order in ζ. Two are given in (4.5.34). The remaining two must be derived from the condition that χ_1 go to its asymptotic form, equation (4.5.35). This is done by choosing a large value of ζ, in this case $\zeta = 10$, and requiring χ_1 and its second derivative (the only remaining unspecified derivative) to take on the form required by (4.5.35) there.

The results of the integration are shown below in Figures 4.11a and 4.11b. The first graph shows χ_1 and the second shows $\zeta^2 \chi_1$, which should approach unity if the asymptotic behavior is correct. Note how smoothly this occurs; it starts well before the asymptotic from is imposed at $\zeta = 10$.

Based on this graph, it is reasonable to say that the asymptotic region begins at $\zeta = 5$. Thus, choose $w = 5$ in evaluating ω in (4.5.52).

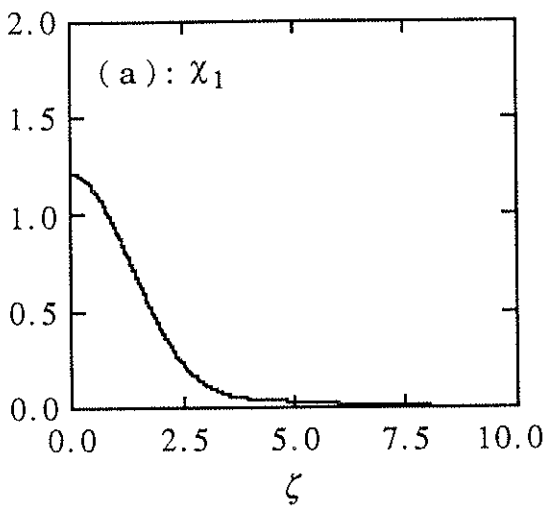

Figure 4.11 a Profile of χ_1 found by integration.

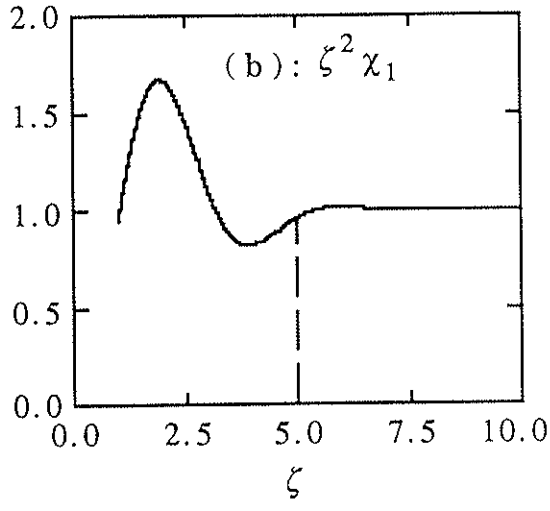

Figure 4.11 b Profile of χ_1 divided by its asymptotic value. χ_1 reaches its proper value near $\zeta = 5$.

The equation for $C^* = b_r(r_s)$ can now be evaluated. Equation (4.5.58) is plotted in Figure 4.12 below. The plot shows $C^* / b_r(a)$ as a function of normalized layer width l_s. For $l_s = 0$, the value is given by $[b_r(r_s)]_{\text{NO LAYER}} / b_r(a)$. The effect of a finite layer, $l_s > 0$, is to reduce the value of $b_r(r_s) / b_r(a)$. Considering the bulge in the b_r-profile near the resonant surface in the finite grad-λ case, shown in Figure 4.10, this reduction suggests a smoothing of the b_r-profile by the layer. For larger layers, the reduction in $| b_r(r_s) |$ increases. For a layer of a certain size,

$|b_r(r_s)|$ falls below the value it would have for a vacuum profile. This supports the idea, originally presented in Section 4.3, that the profile smoothing has a large effect in the presence of the sharply bent profiles created by finite grad$-\lambda$. The largest value of l_s shown ($l_s = 0.033$) corresponds to a layer whose region of influence, from $x/r_s = -5\,l_s$ to $x/r_s = +5\,l_s$, covers the entire finite grad$-\lambda$ region.

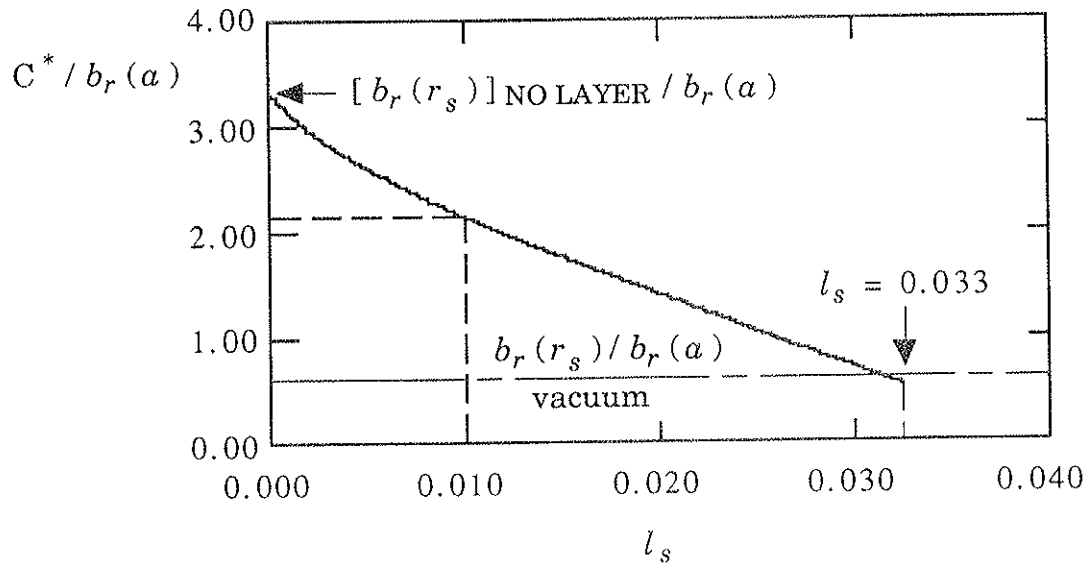

Figure 4.12 Plot of C* / $b_r(a)$ as a function of normalized layer width l_s. The effect of a finite layer, $l_s > 0$, is to reduce the value of $b_r(r_s)$ / $b_r(a)$.

Now the profiles in the layer will be considered. In each order, equation (4.5.39) is integrated for χ_k . The right side of the equation is evaluated using the lower order B_k and χ_k in Table 4.5. The method of integration is the same as that outlined above for χ_1. The boundary

conditions at the center of the layer are given in Table 4.7 . The asymptotic boundary conditions require that χ_k and its second derivative ($k = 1,3$) or the first and third derivatives of χ_k ($k = 2,4$) take on their asymptotic form at $\zeta = 5$. This form is calculated using the asymptotic form of the lower order B_k, from (4.5.46) and Table 4.8, in (4.5.43). After finding χ_k, equation (4.5.41) and Table 4.6 are used to find B_k.

The right sides of equations (4.5.39) and (4.5.41) involve functions of the lower order B_k and χ_k which must be evaluated during integration. This is done by using a spline fit to obtain a polynomial representation of these functions, which were previously obtained in numerical form. The fits were then available to the integrator to be evaluated at the needed points. Various routines from the mathematical library IMSL[13] were used for this purpose: ICSICU calculates the spline fit, DCSQDU integrates it, and ICSEVU evaluates it at a given point.

The following plots show the profiles of χ_k and B_k in each order. Accompanying each profile is a plot showing the profile divided by its asymptotic value. This plot should approach unity as $\zeta \rightarrow 5$. (It was stated in the explanation of the 0.07ζ term in (4.5.44) that similar terms in higher orders would be ignored, for matching purposes. These terms have been calculated and restored here to improve the asymptotic forms of the B_k.)

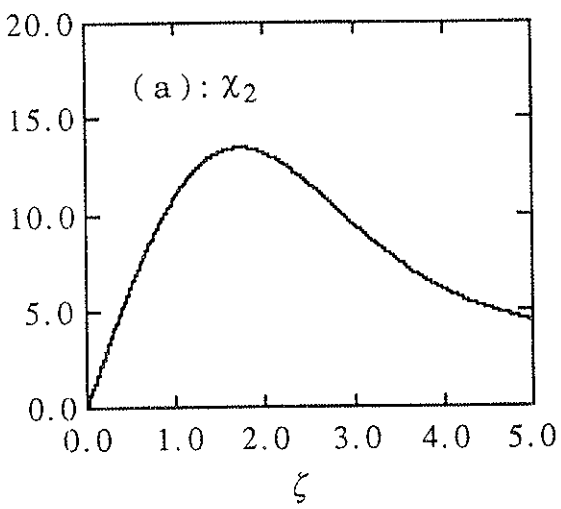

Figure 4.13a Profile of χ_2 found by integration.

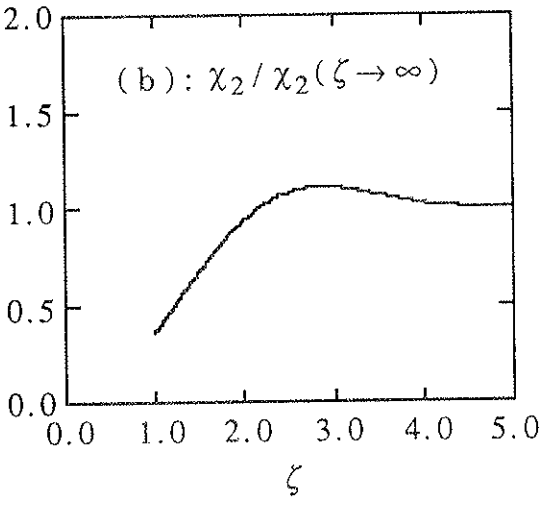

Figure 4.13b Profile of χ_2 divided by its asymptotic value. χ_2 reaches its proper value by $\zeta = 5$.

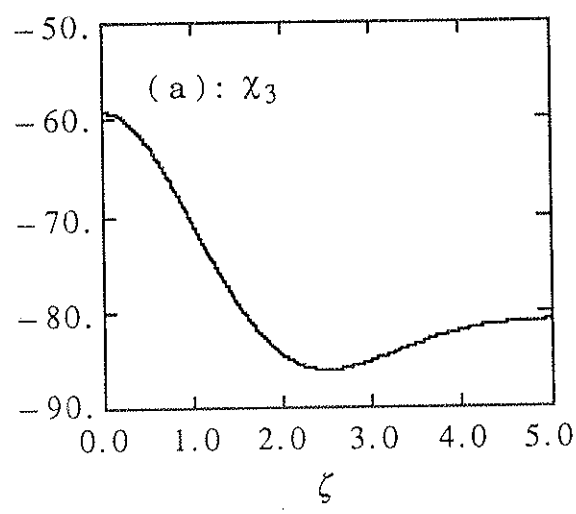

Figure 4.14a Profile of χ_3 found by integration.

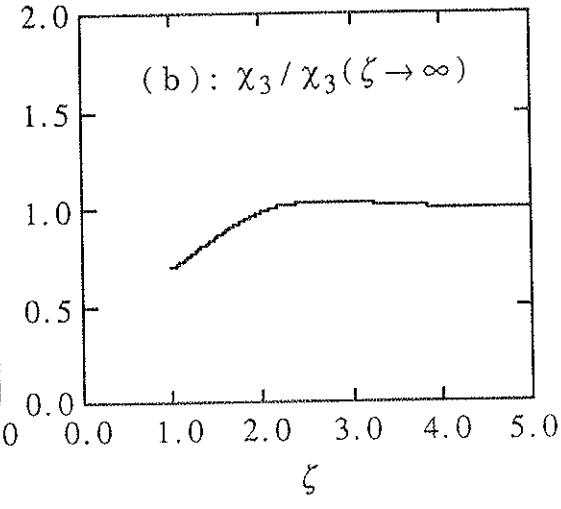

Figure 4.14b Profile of χ_3 divided by its asymptotic value. χ_3 reaches its proper value by $\zeta = 5$.

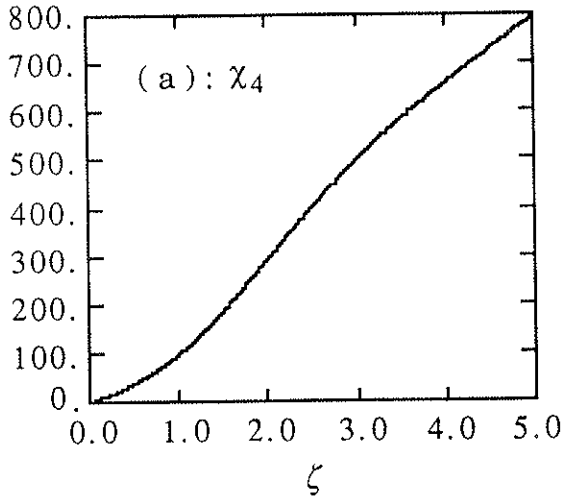

Figure 4.15 a Profile of χ_4 found by integration.

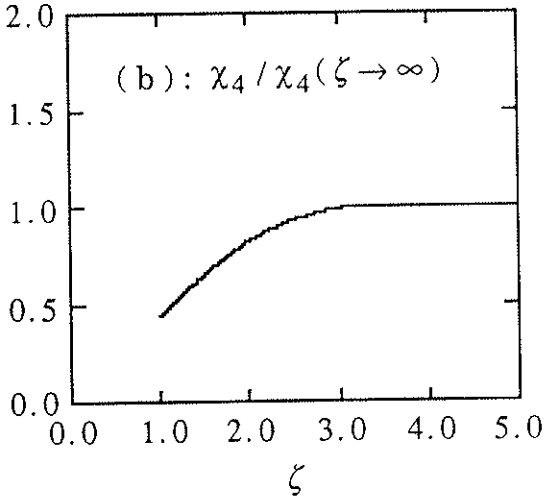

Figure 4.15 b Profile of χ_4 divided by its asymptotic value. χ_4 reaches its proper value by $\zeta = 5$.

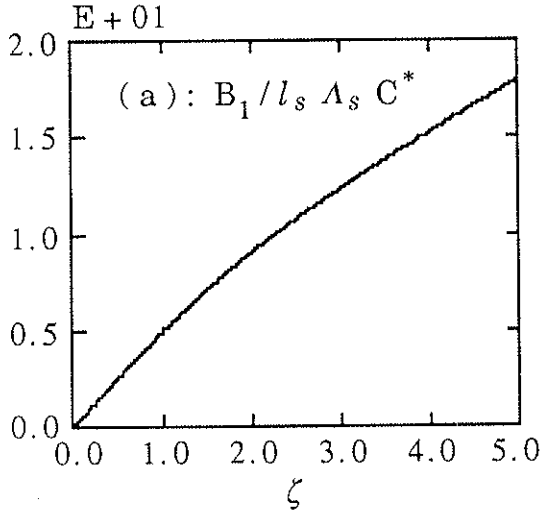

Figure 4.16 a Profile of B_1 found by integration.

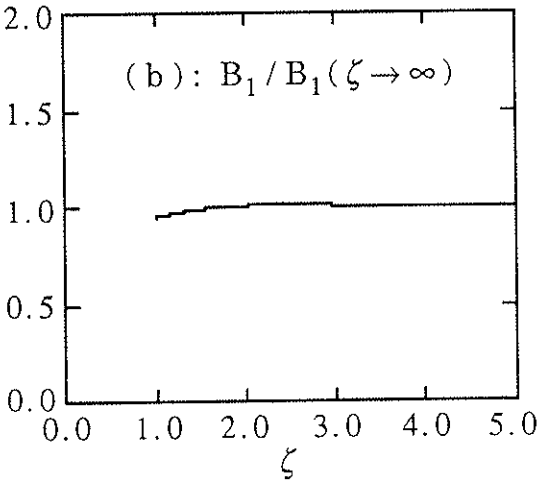

Figure 4.16 b Profile of B_1 divided by its asymptotic value. B_1 reaches its proper value by $\zeta = 5$.

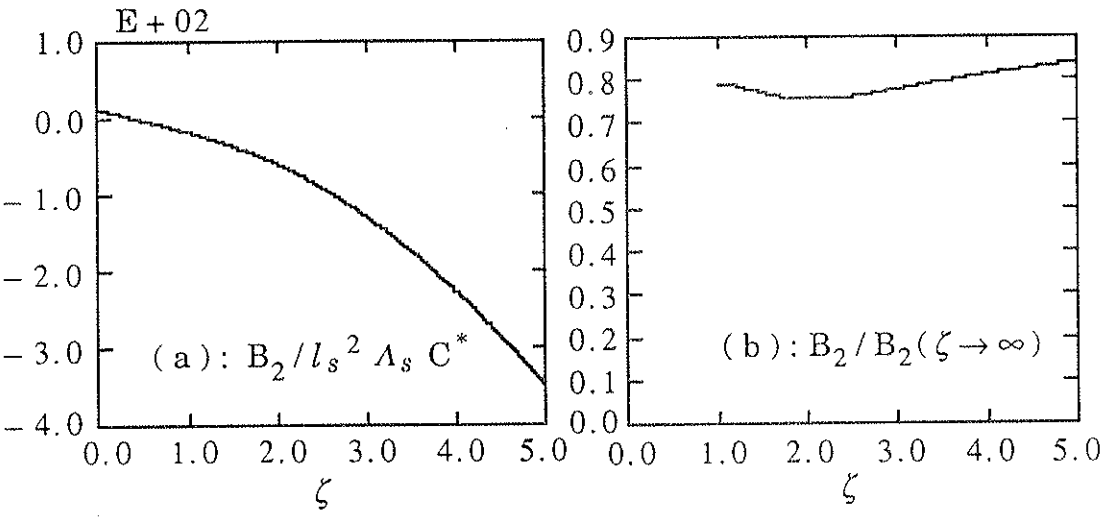

Figure 4.17a Profile of B_2 found by integration.

Figure 4.17b Profile of B_2 divided by its asymptotic value. B_2 nears its proper value by $\zeta = 5$.

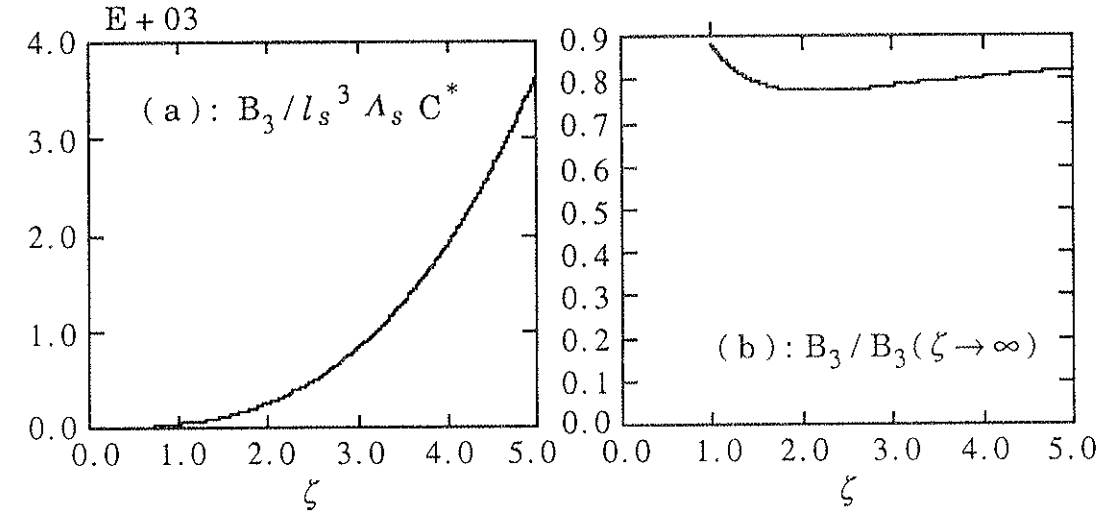

Figure 4.18a Profile of B_3 found by integration.

Figure 4.18b Profile of B_3 divided by its asymptotic value. B_3 nears its proper value by $\zeta = 5$.

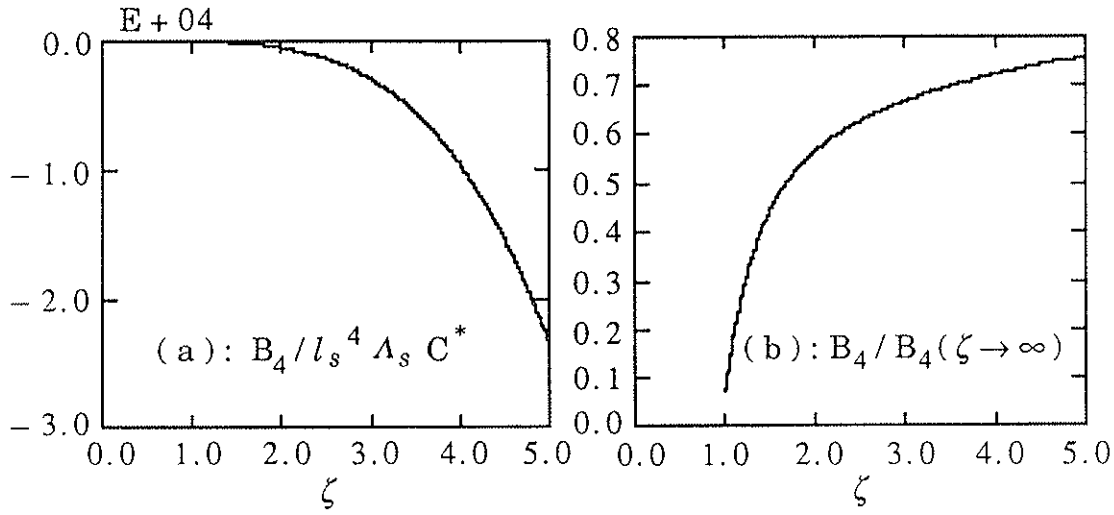

Figure 4.19a Profile of B_4 found by integration.

Figure 4.19b Profile of B_4 divided by its asymptotic value. B_4 nears its proper value by $\zeta = 5$.

The graphs that follow show the total solutions for V and B. The solutions in the layer are obtained by multiplying χ_k and B_k at each order by the appropriate constants (see (4.5.38), for example, for the relation between χ_k and V_k) and then summing over all orders. These "inner region" solutions are then matched to the solutions in the "outer region" by using the proper values of $A_L{}^*$, $A_R{}^*$, $B_L{}^*$, and $B_R{}^*$. (See the end of Section 4.5c, after equation (4.5.58), for a brief discussion of this point.) The results are presented for three values of layer width l.

$l / a = 0.005$ $b_r(r_s) = -1.93\,e-4$

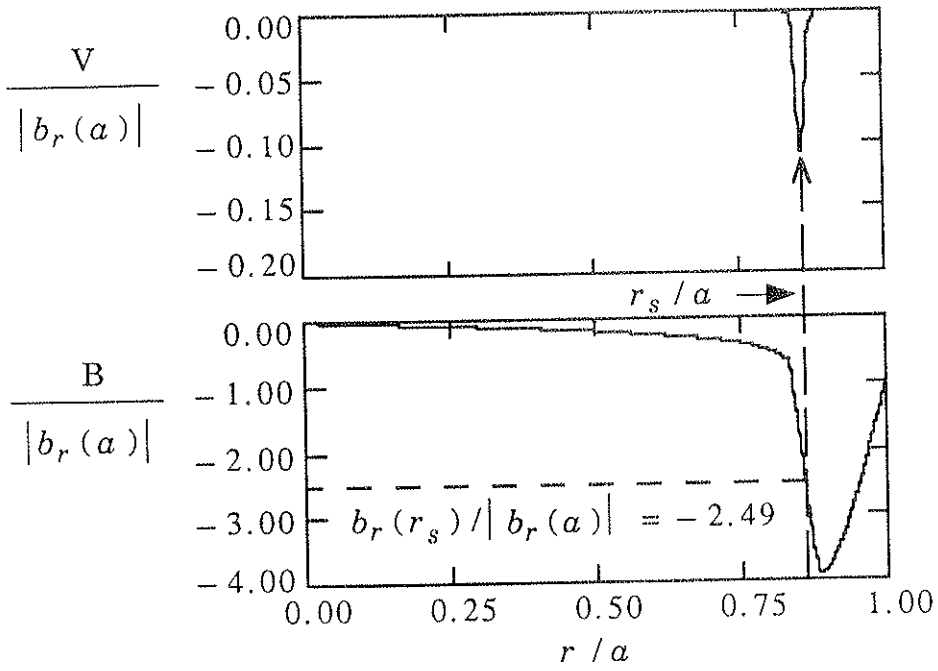

Figure 4.20 Radial profiles of V ~ $v_r(0, 24)$ (real part) and B = $b_r(0, 24)$ (imaginary part) illustrating the effects of the "dissipative layer." The value of $|b_r(r_s)|$ is smaller than that for the case of finite grad – λ alone. (Compare to Figure 4.10 .)

The profiles show the effects of the "dissipative layer." A velocity profile develops in the region of the layer. The b_r – profile is "pulled down" (in absolute value) to the left of the layer. The matching prevents it from curving as sharply as would be required in the presence of an unresolved singularity in current (or second derivative of b_r) . This results in a reduction in $|b_r(r_s)|$.

$l / a = 0.008$ $b_r(r_s) = -1.70\,e-4$

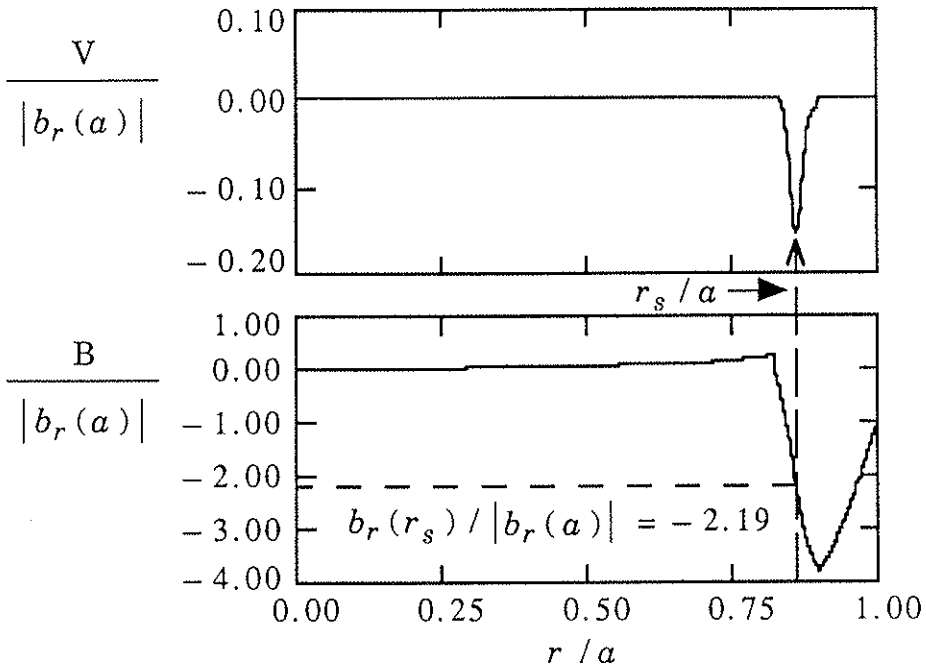

Figure 4.21 Radial profiles of V ~ $v_r(0, 24)$ (real part) and B = $b_r(0, 24)$ (imaginary part) for a larger layer. The value of $|b_r(r_s)|$ is reduced further.

It is worthwhile to note that as the layer gets larger, the calculated profiles of b_r peak in the center and then change sign. In the case of the numerical solutions of the 3-D MHD equations, the large size of the radial velocity profile (see Figure 4.8) suggests the presence of a large layer. However, this non-monotonic behavior is not observed. (Compare with Figure 4.5 .) This lack of agreement indicates a breakdown in convergence for the computed solutions in the matching region. The variable in which

$l / a = 0.028$ $b_r(r_s) = -4.39\,e-5$

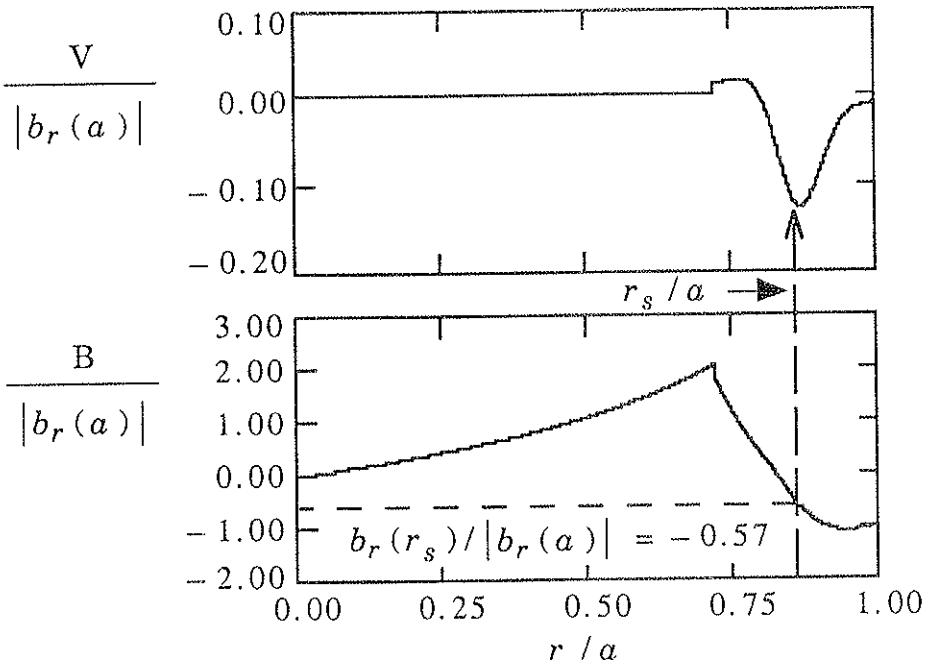

Figure 4.22 Radial profiles of V ~ $v_r(0, 24)$ (real part) and B = $b_r(0, 24)$ (imaginary part) for a large layer. The peaking of B at positive values indicates a lack of convergence.

the solutions are expanded is $\Lambda_s (x / r_s)$. If the expansions are to converge in the matching region, this variable should be much less than one throughout. At the matching point, x_w , this condition amounts to the requirement: $(x_w / r_s) \ll (1 / \Lambda_s)$. Using equation (4.5.51) for x_w and the choice $w = 5$, this becomes $5\, l_s \ll 0.163$. The number on the right is precisely the half-width of the finite grad-λ region (normalized to r_s). Recall that this value of l_s is the largest value used in the expression for

$C^* = b_r(r_s)$, shown in Figure 4.12 . The above restriction indicates that this graph should not be taken too seriously for the larger values of l_s. In fact, if the profile is required not to change sign, the largest value which this analytic model will accomodate is about $l_s = 0.010$. Thus, the above small-layer solutions are not good predictors for the behavior of the solutions of the 3-D MHD code. However, they play an important role in understanding the physics, showing that the simple picture of the role of a dissipative layer developed in Section 4.3 is correct.

4.6 LARGE LAYER RESULTS AND CONCLUSIONS

The dissipative layers produced by the 3-D MHD code are large. The radial velocity profile is supposed to be confined to the inside of the dissipative layer. Figure 4.8 shows that the profile for the n = 24 mode occupies the entire finite grad-λ region. Thus, the picture which has been developed — a small dissipative layer matched to a region of finite grad-λ — cannot be applied directly to these results. However, the concept of the dissipative layer remains valuable. Indeed, the definition of the layer width, l , can be rewritten in terms of the normalized "code units" of Chapter 2 :

$$l = \left[\frac{\nu_0 \eta}{|F_s'|^2} \right]^{\frac{1}{6}} = \left[\frac{\nu^{1/2}}{(\lambda_s a)(nka)\left(\frac{B_{\theta 0}(r_s)}{B_{z 0}(0)} \right) S} \right]^{\frac{1}{3}} , \qquad (4.6.1)$$

with the normalized viscosity given by:

$$\nu = \frac{(\text{rhocon}) \left(\frac{\Delta r}{a} \right)^2}{\left(\frac{\Delta t}{\tau_R} \right)} . \qquad (4.6.2)$$

Then, with the numerical values for n = 24 from Tables 4.9 and 4.10, and

for a "base case," : rhocon = 2.0 S = 1000

with a standard grid: $(\Delta r / a) = 1.59\text{ e}-2$ $(\Delta t / \tau_R) = 2.00\text{ e}-4$,

the value of the layer width is $l / a = 0.082$. The region between the resonant surface and the wall, half of the finite grad$-\lambda$ region and a distance of $0.14a$, does not even extend two layer widths. The large radial velocity profile produced by the 3$-$D MHD code is consistent with the picture of a dissipative layer in which the effects of η, ν_0 are characterized by a single parameter, l. The problem is in finding solutions in the large layer case.

The method chosen to find these solutions is direct integration of the equations describing the layer. These equations are restated below, in terms of $v = (r - r_s) / r_s$, the distance from the layer center normalized to the position of the layer center:

$$v \frac{\partial^2 B}{\partial v^2} + v \frac{\partial B}{\partial v} + \left\{ v \left[(\lambda_s r_s)^2 (1 - \Lambda_s v)^2 - \nu_s{}^2 - 1 \right] + \Lambda_s \right\} B$$

$$= l_s{}^3 \left[\frac{\partial^4 (i V)}{\partial v^4} + 4 \frac{\partial^3 (i V)}{\partial v^3} + (1 - 2\nu_s{}^2) \frac{\partial^2 (i V)}{\partial v^2} + \right.$$

$$\left. (1 - 4\nu_s{}^2) \frac{\partial (i V)}{\partial v} + (\nu_s{}^4 + \nu_s{}^2 - 1)(i V) \right] \qquad (4.6.3)$$

$$v (i V) = -l_s{}^3 \left[\frac{\partial^2 B}{\partial v^2} + \frac{\partial B}{\partial v} - (1 + \nu_s{}^2) B \right] \qquad (4.6.4)$$

These equations are sixth$-$order in $(i\ V)$ or B, and lowest$-$order in an expansion in v. (Here i explicitly shows the phase relation between the

complex amplitudes V and B.) The one exception to this ordering in v is the λ term on the left side of equation (4.6.3) . The value of λa varies from $\lambda a = \lambda_0 a = 2.950$ to $\lambda a = 0$ across the finite grad$-\lambda$ region. This is an important variation, and the squared term multiplying $(\lambda_s r_s)^2$ has been included to account for it. The range of integration is taken to be the region over which the velocity perturbation can be appreciable. This is assumed to be the entire finite grad$-\lambda$ region, in order to make contact with the 3$-$D code results.

Performing a numerical integration of this system to reproduce results calculated numerically via a 3$-$D MHD code seems somewhat redundant. However, the equations assume that η and ν_0 act together to create a dissipative layer characterized by a single parameter, the layer width. In the 3$-$D code, η and ν_0 were not linked to each other *a priori*. Now that the analytic treatment has shed some light on the physical role of the dissipative layer, the results of the integration will be used to see if the layer picture holds up in the code results.

The integration is carried out in the following way. First, equations (4.6.3)$-$(4.6.4) are written as a system of six coupled first$-$order differential equations in the six variables:

$$\mathrm{B} \ , \ \frac{\partial \mathrm{B}}{\partial v} \ , \ (i\,\mathrm{V}) \ , \ \frac{\partial (i\,\mathrm{V})}{\partial v} \ , \ \frac{\partial^2 (i\,\mathrm{V})}{\partial v^2} \ , \ \frac{\partial^3 (i\,\mathrm{V})}{\partial v^3} \ .$$

This set of equations is subject to a total of six boundary conditions. A finite difference program from the IMSL library, called DVCPR, is used to

find the solution which satisfies them. Then, the value of each variable at the beginning of the layer, $r = r_n$, is obtained from this solution. Finally, this set of initial conditions is used in an initial-value integration program (DVERK, mentioned in Chapter 3, Section 3.5), which gives values of the solution at regular intervals that can be used to make better plots.

Before the solutions are presented, a word must be said about the selection of proper boundary conditions. Two conditions on B come directly from those previously imposed on the solution for b_r in the finite grad-λ region. Specifically, these require b_r to match to the solution in the constant-λ region at $r = r_n$ (equation (4.5.14)) and to the field error at the wall (equation (4.5.15)). In the current notation, these conditions become:

$$\left(\frac{1}{r_s}\right)\left[\frac{\partial B}{\partial \upsilon}\right]_{\upsilon_n} - \beta\, B(\upsilon_n) = 0 \qquad \text{at } r = r_n\,, \tag{4.6.5}$$

where $\upsilon_n = (r_n - r_s) / r_s$ and β is given in equation (4.5.4),

and $$B(\upsilon_a) = b_r(a) \qquad \text{at } r = a\,, \tag{4.6.6}$$

where $\upsilon_a = (a - r_s) / r_s$. Two conditions on (i V) at $r = a$ come from the observation that both v_r and v_z go to zero there in the 3-D MHD code. An application of the incompressibility condition, equation (4.4.27), under these conditions gives the following:

$$(i\,\mathrm{V})_{\upsilon_a} = \left[\frac{\partial (i\,\mathrm{V})}{\partial \upsilon}\right]_{\upsilon_a} = 0 \qquad \text{at } r = a\,. \qquad (4.6.7)$$

The final two conditions require a bit more care. These involve the behavior of $(i\ \mathrm{V})$ and its derivatives at $r = r_n$. Since $\upsilon_r = 0$ outside the finite grad$-\lambda$ region, it is tempting to set the velocity perturbation and its derivatives to zero there. However, this ignores the fact that $r = r_n$ is also a point of singularity. The parameter Λ_s , the normalized slope of λ , is finite just to the right of $r = r_n$ and zero just to the left of it. This causes a jump in the profile of B and $(i\ \mathrm{V})$. To see this, assume that the velocity perturbation approaches zero as $r \to r_n$. Then, the right side of (4.6.3) can be ignored, giving:

$$\frac{\partial^2 \mathrm{B}}{\partial \upsilon^2} + \frac{\partial \mathrm{B}}{\partial \upsilon} - \left(1 + \nu_s{}^2\right)\mathrm{B} \sim -\left[\left(\lambda_0\, r_s\right)^2 + \frac{\Lambda_s}{\upsilon}\right]\mathrm{B}\ . \qquad (4.6.8)$$

Using this in (4.6.4) gives:

$$(i\ \mathrm{V}) \sim l_s{}^3\left[\frac{\left(\lambda_0\, r_s\right)^2}{\upsilon} + \frac{\Lambda_s}{\upsilon^2}\right]\mathrm{B}\ . \qquad (4.6.9)$$

The term proportional to Λ_s jumps to zero at the point $r = r_n$, and the value of the velocity changes by this amount. Since the velocity is assumed to be zero just inside $r = r_n$, the velocity at $r = r_n$ can be given by this jump. This will be the fifth boundary condition:

$$(i\ \mathrm{V})_{\upsilon_n} = l_s{}^3\left(\frac{\Lambda_s}{\upsilon_n{}^2}\right)\mathrm{B}(\upsilon_n)\ . \qquad (4.6.10)$$

The final boundary condition is obtained by setting the right side of (4.6.3) equal to zero. This is consistent with what has already been done to obtain (4.6.8) and (4.6.10).

The profiles that result from the above integration procedure are shown in the following figures. The first set is for a "medium-sized" layer with $l/a = 0.034$. Note that the b_r-profile is free from the central peaking and sign changes which plagued the analytic solution for a layer

$l / a = 0.034$ $\qquad\qquad$ $b_r(r_s) = -5.56\,e-5$

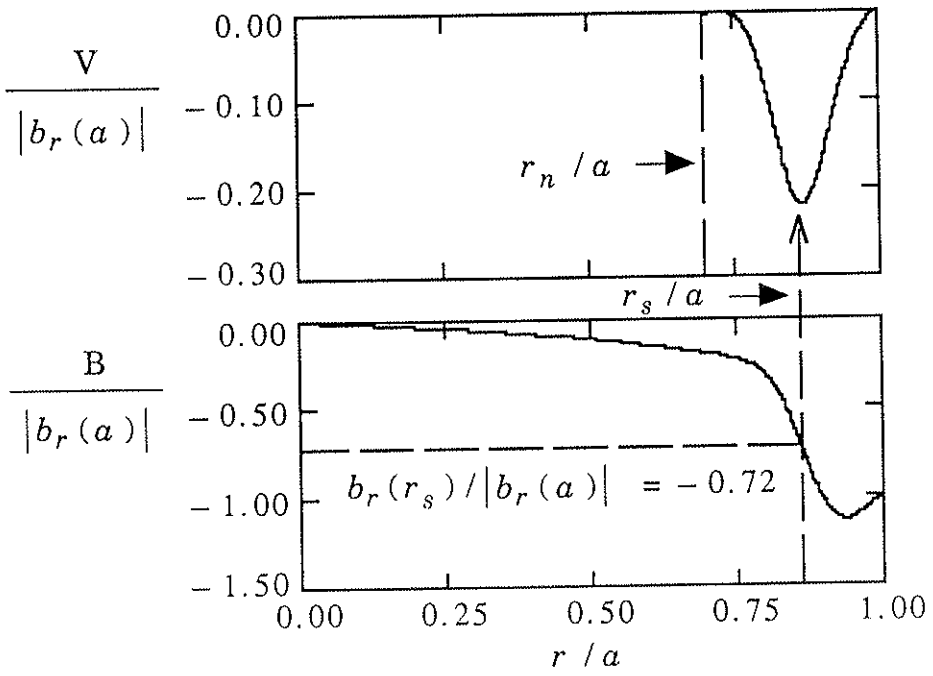

Figure 4.23 Radial profiles of V ~ $v_r(0, 24)$ (real part) and B = $b_r(0, 24)$ (imaginary part) for a "medium-sized" layer. The peaking of B at positive values is gone.

only slightly smaller in Figure 4.22. This shows the success of the current approach. The effect of the large smoothing around the resonant surface is still to "pull down" (in absolute value) the center of the profile and reduce $|b_r(r_s)|$. The radial velocity perturbation has now expanded to occupy most of the finite grad$-\lambda$ region. In the second set, the results for a large layer, with $l/a = 0.082$, are shown. This is exactly the "base case" from the 3-D MHD code. Note that the b_r-profile is monotonic. In fact, both profiles compare quite well with those generated by the 3-D MHD code.

$l/a = 0.082$ $\qquad\qquad$ $b_r(r_s) = -3.865\,e-5$

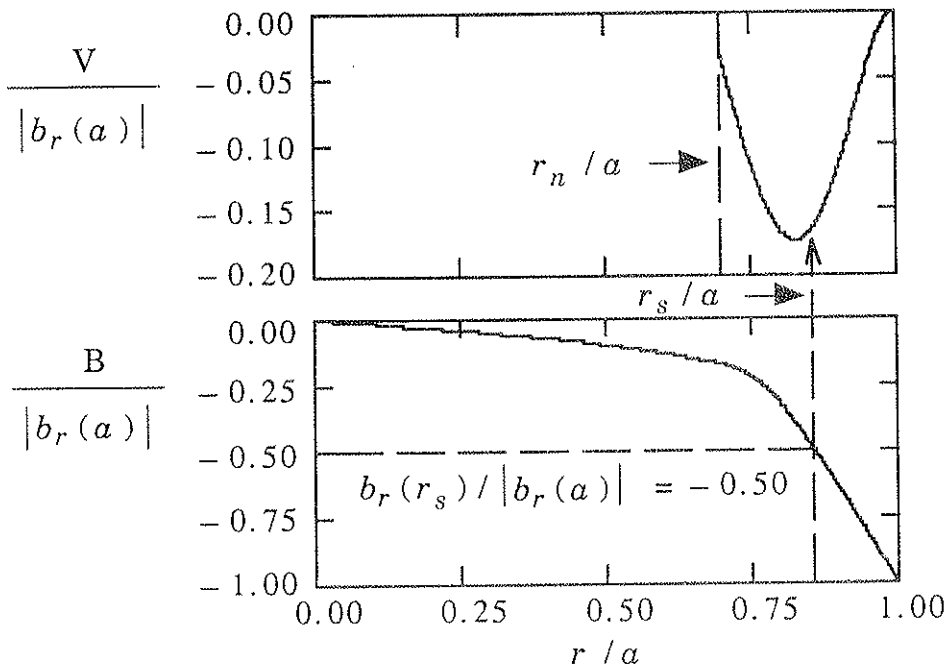

Figure 4.24 Radial profiles of V ~ $v_r(0,24)$ (real part) and B = $b_r(0,24)$ (imaginary part) for a large layer. These profiles show good agreement with those generated by the 3-D MHD code

(See Figures 4.5 and 4.8.) The fact that the v_r-profile jumps abruptly to zero at $r = r_n$ is a reflection of the boundary conditions that were imposed. It is an indication that the velocity perturbation does extend somewhat into the constant-λ region. This is also apparent in Figure 4.8 . A point in favor of the boundary conditions is that the value of $b_r(r_s)$ shown is almost exactly that produced by the 3-D MHD code.

A more detailed comparison of the results of numerical integration of the layer with the results from the 3-D MHD code can be made. The layer widths corresponding to the values of S and ν_0 used in the various MHD code scaling runs were calculated. Then, a series of numerical integrations was performed using these layer widths. The resulting values of $|b_r(r_s)|$ are plotted versus layer width in Figure 4.25 (for n = 24) and Figure 4.26 (for n = 12), along with the values found from the 3-D MHD code for the corresponding values of S and ν_0. The numbers agree to within a few percent in both cases. A similar comparsion of the size of the velocity perturbations (not shown here) shows agreement to within 10 to 20% for n = 24. This reduction in accuracy is due to the cut-off of the velocity profile at the edge of the finite grad-λ region. (The comparison is even less accurate for n = 12, as the profiles are even more drastically chopped by the jump at the boundary.) Note that every value of $|b_r(r_s)|$ is less than that for a vacuum profile ($|b_r(r_s)|_{VACUUM} = 4.71\ e-5$ for n = 24 and $|b_r(r_s)|_{VACUUM} = 3.11\ e-5$ for n = 12). Thus, the dissipative layer picture <u>is</u> able to reproduce the "healing" of the radial magnetic perturbation by the plasma observed in the 3-D MHD code.

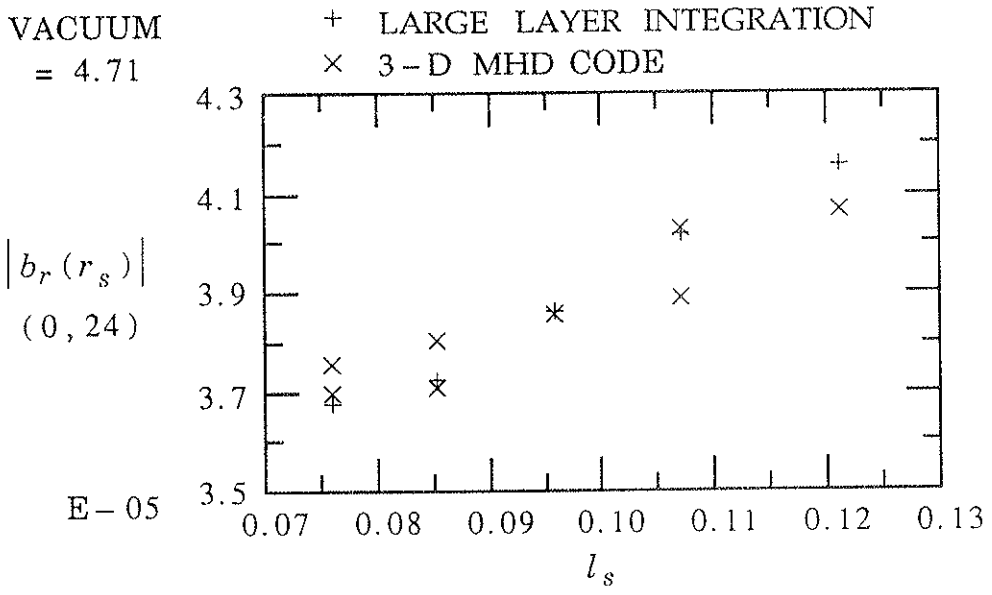

Figure 4.25 Comparison of $|b_r(r_s)|$ versus l_s for the large layer and 3-D MHD code calculations (n = 24). Note the good agreement.

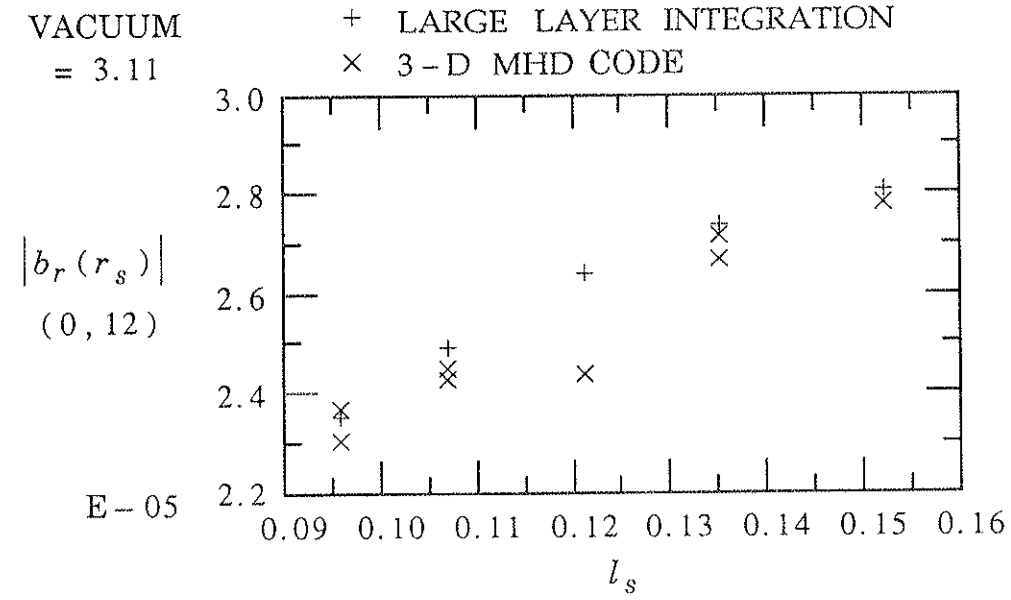

Figure 4.26 Comparison of $|b_r(r_s)|$ versus l_s for the large layer and 3-D MHD code calculations (n = 12). Note the good agreement.

The dissipative layer picture can be used to explain other properties of the velocity and magnetic field perturbations generated by the 3-D MHD code. In Section 4.3, it was observed that the perturbation amplitudes scale with S and ν_0 in a particular way. When represented as a power law — $B_{m,n}(S,\nu_0) = S^a \nu_0^b$ for magnetic perturbations and $V_{m,n}(S,\nu_0) = S^c \nu_0^d$ for velocity perturbations—the amplitude scaling showed the following behavior: a + b = 0 and c + d = − 1. These relations were taken as a sign that the physical effect introduced by finite η, ν_0 links velocity to magnetic field in a particular way. It can be shown that they follow from the presence of a dissipative layer. Assume that the perturbations are correctly given by the dissipative layer picture. Then, the basic parameter involving $S \sim 1/\eta$ and ν_0 is the layer width, l . In addition, generalizing from the case of v_r , the velocity perturbation is related to the velocity solution in the dissipative layer by a function of S and ν_0. The respective dependences are:

$$l \sim \left(\frac{\nu_0}{S}\right)^{1/6} \quad \text{and} \quad v_r \sim (S\nu_0)^{-1/2} V \ , \quad \text{from Table 4.3.}$$

Scaling the perturbation amplitudes as power laws:

$$B_{m,n}(S,\nu_0) = l^p \tag{4.6.11}$$

and

$$V_{m,n}(S,\nu_0) = l^q S^{-1/2} \nu_0^{-1/2} \ , \tag{4.6.12}$$

then gives:

$$B_{m,n}(S,\nu_0) = S^{-p/6} \nu_0^{p/6} \tag{4.6.13}$$

and $$V_{m,n}(S,\nu_0) = S^{-q/6-1/2}\ \nu_0^{\,q/6-1/2}\ . \qquad (4.6.14)$$

Thus, the scaling exponents for the magnetic perturbations always sum to zero and those for velocity perturbations sum to -1. The linking of velocity to magnetic field pertubations observed in the results from the 3-D MHD code arises from the coupling introduced by a dissipative layer.

The actual scaling exponents obtained from numerical integration of the dissipative layer are presented below. Only the radial perturbations are found through the integration. The values of layer width used to obtain the scaling are the same ones that appear in Figures 4.25 and 4.26 . They were calculated from the values of S and ν_0 used in the various 3-D MHD code scaling runs so that a comparison could be made. Values of the scaling exponents "p" and "q" can then be obtained in the manner described prior to Table 4.1 in Section 4.3 . (Note that the extra S , ν_0 terms in (4.6.12) get moved to the left side of the equation since the velocity solution in the layer is scaled by these factors.) To facilitate comparison to the 3-D MHD code scaling laws cited in the previous paragraph, the dissipative layer scaling laws of (4.6.13) and (4.6.14) are rewritten as $B_{m,n}(\eta,\nu_0) = S^{\alpha}\nu_0^{\,\beta}$ and $V_{m,n}(\eta,\nu_0) = S^{\gamma}\nu_0^{\,\delta}$, where:

$$\alpha = -p/6 \qquad \beta = +p/6 \qquad (4.6.15)$$

and $$\gamma = -q/6 - 1/2 \qquad \delta = +q/6 - 1/2\ . \qquad (4.6.16)$$

The values of "α," "β," "γ," and "δ" are presented in the tables that follow. They show reasonable agreement with the corresponding values of

"a," "b," "c," and "d" shown in Tables 4.1 and 4.2, obtained from the 3-D MHD code results. Thus, even though η and ν_0 occur independently in the 3-D MHD code, their effects can be described by a single parameter, the layer width.

Table 4.11: $B_{m,n}(\eta, \nu_0) = S^{\alpha} {\nu_0}^{\beta}$

m , n	COMPONENT	α	β	$\alpha + \beta$
0 , 12	r	- 0.064	0.064	0.000
0 , 24	r	- 0.047	0.047	0.000

Table 4.12: $V_{m,n}(\eta, \nu_0) = S^{\gamma} {\nu_0}^{\delta}$

m , n	COMPONENT	γ	δ	$\gamma + \delta$
0 , 12	r	- 0.492	- 0.508	- 1.000
0 , 24	r	- 0.410	- 0.590	- 1.000

It has been shown that the dissipative layer picture applies even for the large layers expected in the 3-D MHD code. In these cases, it reproduces the "healing" of the radial magnetic perturbation by the plasma. To what extent will this "healing" be relevant to real plasmas? At the end of Section 4.5 it was suggested that the graph of $C^* = b_r(r_s)$ versus

l_s shown in Figure 4.12 is not useful past about $l_s = 0.010$. This limitation is important because the range of l_s which shows the "healing" (a value of $|b_r(r_s)|$ below that for a vacuum profile) is excluded. This shortcoming of the analytic model can be overcome by applying the present numerical integration scheme. Graphs of $b_r(r_s)$ versus l_s which have been extended to large layers are shown below, for n = 12 and n = 24. Various important values of l_s have been indicated.

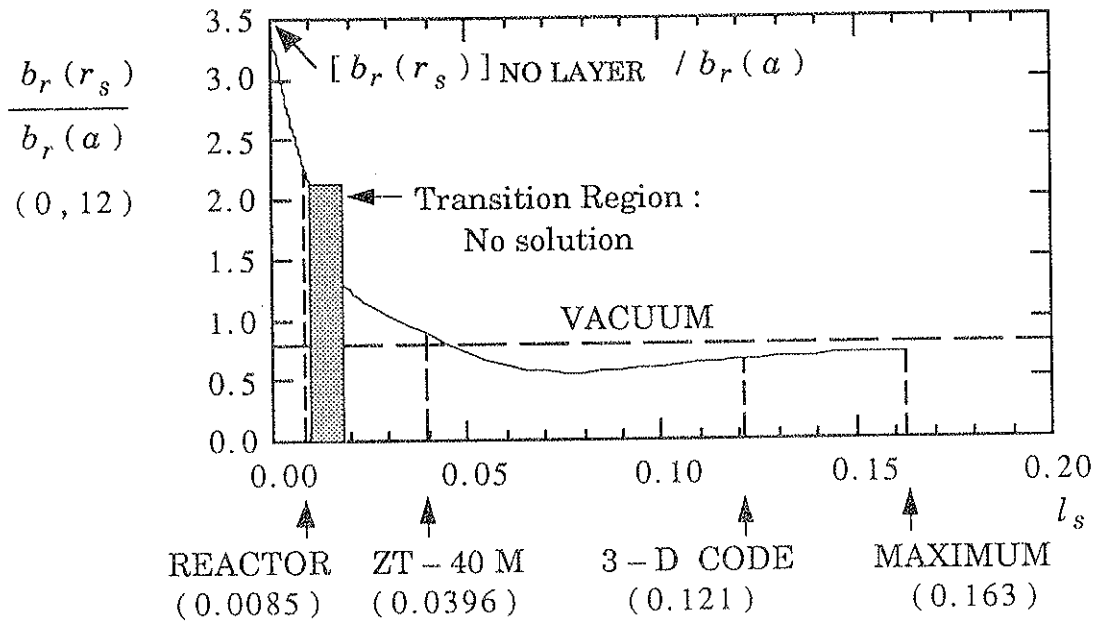

Figure 4.27 Plot of $b_r(r_s) / b_r(a)$ as a function of l_s, for n = 12. Large layers and "healing" of the magnetic perturbation are now included. The value of l_s labeled REACTOR was obtained by scaling the temperature in ZT – 40M: $T_{REACTOR} \sim 100\, T_{ZT-40M}$.
(The shaded area is a transition region in which neither method of solution works well.)

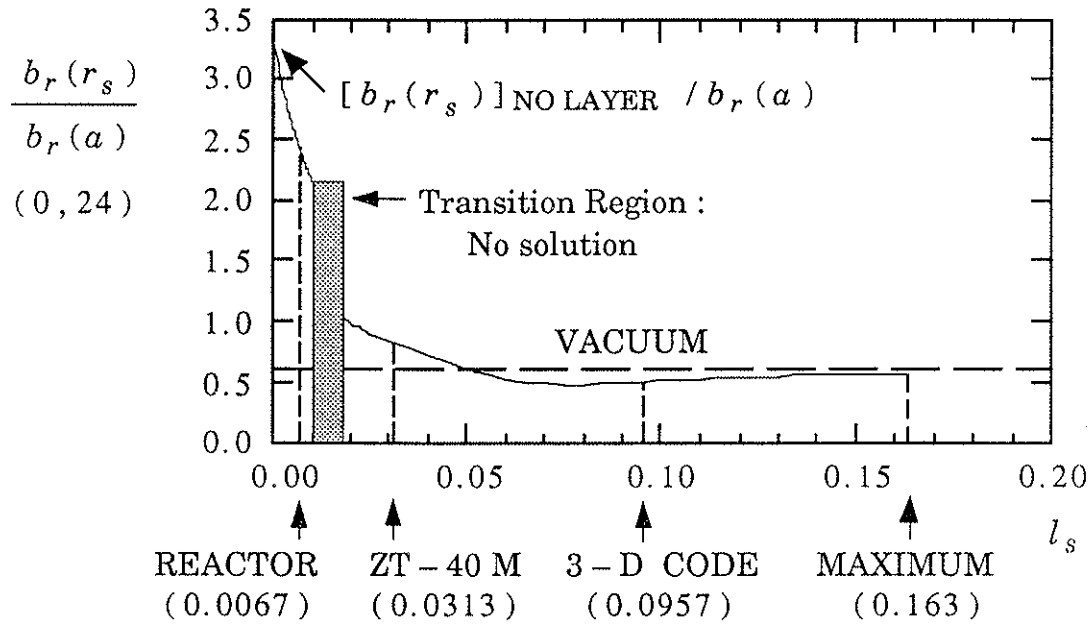

Figure 4.28 Plot of $b_r(r_s) / b_r(a)$ as a function of l_s, for n = 24. Large layers and "healing" of the magnetic perturbation are now included. The value of l_s labeled REACTOR was obtained by scaling the temperature in ZT – 40M: $T_{\text{REACTOR}} \sim 100\, T_{\text{ZT-40M}}$.
(The shaded area is a transition region in which neither method of solution works well.)

These graphs show that "healing" of a magnetic perturbation is not likely to occur at the values of η and ν_0 which characterize a plasma in the laboratory. However, they do show the importance of understanding the roles of both finite grad – λ and finite η, ν_0 on m = 0 radial magnetic perturbations. The presence of finite grad – λ alone (the l_s = 0 point on the graphs) makes the radial magnetic field at the m = 0 resonant surface

much worse than would be expected from a constant-λ calculation. This negative effect can then be balanced by the inclusion of a dissipative layer connected with finite η, ν_0. The existence and size of both of these effects must be understood if the behavior of field errors in the presence of a realistic plasma is desired, at least to the extent that such behavior is examined in the context of a stable, static equilibrium.

REFERENCES

[1] R. I. Pinsker and A. H. Reiman, Phys. Fluids **29**, 782 (1986).

[2] S. Chandrasekhar and P. C. Kendall, Astrophys. J. **126**, 457 (1957).

[3] M. Abramowitz and I. A. Stegun, *Handbook of Mathematical Functions* (Dover, New York, 1965), p. 358.

[4] H. P. Furth, J. Killeen, and M. N. Rosenbluth, Phys. Fluids **6**, 459 (1963).

[5] *Ibid.*, p. 463.

[6] J. M. Greene, lecture notes entitled *Introduction to Resistive Instabilities*, Centre de Recherches en Physique des Plasmas, Ecole Polytechnique Federale de Lausanne, LRP 114/76 (1976).

[7] Same as (6).

[8] M. Abramowitz and I. A. Stegun, *Handbook of Mathematical Functions* (Dover, New York, 1965), p. 358.

[9] *Ibid.*, p. 504.

[10] *Ibid.*, p. 253.

[11] E. Kamke, *Differentialgleichungen* (J. W. Edwards, Ann Arbor, Michigan, 1945).

[12] M. Abramowitz and I. A. Stegun, *Handbook of Mathematical Functions* (Dover, New York, 1965), p. 258.

[13] ICSICU, DCSQDU, and ICSEVU were described in the November, 1975 version of the IMSL manual. DVCPR, mentioned in Section 4.6, was described in the June, 1982 version. For further information , contact:

IMSL
Customer Relations
2500 ParkWest Tower One
2500 CityWest Boulevard
Houston, Texas 77042 – 3020

CHAPTER 5

NUMERICAL RESULTS FOR AN EVOLVING RFP EQUILIBRIUM

5.1 INTRODUCTION

In the previous chapters, attention was focused on the interaction between perturbations induced by external field errors and a static RFP equilibrium. The equilibrium fields were not allowed to evolve away from those of the initial, stable state. This prevented resistive diffusion from producing a new equilibrium that would allow plasma instabilities to grow. Thus, the effects of the externally-induced perturbations on the equilibrium were isolated from those due to saturated instabilities.

The results showed that the magnetic islands that may be expected from externally-induced perturbations of realistic size are small. Given this, it was asserted that these perturbations should not dominate those produced by the growth of plasma instabilities, in the experiments considered. The behavior of resistive MHD instabilities has shown some promise as a means of explaining the physics of the RFP (see the discussion preceeding Figure 1.1 in Chapter 1). Thus, it is important to verify that these instabilities, and not the field errors, will be responsible for the physical effects observed in an experiment and determine what influence, if any, the field errors have on these modes.

Numerical simulations of the response of a plasma with a time-evolving equilibrium and growing instabilities to external field errors were performed to address this question. The details of the 3-D MHD code have already been given in Chapter 2, Section 2.3. The field errors chosen for consideration were those associated with the toroidal coil set of ZT-40M, as described in Section 2.4a. The size of the numerical grid and time interval can be obtained from Table 2.3. The overall calculation was basically the same as a "base case" (see Table 2.2) from Section 2.3 . The most important changes were that the resistivity was "turned on" in the equilibrium ($m = n = 0$) component of Ohm's law and that a different initial RFP equilibrium, one unstable to resistive instabilities, was chosen.

Results of the calculation are primarily presented in terms of magnetic energy spectra for the perturbations and plots of helical flux contours. Given the importance of nonlinear interactions in producing RFP sustainment,[1] an attempt to find analytic solutions for the perturbations showing the effects of the field-error boundary conditions was not attempted. The effects of the field errors on the final RFP state are most easily observed in the quantities mentioned above, as well as the magnetic and kinetic energies and the q-profile. Section 5.2 presents the RFP state produced by the simulation in the absence of field errors. Results from simulations with field errors are then given, and it is shown that the basic characteristics of the final state are indeed determined by the plasma instabilities. In Section 5.3, the effects of the field errors are demonstrated through an examination of the magnetic energy spectra of the

perturbations. Finally, in Section 5.4, the possibility of producing a desired RFP state while reducing the stochastic wandering of field lines is explored. This might be possible by manipulating the plasma instability spectrum through the introduction of specific helical "field errors."

5.2 SIMULATION OF THE RFP STEADY STATE

The numerical simulation of the MHD equations produced a steady state with a reversal of the symmetric ($m = n = 0$) component of the axial magnetic field. The results that follow are for the case of a perfectly-conducting boundary with no field errors. Plasma perturbations were initialized at a very low level. The resistive instabilities necessary to sustain the reversed state took a long time to grow to an appreciable size. By about $0.4\tau_R$, however, the resistive steady state had been reached. Figure 5.1 shows the total radial magnetic energy of the instabilities as a function of time. As can be seen, by $t = 0.4\tau_R$ the instabilities had stopped growing and saturated. The reversal of the symmetric component of the axial field in the final state can be seen by looking at the behavior of two different quantities: $F \equiv \langle B_z(a) \rangle / \langle B_z \rangle_R$, where $\langle \ldots \rangle$ denotes an angular average and $\langle \ldots \rangle_R$ signifies a radial and angular average, and $q = r\langle B_z \rangle / \langle B_\theta \rangle R$. Figure 5.2 is a plot of F versus time. A fairly steady negative value is reached, showing that the symmetric axial field at the edge of the plasma is opposite in sign to the radially-averaged symmetric axial field. The final q-profile, plotted in Figure 5.3, shows that the symmetric axial field has a region of reversed sign inside the plasma column, relative to the strong field on axis.

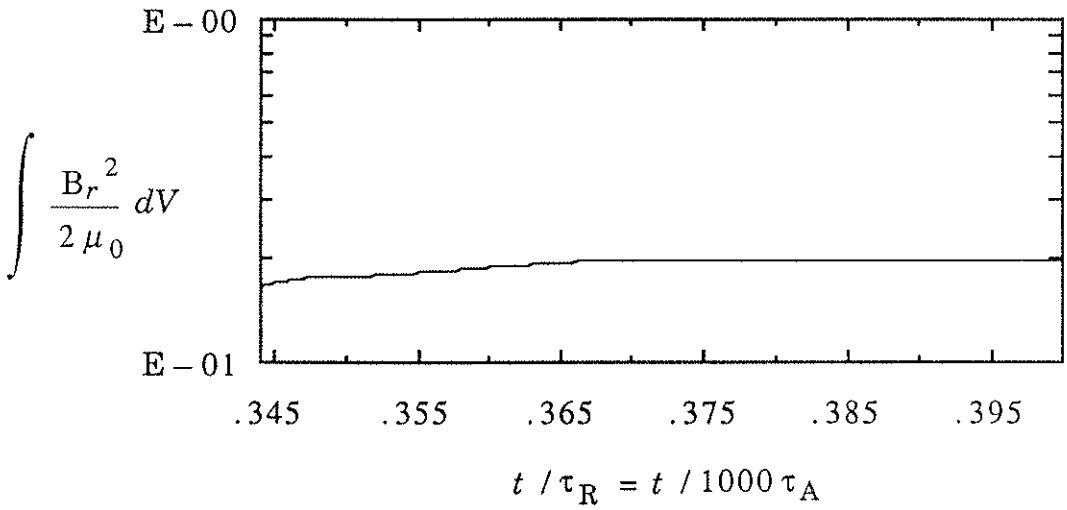

Figure 5.1 Plot of the magnetic energy in the radial magnetic field components as a function of time in the "no field error" case. Note that a steady state has been reached by $0.4\tau_R$.

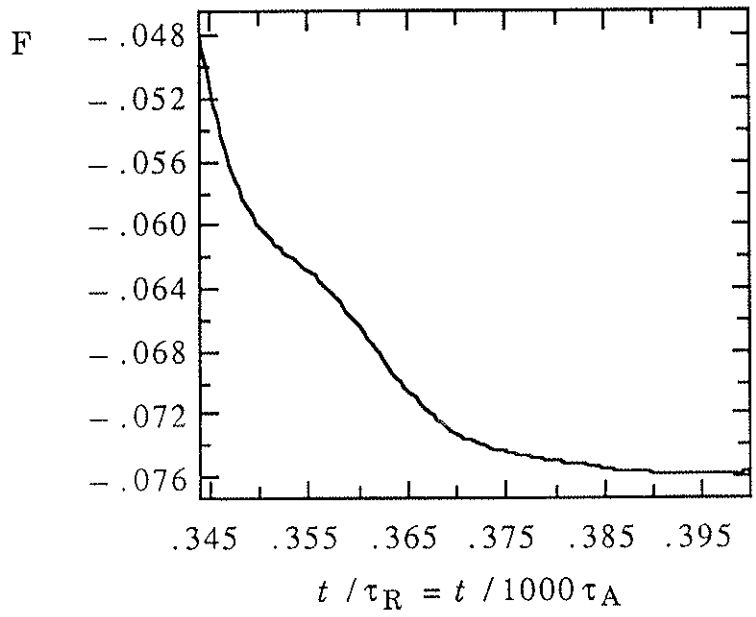

Figure 5.2 Plot of F versus time in the "no field error" case. The negative value indicates a steady state with reversed symmetric axial field.

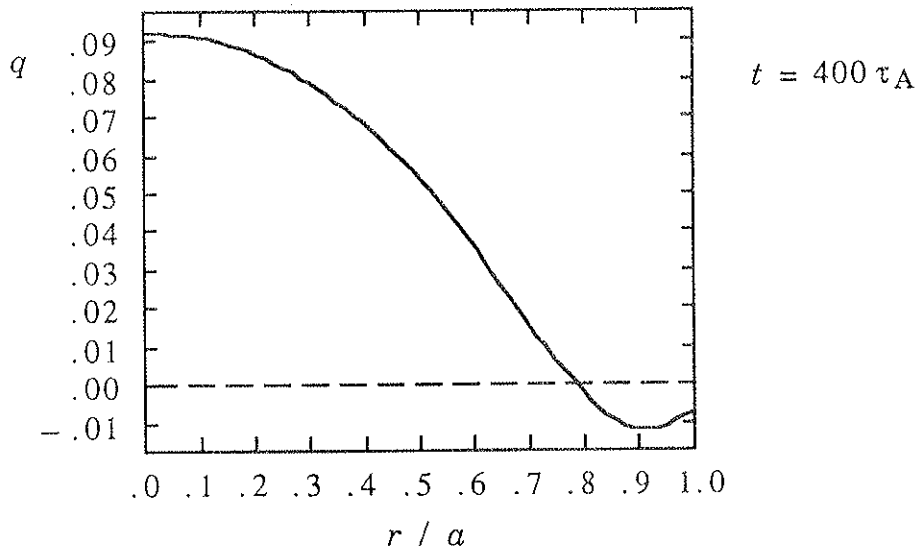

Figure 5.3 Radial profile of q at the conclusion of the "no field error" case. The negative values near the edge indicate a region of symmetric axial field reversal inside the plasma.

When external field errors were introduced at the boundary, a similar reversed steady–state was produced. As in Figure 5.1, Figure 5.4 shows total radial magnetic energy as a function of time. The resistive instabilities grew and saturated at a level almost identical to that shown in the previous figure. In this case, however, this occured by $t = 0.1\,\tau_R$. This indicates that the field errors, which introduced radial perturbations within the plasma that were much greater than those produced by the initial "noise" in the simulation, stimulated the growth of the plasma instabilities. Still, the resulting final state is quite similar to that of the "no error" case. The final value of F in Figure 5.5 is close to that shown in Figure 5.2. The q–profile of Figure 5.6 is practically identical to the one in

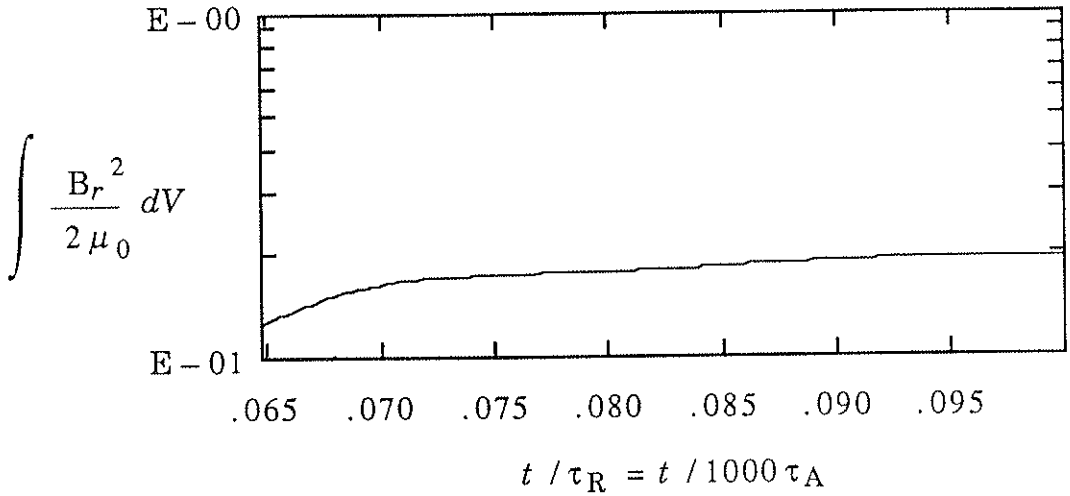

Figure 5.4 Plot of the magnetic energy in the radial magnetic field components as a function of time in the "field error" case. A steady state similar to that in the "no field error" case has been reached by $0.1\,\tau_R$.

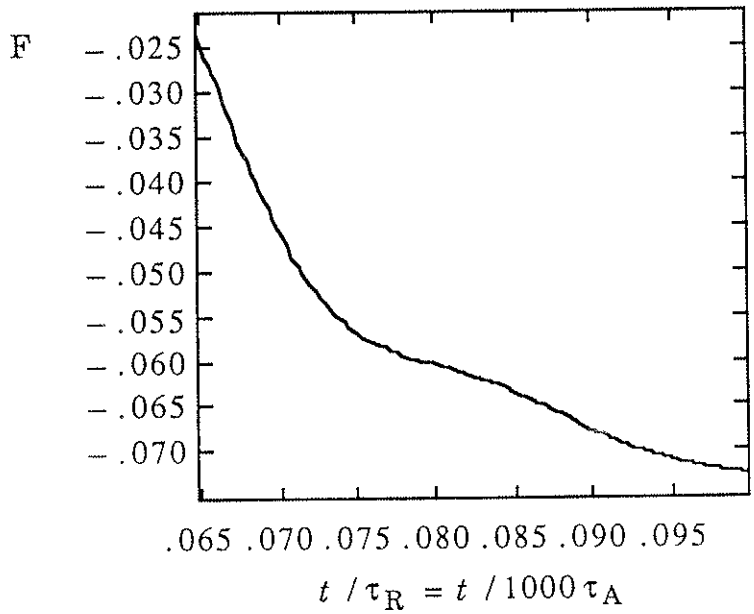

Figure 5.5 Plot of F versus time in the "field error" case. The negative value is close to that obtained in the "no field error" case.

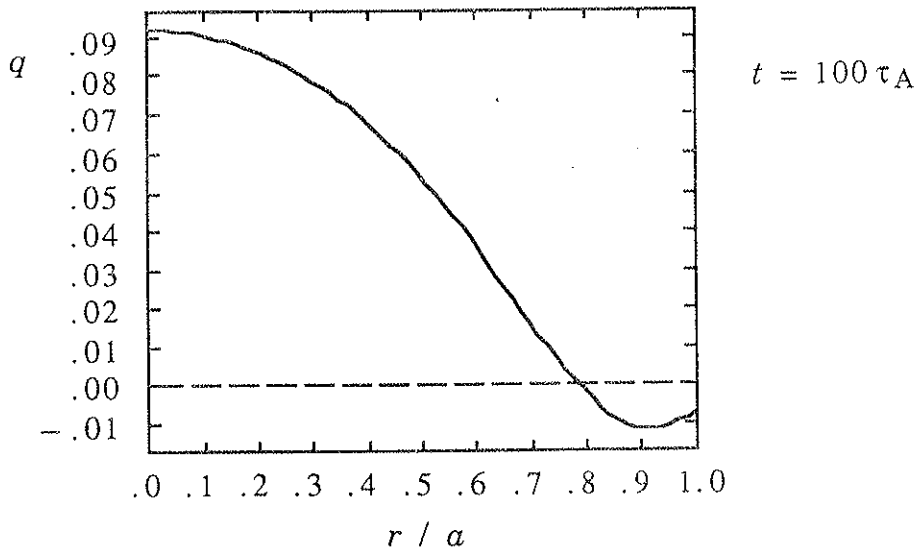

Figure 5.6 Radial profile of q at the conclusion of the "field error" case. The profile is nearly identical to that in the "no field error" case.

Figure 5.3 . Thus, the symmetric field profiles that are used to characterize the RFP state are the same whether or not field errors are present.

Non-symmetric field and velocity perturbations in the reversed steady-state were studied by varying the resistivity and viscosity in the calculation. The magnitudes of these perturbations, determined by both the saturation of resistive instabilities and the influence of the field errors at the boundary, should scale in a way that reveals which of these effects is dominant. The scaling was obtained in the manner described in Section 2.4 c of Chapter 2. Table 2.2, in Section 2.3, gives the range of variation of the resistivity parameter (S) and the viscosity parameter (rhocon).

Typically, perturbations to the symmetric equilibrium include both radial magnetic fields and flows around resonant surfaces. Thus, scaling relations for the radial magnetic energy ($EM_R = \int [B_r^2 / 2\mu_0] dV$) and the axial kinetic energy ($EK_Z = \int [V_z^2 / 2] dV$) were calculated. The energies were first plotted versus S, at constant rhocon, and versus rhocon, at constant S, on log-log plots. Then, the slopes of these plots were used to obtain simple power-law fits.

The power-law fits from the above "evolving RFP" case, in which both resistive instabilities and field errors were present, can be compared to those of the "static RFP" case of Chapter 4, where only field errors were included. The scaling relations for the "evolving RFP" case are:

$$EM_R = S^{0.170} \nu_0^{-0.166}$$

and

$$EK_Z = S^{-2.041} \nu_0^{-0.285}.$$

Although these energies contain contributions from all modes, an analysis of the magnetic field and velocity profiles shows that modes with m=1 make the largest contribution. Amplitude scaling for m=1 modes in the "static RFP" case was also performed, even though the results cited in Chapter 4 were only for m=0. For the leading mode, the energy scaling relations that resulted were:

$$EM_R(1,-16) = S^{0.304} \nu_0^{-0.338}$$

and

$$EK_Z(1,-16) = S^{-1.366} \nu_0^{-0.642}.$$

It is characteristic of the "static RFP" case that the EM_R scaling exponents almost sum to zero. (See Tables 4.1 and 4.2 for m = 0 modes.) This also occurs in the "evolving RFP" case, but these exponents are a factor of two smaller than those expected from the effects of field errors alone. Similarly, EK_Z in the "evolving RFP" case scales too strongly with S and too weakly with ν_0 by roughly a factor of two, compared to the "static RFP" case. It appears that the external field errors were not the leading influence on the perturbations.

The perturbations in the plasma behaved more like those produced by resistive instabilities. A recently published paper on the numerical simulation of reversed-field sustainment[2] asserts that the sustainment mechanism, in the context of the single-fluid MHD model, is dominated by modes with m=1 nonlinearly interacting with themselves only. As a consequence of this, it follows from the MHD equations that the m=1 magnetic fields in the steady-state (normalized to the symmetric fields) are independent of S and the m = 1 velocity fields scale with the resistivity (S^{-1}), like diffusion. This is basically what was observed in the results from the above "evolving RFP" case, even though that case had field errors imposed at the boundary. Modes with m=1 were observed to make the greatest contribution to both the radial magnetic and axial kinetic energies. The scaling of the radial magnetic energy implies that the amplitudes of the dominant m=1 radial fields scale only weakly with S: $B_r \sim S^{0.085}$. (The magnitudes of the symmetric fields were unaffected by S.) Even more notably, the axial kinetic energy scaling shows resistive-

diffusion-like behavior in the m=1 velocity fields: $V_z \sim S^{-1.02}$. The weak S scaling of B_r and the weak ν_0 scaling overall may be attributable to the choice of the time at which EM_R and EK_Z were measured. An attempt was made to choose a time at which each case was equally "relaxed." Some cases may not have been run long enough for oscillations in the energies to have damped out sufficiently, and too early a time may have been selected as a result. The general indication, however, is that edge field errors of a realistic size did not alter the symmetric fields that characterize the RFP steady state or the behavior of the instability-produced perturbations that sustain it.

5.3 FIELD ERROR EFFECTS ON THE RFP STEADY STATE

The field errors did have an effect on the RFP steady state reached in the simulation. As suggested in Section 2.4 d of Chapter 2, they determined which resistive instabilities grew and saturated to form the reversed steady state. This selection can best be observed in the magnetic energy spectra for the dominant instabilities, modes with m=1. The spectra show the total magnetic energy in a (1,n) mode as a function of toroidal mode number, n, and thus indicate the degree to which each (1,n) mode was excited. The following figures show the magnetic energy spectra at the end of the simulations described in Section 5.2. Figure 5.7 is for the case without field errors. The modes that were most strongly excited form a continuous band centered about n = -12, although the peak is rather narrow. Figure 5.8 is obtained from the case with field errors. Here, the spectrum is generally

broader, and the most strongly excited modes are discrete. The spacing between them indicates that the resistive instabilities which grew up to produce these perturbations had values of n which were multiples of four. This is precisely the characteristic of the m = 1 spectrum of the field errors, described in Section 2.4 c of Chapter 2 and illustrated there in Figure 2.4 b. Thus, the presence of external field errors influenced which of the resistive instabilities in the plasma grew to dominate the final steady state.

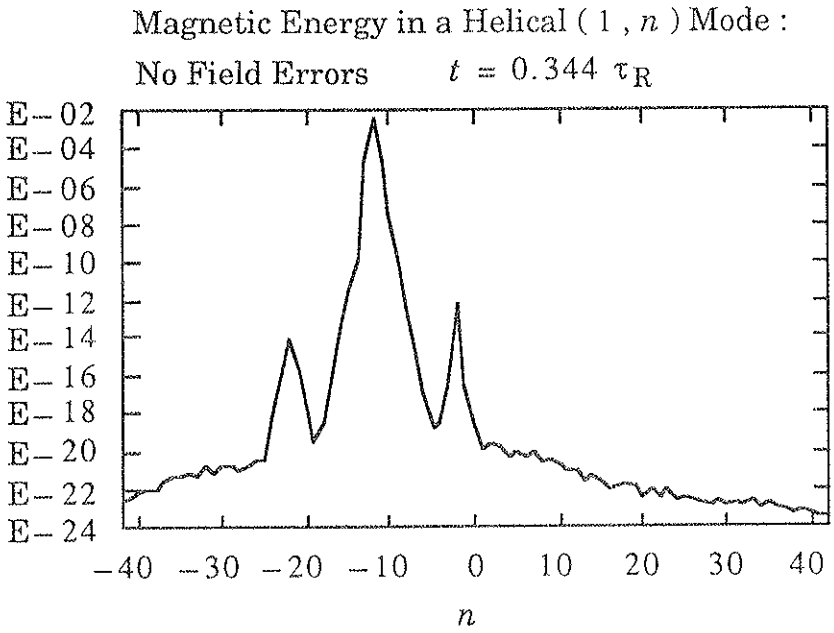

Figure 5.7 Plot of magnetic energy in a (1 , n) Fourier mode as a function of n at the conclusion of the "no field error" case. Note the single narrow peak. (For purposes of comparison to other plots, note that the quantity plotted in spectra of this type is only *proportional* to magnetic energy.)

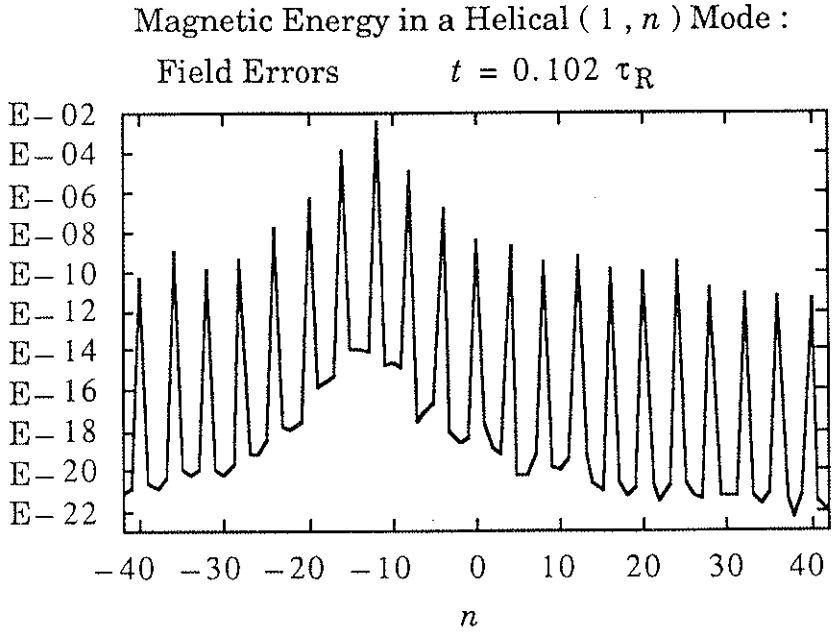

Figure 5.8 Plot of magnetic energy in a (1,n) Fourier mode as a function of n at the conclusion of the "field error" case. Note the discrete peaks.

This influence tended to persist even when the initial plasma perturbations could compete with those produced by the external field errors. As a part of the initialization of the simulation, non-symmetric magnetic fields were introduced along with the initial, symmetric RFP equilibrium. Mode numbers were selected so that the radial perturbations would excite the fastest-growing linear instabilities associated with the given equilibrium fields. In the simulations mentioned above, this initial plasma "noise" had a very low level: the amplitude of those perturbations was roughly ten orders of magnitude smaller than the ones produced by the field errors. Under those conditions, it may not seem

surprising that the instabilities with the same mode numbers as the field errors were the most excited, although more growth among highly unstable modes (n = – 10, – 11 for example) other than the n = – 12, which was also in the error spectrum, might have been expected. However, even when the level of the initial "noise" was equal to that of the field–error perturbations, modes with the same mode numbers as the field errors were still preferentially excited. This is illustrated in the spectrum shown in Figure 5.9 below. Both the "noise" and the field errors were initialized at a low ($B_r / B_\theta(a) \sim 10^{-5}$), but equal, level. The spectrum has filled in somewhat, but the discrete peaks are still apparent. When the initial level

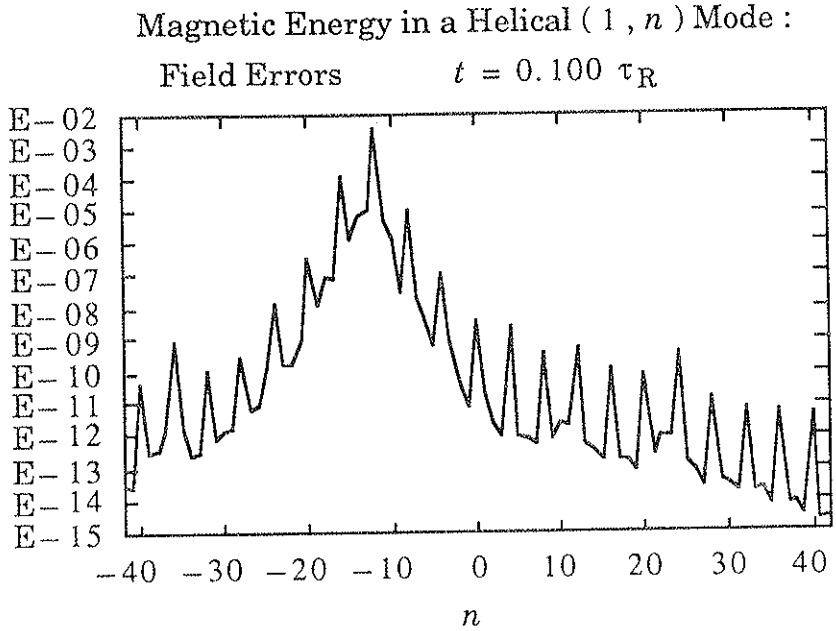

Figure 5.9 Plot of magnetic energy in a (1,n) Fourier mode as a function of n. This is the end of a case in which the level of initial plasma "noise" was equal to that of the field errors. The discrete peaks persist.

of plasma "noise" was made much greater ($B_r / B_\theta(a) \sim 10^{-2}$) than the level of the field errors ($B_r / B_\theta(a) \sim 10^{-5}$), the effect of the field errors on the spectrum disappeared. Figure 5.10 gives the spectrum for this case. It has a single, rather narrow peak similar to that of the "no error" case of Figure 5.7 . Although this latter case reflects the proper relative size of instability-produced and error-produced perturbations in the RFP steady

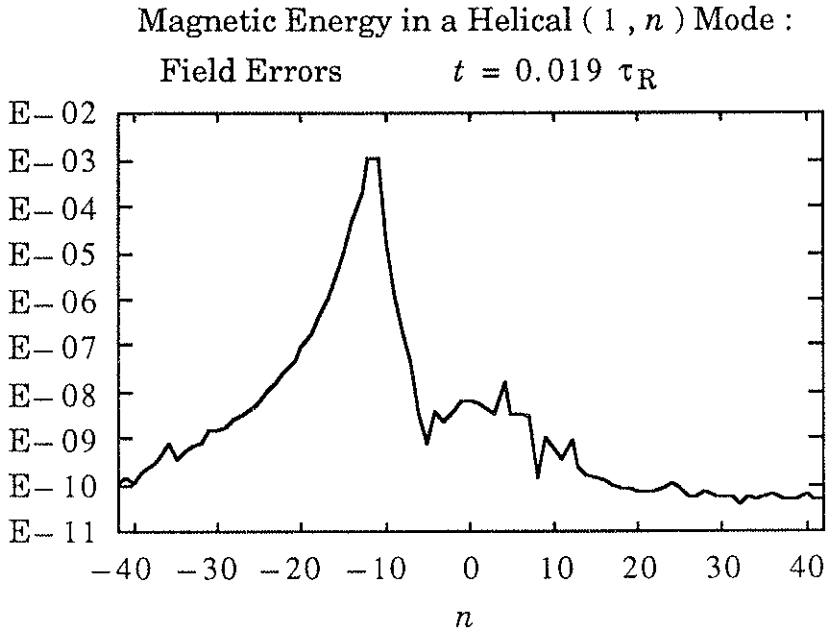

Figure 5.10 Plot of magnetic energy in a (1,n) Fourier mode as a function of n. This is the end of a case in which the level of initial plasma "noise" was much greater than that of the field errors. Only a single peak is evident.

state, the effect of the field errors on the spectrum should still be a source of concern. During start-up, or whenever the instabilities and the field

errors may be of a comparable size, the field errors can affect which modes will grow the most.

If resistive MHD instabilities are to be used in explaining the sustainment of field reversal, it is important that the instabilities measured experimentally are characteristic of the RFP and not of external influences, like field errors. The above results suggest that one way to determine whether this is the case is by analyzing the magnetic energy spectra of the perturbations. Measuring a range of $m=1$ perturbations with large values of $|n|$ to isolate discrete peaks in the spectrum caused by field errors, such as those present in Figures 5.8 and 5.9, would require a large array of coils.

Another way to detect the influence of field errors would be to look at the dominant $(0,N)$ mode produced by the nonlinear interactions of the $(1,n)$ modes. For a typical RFP q-profile, resonant surfaces for $m=1$ modes are closely spaced. Several unstable perturbations with neighboring values of n grow and interact nonlinearly to form an $m=0$ perturbation that is predominantly $N=1$. This is what might typically be expected from the physics of the RFP and what is observed at the end of the "no error" simulation. Such a $(0,1)$ perturbation produced the island shown in the $m=0$ helical flux plot of Figure 5.11 . In contrast, when the field errors impose a discrete spacing in n on the $m=1$ instability spectrum, such as the $\Delta n = 4$ observed above, the nonlinear interaction produces a dominant $m=0$ mode with $N=\Delta n$. This can be clearly observed in the

simulation results, even when the initial plasma "noise" was the same size as the field errors. Figure 5.12 shows a (0,4) island in the m=0 helical flux plot from the end of such a simulation. If, as in this case, the toroidal mode number of the field-error source is expected to be smaller than that of the instabilities, Δn — the spacing of the field-error harmonics — will be small compared to n. To detect m=0 modes with $N = \Delta n$, it would only be necessary to measure small values of N. This could be carried out using

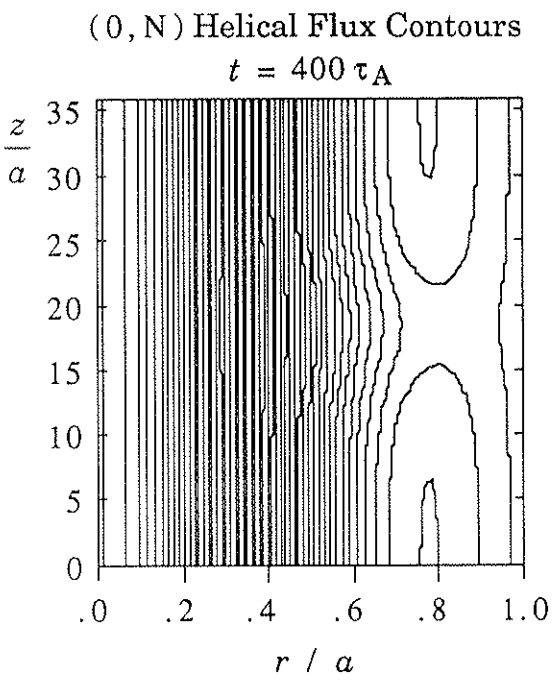

Figure 5.11 Plot of (0,N) helical flux contours at the conclusion of the "no field error" case. Note the (0,1) island.

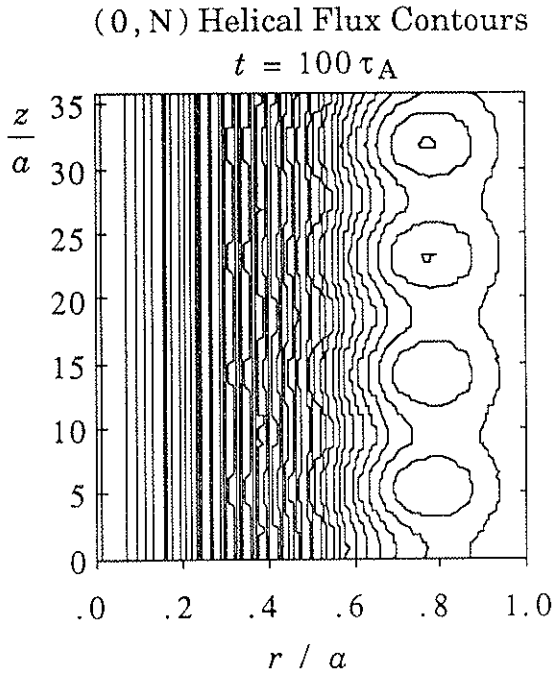

Figure 5.12 Plot of (0,N) helical flux contours at the conclusion of the "field error" case. Note the (0,4) island.

a reasonable number of coils. A dominant value of $N = \Delta n > 1$ would indicate some discreteness in the $m = 1$ spectrum that could be attributed to field errors. Thus, the nonlinear interactions of the resistive instabilities can be used to provide insight into whether the field errors are influencing which modes participate in the RFP steady state.

5.4 TAILORING THE RFP STEADY STATE

The ability of the field errors to influence the spectrum of the resistive instabilities gives rise to an interesting conjecture. A comparison of Figures 5.7 and 5.8 shows that the field errors "encouraged" some modes to grow, at the expense of the growth of others. Perhaps the purposeful introduction of a helical magnectic field with a certain $(1,n)$ mode number (called a "field error" in what follows) would make it possible for one or two modes to grow and maintain the RFP steady state, while suppressing the level of activity in the other modes. The growing modes would produce large islands, but the reduced amount of activity in other modes would lead to less island growth around closely-spaced resonant surfaces. This would result in less island-overlap and stochastic field-line wandering, and perhaps reduce transport.

At first, this idea was bolstered by the observation that a single $m = 1$ mode dominated the RFP steady state in a "no error" simulation. This simulation differed from the previous ones in a few details. Since fine-scale field errors were no longer being considered, the number of grid

points was reduced to make the code smaller and faster. Reducing the length of the cylinder by decreasing the aspect ratio to $R / a = 2$ also helped. The remaining grid allowed modes with $0 \leq m \leq 2$ and $-10 \leq n \leq 10$ to be resolved. In addition, the initial condition on the plasma "noise" was changed to eliminate any prejudice for a particular mode. At the end of the run, an RFP steady state dominated by a $(1,-5)$ mode was reached. Figure 5.13 shows a time plot of the radial magnetic energy in the most unstable $m=1$ modes. Late in time, the $(1,-5)$ energy has saturated at a

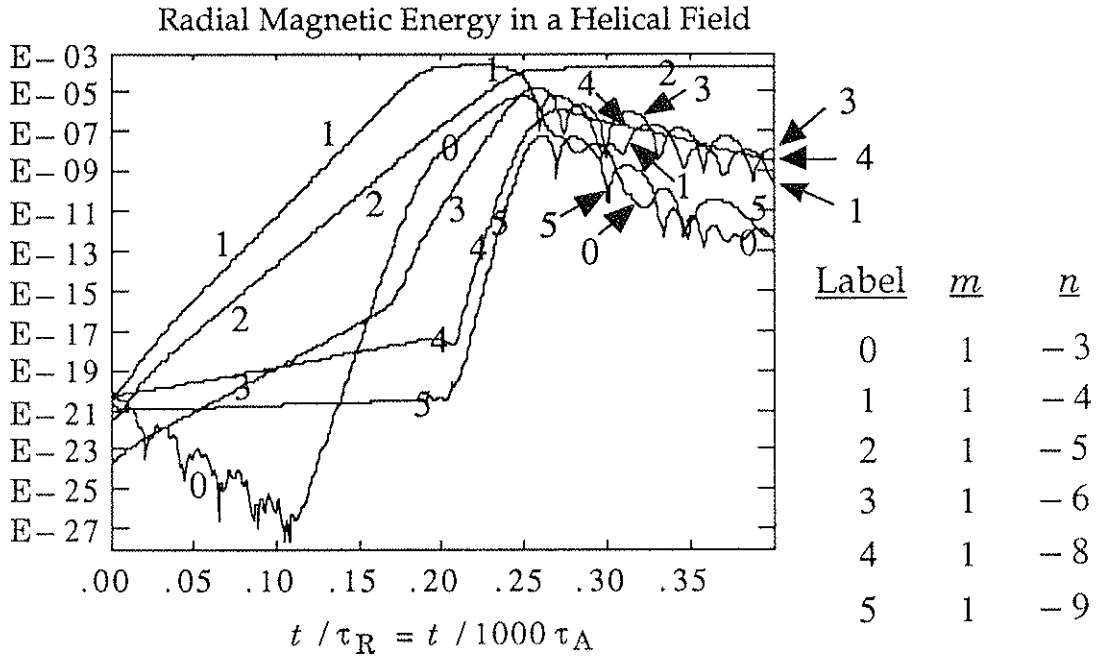

Figure 5.13 Plot of radial magnetic energy in a $(1,n)$ Fourier mode as a function of time in the "no field error" case. The $(1,-5)$ mode dominates at the end of the simulation. (For purposes of comparison to other plots, note that the quantity plotted in spectra of this type is only *proportional* to magnetic energy.)

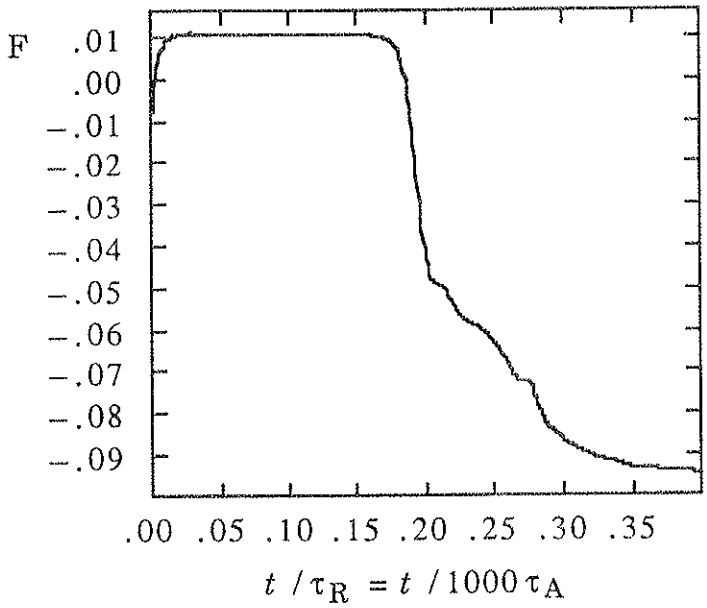

Figure 5.14 Plot of F versus time in the "no field error" case. The final steady negative value indicates a reversed steady-state.

level at least five orders of magnitude above that of the other modes, which are damping away. In Figure 5.14, F settles toward a steady negative value. This indicates that the final steady state is indeed reversed.

These results suggest that if the dominant mode were to be "seeded" at an appropriate level by the application of a "field error," it might grow and saturate before the other modes have a chance to grow appreciably. This did, in fact, occur. In that particular run, a radial magnetic field consisting of a single (1,−5) Fourier mode was applied at the plasma edge and treated in the same manner as the field errors described in Chapter 2. At the start of the simulation, the amplitude of the mode was set to be five orders of magnitude greater than the plasma

"noise" level. For practical purposes, it was assumed that the "field error" would be applied during start-up, when the resistive instabilities are small. Figure 5.15 is a plot of modal energy versus time similar to Figure 5.13 . The (1,-5) mode can be seen to grow quickly and saturate. During its growth, the other modes are at least eight orders of magnitude smaller in energy. After saturation, they are damped and fall an additional six orders of magnitude by the end of the simulation. The rapid growth of the dominant (1,-5) mode caused the steady state to be achieved more quickly than before. Figure 5.16 shows that a value of F similar to that of

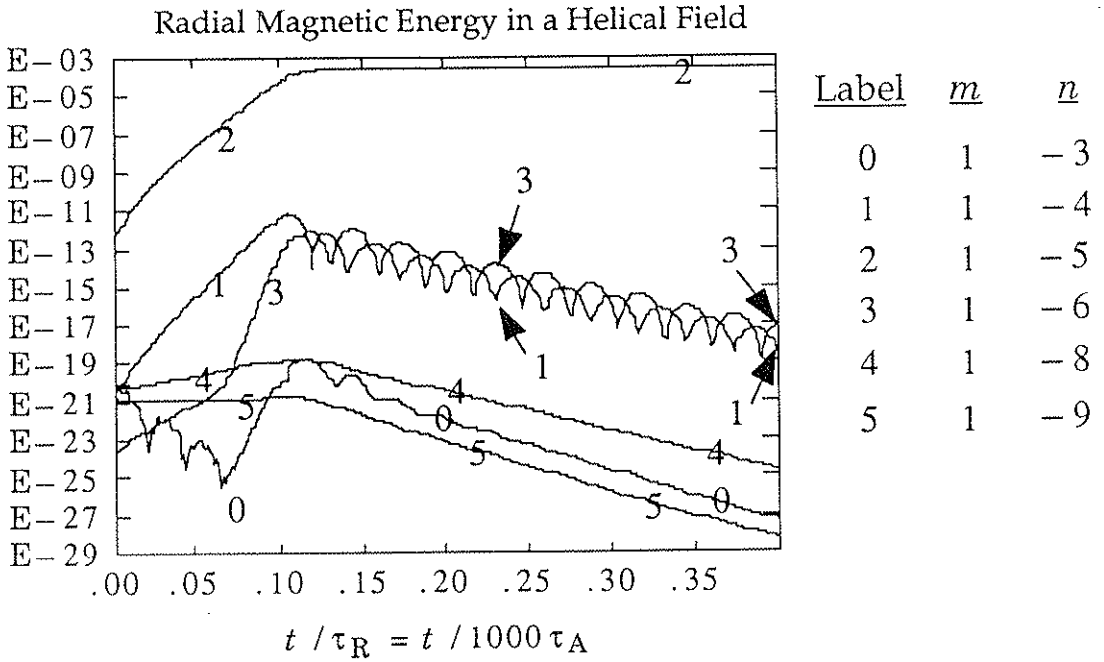

Figure 5.15 Plot of radial magnetic energy in a (1,n) Fourier mode as a function of time in the "field error" case. All modes but the (1,-5) are greatly suppressed at the end of the simulation.

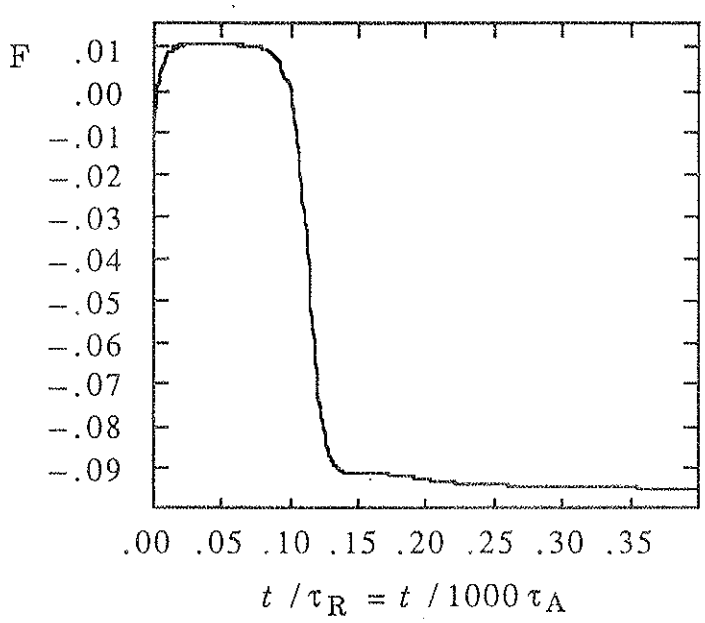

Figure 5.16 Plot of F versus time in the "field error" case. A steady negative value quite close to that of the "no field error" case is reached in half the time.

the "no error" case is reached, but in about half the time. Thus, a steady state close to that of the "no error" case, but with much less instability activity, can be produced.

This scenario would certainly be promising, were it not based on the rather unphysical premise that the RFP reaches an absolutely steady state that is dominated by one mode, rather than a state characterized by the exhange of energy between dominant modes over time. This is certainly not what one would expect from instability theory, nor is it observed experimentally. In fact, it turns out to be a numerical artifact caused by using too low a value of S. Conventional wisdom about this particular 3-

D MHD code holds that a qualitative change in results occurs around S = 6000.[3] Below this value, the magnetic energy gets "locked" into a single mode, as was observed. Above this value, the steady state exhibits some oscillatory behavior as energy is exchanged between several modes. This is a more realistic picture, and the cases described above were re-run with S = 6000 to take this into account.

The results at the higher S indicated that the introduction of a "field error" can spread the unstable m=1 modes somewhat. Figure 5.17 shows the radial magnetic energy in the six most unstable m=1 modes as

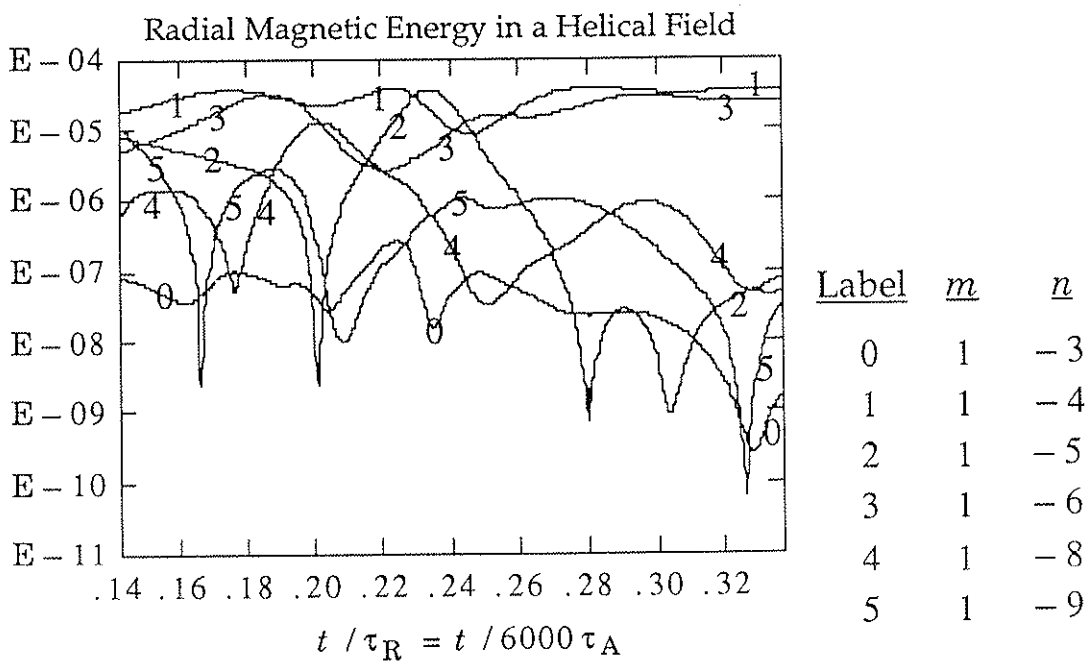

Figure 5.17 Plot of radial magnetic energy in a (1, n) Fourier mode as a function of time: "no field error" case at S = 6000. Both the (1, –4) and (1, –6) modes dominate at the end.

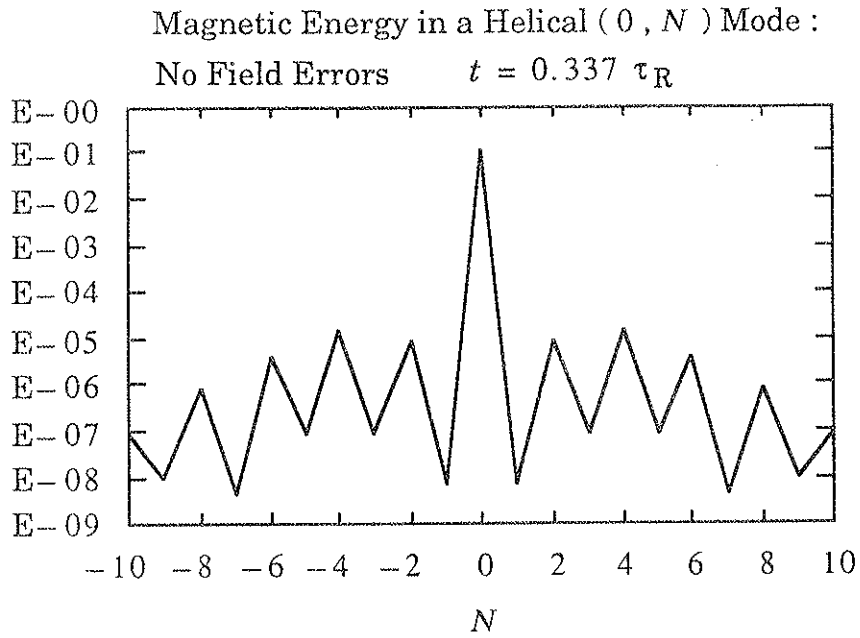

Figure 5.18 Plot of magnetic energy in a (0,N) Fourier mode as a function of n. This is the end of the "no field error" case at S = 6000. The dominant modes have |N| equal to a multiple of two.

a function of time for the later part of a "no error" run. The unstable modes shown undergo considerable interaction and sharing of the total energy up until about $t = 0.26\,\tau_R$. After this time, a reversed steady state is formed by the interaction of the (1 , -4) and (1 , -6) modes. As suggested in Section 5.3, the m=0 spectrum will be used to gain some insight into the n-spacing of the m=1 modes. Figure 5.18 gives the m=0 spectrum at the end of the run. The most prominent modes (apart from the equilibrium N = 0), have |N| equal to a multiple of two. This is not surprising because $\Delta n = 2$ for the dominant m=1 modes. Figures 5.19 and

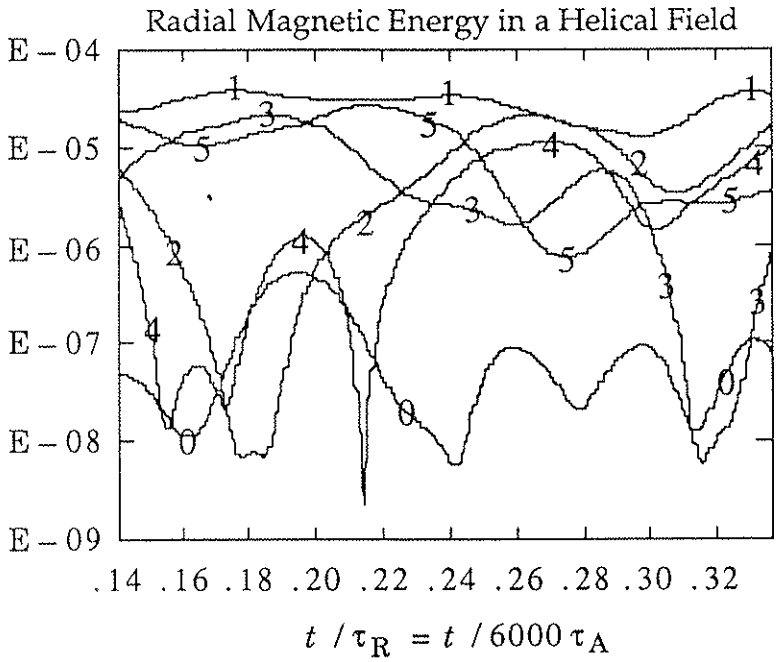

Label	*m*	*n*
0	1	−3
1	1	−4
2	1	−5
3	1	−6
4	1	−8
5	1	−9

Figure 5.19 Plot of radial magnetic energy in a (1, n) Fourier mode as a function of time: "field error" case at S = 6000. No mode is clearly dominant by the end of the simulation.

5.20 are the corresponding plots for the case in which a (1, −4) "field error" was introduced, as in the low−S run. Figure 5.19 shows that considerable sharing of the energy between modes takes place, unlike in the low S case of Figure 5.15. Apparently, no great reduction in the overall instability level is to be had. However, the m = 0 spectrum of Figure 5.20 shows a suppression of N = 2 and a growth around N = 4. The m = 1 modes have "spread out" to a spacing of $\Delta n = 4$. This corresponds to a greater physical separation of resonant surfaces. The island overlap which leads to the creation of stochastic field lines could be reduced. On the other hand,

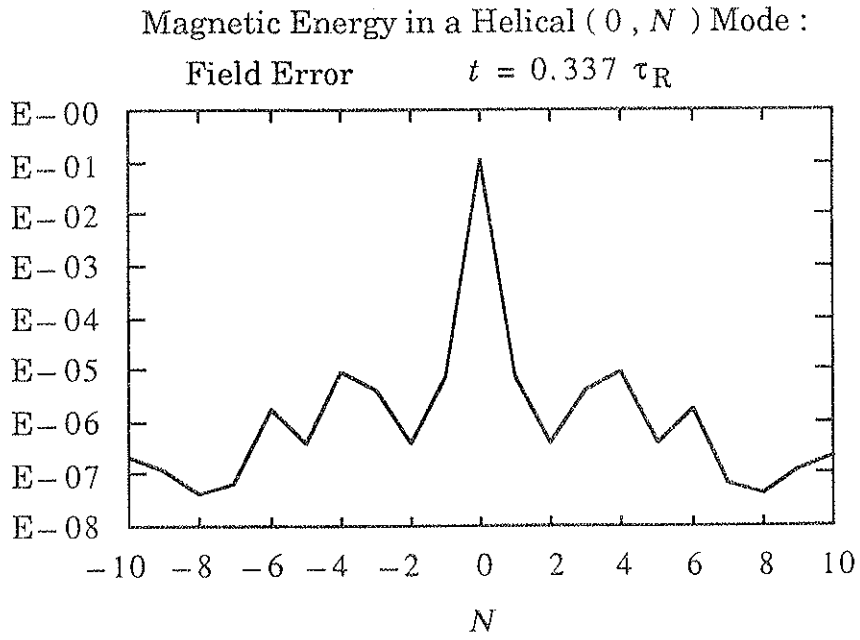

Figure 5.20 Plot of magnetic energy in a (0,N) Fourier mode as a function of n. This is the end of the "field error" case at S = 6000. The dominant mode has moved to |N| = 4 and |N| = 2 has been suppressed.

the spreading of the peak around N = 4 works against this mode separation. No clear advantage is evident.

Thus, although the consequences on mode separation and stochasticity need to be explored further, it appears that introducing a single "field error" in an attempt to control the mode-spectrum in the plasma will not work as first conjectured. The presence of a small level of external field errors can affect an RFP plasma in subtle ways. On the positive side, the error fields will not alter the reversed steady state.

However, they may affect which modes will grow to sustain it. On the negative side, this selection process can not be easily used to control the unstable mode spectrum, although some subtle improvement may be obtained. At this point, the best that can be achieved is an awareness of the presence of field-error effects on the plasma instability spectrum.

REFERENCES

[1] D. D. Schnack, E. J. Caramana, and R. A. Nebel, Phys. Fluids **28**, 330 (1985).

[2] R. A. Nebel, E. J. Caramana, and D. D. Schnack, Phys. Fluids B **1**, 1671 (1989).

[3] D. D. Schnack (private communication).

CHAPTER 6

CONCLUSION

The goal of this work has been to extend the treatment of field-error effects on an RFP plasma by including the plasma response, in the context of the single fluid MHD model. Given the complex physics of the RFP, certain approximations were made in representing the RFP plasma and in separating the effects of field-error perturbations from those of plasma instabilities. Some of these assumptions were rather restrictive, and any prediction based on them must be kept in proper perspective. In general, however, the results produced here illustrate the importance of using the MHD model of plasma-perturbation interactions to supplement the usual picture of the relaxed RFP in understanding field-error effects.

In Chapters 2 through 4 the RFP equilibrium was described by stable field profiles that were held fixed in time. The perturbations caused by edge field errors were able to interact with the equilibrium fields without interference from growing instabilities. This allowed the base level of magnetic island growth that might be expected in the absence of plasma activity to be assessed. It was also determined that islands produced by modes with $m=1$ were larger than those that would have been produced had Bessel Function Model perturbation profiles been used. More significantly, islands produced by $m=0$ modes were smaller than those that would have been expected from Bessel Function Model profiles.

For a realistic plasma, the importance of this latter observation does not lie in the stated values of amplification and reduction, however. Experimental RFP's do not have the fixed, stable equilibrium profiles assumed above. They show evidence of the growth and saturation of resistive instabilites. Simulations suggest that these instabilities give rise to islands that swamp the islands produced by the field errors, let alone any increase or decrease in their size. These numbers are not as important as the gain in physical understanding. Realistic effects in the equilibrium fields (non-constant λ) have been shown to make the field-error perturbations significantly larger at a resonant surface, while certain features governing the plasma-perturbation interaction (finite resistivity, viscosity, and flow) act to lessen this effect. The fact that the use of more detailed physical effects leads to conclusions that differ from those of the commonly used Bessel Function Model indicates the importance of considering the plasma-perturbation interaction in modeling an experimental RFP.

A similar argument can be advanced about interpreting the results of Chapter 5, in which the field errors were allowed to interact with an unstable, evolving RFP plasma. Care should be taken in applying observations from the simulation results directly to the interpretation of experimental data. The numerical results showing the influence of the field errors on the resistive-instability spectrum were obtained at a value of S much smaller ($S = 1000$) than the values that characterize experiments, although the effects were observed to persist in the scaling

runs (up to S = 4000). In addition, this effect required that the initial level of the field errors be comparable to that of the plasma "noise," a situation that may or may not occur experimentally.

Nevertheless, these results can be used as guides toward understanding what is happening in the experiment. Although relaxation theory may describe an RFP experiment well in a time-averaged sense, such a plasma is not relaxed. Instabilties grow and damp away. The approach to reversal, and not just the relaxed state, must be considered. Resistive MHD can be succesful as a means to understanding this process, but only if the experimental results can be interpreted properly. The simulations of Chapter 5 show that the field errors can affect which resistive instabilities contribute and may thus obscure some of the underlying RFP physics. A means of determining this is suggested by the results: the experimental m = 0 instability spectrum can be checked for a value of N that may correspond to a characteristic field-error periodicity. This insight arose from using resistive MHD to model the field-error problem.

Thus, by using resistive MHD to model plasma-perturbation interactions near a relaxed RFP state, this work provides additional physical insights into self-consistent field-error effects on an RFP plasma.

APPENDIX

SOLVING BOUNDARY VALUE PROBLEMS VIA "INVARIANT IMBEDDING"

A.1 INTRODUCTION

Invariant imbedding is a method that can be used to solve two-point boundary value problems. As mentioned in Chapter 3, the method employs a form of solution that converts the equations to be solved from a linear, first-order system subject to boundary conditions to a nonlinear, first-order system subject to initial conditions. The original boundary conditions are then imposed as constraints on the solution. Other constraints arise from the assumed form of the solution, and the entire set form a system of simultaneous linear equations. These can be solved by matrix methods to find the quantities needed to specify the solution satisfying the boundary conditions.

All this sounds rather complicated, but invariant imbedding has a few advantages over other well-known methods of solution, such as "shooting" or finite-differences. The boundary conditions are imposed in a matrix problem that is separate from the integration of the initial-value system. Thus, a change in the boundary conditions does not require that the entire problem be solved again, unlike in either of the other

methods. In problems with a boundary value at "infinity," like the equations in Chapter 4, the convergence of the solution at different interval lengths can be checked by simply extending the integration. Also, in contrast to a "shooting" method, efficient implementation of an imbedding algorithm only requires one integration per problem. The initial-value equations involved are easier to handle numerically.

This Appendix is not intended as a review of invariant imbedding. This has been adequately done elsewhere.[1] In fact, in the reference just given, the author cites a bibliography "... which contains over 500 articles on invariant imbedding and related topics."[2] The purpose here is to outline the method as it was applied to the equations of Chapters 3 and 4.

A.2 NUMERICAL METHOD

Consider a second-order boundary-value problem similar in form to the problems in Chapters 3 and 4. The independent variable is taken to be x, on the interval $0 \le x \le a$. The differential equation is written as a set of coupled first-order equations, with u as the dependent variable:

$$\frac{\partial u}{\partial x} = v(x) \qquad \text{(A.2.1)}$$

and

$$-\frac{\partial v}{\partial x} = c(x)\,u(x) + d(x)\,v(x) + f(x) \ . \qquad \text{(A.2.2)}$$

The solutions are required to obey the following boundary conditions:

$$\alpha_0 u(0) + \beta_0 v(0) = \gamma_0 \qquad \text{(A.2.3)}$$

and

$$\alpha_a u(a) + \beta_a v(a) = \gamma_a \ . \qquad \text{(A.2.4)}$$

(In the case of the fourth-order equations of Chapter 4, the problem must be written as a second-order matrix problem. If the problem is fourth-order in the dependent variable y, the two-vectors $\mathbf{u}$ and $\mathbf{v}$ can be defined as follows: $\mathbf{u} \equiv [\, y \,,\, \partial^2 y / \partial x^2 \,]$ and $\mathbf{v} \equiv [\, \partial y / \partial x \,,\, \partial^3 y / \partial x^3 \,]$. Then the problem can be cast in the above form, using two-by-two matrices for c, d and the α's and β's, and two-vectors for f and the γ's.)

The invariant imbedding method proceeds by assuming a certain form of solution. The assumed form is given below:

$$v(x) = s_1(x)\, u(x) + s_2(x)\, v(0) + s_3(x) \qquad \text{(A.2.5)}$$

$$u(0) = t_1(x)\, u(x) + t_2(x)\, v(0) + t_3(x) \ . \qquad \text{(A.2.6)}$$

The s and t functions can be shown to obey the following equations:

$$-\frac{\partial s_1}{\partial x} = c(x) + d(x)\, s_1(x) + s_1{}^2(x) \ , \quad s_1(0) = 0 \qquad \text{(A.2.7)}$$

$$-\frac{\partial s_2}{\partial x} = [\, d(x) + s_1(x) \,]\, s_2(x) \ , \qquad s_2(0) = 1 \qquad \text{(A.2.8)}$$

$$-\frac{\partial s_3}{\partial x} = [\, d(x) + s_1(x) \,]\, s_3(x) + f(x) \ , \quad s_3(0) = 0 \qquad \text{(A.2.9)}$$

$$-\frac{\partial t_1}{\partial x} = t_1(x)\, s_1(x) \ , \qquad t_1(0) = 1 \qquad \text{(A.2.10)}$$

$$-\frac{\partial t_2}{\partial x} = t_1(x)\, s_2(x)\,, \qquad t_2(0) = 0 \qquad \text{(A.2.11)}$$

$$-\frac{\partial t_3}{\partial x} = t_1(x)\, s_3(x)\,, \qquad t_3(0) = 0\,. \qquad \text{(A.2.12)}$$

This is the set of nonlinear, first-order, initial-value equations that replaces the set of linear, first-order, boundary-value equations (A.2.1)-(A.2.2). (In the fourth-order problem, s_1, s_2, t_1, and t_2 become two-by-two matrices, s_3 and t_3 become two-vectors, and "1" becomes the two-by-two identity matrix. Both the equations above and those to be given below, read as matrix equations, show the matrices in the proper order for multiplication.)

The solution process begins with the integration of equations (A.2.7)-(A.2.12). These are integrated over the interval $0 \le x \le a$ using the Runge-Kutta-Verner fifth and sixth order method mentioned in Chapter 3. After the integration, equation (A.2.6) is evaluated at $x = a$. Using this result, equations (A.2.5) and (A.2.6) can be inverted:

$$u(x) = t_1^{-1}(x) \left\{ t_1(a)\, u(a) + \left[t_2(a) - t_2(x) \right] v(0) + \left[t_3(a) - t_3(x) \right] \right\} \qquad \text{(A.2.13)}$$

$$v(x) = s_1(x)\, u(x) + s_2(x)\, v(0) + s_3(x)\,, \qquad \text{(A.2.14)}$$

producing the desired solutions for $u(x)$ and $v(x)$.

The final part of the solution lies in the identification of the boundary values $u(a)$ and $v(0)$. These must be obtained from the boundary equations (A.2.3)–(A.2.4). However, these two equations contain four variables — $u(0)$ and $v(a)$ as well as $u(a)$ and $v(0)$. An additional two equations in these variables can be obtained by evaluating equations (A.2.5) and (A.2.6) at $x = a$:

$$-s_1(a)\,u(a) + v(a) - s_2(a)\,v(0) = s_3(a) \qquad \text{(A.2.15)}$$

$$-t_1(a)\,u(a) + u(0) - t_2(a)\,v(0) = t_3(a)\ . \qquad \text{(A.2.16)}$$

The problem can be written as a four–by–four matrix equation:

(A.2.17)

$$\begin{bmatrix} -s_1(a) & 1 & 0 & -s_2(a) \\ -t_1(a) & 0 & 1 & -t_2(a) \\ 0 & 0 & \alpha_0 & \beta_0 \\ \alpha_a & \beta_a & 0 & 0 \end{bmatrix} \begin{bmatrix} u(a) \\ v(a) \\ u(0) \\ v(0) \end{bmatrix} = \begin{bmatrix} s_3(a) \\ t_3(a) \\ \gamma_0 \\ \gamma_a \end{bmatrix}$$

The matrix can then be inverted, and the values of $u(a)$ and $v(0)$ found in terms of the known α's , β's , γ's , and integrated functions. At this point, the solution of the problem has been specified completely.

Although the "formal" procedure for obtaining a solution by invariant imbedding has been completely given above, there are some

practical considerations that are worth knowing. An evaluation of the two differences in equation (A.2.13) — $[\, t_2(a) - t_2(x)\,]$ and $[\, t_3(a) - t_3(x)\,]$ — sometimes amounts to subtracting two large, nearly-identical numbers to find a small number. This produces a loss of significance. It is useful to take advantage of the fact that the differential equation for $t_2(x)$, equation (A.2.11), does not depend on the value of $t_2(x)$. The same is true of equation (A.2.12) for $t_3(x)$. Moreover, these equations have the initial conditions $t_2(0) = t_3(0) = 0$. Thus, the interval $0 \le x \le a$ can be divided into M subintervals, and the integration can be restarted from zero on each subinterval. The values of $t_2(x)$ and $t_3(x)$ will not become very large on any one subinterval, and the difference functions $d_2(x) \equiv [\, t_2(a) - t_2(x)\,]$ and $d_3(x) \equiv [\, t_3(a) - t_3(x)\,]$ can be accurately constructed from the values on these subintervals. With the subinterval ends identified as a set of M + 1 positions x_i ($i = 1, \ldots, M+1$ with $x_1 = 0$ and $x_{M+1} = a$), define $\tau_2(i) = t_2(x_i)$ and $\tau_3(i) = t_3(x_i)$. Then, if $x_i \le x \le x_{i+1}$:

$$d_2(x) = \left[\, \tau_2(i+1) - t_2(x) \,\right] + \sum_{k=i+2}^{M+1} \tau_2(k) \qquad \text{(A.2.18)}$$

and

$$d_3(x) = \left[\, \tau_3(i+1) - t_3(x) \,\right] + \sum_{k=i+2}^{M+1} \tau_3(k) \; . \qquad \text{(A.2.19)}$$

The second consideration is an extension of this idea. Given the nonlinear nature of the equations, any of the integrated functions can become large when the integration extends over a large interval. This can result in a loss of accuracy in the numerical integration. In that case, it is

wise to periodically restart the entire problem. If the same M + 1 subintervals as above are considered, the form of the solution given by equations (A.2.5) and (A.2.6) is replaced by:

$$v(x) = s_1(x)\,u(x) + s_2(x)\,v(x_i) + s_3(x) \qquad \text{(A.2.20)}$$

$$u(x_i) = t_1(x)\,u(x) + t_2(x)\,v(x_i) + t_3(x) \qquad \text{(A.2.21)}$$

for $x_i \leq x \leq x_{i+1}$. Within each subinterval, the integrations proceed as before. The construction of $u(x)$ and $v(x)$, however, depends on a knowledge of $u(x_{i+1})$ and $v(x_i)$. These are determined by an expanded version of the matrix boundary-value problem, (A.2.17). For each interval, equations (A.2.20) and (A.2.21) are evaluated at the end of the interval, at $x = x_{i+1}$. All these equations are then included with the boundary equations (A.2.3) and (A.2.4). The vector of unknowns is expanded to include all the $u(x_i)$ and $v(x_i)$. After the matrix problem has been solved, an inversion similar to that shown in equations (A.2.13) and (A.2.14) can be performed in each interval. Thus, with some clever and careful programming, the invariant imbedding algorithm can be successfully implemented with some very satisfactory results.

REFERENCES

[1] M. R. Scott, in *Numerical Solutions of Boundary Value Problems for Ordinary Differential Equations*, edited by A. K. Aziz (Academic Press, New York, 1975), p.89.

[2] *Ibid.*, p. 90.